SÃO PAULO STATE UNIVERSITY (UNESP) "JÚLIO DE MESQUITA FILHO"
SCHOOL OF ENGINEERING
CÂMPUS OF ILHA SOLTEIRA

Iago Lessa de Oliveira

On the mechanics of intracranial aneurysms walls: Numerical assessment of the influence of tissue hyperelastic laws and heterogeneity and the major role played by curvature on pathways to rupture

Ilha Solteira, Brazil
2022

UNIVERSIDADE ESTADUAL PAULISTA
"JÚLIO DE MESQUITA FILHO"
Câmpus de Ilha Solteira

Mechanical Engineering Graduate Programme of the
School of Engineering of Ilha Solteira

Iago Lessa de Oliveira

On the mechanics of intracranial aneurysms walls: Numerical assessment of the influence of tissue hyperelastic laws and heterogeneity and the major role played by curvature on pathways to rupture

Doctorate Thesis submitted to the Doctorate Course of the Mechanical Engineering Graduate Programme of the São Paulo State University (UNESP), School of Engineering, Câmpus of Ilha Solteira (FEIS).

Supervisor: Prof. Dr. José Luiz Gasche
Professor of the Mechanical Engineering Department of FEIS/UNESP

Ilha Solteira, Brazil
2022

FICHA CATALOGRÁFICA
Desenvolvido pelo Serviço Técnico de Biblioteca e Documentação

O48m

Oliveira, Iago Lessa.
On the mechanics of intracranial aneurysms walls: numerical assessment of the infuence of tissue hyperelastic laws and heterogeneity and the major role played by curvature on pathways to rupture / Iago Lessa Oliveira. -- Ilha Solteira: [s.n.], 2022
247 f. : il.

Tese (doutorado) - Universidade Estadual Paulista. Faculdade de Engenharia de Ilha Solteira. Área de conhecimento: Ciências Térmicas, 2022

Orientador: José Luiz Gasche
Coorientador: Julio Militzer e Carlos Eduardo Baccin
Inclui bibliografia

1. Intracranial aneurysms. 2. Fluid-solid interaction. 3. Hyperelasticity. 4. Heterogeneous properties. 5. Numerical simulations.

Raiane da Silva Santos
Supervisora Técnica de Seção
Seção Técnica de Referência, Atendimento ao usuário e Documentação
Diretoria Técnica de Biblioteca e Documentação
CRB/8 - 9999

UNIVERSIDADE ESTADUAL PAULISTA

Câmpus de Ilha Solteira

CERTIFICADO DE APROVAÇÃO

TÍTULO DA TESE: On the mechanics of intracranial aneurysms walls: Numerical assessment of the influence of tissue hyperelastic laws and heterogeneity and the major role played by curvature on pathways to rupture

AUTOR: IAGO LESSA DE OLIVEIRA
ORIENTADOR: JOSE LUIZ GASCHE
COORIENTADOR: CARLOS EDUARDO BACCIN
COORIENTADOR: JULIO MILITZER

Aprovado como parte das exigências para obtenção do Título de Doutor em ENGENHARIA MECÂNICA, área: Ciências Térmicas pela Comissão Examinadora:

Prof. Dr. JOSE LUIZ GASCHE (Participaçao Virtual)
Departamento de Engenharia Mecânica / Faculdade de Engenharia de Ilha Solteira - UNESP

Prof. Dr. EMANUEL ROCHA WOISKI (Participaçao Virtual)
Departamento de Engenharia Mecânica / Faculdade de Engenharia de Ilha Solteira - UNESP

Prof. Dr. LEANDRO OLIVEIRA SALVIANO (Participaçao Virtual)
Departamento de Engenharia Mecânica / Faculdade de Engenharia de Ilha Solteira - UNESP

Prof. Dr. PHILIP CARDIFF (Participaçao Virtual)
School of Mechanical and Materials Engineering / University College Dublin - UCD

Prof. Dr. ANDRE RICARDO OLIVEIRA DA FONSECA (Participaçao Virtual)
Universidade Federal do ABC

Ilha Solteira, 20 de junho de 2022

Dedico este trabalho à memória de dois mentores

Ao Prof. Julio Militzer,
pela irrestrita ajuda, sem a qual este trabalho não teria terminado.

Ao meu avô, Edmar,
pois, sem seus esforços em vida, eu não o teria nem começado.

To the memory of two mentors

To Prof. Julio Militzer
for the constant support, without which this work would not have been finished.

To my grandfather, Edmar,
because without his efforts in life I would not have even started it.

ACKNOWLEDGEMENTS

This work could not be accomplished without the warm support of my family. To them I am infinitely grateful and, especially, to my mother, Selma, who provided constant motivation.

To the friends of *república* and the close ones that were always there for the weekend beer, a second family. They helped and shared moments of both happiness and sadness during the struggling years that a doctorate often imposes. A more than special thanks to Leonardo Lachi Manetti for the warm friendship and all the help and support.

To the friends of the Mechanical Engineering Department of FEIS and the ones that I got to know while working in the Hospital Israelita Albert Einstein. Each of them contributed in some way to make me accomplish this work.

My sincere gratitude also goes to my supervisors Dr. José Luiz Gasche (FEIS/UNESP) and to Dr. Julio Militzer (Dalhousie University, Halifax, Canada) for all their help, support, guidance, and meaningful discussions. To Dr. Carlos Eduardo Baccin for teaching a lot on intracranial aneurysms and how their are dealt with in the medical practice as also for providing part of the images used in this work. A special thanks to Dr. Philip Cardiff (University College Dublin, Ireland) for receiving me for an internship in Dublin and for all the important discussions and contributions without which this work could not be accomplished.

I gratefully acknowledge the Mechanical Engineering Department of the School of Engineering of Ilha Solteira and the Mechanical Engineering Graduate Programme (PPGEM) for the provided infrastructure to develop this work as also the financial supports by grant 2017/18514-1 and grant 2019/19098-7, São Paulo Research Foundation (FAPESP). This study was financed in part by the Coordenação de Aperfeiçoamento de Pessoal de Nível Superior – Brasil (CAPES) – Finance Code 001. Thanks also to the technical support and resources supplied by the Center for Scientific Computing (NCC/GridUNESP) of UNESP, by ACENET through Dalhousie University and Compute Canada.

Finally, I would like to express my gratitude to the open-source software users communities, which have always been willing to help.

For every complex problem there is an answer that is clear, simple, and wrong.

Henry L. Mencken
American journalist, essayist and satirist

ABSTRACT

Intracranial aneurysms (IAs) are abnormalities formed in the cerebral arteries characterized by outpouching regions of their walls. The danger with these lesions occurs if they rupture, which causes intracranial hemorrhage and possibly leads to the death of the patient, presenting a mortality rate as high as 50 %. The rupture event is hard to predict, though, and, currently, surgical treatments also pose risks to the patient. Numerical simulations of the blood flow inside IAs have been extensively used to study them because of the well-known connections between hemodynamics and their inception, growth, and rupture. Physically, although it should be modeled as a Fluid-Solid Interaction (FSI) problem, the majority of those works have solely focused on the hemodynamics while either ignoring the wall tissue motion entirely, through rigid-wall modeling, or using limited assumptions for it. One possible explanation is the scarcity of measurements of their wall mechanical properties and also its thickness, which limits the use of better modeling options. Consequently, few works have investigated the impact of tissue modeling on their mechanical response, an important endeavor to try to predict the likelihood of rupture, because it is a wall-exclusive event that theoretically depends on the level of stress. In this context, this work investigated the influence of different hyperelastic laws and the material properties and thickness heterogeneity on the wall mechanics of IAs, given their rupture status. Pulsatile numerical simulations with patient-specific vascular geometries harboring IAs were carried out using the one-way fluid-solid interaction solution strategy implemented in solids4foam, an extension of OpenFOAM®, in which the blood flow is solved and applied as the driving force of the wall motion. First, it was found that different wall morphology models yielded smaller absolute differences in the mechanical response than different hyperelastic laws. Second, the stretch levels of IAs walls were more sensitive to the hyperelastic laws and material constants than the stress, especially for ruptured IAs, allowing the identification of these by the higher stretch levels instead of stress levels. Additionally, the morphology variable that best correlated with regions of high stress and stretch was the wall curvature. Finally, these findings could be used to guide modeling decisions on IA simulations and also suggest new metrics based on the wall curvature to predict the likelihood of rupture.

Keywords: Intracranial aneurysms. Fluid-solid interaction. Hyperelasticity. Heterogeneous properties. Numerical simulations.

RESUMO

Os aneurismas intracranianos (AIs) são dilatações nas artérias cerebrais, que podem ocasionar grande perigo caso elas rompam, causando hemorragia intracraniana e possivelmente levando à morte do paciente — AIs apresentam uma taxa de mortalidade de até 50 %. A ruptura, porém, é difícil de prever e, atualmente, os tratamentos cirúrgicos também apresentam riscos para o paciente. Simulações numéricas do escoamento dentro de AIs têm sido amplamente utilizadas para estudá-los devido à conexão entre hemodinâmica e o início, crescimento e ruptura dos aneurismas. Embora deva ser modelado como um problema de interação fluido-sólido (IFS), a maioria desses trabalhos se concentrou exclusivamente na hemodinâmica, ignorando completamente o movimento da parede, por meio de modelagem de parede rígida, ou usando modelos bastante limitadas. Uma possível explicação é a escassez de medidas experimentais das propriedades mecânicas do tecido e também da espessura da parede, o que limita o uso de melhores modelos. Consequentemente, poucos trabalhos investigaram o impacto dos differents modelos do tecido de AIs em sua resposta mecânica, o que seria importante para tentar prever a ruptura, pois este é um evento que, teoricamente, depende dos níveis de tensão. Neste contexto, este trabalho investigou a influência de diferentes leis hiperelásticas e da heterogeneidade das propriedades mecânicas e da espessura na resposta mecânica de uma amostra de AIs rompidos e não rompidos. Simulações numéricas com geometrias vasculares reais foram realizadas usando a técnica de IFS unidirecional, implementada no solids4foam, uma extensão do OpenFOAM®, na qual o escoamento é resolvido e aplicado como força motriz do movimento da parede. Diferentes modelos de morfologia de parede tiveram menor influência na resposta mecânica do que diferentes leis hiperelásticas. Também foi encontrado que os níveis de deformação foram mais sensíveis às leis hiperelásticas e propriedades do material do que a tensão de Cauchy, especialmente para os AIs rompidos, permitindo a identificação destes pelos níveis de deformação mais elevados ao invés da tensão. Além disso, a variável morfológica que melhor se correlacionou com regiões de alta tensão e deformação foi a curvatura da parede. Finalmente, essas descobertas podem ser usadas para orientar as decisões de modelagem em simulações com AIs e também sugerir novas métricas baseadas na curvatura da parede para prever a probabilidade de ruptura.

Palavras-chave: Aneurismas intracranianos. Interação fluido-sólido. Hiperelasticidade. Propriedades heterogêneas. Simulação numérica.

RÉSUMÉ

Les anévrismes intracrâniens (AIs) sont des anomalies formées sur certaines régions du système vasculaire humain caractérisées par la dilatation de leur paroi. Le danger avec ces lésions survient si elles se rompent, ce qui provoque une hémorragie intracrânienne et peut entraîner la mort du patient — la maladie présente un taux de mortalité pouvant atteindre 50 %. Malheureusement, la rupture est difficile à prévoir et, actuellement, les traitements chirurgicaux présentent également des risques pour le patient. Les simulations numériques de l'écoulement du sang dans les AIs ont été largement utilisées pour les étudier en raison des liens biens connus entre l'hémodynamique et leur apparition, croissance et rupture. Bien qu'il s'agisse d'un problème d'interaction fluide-solide (IFS), la majorité de ces travaux se sont uniquement concentrés sur l'hémodynamique tout en ignorant le mouvement de la paroi soit par une modélisation de paroi rigide, soit en utilisant des hypothèses très limitées. Une explication possible est la difficulté à trouver des mesures des propriétés mécaniques ou de l'épaisseur de la paroi, ce qui limite l'utilisation de meilleures options de modélisation. Par conséquent, une minorité de recherches ont étudié l'influence de la modélisation de la paroi des AIs sur leur réponse mécanique, un effort assez important afin de calculer leur probabilité de rupture, car il s'agit d'un événement qui dépend, théoriquement, du niveau de tension. Dans ce contexte, ce travail a étudié l'influence de différentes lois hyperélastiques, de l'hétérogénéité des propriétés mécaniques et de l'épaisseur de la paroi sur la réponse mécanique des AIs rompus et non rompus. Des simulations numériques pulsatiles avec des géométries vasculaires réelles ont été réalisées à l'aide de la technique de IFS unidirectionnelle avec le logiciel *solids4foam*. Premièrement, les résultats montrent que différents modèles de morphologie ont une influence plus petite sur la réponse mécanique que différentes lois hyperélastiques. Deuxièmement, les niveaux de déformation étaient plus sensibles aux lois hyperélastiques et aux propriétés mécaniques qu'à la tension, en particulier dans le cas d'AIs rompus, permettant leur identification par le plus haut niveau de déformation plutôt que par la tension. De plus, la propriété morphologique que a mieux corrélée avec les régions de déformations élevées était la courbure de la paroi. Finalement, ces résultats pourraient être utilisés pour guider les décisions de modélisation sur les simulations des AIs et, également, pour suggérer de nouvelles métriques basées sur la courbure pour calculer la probabilité de rupture.

Mots clé : Anévrismes intracrâniens. Interaction fluide-solide. Hyperélasticité. Proprietés hétérogènes. Simulation numérique.

LIST OF FIGURES

LIST OF TABLES

LIST OF ACRONYMS

1WFSI	One-way Fluid-solid Interaction
2WFSI	Two-way Fluid-solid Interaction
ACA	Anterior Cerebral Artery
ACoA	Anterior Communicating Artery
AFI	Aneurysm Formation Indicator
ALE	Arbitrary Lagrangian-Eulerian
BA	Basilar Artery
BC	Boundary Condition
CFD	Computational Fluid Dynamics
CSD	Computational Solid Dynamics
CTA	Computational Tomography Angiography
DSA	Digital Subtraction Angiography
EC	Endothelial Cell
FEM	Finite Element Method
FSI	Fluid-Solid Interaction
FVM	Finite Volume Method
HWP	Hemodynamic Wall Parameter
IA	Intracranial Aneurysm
ICA	Internal Carotid Artery
IEL	Internal Elastic Lamina
IQN-ILS	Interface Quasi-Newton-Implicit Jacobian Least-Squares
MCA	Middle Cerebral Artery
MR	Mooney-Rivlin
NO	Nitric Oxide
OSI	Oscillatory Shear Index
PDE	Partial Differential Equations
SAH	Subarachnoid Hemorrhage
SD	Standard Deviation
SMC	Smooth Muscle Cell
SVK	St. Venant-Kirchhoff
TAWSS	Time-averaged Wall Shear Stress

VA	Vertebral Arteries
VOI	Volume Of Interest
WLR	Wall-to-lumen Ratio
WSS	Wall Shear Stress

NOTATION

Tensors of the Euclidean three-dimensional space of ranks 1 and 2 are typed in italic boldface letters, with first-order tensors, or vectors, represented by lowercase bold letters ($\boldsymbol{a}$, $\boldsymbol{b}$...) and tensors of rank 2 by uppercase boldface letters ($\boldsymbol{A}$, $\boldsymbol{B}$...); the major exceptions are the Cauchy stress tensor, $\boldsymbol{\sigma}$, its viscous part, $\boldsymbol{\tau}$, and the linear or engineering strain tensor, $\boldsymbol{\varepsilon}$, because these are common symbols found in the literature to represent them. Tensors of rank 4 are represented by uppercase blackboard Latin letters ($\mathbb{A}$, $\mathbb{B}$...) and tensors of zeroth order, or scalars, are represented by italic not-boldface letters (a, b...) — this also includes the components of tensors of order ≥ 1.

Matrices that belong to the general $\mathbb{R}^{m\times n}$ space and vectors of $\mathbb{R}^n$, which are considered to be column vectors, are represented by boldface letters: the former in uppercase typeface and the latter in the lowercase typeface. The main difference between generic matrices of $\mathbb{R}^{m\times n}$ and tensors of the three-dimensional Euclidean space is made explicit in the context and/or by the operators used between them, for example, the equation $\boldsymbol{x}\cdot\boldsymbol{A}\cdot\boldsymbol{x}$, where "$\cdot$" is the commonly used notation for the scalar product indicates that $\boldsymbol{x}$ is a vector and $\boldsymbol{A}$ is a tensor of order ≥ 2 of the Euclidean space, whereas $\mathbf{x}^{\mathrm{T}}\mathbf{A}\mathbf{x}$ indicates that $\mathbf{x}$ is a column vector and $\mathbf{A}$ a matrix. If they overlap in the text, then matrices were explicitly represented with their symbols between brackets and column vectors with braces, for clarity as follows: $\mathbf{A}$ is $[\mathrm{A}]$, and $\mathbf{x}$ is $\{\mathrm{x}\}$.

The vector notation was mainly used to represent the equations of Continuum Mechanics instead of using Einstein's index notation, which was preferred only in demonstrations of tensorial equations, in which case lowercase Latin subscripts were used to represent the tensor components.

LIST OF LATIN SYMBOLS

Symbol	Description	Unit
A	Area of a surface or region	m^2
E	Young's modulus of a solid	Pa
G	Shear modulus of a solid	Pa
H	Mean curvature of a surface	m^{-1}
I_1	First principal invariant of the deformation tensors	–
I_2	Second principal invariant of the deformation tensors	–

Symbol	Description	Unit
J	Jacobian (determinant of the deformation gradient)	–
K	Gaussian curvature of a surface	m^{-2}
L	Length	m
N	Number of moles of a species i in a system	mol
P_r^{IA}	Rupture probability of an intracranial aneurysm	–
P	Perimeter of a contour	m
Q	Function of the strain tensor components used in the generic Fung-type models	–
R_i	Cylinder inner radius	m
R_o	Cylinder outer radius	m
S	Entropy of a system	$\mathrm{J\,K}^{-1}$
S	Surface of volume V, ∂V, in spatial coordinates	m^2
T_c	Cardiac period	s
T	Temperature	K
U	Internal energy of a system	J
V	Volume of a region in spatial coordinates	m^3
$\bar{q}_a$	Mean blood flow rate through an artery section	$\mathrm{ml\,s}^{-1}$
$\boldsymbol{\mathcal{M}}_{\mathbf{a}}$	Symbolic representation of the added-mass operator	–
$\dot{\gamma}$	Shear rate components in a fluid flow	s^{-1}
$\dot{w}_{int}$	Internal mechanical power in a system, caused by the stress and deformation	W
$\mathbb{C}$	Elastic moduli tensor	Pa
$\mathbb{I}$	Fourth-order identity tensor	–
$\mathbb{P}$	Projection tensor that maps the isochoric stress tensors to the physical stress tensor in Lagrangian coordinates	–
a_C	Diagonal coefficients of the linearized transport equation for the volume V_C	$\mathrm{kg\,s}^{-1}$
p_o	Intracranial pressure	Pa
p_{tr}	Transmural pressure	Pa
V_C	Volume of a cell with centroid C in a finite volume mesh	m^3
$\mathcal{M}$	A mathematical metric of the stress and stretch fields over V_{ia}	–

Symbol	Description	Unit
$\mathcal{R}$	The group of ruptured aneurysms	–
$\mathcal{U}$	The group of unruptured aneurysms	–
AFI	The *potential* aneurysm formation indicator	–
AR	Aspect ratio of an aneurysm, defined as the ratio between dome height and neck diameter	–
EI	Ellipticity index	–
GAA	Area-averaged Gaussian curvature of a surface	mm^{-2}
GLN	L2-norm of the Gaussian curvature field of a surface	–
GON	The gradient oscillatory number	–
MAA	Area-averaged mean curvature of a surface	mm^{-1}
MLN	L2-norm of the mean curvature of a surface	–
NSI	Nonsphericity index	–
OSI	The oscillatory shear index	–
RRT	The relative residence time indicator	–
SR	Size ratio	–
TAWSSG	Surface gradient of the time-averaged wall shear stress gradient vector, defined on the surface p-coordinate direction (the flow direction)	$\mathrm{Pa\,m}^{-1}$
TAWSS	Time-average WSS field	$\mathrm{Pa\,m}^{-1}$
UI	Undulation index	–
WLR	Wall to lumen ratio	–
WSSPI	Pulsatility index of the wall shear stress magnitude	–
WSSTG	Maximal temporal derivative of the wall shear stress magnitude	$\mathrm{Pa\,s}^{-1}$
transWSS	Temporal average of the wall shear stress vector along its average transversal direction	Pa
$\mathbf{A}$	Coefficients matrix of a system of equations assembled for a finite volume mesh	$[\phi]$
$\boldsymbol{B}$	Left Cauchy-Green deformation tensor	–
$\boldsymbol{C}$	Right Cauchy-Green deformation tensor	–
$\boldsymbol{D}$	Rate of deformation tensor	s^{-1}

Symbol	Description	Unit
$\boldsymbol{E}$	Green-Lagrange strain tensor	–
$\boldsymbol{F}$	Deformation gradient tensor	–
$\boldsymbol{I}$	Second order identity tensor	–
$\boldsymbol{P}$	Nominal stress tensor	Pa
$\boldsymbol{R}$	Rotation tensor	–
$\boldsymbol{S}$	Second Piola-Kirchhoff stress tensor	Pa
$\boldsymbol{G}$	Wall shear stress gradient vector, defined on the surface pq-coordinate system	$\mathrm{Pa\,m^{-1}}$
$\boldsymbol{S}_f$	Normal vector to the face f of a polyhedral cell	$\mathrm{m^2}$
$\boldsymbol{b}$	Body forces per unit mass	$\mathrm{N\,kg^{-1}}$
$\boldsymbol{b}$	Source vector of the linearized momentum equations for a control volume	$[\phi]\mathrm{kg\,s^{-1}}$
$\boldsymbol{d}_{CN}$	Vector joining the centroids of adjacent cells in a finite volume mesh	m
$\boldsymbol{f}$	Generic force vector	N
$\boldsymbol{n}$	Unit normal vector to the surface S pointing outwards	–
$\boldsymbol{p}$	Mean flow direction adjacent to an artery's lumen	–
$\boldsymbol{q}$	Heat flux or heat flow vector, defined as the heat transfer per unit surface area	$\mathrm{W\,m^{-2}}$
$\boldsymbol{q}$	Transversal direction to the mean flow direction ($\boldsymbol{p}$)	–
$\boldsymbol{t}$	Generic traction vector	$\mathrm{N\,m^{-2}}$
$\boldsymbol{u}$	Solid displacement vector	m
$\boldsymbol{v}$	Material velocity	$\mathrm{m\,s^{-1}}$
$\boldsymbol{x}$	Eulerian or spatial coordinates system (Cartesian coordinates)	m
a	Generic coefficients of the linearized transport equation for the volume V_C	$\mathrm{kg\,s^{-1}}$
d_d	Maximum diameter of an aneurysm's dome	m
d_l	Vasculature lumen diameter at a specified section	mm
d_n	Maximum diameter of an aneurysm's neck	m
d_{pa}	Diameter of an aneurysm's parent artery section	m

Symbol	Description	Unit
e^{R}	Discretization error of a particular mesh computed using Richardson's extrapolation	–
e_{ia}	Thickness field of an aneurysm's wall	mm
f_a	Scale factor used on the calculation of the aneurysm thickness	–
g_n	Local geodesic distance to the aneurysm neck contour	mm
h_b	Bulge height of an aneurysm's dome	m
h_d	Maximum height of an aneurysm's dome perpendicular to ostium surface	m
h_{max}	Maximum height of an aneurysm's dome, measured from the ostium center	m
k	Consistency coefficient of Casson's model	Pa s
m	Mass	kg
n	Number of moles of a species i in a system	
p	Pressure field of a fluid flow	Pa
t	Time	s
v	Specific volume – volume per mass	$\mathrm{m^3\,kg^{-1}}$
w_{int}	Internal mechanical work in a system, caused by stress and deformation	J
T_{m}	Membrane tension	Pa m
e_w	Thickness field of arterial walls	mm
e_b	Thickness field of the branches walls	mm

LIST OF GREEK SYMBOLS

Symbol	Description	Unit
$\rho^{\mathrm{f}}_{\mathrm{ref}}$	Reference density of the weakly compressible model	$\mathrm{kg\,m^{-3}}$
$\boldsymbol{\tau}_w$	Wall shear stress vector defined on a vessel and aneurysm surface	Pa
Γ	Generic three-dimensional contour; boundary of an open surface S, ∂S, in spatial coordinates	m
Λ	Boundary of the domain Ω	$\mathrm{m^2}$
Ω	Spatial solution domain	$\mathrm{m^3}$

Symbol	Description	Unit
Ψ	Deformation work function or strain energy function	$\mathrm{J\,m^{-3}}$
Υ	Generalized displacement of a system	–
δ_v	Pulsatility of an intracranial aneurysm	–
η^{f}	Apparent viscosity of a non-Newtonian fluid	Pa s
σ_0	Von Mises or equivalent stress	Pa
σ_1	Maximum principal component of the Cauchy stress tensor	Pa
Λ^{fs}	Fluid-solid interface = $\Lambda^f \cap \Lambda^s$	–
$\Lambda^{\mathrm{fs}}_{fluid}$	Fluid mesh boundary corresponding to the fluid-solid interface	–
$\Lambda^{\mathrm{fs}}_{solid}$	Solid mesh boundary corresponding to the fluid-solid interface	–
ψ^{f^*}	Modified isothermal compressibility of a weakly compressible fluid	$\mathrm{s^2\,m^{-2}}$
λ_1	Largest eigenvalue of the stretch tensor	Pa
$\boldsymbol{\chi}$	Referential coordinates system for the arbitrary Lagrangian-Eulerian description	m
$\boldsymbol{\omega}$	Mesh velocity	$\mathrm{m\,s^{-1}}$
$\boldsymbol{\tau}$	Viscous part of the Cauchy stress tensor of a fluid flow	Pa
$\boldsymbol{\xi}$	Lagrangian or material coordinates system	m
κ_1	First principal curvature of a surface	$\mathrm{m^{-1}}$
κ_2	Second principal curvature of a surface	$\mathrm{m^{-1}}$
κ	Bulk modulus	Pa
λ^{s}	Second Lamé's constant of a solid	Pa
λ	Uniaxial stretch of a solid deforming	–
μ^{f}	Dynamic viscosity of a fluid	Pa s
μ^{s}	First Lamé's constant of a solid	Pa
μ_{a}	Eigenvalue of the added-mass operator	–
μ	Generic representation of Ogden's law material constants	Pa
μ	Chemical potential of a species crossing the boundary of a system	$\mathrm{J\,K^{-1}}$
ν^{f}	Kinematic viscosity of a fluid	$\mathrm{m^2\,s^{-1}}$

Symbol	Description	Unit
ν^{S}	Poisson's ratio of a solid	–
ϕ	Generic intensive (per unit mass) variable transported by a fluid flow	$[\phi]/\mathrm{kg}$
ψ	Isothermal compressibility of a fluid	$\mathrm{s}^2\,\mathrm{m}^{-2}$
ρ_{P}	Pearson's correlation coefficient	–
ρ_{S}	Spearman's correlation coefficient	–
ρ	Density	$\mathrm{kg\,m}^{-3}$
τ	Generalized force applied to a system	–
$\boldsymbol{\sigma}$	Cauchy stress tensor	Pa
$\boldsymbol{\varepsilon}$	Linear or engineering strain tensor	–
$\boldsymbol{e}$	True or logarithmic strain tensor	–
υ	Intensive generalized displacement state of a system	–
ξ	Representation of a material particle	–

SUBSCRIPTS

99	Indicates the 99th percentile of a distribution
C	Indicates variables evaluated at the centroid of a control volume
N	Indicates variables evaluated at the centroid of a neighbor control volume to cell V_C
0	Indicates variables at the initial instant $t = 0$
ab	Indicates a property of the aneurysm wall due to abnormal hemodynamics patches
b	Indicates variables defined on the branches of a vasculature
f	Indicate a face of a polyhedral control volume and a property evaluated at it
ia	Indicates variables defined or integrated on an aneurysm surface
max	Indicates the maximum value of a sample

SUPERSCRIPTS

F	Indicates variables defined for the Fung hyperelastic law
MR	Indicates variables defined for the Mooney-Rivlin hyperelastic law
Y	Indicates variables defined for the Yeoh hyperelastic law
fs	Used for variables related to the fluid-solid interface
f	Used for fluid-related variables
n	Time index
s	Used for solid-related variables

COLORMAPS PATTERNS

The colormaps used to depict the fields of the physical variables analyzed in this work are presented in the following table, together with their name, source, and the variable to which each of them was applied consistently.

Name and Source	Colormap	Employed with
Viridis (1)		Cauchy stress, $\boldsymbol{\sigma}$, and its components
Batlow (2)		Displacement field, $\boldsymbol{u}$
Lapaz (2)		Strain measures and stretch, λ
Imola (2)		Thickness of the aneurysm sac and arteries
RdOrYl (3)		Material constants c_{ij} and distance-to-neck, g_n, fields
Plasma (1)		Time-averaged wall shear stress (TAWSS)
Nuuk (2)		Oscillatory shear index (OSI)
PRGn (4, 5)		Gauss, K, and mean, H, curvatures

Only perceptually-uniform colormaps were selected (6, 7) that were freely available at the time of writing (1, 2). Due to the comparative nature of some discussions, note that instead of a continuous colormap, a discrete version of them was employed.

CONTENTS

Chapter 1

INTRODUCTION

1.1 BACKGROUND AND MOTIVATION

The word "aneurysm" originated from the Ancient Greek ἀνεύρυσμα (*aneúrusma*), meaning "a widening, a dilatation", based on the combination of ἀνά (*aná*) meaning "up" and εὐρύς ("eurús") meaning "wide". Today, it is the name of dilated regions of an artery wall that can arise in different sites of the human vascular system, more commonly found on the abdominal aorta and the arteries that reach the brain. In the latter case, they are called *intracranial aneurysms (IAs)* and generally occur on arterial bifurcations at the base of the brain. They are considered a dangerous pathology, are normally asymptomatic, and, in case of rupture, are likely to cause the death of the patient. Rupture prediction, though, is a complex problem and one goal that several works still try to accomplish, but a definitive answer to when an IA will rupture is hard to obtain, and depends on a complete understanding of their mechanobiology.

The disease and the rupture event have been experimentally studied since early by the medical community. In the last two decades, though, the number of works using numerical techniques to study it have increased substantially and several methodologies have been employed to analyze the different physical aspects of this disease. Computational Fluid Dynamics (CFD), for example, solves for the blood flow, while Computational Solid Dynamics (CSD) can be used to study the wall mechanics. A more complete approach, although more challenging, can be accomplished via Fluid-Solid Interaction (FSI) strategies, which include numerical techniques that account for the mechanical coupling between the blood flow and the artery motion. The flexibility of these numerical techniques, even with their own limitations, have dramatically improved the accumulated knowledge on the mechanics and mechanobiology of IAs as also on their inception, enlargement, and final rupture.

1.2 MAIN GOALS OF THIS THESIS

Nevertheless, several questions still remain. The one tackled in this work relates to the rupture of an IA, the event where the aneurysm wall is, in principle, degraded enough to the point that the blood flow forces cause a bleeding, potentially leading to the death of the patient. The rupture occurs in the wall, hence, from a theoretical and mechanical point of view, it will happen when the stress in the wall exceeds the strength of the tissue. CSD and FSI techniques have been used to predict the stresses in the wall and require the mathematical modeling of the aneurysm wall motion. To that end, a complex physical modeling of the wall of an IA is required, encompassing several elements such as the tissue constitutive law and the wall thickness. Several researchers suggest which laws are applicable, but many exist and, consequently, different ones have been used in past works. Currently, it is difficult to know precisely what are the effects of using different modeling approaches on the mechanical response, i.e. stress and strains, of patient-specific IAs geometries. The main goal of this work is to investigate this issue, i.e. to assess the influence of different modeling choices regarding the tissue of IAs and which one could predict the rupture by using an FSI numerical technique and using patient-specific IAs, and accounting for ruptured and unruptured cases.

1.3 THESIS OUTLINE

Chapter 2 presents a review of what is currently know on several subjects intimately related to IAs: clinical aspects of the disease and how surgeons treat them and try to predict their likelihood of rupture (Section 2.1) as also the mechanical behavior of blood and its flow (Section 2.2), whose forces are know to be related to the aneurysm inception. Details on the biological and constitutive behaviors of the wall tissue — essential to understand the natural history of an IA — are also discussed (Sections 2.3 and 2.4) and, then, complemented by a presentation of the works that studied the heterogeneity of IAs walls (Section 2.5).

The goals of this thesis are further solidified by a review of the numerical studies of IAs, given in Chapter 3. Their role in helping to better understand the pathology and why they were the chosen ones are explored and detailed.

Chapter 4 presents the techniques employed to extract, treat, and convert the medical images of patient-specific vasculatures into geometries that can be readily used to created computational meshes. Additionally, it also presents the IA sample chosen and its morphological characteri-

zation.

Chapter 5 introduces the complete modeling approaches used to deal with the FSI physics (Section 5.1), the blood flow modeling (Section 5.2), and the arteries and IA tissue constitutive and morphology model (Section 5.3). Chapter 6 then shows how these were implemented in an open-source framework, and also the numerical method, discretization details, and algorithms used to numerically solve the resulting mathematical problem.

The solution of the numerical simulations are presented in two different chapters, separated for didactic and content reasons. Chapter 7 presents the comparison among the different modeling approaches used to represent the motion of the IA wall, whereas Chapter 8 focus on comparing the mechanical response of ruptured and unruptured IAs, in search for a better explanation for the rupture event. Chapter 9 presents a final discussion and summary of the main findings, as well as a discussion on the relevance of this work to the medical community, limitations and recommendations for future works.

Finally, Chapter 10 shows the papers arising from this work that were published, or submitted by the time of writing, to scientific journals and conferences. The contributions in terms of computational codes are also outlined.

Chapter 2

INTRACRANIAL ANEURYSMS

2.1 CLINICAL ASPECTS

Intracranial aneurysms (IAs) are pathological dilatations of the human vascular system arising on the arteries that reach the brain. There are two different types of aneurysms in terms of their shape: *saccular aneurysms*, characterized by a spherical-like sac, and *fusiform aneurysms*, in the form of a radial bulge of an artery. The most common ones arising in the cerebral arteries are saccular with a prevalence of around 90 % against 10 % of fusiform ones (8). Furthermore, saccular IAs are subdivided into two classes: *lateral aneurysms*, that forms laterally on an artery, and *bifurcation aneurysms* because this type originates at a bifurcation. Figure 2.1 illustrates these two types and show 1D metrics typically used in the medical practice to characterize the geometry of a saccular aneurysm: the sac height, h_d, and its maximum diameter, d_d. The *dome* is the upper part of the aneurysm sac and the artery that "feeds" the aneurysm with blood is called the *parent artery*. These metrics and definitions are commonly used by physicians in the planning of surgical interventions. The maximum sac diameter is normally employed to indicate whether an aneurysm is small or large, although some reports also used the dome height.

They are normally found in the bifurcations of the cerebral arteries tree, schematically pictured in Fig. 2.2 with a view of the base of the brain showing the so-called circle or "polygon" of Willis and its arteries. The figure includes a rough approximation of the IAs prevalence in terms of location, with the most common spots being the internal carotid artery (ICA), middle cerebral artery (MCA), and the basilar artery (BA), with the rest occurring at other arteries such as the vertebral arteries (VA), anterior cerebral artery (ACA), the posterior inferior cerebellar artery, and the posterior cerebral artery (9). The figure also shows examples of three

Figure 2.1 – Schematic representations of the two types of saccular aneurysms: (a) a lateral one, and (b) a bifurcation one. Typical 1D metrics depicted are the sac height, h_d, the neck diameter, d_n, d_{pa} is the parent artery diameter, and d_d is the maximum aneurysm sac diameter.

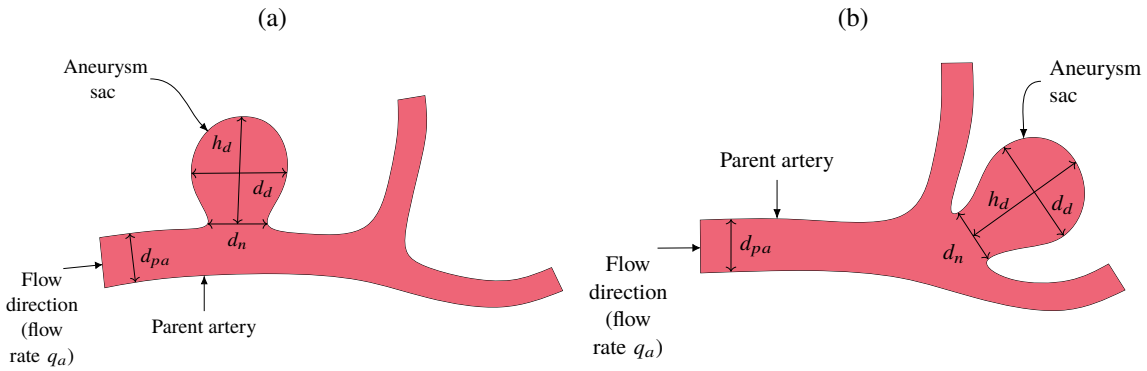

Source: Prepared by the author.

computational images and one reconstructed surface of patient-specific IAs, exemplifying how large aneurysms can be, ranging from 3 to 19 mm in height, in this case. Indeed, reports show their size can vary from 1 to 25 mm and larger, with the following distribution: 62 % of small aneurysms (2 to 7 mm), 23 % of medium-sized aneurysms (7 to 13 mm), and approximately 15 % of large aneurysms (>13 mm) according to a study with a set of 1692 patients with unruptured aneurysms (10).

IAs represent a high risk to a patient because their rupture its associated with a mortality rate between 40 and 60 % (12, 13) and also present a risk of permanent injury. According to Malmivaara et al. (14), only 60 % of those who survive can return to work. It is also estimated that 2 to 3 % of the world's population have intracranial aneurysms (15), but some reports show that this number can reach almost 10 % in the general population (16).

Several outcomes are possible when an IA ruptures, such as intraventricular hemorrhage and intracerebral hemorrhage (17), although one of the most common outcomes is a devastating event called subarachnoid hemorrhage (SAH), which can lead to a severe neurological deficit. Reports show that 85 % of SAH cases are caused by the rupture of these aneurysms (18–20). Hop et al. (21) concluded that fatal cases of SAH occurred from 32 to 67 % and about one-third of morbidity among the patients who survived. The work of The International Study of Unruptured Intracranial Aneurysms Investigators (10), one of the most relevant scientific research on rupture of IAs, still used for the decision on their treatment, evaluated the probability of SAH over time with a group of 1077 patients followed-up for five years and for different aneurysm sizes. According to their findings, the risk of SAH increases over time and for larger aneurysms (see Fig. 2.3). This study employed the maximum dome diameter as size metric (22) and classified

Figure 2.2 – Inferior view of the base of the brain with detail of the arteries tree composing the circle of Willis also depicted schematically: the right and left branches of the ICA with the vertebrobasilar system, composed of the BA, the MCA, ACA and the anterior communicating artery (ACoA). The small pictures show three volume-rendering representations of DICOM images of digital subtraction angiography (DSA) studies and one surface reconstruction of IAs examples: a bifurcation aneurysm at the BA, an aneurysm arising at the ACoA, a bifurcation aneurysm at the ICA, and an aneurysm at the MCA bifurcation with height ≈ 19 mm.

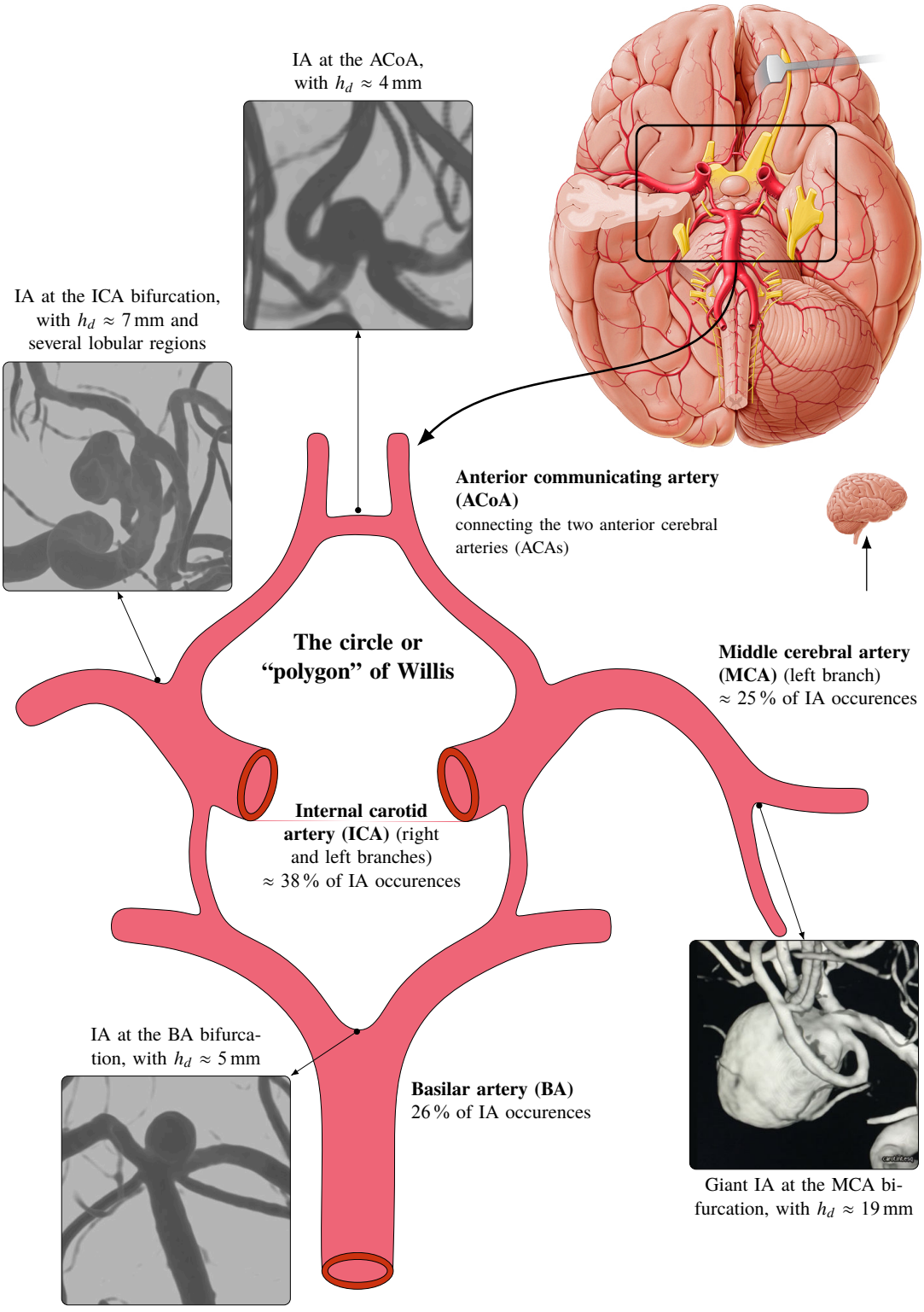

Source: Prepared by the author with the brain pictures extracted from KenHub (11) and IAs images provided by Dr. Carlos Eduardo Baccin .

them as small (≤ 7 mm), medium (7 to 12 mm), large (13 to 24 mm), and giant IAs (≥ 25 mm). The same study reported that, of the 193 patients who died during the follow-up period, 27 % died of intracranial hemorrhage.

Figure 2.3 – Probability of SAH over time for a group of 1077 patients followed up over five years who did not have previous cases of SAH, according to maximum dome diameter.

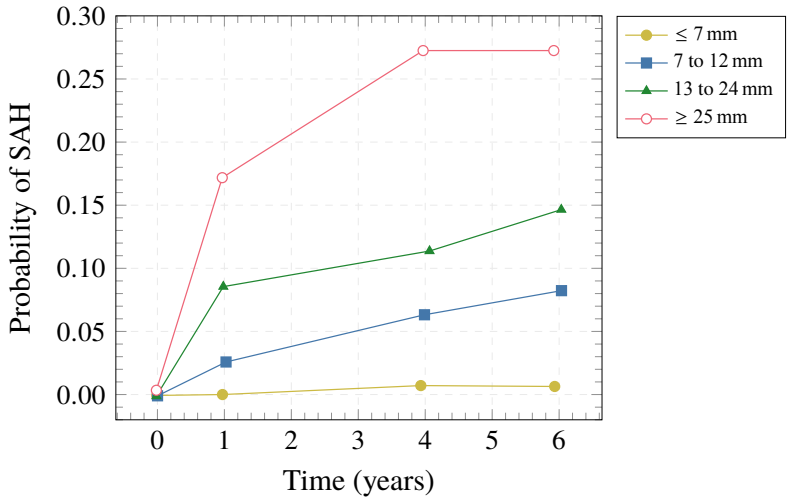

Source: Prepared by the author based on data found in The International Study of Unruptured Intracranial Aneurysms Investigators (10).

Despite small and medium-sized aneurysms being normally asymptomatic, their diagnostic has increased in the past decades due, especially, to the development of better imaging techniques such as 3D DSA, 3D Rotational Angiography, Magnetic Resonance Angiography and computational tomography angiography (CTA) (23). The images shown in three panels of Fig. 2.2, for example, show images generated by DSA of IAs of different patients and in different positions of the brain vessels tree.

Currently, the two major treatments for IAs are direct surgical intervention, i.e. the clipping of the aneurysm neck, clearly a very invasive treatment, or endovascular treatment, with intravascular placement of stents around the aneurysm and subsequent filling of the sac volume with coils (15), for example.

However, these interventions also present risks to patients. According to Torii et al. (24), risks of permanent damage and death due to treatment and post-operative procedures are about 10 %. By comparing this value with the risk of IA rupture, according to data collected by The International Study of Unruptured Intracranial Aneurysms Investigators (10) (Table 2.1), one can conclude that the most evident problem may occur for aneurysms whose size is between 7 and 12 mm and also for those smaller than 7 mm. Although the risk of rupture was lower than the risk of treatment, the percentage of rupture for those sizes is not negligible when considering the

risk of death. Especially for small cases that are highly prevalent, approximately 62 %, as given above, with some reports indicating that they account for approximately 50 % of all ruptures (25). Therefore, it is a tough decision for a physician to treat or not an IA.

Table 2.1 – Cumulative rupture rate of IAs according to their maximum dome diameter and location by monitoring patients for a period of five years after being detected for different arteries of the brain (group 1 had no previous SAH and group 2 had previous SAH and n is the number of patients in the sample).

Parent Artery	< 7 mm		7–12 mm	13–24 mm	≥ 25 mm
	Group 1	Group 2			
ACA/MCA/ICA (n = 1037)	0 %	1.5 %	2.6 %	14.5 %	40.0 %
BA/VA (n = 445)	2.5 %	3.4 %	14.5 %	18.4 %	50.0 %

Source: Experimental data from The International Study of Unruptured Intracranial Aneurysms Investigators (10).

2.1.1 Decision-guiding Metrics for the Rupture of IAs

Currently, physicians base their decision primarily on one or more 1D size metrics of an aneurysm (such as the ones shown in Fig. 2.1) to assess the likelihood of rupture, by roughly comparing those values with statistics of IAs rupture rates, e.g. Table 2.1. Other morphological aspects are also taken into account such as the presence of “blebs” and lobular regions on the aneurysm sac, which were already associated with higher rupture risk (26, 27). Clinical factors are also considered, such as age, family history or previous SAH, hypertension, cigarette smoking, female gender (probably related to post-menopausal estrogen dysfunctions), and also some genetic disorders that cause vascular abnormalities (9). Nonetheless, a final decision on the treatment options may be often inconclusive. For example, Etminan et al. (28) proposed the “unruptured IA treatment score (UIATS)”, a metric based on “consensus” among 69 interdisciplinary specialists and accounting for 29 factors in IA management. By using the UIATS, Rajabzadeh-Oghaz et al. (29) then classified a cohort of IAs and found the following recommendations: observation for 30 % IAs, treatment for 27 % IAs, and an astounding 43 % of “not definitive” — the last case indicating that “additional factors, apart from those used in the development of the UIATS, may be considered in making a final decision”.

Other morphological metrics to characterize an IA sac, both in shape and size, have been proposed (the mathematical definitions of the most important ones are presented in Appendix A.1), and several studies correlated these metrics with the likelihood of rupture. Weir et al.

(30), for example, performed a statistical analysis relating the aspect ratio of an IA (defined as dome height per neck width) to the probability of rupture. According to the authors, chances of rupture were 20 times higher when the aspect ratio was larger than 3.47 compared to an aspect ratio lower than or equal to 1.38. In their samples, only 7 % of ruptured aneurysms had an aspect ratio lower than 1.38 compared to 45 % of unruptured aneurysms. Juvela et al. (31), through a long-term follow-up study of 142 patients that suffered SAH, found that the aneurysm sac volume, volume-to-ostium-area ratio, and bottleneck factor seem to correlate separately with aneurysm rupture. Furthermore, the authors also show that smoking, location in the ACoA, and a sac diameter greater than 7 mm were independent risk factors for future rupture. The list of similar studies is large with, for example, Rahman et al. (32) who found that size ratio (the ratio between the maximum IA sac diameter and its parent artery diameter, d_{pa}) correlates with aneurysm rupture status, but also Raghavan et al. (33) that investigated the whether curvature and shape merics could predict the ruptured cases.

Apart from those based on size and shape metrics, other "scores", such as the aforementioned UIATS, were built to help the decision-making process. The PHASES score, proposed by Greving et al. (34), for example, used 6 clinical factors: population to which the patient belongs, hypertension, age, aneurysm size, previous SAH from another aneurysm, and aneurysm site. More recently, the "rupture resamblance score (RRS)" was developed by Rajabzadeh-Oghaz et al. (29) and, apart from morphological metrics, it also accounted for metrics based on the wall shear stress (WSS) adjacent to the IA lumen, such as the sac surface-averages of the time-averaged wall shear stress (TAWSS) and the oscillatory shear index (OSI), in line with several studies attesting to the importance of hemodynamics in the natural history of an IA — i.e. its inception, enlargement, and final rupture (see Section 2.3 for more details and Appendix A.2 for a brief overview of other WSS-related *hemodynamic wall parameters (HWPs)*). The authors computed the probability of an IA being ruptured, P_r^{IA}, by first estimating the *odds* ratio of their rupture resamblance score using a multivariate logistic regression with the parameters above, finding the following relationship:

$$odds = \mathrm{e}^{0.58SR - 0.33TAWSS_{avg} + 2.14OSI_{avg} - 2.43}, \tag{2.1}$$

where SR is the size ratio, and $TAWSS_{avg}$ and OSI_{avg} are the normalized surface-averaged TAWSS and surface-averaged OSI over the IA sac surface, respectively. In the sequence, P_r^{IA}

can be found as follows (derived from the so-called *logit* function):

$$P_r^{\mathrm{IA}} = \frac{odds}{1 + odds} \,. \tag{2.2}$$

Despite all these advances, in the medical practice, the most used parameter for the treatment decision is still the IA size, with statistical data provided by studies such as The International Study of Unruptured Intracranial Aneurysms Investigators (10). Based on the scores presented above, it is comprehensible to expect that clinical factors and IA size metrics were included in their statistical definitions. Furthermore, with the mounting evidence gathered along the past two decades on the relevance of hemodynamics in the understanding of IAs mechanobiology, it is no surprise the inclusion of the TAWSS and OSI in such scores. Such statistical studies, commonly using hundreds or thousands of IA cases, can be valuable because they may provide relatively simple mathematical tools that could potentially help physicians to decide whether or not an IA is in danger of rupture. Nevertheless, to decide which particular metrics are worthy including in such scores, a better understanding of the aneurysm pathology itself and the mechanisms behind its natural history, such as the hemodynamics inside an aneurysm sac due to the blood flow and the mechanobiology of its wall tissue, are essential for defining an enhanced "score" or rupture predictor.

2.2 THE MECHANICAL BEHAVIOR OF BLOOD

Human blood is a mixture of different solid components, red and white blood cells among them, suspended in a liquid known as *plasma* (35, 36). The volume percentage of red blood cells in this mixture is known as *hematocrit*. While the plasma is essentially Newtonian because it is mainly composed of water (35), the blood mixture is a non-Newtonian fluid because its apparent viscosity, η^{f}, depends on the shear rate, $\dot{\gamma}$, levels of the flow, more specifically, as $\dot{\gamma}$ increases, η^{f} decreases (37) (see Fig. 2.4). This is a typical non-Newtonian behavior known as *shear-thinning*. Moreover, for the rheology of blood, η^{f} also depends on the hematocrit level and temperature (35, 37) and, in terms of compressibility, blood is essentially a compressible fluid, although incompressibility may be assumed in some situations (38).

Although the flow in human vessels is inherently 3D, the apparent viscosity of blood, and more generally of any other non-Newtonian fluid, is defined for pure-shear flows, typically found in rheometric instruments, where the shear rate, $\dot{\gamma}$, and the viscous part of the Cauchy stress, τ

Figure 2.4 – Blood apparent viscosity, η^{f}, dependence with the flow shear rate, $\dot{\gamma}$, for pure-shear flow and its dependence with the hematocrit.

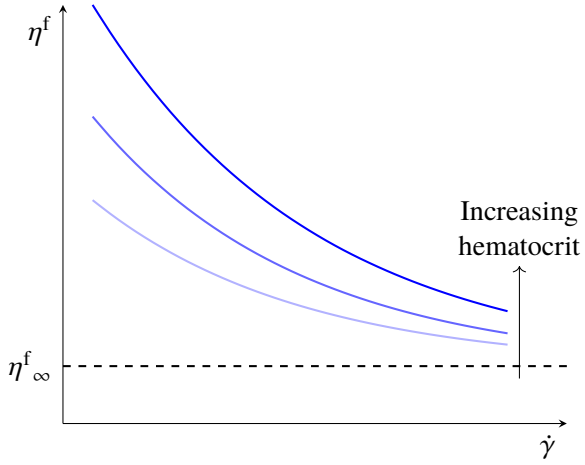

Source: Prepared by the author.

are easier to measure. Hence, it is defined as:

$$\eta^{\mathrm{f}} \equiv \frac{\tau}{\dot{\gamma}} \,. \tag{2.3}$$

Based on this definition, several constitutive laws, given in terms of η^{f}, were proposed over time that captures blood's non-Newtonian features such as shear-thinning and the yield stress (39, 40, 36). The yield stress is the minimum stress required to start the flow and whether blood has or not a finite yield stress was already a very debated subject in the literature (39, 41). However, the issues in determining this behavior are intrinsic to the type of measurement itself, i.e. the difficulty in performing measurements when $\dot{\gamma} \to 0$. Nevertheless, today the literature agrees that blood has a small, but finite, yield stress, which also varies with temperature and the hematocrit level of the blood sample. It is also accepted that the apparent viscosity reaches a plateau for shear rate levels typically above $100\,\mathrm{s}^{-1}$, therefore in this shear rate range, blood could be considered a Newtonian fluid (this is illustrated in Fig. 2.4 with the asymptotic plateau with value $\eta^{\mathrm{f}}{}_{\infty}$) (42, 37).

The literature reports several constitutive laws that have already been used to model blood behavior (some examples are given in Table 2.2). A review by Campo-Deaño et al. (37) classifies them into two groups: the constitutive equations that are based on the so-called *generalized Newtonian* model and more complex ones that capture the viscoelastic properties of blood, such as thixotropy. Probably the most classical model for blood is known as *Casson law* (41, 43, 40) that captures both shear-thinning and the yield stress features. Another traditional model used for blood is known as the *Carreau-Yasuda law* that accounts for the shear-thinning feature and

Table 2.2 – Non-Newtonian laws with coefficients calibrated for human blood and based on the generalized Newtonian modeling approach (material constants found in (40)).

Model Name	$\eta^{\mathrm{f}}(\dot{\gamma})$	Material Constants (for human blood)
Casson	$\left(\sqrt{\frac{\tau_C}{\dot{\gamma}}} + \sqrt{k}\right)^2$	$\tau_C \approx 2.7 \times 10^{-3}$ Pa $k = 3.4 \times 10^{-3}$ Pa s
Power-law	$k_n \dot{\gamma}^{n-1}$	$k_n = 14.67\,\mathrm{Pas^n}$ $n = 0.775$
Carreau-Yasuda	$\eta^{\mathrm{f}}{}_\infty + (\eta^{\mathrm{f}}{}_0 - \eta^{\mathrm{f}}{}_\infty)\left[1 + (\lambda\dot{\gamma})^a\right]^{(n-1)/a}$	$\eta^{\mathrm{f}}{}_\infty = 3.45 \times 10^{-3}$ Pa s $\eta^{\mathrm{f}}{}_0 = 5.6 \times 10^{-2}$ Pa s $\lambda = 1.902$ s, $a = 1.25$, $n = 0.22$
Modified generalized Oldroyd-B	$\eta^{\mathrm{f}}{}_\infty + (\eta^{\mathrm{f}}{}_0 - \eta^{\mathrm{f}}{}_\infty)\left[\frac{1 + \ln(1 + \Lambda\dot{\gamma})}{1 + \Lambda\dot{\gamma}}\right]$	$\eta^{\mathrm{f}}{}_\infty = 5.5 \times 10^{-3}$ Pa s $\eta^{\mathrm{f}}{}_0 = 0.0736$ Pa s $\Lambda = 14.81$ s

Source: Prepared by the author.

also the information of the known Newtonian-like behavior for high shear rate, with $\eta^{\mathrm{f}}{}_\infty$ being the blood viscosity in this case, and $\eta^{\mathrm{f}}{}_0$ the viscosity when $\dot{\gamma} \to 0$.

Other laws for blood usually take into account its history-dependent and thixotropy effects (36) associated with viscoelasticity and with its microstructure (44, 37). These effects are known to be less significant in the large vessels of the human body, where shear thinning is far more important (36). They begin to have a larger influence on blood behavior in small and capillary vessels, where the size of blood cells is of the same order as the vessel diameter. Therefore, in the cerebral arteries, constitutive laws based on the apparent viscosity are often used, due to their relative simplicity and applicability.

Although the definition in Eq. (2.3) and its mathematical forms in Table 2.2 were built based on pure-shear flows, for 3D flows, the obvious case in human arteries and IAs, they are still used, but $\dot{\gamma}$ depends on the components of the rate of deformation, $\boldsymbol{D}$, a second-order tensor, defined as:

$$\boldsymbol{D} = \frac{1}{2}\left[\nabla \boldsymbol{v} + (\nabla \boldsymbol{v})^{\mathrm{T}}\right], \tag{2.4}$$

where $\boldsymbol{v}$ is the flow velocity field. The viscous part of the Cauchy stress tensor, $\boldsymbol{\tau}$, is then modeled using the so-called *generalized Newtonian model*, given by:

$$\boldsymbol{\tau} = 2\eta^{\mathrm{f}}(D_{ij})\boldsymbol{D}\,. \tag{2.5}$$

If the classical Newtonian law is assumed for blood, and additionally considered an incom-

pressible fluid, then the apparent viscosity reduces naturally to the dynamic viscosity, μ^{f}. Thus Eq. (2.5), with Eq. (2.4), becomes:

$$\boldsymbol{\tau} = \mu^{\mathrm{f}} \left[\nabla \boldsymbol{v} + (\nabla \boldsymbol{v})^{\mathrm{T}} \right] . \tag{2.6}$$

The correct prediction of $\boldsymbol{\tau}$ is an important issue for flow in vessels because one of the most important hemodynamics quantities associated with blood flow and, more importantly, with pathologies such as IAs, is the WSS, already mentioned in Section 2.1, and defined as the tangential component of the viscous traction, $\boldsymbol{t} = \boldsymbol{n} \cdot \boldsymbol{\tau}$, acting on a surface S with outward unit normal $\boldsymbol{n}$ adjacent to the flow, such as the lumen surface of an artery or an IA. Mathematically, the WSS, symbolically represented by $\boldsymbol{\tau}_w$ in this text, is then defined as:

$$\boldsymbol{\tau}_w = \boldsymbol{\tau}_w(\boldsymbol{x}, t) = \left[\boldsymbol{t} - (\boldsymbol{n} \cdot \boldsymbol{t})\, \boldsymbol{n} \right] \Big|_S , \tag{2.7}$$

and is a function of space and time, $(\boldsymbol{x}, t)$ for the flow in a human vessel due to the temporal nature of the cardiac cycle.

Particularly for cerebral arteries with IAs, the question of which constitutive law should be used is an often debated topic. Indeed, different studies showed that it is important to consider a non-Newtonian model when simulating blood flow (45–47). However, Perktold et al. (48) showed that for a bifurcation of the internal carotid non-Newtonian effects are negligible for the flow velocity field. Furthermore, Valencia et al. (49) showed that predictions of flow variables on an aneurysmal wall using non-Newtonian models were similar to the predictions with the Newtonian model. This could be explained by the shear strain levels found in the arteries that reach the brain, which are typically higher than $100\,\mathrm{s}^{-1}$, and therefore the nonlinear effects of the non-Newtonian features would be negligible. However, IA geometries can present a sac elongated and with complex shapes that might lead to particular flow behaviors, like slow recirculation zones in the aneurysm lumen, in which the blood rheology model may play an important role in determining local hemodynamics. In this context, more numerical studies appeared in the last decade that performed evaluation of the influence of the rheology model on the hemodynamic specifically for patient-specific IAs.

Xiang et al. (50) compared non-Newtonian and Newtonian models in three ICA aneurysms and concluded that the Newtonian model overestimates the WSS in slow recirculating flow zones, which could underestimate the risk of aneurysm rupture. In a similar investigation, Evju et al. (51) compared the Newtonian *vs.* non-Newtonian laws on 12 MCA aneurysms and reported that

differences in WSS caused by different constitutive laws models were relatively small compared to WSS variations caused by morphological variations. Castro et al. (52) performed a similar comparison on 10 IAs and found no correlations between low WSS regions and overestimation of local WSS field by either Newtonian or non-Newtonian models. Hippelheuser et al. (53) investigated the influence of different rheology laws on IAs with and without blebs and reported that the Newtonian model overestimated WSS metrics, especially in areas of low WSS on the surface of blebs.

The results of these studies are quite contradictory and, unfortunately, do not offer a straightforward conclusion on the more correct rheology model to use for IAs geometries. Furthermore, the situation may be more complex in a sense that the specific choice of a rheology law for blood is probably application-dependent, as the findings of a recent study suggest (54). Additionally, their conclusions did not discard performing parametric studies with different rheology laws to assess their impact on the hemodynamics, for a particular IA geometry.

2.3 THE MECHANOBIOLOGY OF IAs TISSUE

The blood vessels of the human vascular system belong to the class of soft tissues. The tissue of arterial walls is mainly composed of three different layers: *intima*, *media* and *adventitia*. The intima is the inner layer, normally thinner than the others, in direct contact with the vessel lumen, containing endothelial cells (ECs) and a basal lamina; the media is the middle layer and is mainly composed of smooth muscle cells (SMCs), collagen and elastin fibers as structural components. The adventitia is the outermost layer being mainly constituted of collagen fibers, fibroblasts, and ground substance (41). Arteries can be classified as *elastic* or *muscular*, and both of them are composed of the same three layers mentioned above, however, the main differences are their size and some aspects of their constitution. In terms of size, muscular arteries, more peripheral with respect to the heart, have diameters ranging from 0.3 to 10 mm, whereas elastic arteries, closer to the heart, like the aorta, have a larger diameter. Regarding their constitution, elastic arteries have several elastic membranes, called *elastic laminae*, composed of elastin and disposed in a concentric form along the media. On the other hand, in the media layer of muscular arteries, these laminae are almost nonexistent, but appear as two prominent structures separating the media from the intima and adventitia. In this case, they are called the internal and external elastic laminae (55), respectively.

The cerebral arteries are classified as muscular arteries with a similar constitution that was

Figure 2.5 – Schematic representation of the structure and cell composition of a healthy cerebral artery, mainly composed of three layers and the IEL; the force interactions caused by blood flow and the perivascular environment are also depicted.

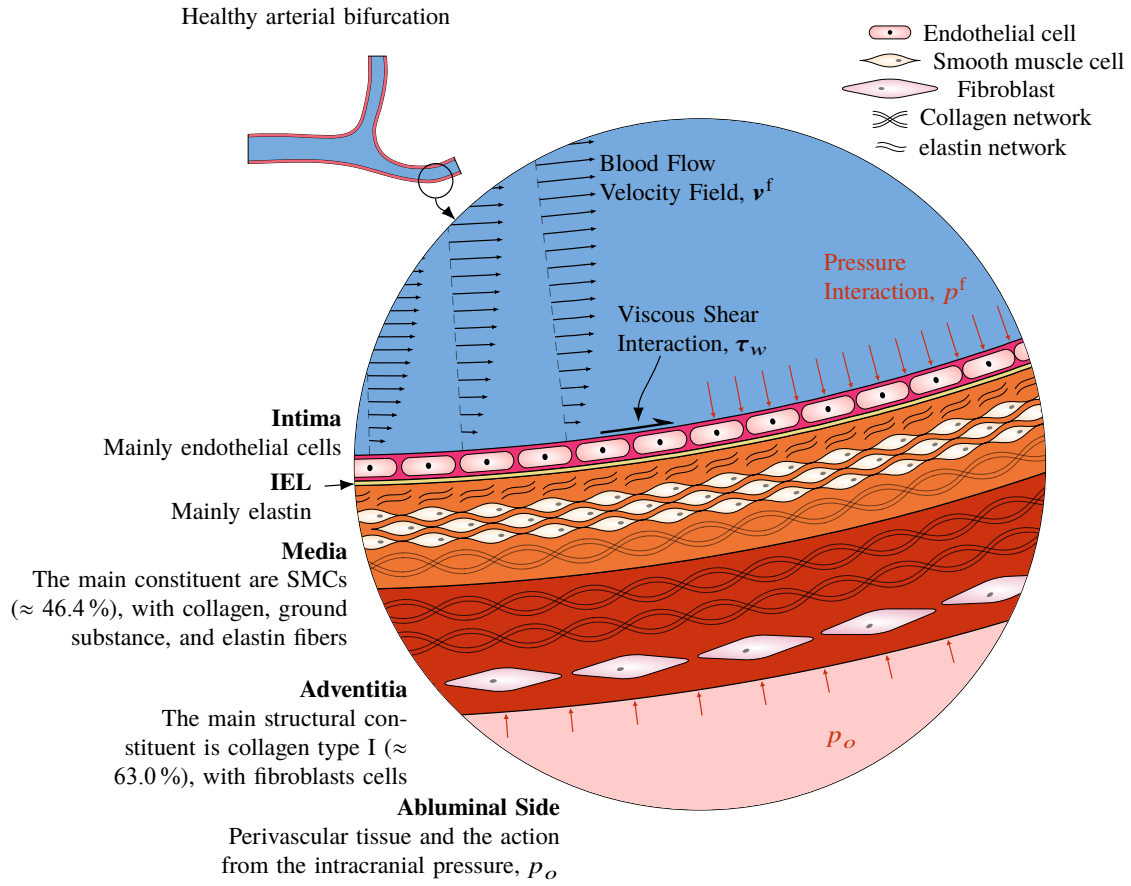

Source: Prepared by the author.

outlined above, although there is an important difference between the structure of the cerebral and other muscular arteries. While the intima and the media are clearly separated in cerebral arteries by the internal elastic lamina (IEL), there is no clear separation between the media and adventitia through the external elastic lamina (56) (see Fig. 2.5). The main load-bearing components of these arteries are the elastin, responsible for their high extensibility, and collagen fibers, which provide high stiffness upon stretching — collagen is initially a "wavy" structure when unloaded, thus not playing a large role under small or normal loads.

Figure 2.5 also shows a representation of the main force interactions acting on the artery wall, due to the blood flow, namely, the WSS, defined in Eq. (2.7), and the pressure forces acting on its inner and outer surfaces. These two pressure interactions give rise to the so-called *transmural pressure*, p_{tr}, defined as the difference between the blood flow pressure, p^{f}, acting on the lumen's surface and the vessels outer pressure, which is mainly characterized by the intracranial pressure, p_o, in the case of the cerebral arteries — note, moreover, that there may be local physical support

due to surrounding structures in the so-called *peri-aneurysmal environment*. The transmural pressure effectively induces the mechanical stress distribution in the tissue. The classical law of Laplace shows this in a simple form applied to an infinitely thin membrane, with principal curvatures κ_1 and κ_2, subjected to a transmural pressure, where the wall tension in each principal direction, $T_{\mathrm{m}i}$, $i = 1, 2$, are given by (56):

$$T_{\mathrm{m}1} = \frac{p_{tr}}{2\kappa_2} \ , \quad T_{\mathrm{m}2} = \frac{p_{tr}}{\kappa_2}\left(1 - \frac{\kappa_1}{2\kappa_2}\right) \ . \tag{2.8}$$

Clearly, the stress developed in an artery or IA wall may not be represented by Eq. (2.8) due to their thicker nature and highly curved regions. In any case, the mechanical stress developed in the arterial tissue is an important regulator of some cellular activities within it (57).

It is thoroughly recognized today that the WSS is intimately related to a healthy functioning of the ECs that lies on the lumen of arteries. Actually, even the shape of these cells seems to be dictated by the direction of vector $\boldsymbol{\tau}_w$ (58). This hemodynamic quantity is also associated with causes of vascular diseases such as atherosclerosis, arterial malformations (59), and the development of IAs (60, 58, 61).

The normal physiological level of WSS in the human vascular system has been reported to be in the range of 1–7 Pa (59) throughout the cardiac cycle with a time-averaged magnitude around 1.5–2.5 Pa (62). However, in certain regions of the vessels network, such as outer curves or bifurcations, where complex hemodynamics conditions are common (63, 64), local elevations of the WSS often occur accompanied by highly disoriented WSS directions with positive and high spatial gradients. These conditions may also occur due to malformations in the brain vessels tree. These hemodynamics effects cause malfunctioning of the endothelial cells that, consequently, trigger biological responses in the vascular wall as a mechanism to maintain the vascular homeostasis through *vascular remodeling* (63, 58, 65, 66). For example, when a WSS elevation is sensed by ECs, these cells release nitric oxide (NO), a well-known vasodilator that acts by relaxing SMC and inhibiting their proliferation while synthesizing new collagen. On the other hand, if lower local WSS levels are sensed by the ECs, they produce endothelin-1, a vasoconstrictor molecule that promotes SMCs proliferation and collagen synthesis (67). By these normal mechanisms, the arteries can adapt to aberrant hemodynamical conditions seeking to reestablish the normal physiological levels of WSS.

Although these are normal processes occurring in a vessel tissue, they have been linked to the formation of IAs. That IAs form as a result of local WSS elevation and local high and

positive time-averaged WSS gradient is a consensus and can be explained by a cascade of events occurring in bifurcations that lead to the early signs of IA inception in these regions (62, 57), such as:

- loss of the IEL, one of the first indicators (68);
- media thinning with a reduced number of SMCs;
- presence of inflammatory cells;
- bulge formation with disrupted endothelium.

In a recent review, Frösen et al. (57) described an "inflammation-mediated" pathway that may explain the early signs of an IA. As explained above, ECs produce NO in response to high WSS (assumed as $\gg 1.5\,\text{Pa}$ for humans). This increase in NO induces the ECs to release, among other products, macrophage chemotactic protein 1 (MCP1) in the tissue that is responsible for recruiting blood flow circulating monocytes (a type of white blood cell) into the wall, being turned into macrophages (cell agents responsible for the phagocytosis). Moreover, at the apex of bifurcations, the mechanical stress is also elevated due to higher intramural pressure, hence increasing the stretch locally that causes the fibroblasts in adventitia to also produce MCP1, further stimulating the migration of the macrophages from the intima towards the outer layers. This migration of inflammatory cells causes the early disruption of the IEL and collagen destruction in the media. At the same time, the vasodilating action of NO occurs concomitantly and the SMCs relax leading to vessel dilation — or "ectatic" remodeling, i.e. the expansion of a tubular organ. In this process, the SMCs in the media synthesize more collagen fibers as a response to the destructive action of macrophages, but also gain the ability to produce matrix metalloproteinase that further degrades the structural proteins such as collagen and elastin. This inflammatory process continues through a feedback loop because the macrophages in the media also gain the ability to synthesize MCP1, which further increases their quantity and induces the proliferation of more SMCs. Hence, even if the WSS levels are reestablished to baseline levels, this whole process may continue. Finally, they can occur in different regions of the wall, and the combination of *constructive remodeling*, i.e. cell proliferation with *intimal hyperplasia* when SMCs migrate into the media causing it to thicken (this was identified at the apex of bifurcations in studies with rabbits by Meng et al. (63)), and *destructive remodeling*, the disruption of the IEL and thinning of the media due to loss of SMCs, cause the formation of a bulge, the early

Figure 2.6 – Schematic representation of the structure and cell composition of an IA wall, still with three layers but with a thinner media and fragmented, sometimes absent, IEL; also, the macrophages infiltrated in the tissue are responsible for part of the destructive and constructive remodeling taking place as the aneurysm grows.

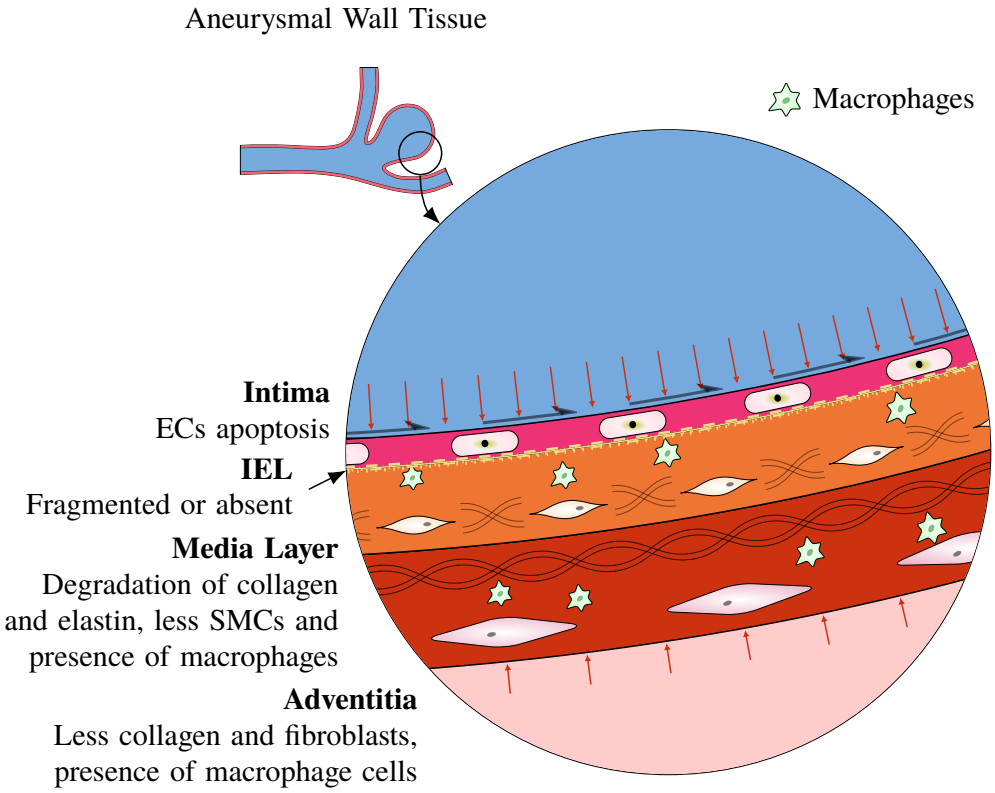

Source: Prepared by the author.

sign of an IA. While these processes continue to occur, the wall structure of the new aneurysm will be dictated by their consequences, (see Fig. 2.6).

Although there is a consensus on IA inception, the story is different and inconclusive regarding its subsequent growth. Once a new hemodynamical environment is established because of the updated vessel geometry, the same mechanisms outlined above can continue to occur due to eventual local high WSS, but new ones may take place. Early in the last decade, Meng et al. (61) proposed a unified view of the mechanisms which causes an IA to grow: the *low-flow* and the *high-flow* effects theories (see Fig. 2.7, based on a similar diagram presented in their study).

The high-flow theory proposed by the authors was related to the same mechanisms outlined above, i.e. caused by abnormally high WSS with positive WSS spatial gradient that, if still present in the early-aneurysm environment, may lead to further remodeling, growth and, eventually, to the formation of a bleb on its surface. This bleb would be formed by the same mechanisms that initially caused the aneurysmal bulge, but on an even weaker wall.

Their low-flow theory claimed that low WSS, and also high OSI (a measure of how much the

WSS vector oscillates during a cardiac cycle (69); see Appendix A.2), cause dysfunction of flow-induced NO, resulting in the aggregation of red blood cells and the accumulation and adhesion of platelets and leukocytes, which in turn cause intimal damage and inflammation. These inflammatory cells infiltrate the tissue leading to localized degeneration of the aneurysm wall, matrix degradation, and cell death, hence the aneurysm grows but with different wall composition and mechanical properties. These two pathways were named as "mural-cell-mediated pathway" and "inflammatory-mediated pathway", respectively, by Meng et al. (61).

It is important to note that, as highlighted by the authors, these two pathways may co-exist in a single IA and both could explain a rupture event, but also their stabilization, since not every IA do ruptures. Their stabilization may be related to a balance between deposition and destruction of the main components in the aneurysm wall in such a way that the resulting tissue strength may sustain the stresses caused by the intramural stress developed by the intra-aneurysmal flow.

Meng et al. (61) went further and hypothesized that each pathway may lead to different wall phenotypes, which could explain the large variability of IA morphology (see the bottom of Fig. 2.7). For example, regarding wall thickness, although the aneurysm wall is expected to be thinner compared to its surrounding arteries, an early study by Suzuki et al. (71) found the following distribution in a sample with 23 unruptured IAs:

- 21.7 % were uniformly thin;
- 17.4 % were thick at the dome and thin at the neck;
- 43.5 % were thin at the neck with an irregular dome;
- 17.4 % were thick at the neck with an irregular dome.

Hence, indeed the majority of aneurysms have a heterogeneous distribution of thickness. Furthermore, due to the different impacts on tissue load-bearing components, heterogeneity can certainly be expected from its mechanical properties. This heterogeneity was more recently studied by other authors (72, 73). Cebral et al. (73), for example, subdivided the aneurysm wall into 5 regions with specific phenotypes: atherosclerotic, hyperplastic, thin, the rupture region, and "normal appearing" by intraoperative observation and correlated each phenotype with local hemodynamics. The characteristics of these 5 regions fit into the hypothesis by Meng et al. (61) in which the two pathways described above and their coexistence may lead to a spectrum of IAs phenotypes ranging from what they name aneurysms of "type I" and "type II", which present the following characteristics:

Figure 2.7 – Flowchart representation of the mechanisms responsible for IAs initiation and the two main theories that may explain saccular IAs growth and, eventually, lead to rupture or stabilization, according to Meng et al. (61).

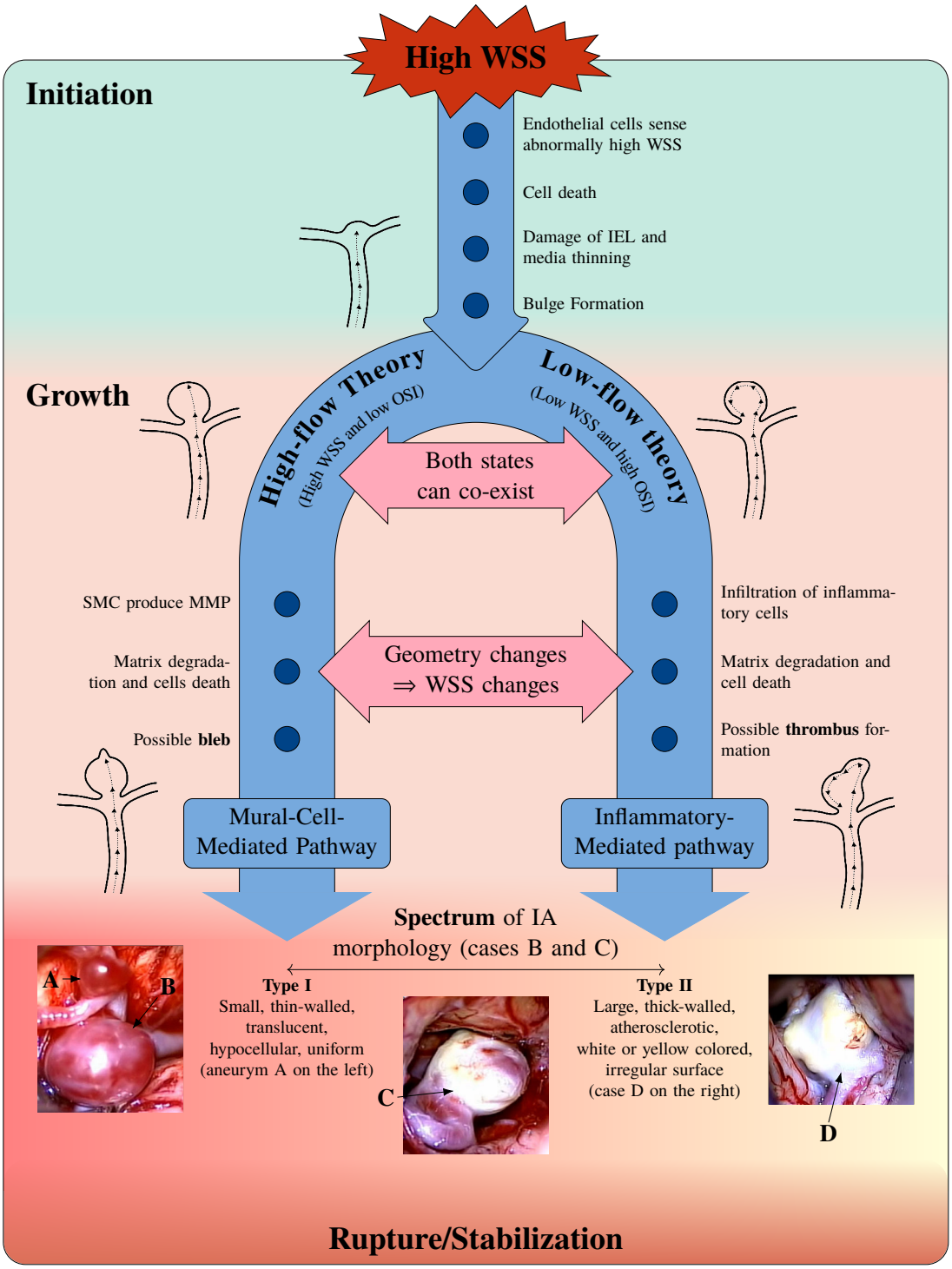

Source: Prepared by the author based on a diagram presented in Meng et al. (61); the intraoperative microscopic pictures of patient-specific IAs were adapted with permission from Kadasi et al. (70). .

- small (< 4 mm) [1], thin-walled, translucent, hypocellular, and uniform;
- large (> 10 mm), thick-walled, atherosclerotic, white or yellow-colored, and irregular

[1]The authors did not mention which metric was used for this definition of small and large IAs

surface.

Kadasi et al. (74), for example, showed that the incidence of unruptured IAs is the following: 27 % are type-I, 8 % are type-II aneurysms, and 65 % contains both regions shown in the lower part of Fig. 2.7, i.e. it seems that the rule among aneurysms is a fully heterogeneous wall structure.

During IA evolution, there is a last factor that may influence the growing process: the environment around the aneurysmal bulge, also known as the *peri-aneurysmal environment*, mentioned at the beginning of this section. An IA grows in a region called the subarachnoid space and, hence, is surrounded by other structures such as bone, brain tissue, and nerves, for example. As an IA grows, it may come in contact with one of these structures and, consequently, its shape will be probably influenced. Ruíz et al. (75), for example, showed that peri-aneurysmal environment contact constraints may influence both the shape and the risk of rupture of the aneurysm, with ruptured IAs being more frequently in contact with peri-aneurysmal environment structures, compared to unruptured IAs. However, this interaction is still very poorly understood and, unfortunately, it is also hard to inspect through the current imaging exams what are the structures present around a particular IA. Therefore, more investigations are necessary in this area.

2.4 THE MECHANICAL BEHAVIOR OF IAs TISSUE

As seen in Section 2.3, the main structural components of arteries and IAs are the elastin and collagen fibers. Elastin is a highly elastic component (41) commonly found in several tissues of the human body, such as in the large elastic arteries near the heart. Collagen fibers, on the other hand, with their characteristic helical structure and nonlinear mechanical behavior, are responsible for the anisotropic behavior of tissues such as tendons, muscles, and artery walls (76).

Fung (41) presented experimental results on the mechanical behavior of collagen and its typical load-elongation curves (Fig. 2.8a). The curve is mainly nonlinear for small deformations and exhibits an approximately linear region, with high stiffness, after the “toe” part of the curve. This increase in stiffness is due to the elongation of collagen fibers when loaded, also known as *fiber recruitment*, since collagen fibers, which are wavy-shaped when unloaded, when stretched increases the stiffness of the material, reaching a maximum just before failure.

Figure 2.8 – Main features of the mechanical behavior of collagen: (a) typical load-elongation curve and (b) the phenomena of hysteresis and preconditioning, where n is the number of loading-unloading cycles.

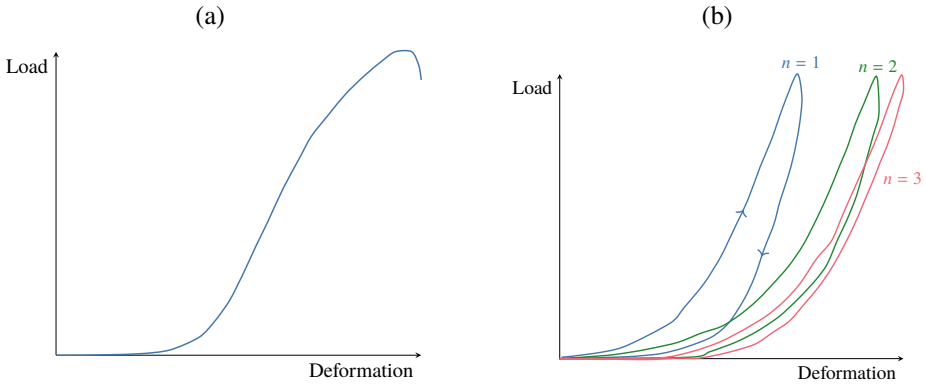

Source: Prepared by the author based on data found in Fung (41).

Soft tissues, in general, also exhibit a behavior similar to collagen's. Moreover, under normal physiological conditions, soft tissues have several common features that characterize their mechanical behavior (41, 55):

- inherent nonlinear stress-strain relationship;
- hysteresis under cyclic loading and unloading;
- stress relaxation under constant deformation and creeping under constant load; and
- stress softening, which requires the material to be *preconditioned* when tested.

A typical hysteresis loop is depicted in Fig. 2.8b for three cycles of a *preconditioning* test. The preconditioning of a specimen tested under loading consists of repeating the loading-unloading procedure a finite number of times until a "steady-state" is reached when the curve does not change anymore *for that load condition*. Figure 2.8b shows an example of how the stress-strain curves change for loading-unloading between consecutive tests. According to Fung (41), preconditioning occurs in a specimen because its internal structure changes with the loading process, therefore if the load levels change, the structure will be modified again.

Both elastic and muscular arteries also exhibit these features. However, the normal response of elastic arteries after preconditioning can be considered as almost perfectly elastic, whereas the response of muscular arteries is viscoelastic (55). Nevertheless, these "bio-solids" are normally modeled with the so-called *pseudo-elastic* approach (41), thus allowing for the application of elastic laws in different portions of the load-unload cycle. Furthermore, arteries can also be assumed as incompressible in general (77).

The mechanical response of IA tissue under failure tests has been reported in few works in the past decades, but the number of works on this subject has increased in the last decade. For instance, Scott et al. (68) compared experimental pressure-volume curves between tissue samples of IAs and their surrounding arteries. The authors showed that the stress-strain curve was similar in form to the collagen one, but the aneurysm tissue is less distensible than its surrounding vessels because of the lack of elastin, as the authors already reasoned. Later on, Steiger et al. (78) measured several mechanical properties of IAs by uniaxial strain/stress tests and also investigated how they changed from the aneurysm neck to its dome, or fundus, thus effectively providing an idea of their heterogeneity. For example, the elastic modulus, which they estimated by dividing the yield stress by the yield strain, was found to be the greatest at the aneurysm neck, 3.1 ± 0.9 MPa, compared with 1.7 ± 0.8 MPa and 2.5 ± 1.1 MPa at the aneurysm fundus and its surrounding arteries, respectively. They also found a smaller yield stress at the fundus of the aneurysm than at the neck and arteries, which agrees with empirical evidence that the rupture normally occurs at the fundus (56).

More recently, Robertson et al. (79) compared the mechanical response of cerebral arteries and IAs tissue samples by performing uniaxial traction tests with 15 rectangular strips from the meridional section of unruptured IAs and 12 circumferential samples of arteries of the circle of Willis — 6 specimens of the BA and 6 of the ICA extracted from human cadavers (see Fig. 2.9a). They mechanically characterized the samples by fitting the stress-strain curve with an exponential constitutive law for isotropic materials similar to a Fung-like strain-energy function, characterized by two material constants k_1 and k_2 (its uniaxial stress-strain relation can be found in Appendix E, under the label "isotropic quadratic Fung"). Furthermore, as done by the authors and also found in other works (80), the typical curve they found was divided into different regions (see Fig. 2.9b). Initially, there was a quasi-linear region at lower stress in which the authors defined a "low-stress stiffness", E_L; a transition quantitatively characterized by a "transition stretch", λ_t, and another quasi-linear part with a higher stiffness response, where they defined a "high-stress stiffness", E_H, and, finally, the failure of the material, which are identified by the ultimate stretch, λ_S, and the ultimate Cauchy stress, σ_S. The averaged values they have found, per tissue type, are summarized in Table 2.3.

The data in Table 2.3 and in Fig. 2.9a clearly reflect the histological characteristics of IAs outlined in Section 2.3 such as an overall higher stiffness than the surrounding arteries, evidenced by the elasticity parameters, E_H, E_L, k_1, and k_2. Nonetheless, only the low-stress stiffness was

Figure 2.9 – (a) Uniaxial stress-strain curves of IAs and control arteries samples in experiments performed by Robertson et al. (79). The bars indicate the averaged failure strength of the aneurysms and the control arteries. (b) Schematic representation of the mechanical parameters defined and calculated for aneurysms and arteries tissue by Robertson et al. (79). Their calculation is based on experimental data from uniaxial traction tests and the lines defining the low-stress and high-stress stiffnesses were computed by the authors based on linear regressions of the points collected in each regime, respectively.

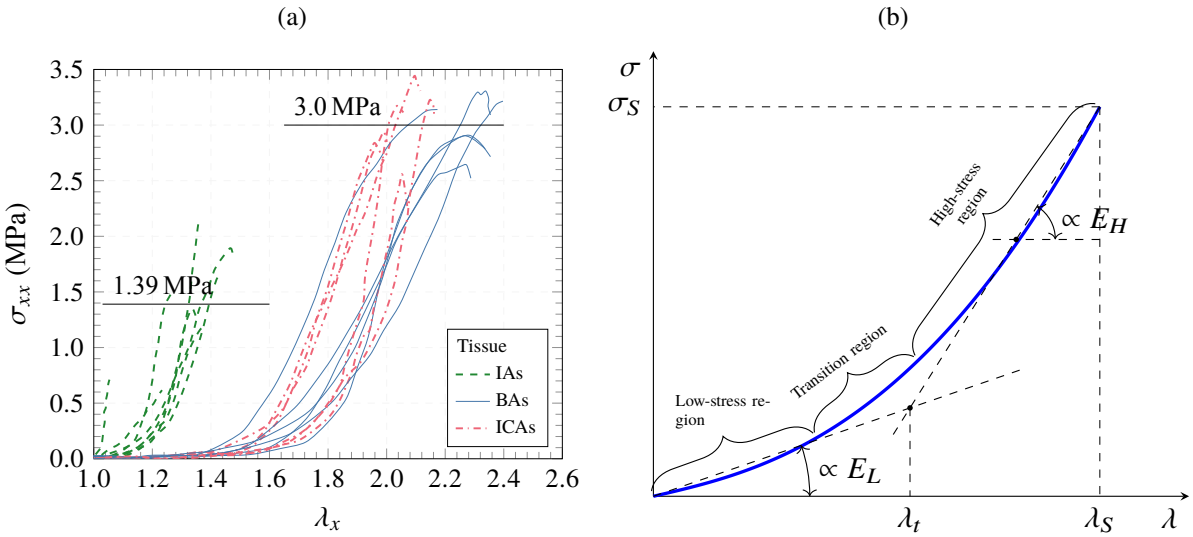

Source: Prepared by the author with data found in Robertson et al. (79).

found to be statistically different between IA and cerebral arteries samples. Furthermore, the aneurysm tissue was much weaker than the arteries with smaller ultimate stretch and stress. The ultimate stress for the control arteries was, approximately, 3.0 MPa for ICA and BA, whereas for the IA sample was 1.39 MPa and even the strongest aneurysm sample was considerably weaker than any of the control arteries. Therefore, there is significant mechanical differences between healthy arteries and aneurysm tissues.

The microstructure of IAs was also analyzed by Robertson et al. (79). The authors made use of recent advances in multiphoton microscopy to study the tissue fibers network of the aneurysms and arteries tissue under loading. Their findings confirmed the loss of the IEL as the cause of the smaller toe region for aneurysms tissue, and, moreover, they showed the collagen

Table 2.3 – Averaged material parameters obtained in uniaxial traction tests to failure of IAs and healthy cerebral arteries tissue samples by Robertson et al. (79). The definition of each parameter is schematically shown in Fig. 2.9b. The authors also measured the thickness of the IA samples, given by e_{ia}.

	λ_t	E_L (MPa)	E_H (MPa)	λ_S	σ_S (MPa)	k_1 (MPa)	k_2	e_{ia} (mm)
IAs	1.18	0.82	12.38	1.31	1.39	44.39	3.10	0.219
BAs	1.70	0.08	6.21	2.26	3.01	0.093	0.106	0.277
ICAs	1.68	0.07	6.80	2.06	3.03	0.08	0.33	-

Source: Experimental data from Robertson et al. (79).

fibers matrix at each stage of the loading test, verifying the recruitment of the collagen fibers, responsible for the increase in stiffness after the transition region of the stress-strain curve.

Other experimental studies reported interesting details of IAs behavior towards a state closer to rupture. Costalat et al. (81), using uniaxial stress tests, found that unruptured IA tissue is stiffer than ruptured tissue. Moreover, their results suggest that the tissue becomes increasingly soft as the aneurysm progresses towards a rupture event (see Fig. 2.10).

Figure 2.10 – Average strain-stress curves constructed from traction tests of rectangular strips of an IA wall tissue for different stages of the aneurysm: unruptured (stiff) and pre-ruptured (intermediate) or ruptured (soft).

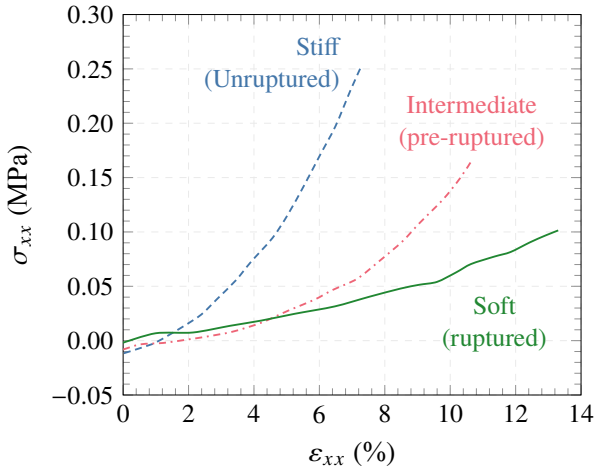

Source: Prepared by the author with data from Costalat et al. (81).

They fitted the stress-strain curve of the aneurysms samples using the uniaxial 3-parameters Mooney-Rivlin (MR) model (its uniaxial constitutive equation can be found in Appendix E) and classified the tissue samples as “stiff”, “intermediate”, and “soft” according to the values found. The averaged material constants per aneurysm status and observed mechanical behavior are in Table 2.4, which also shows the thickness of the IA samples, e_{ia}. According to the authors, the main difference in stiffness among the samples was observed by the change in the coefficient c_{11} of the MR model, mathematically responsible by the curvature of the stress-strain curve and a measure of the “high-stress” stiffness, i.e. the tissue stiffness when the collagen fibers are recruited.

Additional studies further support the aforementioned findings. Brunel et al. (82), for example, also found that unruptured aneurysms are stiffer than ruptured ones, as can be seen in Table 2.5, with the coefficients c_{10} and c_{20} of the Yeoh hyperelastic model (see Appendix E).

All the tests performed in the studies mentioned in this section were uniaxial tests, but to fully characterize the mechanical response of arteries and IAs tissue, a biaxial test would be more suitable (41). Nevertheless, uniaxial tests provide valuable data. Furthermore, in most of

Table 2.4 – Averaged material constants obtained in uniaxial traction tests up to failure of IAs tissue samples by Costalat et al. (81) according to aneurysm rupture status and type of identified mechanical behavior. The last row gives the average thickness of the samples, e_{ia}, also reported in their study.

Property	Mechanical Behavior			Aneurysm Status	
	Soft	Intermediate	Stiff	Unruptured	Ruptured
c_{10} (MPa)	0.1911	0.0598	0.3916	0.190	0.190
c_{01} (MPa)	0.0267	0.0168	0.0322	0.023	0.026
c_{11} (MPa)	1.37	5.71	20.87	11.78	1.377
e_{ia} (mm)	0.36	0.36	0.39	0.37	0.36

Source: Experimental data from Costalat et al. (81).

Table 2.5 – Averaged material constants obtained in uniaxial traction tests to failure of IAs tissue samples by Brunel et al. (82) according to aneurysm rupture status.

Property	Aneurysm Status		Samples Average
	Unruptured	Ruptured	
c_{10} (MPa)	0.12	0.07	0.10
c_{20} (MPa)	6.80	2.10	5.16

Source: Experimental data from Brunel et al. (82).

the studies mentioned here, the authors also measured the thickness of the sample, a piece of important information about the aneurysm wall.

2.5 HETEROGENEITY OF IAs WALL

An additional drawback of uniaxial tests is the lack of information on the heterogeneity of the wall of an IA sac, for thickness and material constants, which is still a challenge to obtain experimentally. Nevertheless, attempts have been made, partly by the same studies mentioned in Section 2.4. The differences in thickness and mechanical properties between cerebral arteries and aneurysms have been reported by Scott et al. (68) who performed pressure-inflation tests with arteries of the circle of Willis and IAs. They found the thickness of the cerebral arteries to be around 0.1 to 0.2 mm, with aneurysms walls much thinner and varying greatly, in general, with the rupture point of some aneurysms as thin as 0.025 mm.

More recent evidence confirmed the expected thinner IA wall compared to its surrounding arteries. Reports showed that the cerebral arteries have a mean thickness of 0.60 ± 0.12 mm and 0.51 ± 0.08 mm in the basilar and middle cerebral arteries, respectively. As for IAs, Steiger et al. (78), for example, also measured the thickness of their IAs samples, showing a great variability, ranging from less than 0.1 mm up to 0.5 mm. Abruzzo et al. (83) studied ruptured human IAs

and reported an averaged value of 0.51 mm. Table 2.4 and Table 2.3 also shows the averaged thickness found by Costalat et al. (81) and Robertson et al. (79), respectively, who estimated an aneurysm averaged thickness to be around 0.2 to 0.3 mm, and ranging from 0.1 to 0.6 mm. Cebral et al. (80) measured an average aneurysm sample thickness of, approximately, 0.25 mm.

Since it is difficult to obtain an artery or aneurysm wall thickness without employing invasive techniques, an interesting way to predict the artery wall thickness, on a patient-specific basis, is to use the parameter proposed by Nakagawa et al. (84), who measured the so-called *wall-to-lumen ratio (WLR)*, defined as:

$$WLR = \frac{\text{artery wall thickness}}{\text{artery lumen diameter}}, \tag{2.9}$$

in patients being operated. During the procedure, they measured the outer diameter along different positions of healthy intracranial arteries, while the inner diameter was measured by "indocyanine green angiography", a technique used for flow measurements during surgeries. The authors claimed that their study was the first to have directly measured this parameter *in vivo* — former studies have calculated it in rats and human cadavers. Their results showed that the mean WLR, for medium-sized intracranial arteries (lumen diameter between 2 to 3 mm), was 0.070 ± 0.010 and for large-sized intracranial arteries (lumen diameter greater than 3 mm) was 0.088 ± 0.012. Therefore, these mean values could be used to calculate a value for the mean thickness of intracranial artery walls based on their diameter that can be measured from the image examinations. Unfortunately, no study reported the WLR for IAs, or any measurement related to it. In any case, because the aneurysm wall thickness is heterogeneous, probably the WLR definition as given above is not suitably applicable to them.

Although, in the aforementioned studies, the researchers have directly measured the thickness of IAs tissues samples, some attempts have been made using imaging techniques to estimate IA wall thickness *in vivo*. Kleinloog et al. (85) performed an experimental study in which the wall thickness of IAs was measured using a 7-Tesla (7T) Magnetic Resonance Imaging (MRI). The wall was visible in 28 of the 33 cases studied with the image signal intensity and the actual thickness being positively correlated. The authors concluded that IA walls can be visualized using the 7T MRI equipment, although this equipment is rarely available in common medical examinations, where 1.5-Tesla or 3-Tesla MRI machines are more commonly employed. Nevetheless, 7T MRI provides a promising way to measure the tissue thickness *in vivo*, despite the technique still being in its infancy for a more widespread use (86).

To investigate the intrinsic heterogeneity exhibited by the sac wall of IAs, Signorelli et al.

(87) usied an "indentation device" to measure, in a point-wise manner, Young's modulus of an IA sac sample with a resolution of 1 mm^2. Their findings suggest that the rupture zone is less stiff, i.e. with a smaller Young's modulus, than the rest of the sac, where stiffer regions mixed with thin regions were found. The technique has the same drawbacks as classical uniaxial tests because it still requires the aneurysm tissue to be collected, hence *in-vivo* measurements are unfeasible, but it seems to be a promising test to quantify the heterogeneity of an aneurysm wall, allowing for comparative studies with histological analyses.

This point-wise assessment of IA mechanical properties would help to better understand particular regions of the aneurysm wall, such as the two types of phenotypes found in Meng's spectrum (see Fig. 2.7). Data on the morphology of atherosclerotic regions in IAs (type-II regions, according to Meng's classification), are scarce, since most studies on this particular subject focused on large arteries of the vascular system (88). Nevertheless, they provided evidence that this phenotype leads to a wall characteristically thicker (59), stiffer, and with larger elastic modulus than its surroundings. Holzapfel et al. (89) gathered data of several studies suggesting that, along the progression of atherosclerotic plaques, the elastic modulus of these plaques is increasingly larger only if calcified regions were present in these plaques. Once recent studies (90, 91) have shown that calcified portions are predominant in IAs walls, independently of being atherosclerotic or not, then it is reasonable to assume that atherosclerotic plaques in IAs have a larger elastic modulus than their surroundings.

Meng et al. (61) suggested that the red-looking thin regions, labeled type-I by the authors, were stiffer, although much lesser evidence could be found to support this affirmation, compared to type-II regions. Nevertheless, due to the dominant presence of collagen fibers in IA tissue, that most IAs have calcified regions, confirmed by Gade et al. (90) and found to be stiffer by Signorelli et al. (87), it is reasonable to expect that the suggestion by Meng et al. (61) was indeed the case.

Alternatively, based on the hemodynamics-driven mechanobiology of IA wall, some researchers investigated correlations between the hemodynamics adjacent to an IA wall with its tissue phenotype, assessed after intraoperative inspection, thus allowing for patient-specific predictions of an IA wall morphology and mechanical properties. Furukawa et al. (72), for example, correlated local hemodynamics with regions of hyperplastic remodeling, i.e. where atherosclerotic plaques occur. They found that these regions were significantly correlated with patches of the aneurysm walls that presented low TAWSS (< 1.08 Pa), high OSI (> 0.0152),

high relative residence time ($> 1.07\,\mathrm{Pa}^{-1}$), and aneurysm formation indicator (AFI) ≈ 0.973 (the defintions of the relative residence time and AFI, two HWP that depend on the WSS, are defined in Appendix A.2).

Cebral et al. (73) subdivided IA wall patches into five classes: atherosclerotic, hyperplastic, thin (red-appearing), ruptured region, and "normal-appearing" region. In atherosclerotic and hyperplastic regions, their findings were similar to Furukawa et al. (72) where the local hemodynamics was characterized by slow swirling flow with low TAWSS, high OSI and high relative residence time. Thin regions were characterized, in 90 % of the cases, by regions of "faster" flow and high TAWSS levels. In any case, this relationships may not be the rule. Kadasi et al. (74), for example, found a correlation between thin regions and low WSS levels.

In the same line, Kimura et al. (92) tried to find thin regions on IA wall by using a HWP that measures the WSS vector oscillation, called the "WSS vector cycle variation". Unfortunately, it was not able to detect thin regions in all the aneurysms of the sample analyzed.

In conclusion, the wall of patient-specific IAs is most likely to be heterogeneous regarding their morphology and mechanical properties. Furthermore, the hemodynamics-driven assessment of the wall morphology, which was used by very few studies to numerically simulate the wall mechanics of IAs (93), seems to be a suitable approach that balances feasibility, once it can be carried out based on the images of aneurysms from medical examinations, with realistic and patient-specific modeling.

2.6 CLOSING REMARKS

Intracranial aneurysms are caused by a combination of aberrant hemodynamics, wall biomechanics, mechanobiological mechanisms, and the external vessel environment. Based on this, one can conclude that an IA wall tissue have the following mechanical and morphological properties:

- It consists primarily of a multidirectional network of collagen, acting as its main structural component. Hence, its mechanical response is nonlinear and anisotropic over the finite-strain regime with heterogeneous mechanical properties and weaker than its surrounding arteries.

- It is a globally thin-walled shell-like structure, i.e. thinner than the surrounding arteries, although its thickness is most likely to vary locally too (a heterogeneous distribution).

- Initially, their walls are stiffer than its surrounding arteries, but may become less stiff as it progresses towards a ruptured condition.

In summary, an IA is a dangerous disease that may affect the lives of millions of people. Searching for better ways to predict its rupture is a pressing issue in the medical community. Further progress to that end must be met by a deeper understanding of the mechanics and mechanobiology of this disease because, ultimately, the rupture occurs in the wall tissue.

Chapter 3

NUMERICAL METHODS AND IAs: *L'ÉTAT DE L'ART*

Early in this century, the improvement in computational imaging techniques, traditionally used in medicine to help the diagnostic of several diseases including intracranial aneurysms (IAs), allowed the geometry of patient-specific IAs cases to be obtained (94). Consequently, numerical simulations, by the time already used in several engineering fields, began to be used to study hemodynamics in patient-specific vessels and aneurysms.

This can be confirmed by inspecting Fig. 3.1, which shows the number of publications and citations, in the past three decades, of works containing terms in their topic — i.e. including their title, abstract, and keywords — related to "intracranial aneurysms" and terms related to different numerical strategies employed to study them. Computational Fluid Dynamics (CFD) solves for the blood flow, whereas Computational Solid Dynamics (CSD) is used to study the IA wall mechanics, and Fluid-Solid Interaction (FSI) includes numerical techniques that solve for the mechanical coupling between the blood flow and the wall motion. After the beginning of the millennium, the number of publications and citations involving CFD and IAs increased substantially. On the other hand, the quantity of the ones that specifically investigated the IA wall motion — only possible with CSD and FSI strategies, since CFD ignores the wall flexibility — remained relatively low. Furthermore, the number of publications and citations of CFD-related works appear to keep increasing, while the CSD- and FSI-related ones peaked around 2010 and, then, seem to be decreasing over the past decade.

The flexibility of these numerical techniques, even with their own limitations, have dramatically improved the accumulated knowledge on the mechanics and mechanobiology of IAs as also on their inception, enlargement, and final rupture. However, the large number of, especially,

Figure 3.1 – Number of publications (left axis, bars), and citations (right axis, lines), over time, of works involving terms related to “intracranial aneurysm” and different numerical strategies to study its mechanics, found after a query in Web of Science® database.

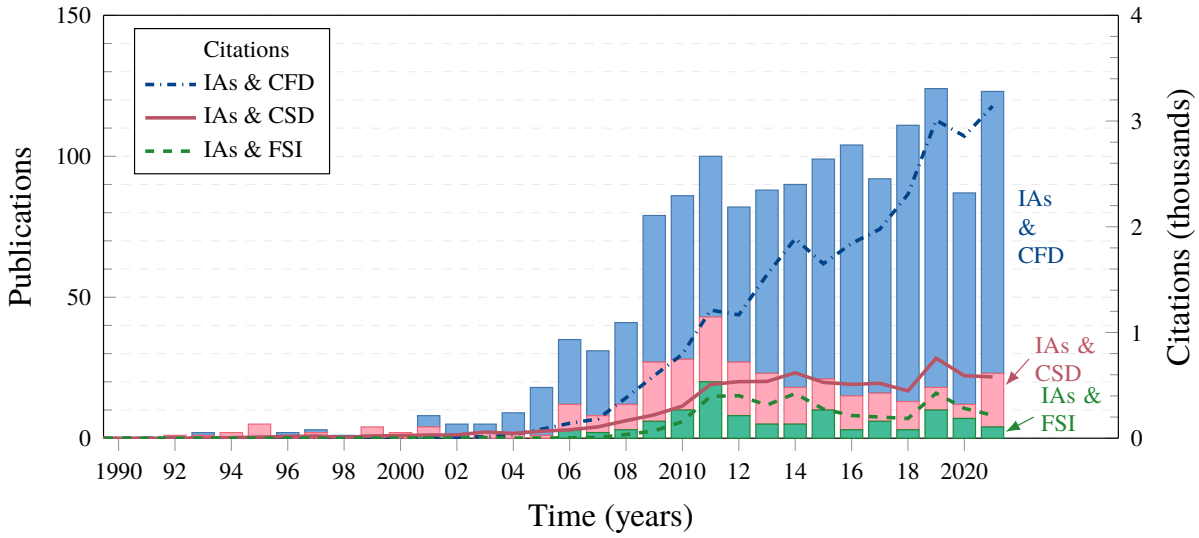

Source: Prepared by the author with data collected in the Web of Science® database.

CFD studies with IA may also have led to some confusion on the use of different parameters to study IAs, as explained in the following two sections.

3.1 THE ROLE OF CFD ON THE STUDY OF IAs

CFD has been widely used to describe the behavior of blood flow in arteries and idealized or patient-specific IA geometries, by assuming that their wall tissue was rigid, which is, in principle, a strong assumption since the vessels are elastic. Nonetheless, this was normally based on assumptions that, for the cerebral arteries, the motion of the artery tissue would have a second-order effect on the hemodynamics. Due to CFD’s inherent versatility, it allows to take into account several factors that may influence the flow, such as different blood rheology models (51), different boundary conditions (BCs) (95–97), the effect of the parent artery segmentation (98) or the curvature of the artery (64), and the effect of transient or steady modeling (99), just to cite a few examples.

In view of this power, many researchers conjectured that, in the future, CFD results for hemodynamics could help in guiding an IA treatment decision and its planning (100), e.g. through hemodynamics-based scores, such as the rupture resamblance score given by Eq. (2.2), although many still remain skeptical (101). Nevertheless, some studies provide good examples on how CFD can provide data that would be hard to obtain using experiments. Shojima et al. (60), for example, performed numerical simulations on different geometries of patient-specific

ruptured and unruptured IAs, to analyze the influence of the wall shear stress (WSS) on the rupture. According to their results, the authors concluded that a minimum level of WSS should be maintained at the interface, WSS ≈ 2.0 Pa, to preserve the endothelial structure of the wall tissue, whereas if WSS is lower than 1.5 Pa endothelial cells (ECs) could degenerate. This agrees with biological observations on the level of stress supported by the EC (see Section 2.3). Similarly, Cebral et al. (102) performed simulations using geometric data of 62 aneurysms, ruptured and unruptured, from different locations on the circle of Willis, and performed a statistical analysis correlating the flow "type" — based on different features such as the area and direction of the jet colliding at the entry of the aneurysm or formation of vortex structures inside the dome — with the risk of rupture. The authors concluded that the area and direction of the jet colliding with the aneurysm dome are important for predicting rupture, but caution was advised, since other important factors were not taken into account in their simulations, such as the already mentioned effects of the wall elasticity. The same authors, in a previous study (103) carried out an analysis of the hemodynamic characteristics in aneurysms under diverse biological conditions, concluding that the vascular geometry has a significant influence on the flow field, due to the nonlinear behavior of the Navier-Stokes equations.

As a consequence of the large number of these types of CFD studies, as occurred with morphological parameters, several hemodynamic wall parameters (HWPs) appeared in the past two decades that were associated with IA rupture (104–107). This number is actually so high, that some authors critically questioned the real utility that CFD may have in the clinical practice, eventually being only a *confounding factor dissemination* agent (101, 108). Almost all these parameters depend on the WSS, like simple averaged metrics of it, calculated on the aneurysm surface, or more biologically significant derived quantities like the oscillatory shear index (OSI) (69). Cebral et al. (109) and Cebral et al. (110), for example, proposed and analyzed nine different hemodynamics parameters with a sample of 210 patient-specific IA geometries, concluding that concentrated inflow streams and elevated levels of maximum WSS and low aneurysmal viscous dissipation were statistically associated with aneurysm rupture. Longo et al. (111) presented a review on the most significant HWPs and in Appendix A.2 the definition of the most relevant ones, mainly the ones that depend on the WSS, and their physical meaning are presented.

Other works also investigated the inception and subsequent enlargement of IAs, although in a smaller number, probably because they require longitudinal imaging examinations of a single patient-specific IA, which are not trivial to obtain and depend on the decision of the physician

following the patient. Based on CFD studies, Mantha et al. (112) and Shimogonya et al. (104) independently proposed two HWP, baptized respectively as aneurysm formation indicator (AFI) and gradient oscillatory number, as potential indicators of aneurysms formation (see Appendix A.2 for their mathematical definition). Briefly, the former captures the instantaneous effect of WSS fluctuations on ECs of the luminal side of a healthy artery, whereas the latter measures the variation of the spatial-gradient WSS vector field on the vessels luminal surface. Unfortunately, their works employed a small number of aneurysms (3 and 1, respectively), hardly achieving statistically significant results regarding the usefulness of the parameters. Indeed, Chen et al. (113), which also investigated IAs inception, found no correlations between the AFI and the region where an IA grew, whereas their findings indicate high correlations between these regions and time-averaged wall shear stress (TAWSS) and gradient oscillatory number.

The hemodynamics of lateral and bifurcation IAs was also subject of CFD studies. Although the majority of IAs occurs at bifurcations, lateral aneurysms are also common (see Section 2.1). Lauric et al. (64) investigated the initiation of these aneurysms, with CFD, by virtually removing the aneurysm sac in cases born on the outer siphon of internal carotid artery (ICA). Their goal was to assess the influence of the curvature of the ICA on the onset of these aneurysms. Their findings suggest that peak of local curvatures correlate with regions of high WSS that are flanked by high and positive WSS spatial gradient for aneurysmal arteries in contrast with "control arteries", i.e. arteries with similar morphological features but with no aneurysm development, thus indicating that a peak in the curvature is a better measure to predict aneurysm formation instead of the global siphon curvature. In a similar study, Geers et al. (114) investigated several hemodynamics indicators in aneurysms cases consistently found on the A1 segment of the anterior cerebral artery (ACA), an arterial regions that do not exhibit high levels of WSS naturally. The authors concluded that the parameter that most correlated with aneurysm initiation site, in those cases, was the wall shear stress pulsatility index. Moreover, they also explored correlations between different HWPs: according to them the OSI correlates with the AFI and the gradient oscillatory number correlates with the time-averaged WSS gradient. This could potentially eliminate redundancy given the large number of HWPs. Finally, by using two longitudinal digital subtraction angiography (DSA) examinations of one patient-specific IA case, Oliveira et al. (115) conducted a CFD study where particular levels of the TAWSS and OSI were correlated with the growth of that particular aneurysm case.

All these works exemplify how useful CFD can be: from allowing the study of the rupture

event, into further understanding of the hemodynamics itself, as also investigating the origins of a particular aneurysm case. However, many challenges and controversies remain and, among them, to accurately model the aneurysm wall motion is of foremost importance to study the wall mechanics and gather a deeper understanding of the aneurysm rupture event. This was accomplished by some works in which researchers numerically implemented the vessel wall motion in the computational model (24, 116–118), therefore accounting for the interaction between the blood flow and the artery wall flexibility.

3.2 THE ROLE OF COMPUTATIONAL FSI ON THE STUDY OF IAs

When numerically simulating the flow inside an IA, if the rigid-wall assumption is dropped, then the wall tissue must be modeled too, e.g. based on the mechanical behavior of IAs tissue presented in Section 2.4. In this case, one must deal with a *coupled physical system*, in which heterogeneous mechanical *domains* interact dynamically (119) or, more specifically, a FSI problem. In the IA flow problem, the blood flowing and the artery and aneurysm walls are governed by different field laws that are interdependent via the *coupling interface* or, in the case of FSI, the *fluid-solid interface*. These laws yield a system of partial differential equationss (PDEs) that must be solved together with a set of BCs for each domain.

From the numerical point of view, two different methodologies are usually used to solve this system (119, 120):

- The monolithic strategy employs a fully coupled approach in which all the governing equations are solved together by discretizing them into a single, usually large, system of linearized algebraic equations for one time-step, in the context of a time-marching technique. Thus, the whole system of PDEs advances simultaneously in time.

- The partitioned strategy, on the other hand, treats the solid and fluid subdomains as separate entities, and their respective systems of PDEs are discretized and solved separately, being the coupling on the fluid-solid interface enforced using different techniques.

It is important to highlight that the discretization process usually follows the same general procedure of classical discretization methods such as the Finite Volume Method (FVM), commonly employed in CFD, or the Finite Element Method (FEM), commonly employed in CSD, for example.

Both monolithic and partitioned strategies have been used to solve IAs motion in the last decade, although in a smaller number compared to CFD studies (see Fig. 3.1). Furthermore, most of them applied simplified hypotheses too. The majority of these studies had a parametric nature, with the influence of different modeling choices, related to the wall tissue, on the hemodynamics being the main subject of investigation.

For example, Bazilevs et al. (121) applied a monolithic strategy to solve for the motion of patient-specific IAs and compared the hemodynamics resulted with similar simulations but using the rigid wall model. They used a uniform thickness applied to the whole wall and concluded that the FSI played an important role in the prediction of the peak-systole WSS for aneurysms geometries, whereas the flow velocities were similar using both models.

The monolithic procedure employed by the studies mentioned in the preceding paragraph was developed by Bazilevs et al. (122) to simulate FSI in a total cavopulmonary connection, but subsequently used to study arterial blood flow (123). It employed the FEM to discretize both fluid and solid PDEs, in which the fluid was assumed as incompressible Newtonian flowing in a laminar regime and the neo-Hookean hyperelastic model was used for the artery and aneurysm walls (116). Alternatively, Eken et al. (124), for example, proposed a novel framework to simulate FSI by using the FVM to discretize the fluid equations while the FEM was employed for the solid equations (the tissue was modeled by using the St. Venant-Kirchhoff (SVK) law under finite strain and a single bifurcation aneurysm was solved). The coupling was also enforced through the monolithic strategy. Although the authors did not discuss the potential benefits of this combination of discretization methods, it is an interesting approach because it applies different discretization methods that are broadly recognized as adequate for each type of sub-problem.

Although robust due to the level o coupling in the discretized equations, the monolithic strategy lacks flexibility because it is normally implemented for a single model for the fluid and solid domains. Partitioned methodologies, on the other hand, can profit from already developed codes that solve only the fluid flow or the solid motion. This is the case for the majority of already available CFD and CSD codes, which are capable of efficiently solving each sub-problem.

Lee et al. (117) and Lee et al. (125), for example, used fluid and solid solvers commercially offered by Ansys®— through their packages CFX® and Mechanical®, respectively — to solve FSI in IAs, by using the coupling capabilities included in the Ansys® Workbench platform, which used a partitioned methodology to couple both physics. Lee et al. (117) analyzed the influence

of the parent artery length in IAs hemodynamics by modeling blood as a Newtonian fluid and the artery and aneurysm walls as a linear elastic solid, i.e. assumed to be under small displacements (Hookean solid). In a subsequent study, Lee et al. (125) analyzed the hemodynamics in five lateral aneurysms cases (2 ruptured and 3 unruptured) with respect to several physical conditions: different hypertension, morphology, and elastic moduli, while using the same physics models for the fluid and solid domains. Their study suggests that hypertensive blood pressure increases the magnitude of wall displacement and wall stress, whereas the WSS decreases compared to normal blood pressure conditions, regardless of the aneurysm morphology or material properties. Finally, their findings suggest that decreasing the elastic modulus yields an increase of the wall displacement, decrease in the area-average WSS and almost negligible changes in the stress distribution in the wall tissue.

By also using partitioned techniques based on a block-iterative approach, Torii et al. (24) analyzed one patient-specific cerebral aneurysm case by modeling blood as a Newtonian fluid and the aneurysm wall tissue as a Hookean solid, for different outflow BCs: normal blood pressure (80–120 mmHg) and hypertensive blood pressure conditions (100–170 mmHg), concluding that the latter condition can cause significant changes in the WSS distribution and in the wall stress field, as similarly found by Lee et al. (125).

The same authors then performed several parametric studies of FSI in brain aneurysms by using their framework, unfortunately with a small aneurysm sample, a recurrent limitation in numerical studies with aneurysms, nevertheless that further deepen our understanding of the problem. For example, Torii et al. (126) found interesting results for the aneurysm hemodynamics by directly assessing the influence of the wall elasticity in a comparison between the Hookean solid model with the traditionally used rigid wall model for two aneurysms geometries (a lateral and a bifurcation case). According to their findings, for both cases the blood flow was not influenced by the wall motion, while the larger difference in the WSS distribution occurred on the aneurysm neck. Furthermore, this influence depended on whether the larger displacement and larger WSS occurred in the same area, which is typically found when the flow impinges the lumen wall. This type of flow occurred for both cases analyzed, the flow impinging on the aneurysm neck.

In a subsequent study, Torii et al. (127) used an improved solid model, compared to Torii et al. (126), and performed simulations for one IA case, by assuming, first, the rigid wall assumption, hence “pure” CFD simulations, and three elastic laws: the Hookean law (thus,

assuming small strains), the SVK law, and a hyperelastic law using the exponential strain-energy function proposed by Demiray (128). Their findings showed that the displacement profiles were qualitatively similar for either the rigid-wall assumption, and the three elastic laws, although the maximum displacement for Demiray's law was 36 % smaller than that for the SVK law. Moreover, the minimum WSS, near the aneurysm apex in this case, is 36 % smaller for Demiray's law compared with the Hookean law. It is also interesting to note that both small and finite-strain linear elastic models predicted higher WSS on the aneurysm surface compared to the rigid wall results, which contrasts with Bazilevs et al. (121), where the rigid wall assumption overestimated the WSS. This difference may have been caused by different aneurysm morphologies and parent artery orientation, which drives the inflow in different ways and, thus, may change the flow type and influence the degree of difference for WSS between rigid and elastic wall models.

Torii et al. (129) investigated the hemodynamic changes with respect to different artery and aneurysm shapes. They found that the aneurysm shape is important because it determines the main features of the flow (102) and their results suggest that, when the flow impinges on the aneurysm wall, the maximum WSS tends to decrease when the elastic wall was used, whereas when a slowly recirculating flow is induced by the wall motion, the minimum WSS raises on the aneurysm wall.

It is important to note that all the works mentioned in previous paragraphs modeled the wall thickness as homogeneous over the entire solid domain, although a heterogeneous sac surface is a rule for IAs (see Section 2.3). To assess the influence of a heterogeneous wall thickness on the hemodynamics, Torii et al. (130), which focused on the hemodynamics, modeled the arteries with a uniform thickness (0.3 mm) and the aneurysm wall with a so-called "pathological" thicknesses, as named by the authors, which was smaller (0.05 mm) and still uniform over the sac surface. They compared the resulting hemodynamics with similar simulations, but with a uniform thickness throughout the wall domain (0.3 mm). According to their results, low WSS regions appeared to be more pronounced for the pathological wall thickness. Bazilevs et al. (131) used a lumen-diameter-dependent wall thickness distribution and also included the tissue prestress in their modeling (132), something unprecedented at the time. Their study found a consistent overestimation of the peak-systole WSS on the aneurysm surface by the rigid wall model. None of the studies, however, used local heterogeneous material properties on the aneurysm and the artery walls.

In Torii et al. (130), however, the authors did not perform any comparison regarding the wall stress, which is probably one of the variables that suffer the influence of the wall thickness. This was assessed in a recent study (133) where the authors obtained the complete IA-sac wall thickness distribution by μCT exams after aneurysm removal of a human cadaver. Moreover, after dissection, the rupture point was visible on the aneurysm surface. Their study, then, focused primarily on the comparison of the structural variables at the rupture point and on the complete aneurysm surface for patient-specific and uniform wall thickness. They showed that the average wall stress on the sac surface did not show much difference between the uniform and patient-specific wall thickness, whereas in the rupture site specifically, this difference reaches up to 55.2 %, with the wall stress being much higher at the rupture site for the patient-specific thickness. Both studies reinforced the importance of considering a heterogeneous or, better, patient-specific wall thickness distribution.

Let us take a closer look at the material laws and other modeling choices that the aforementioned studies employed (a summary of wall-tissue-related models is given in Table 3.1 with the aneurysm, e_{ia}, and artery, e_w, thicknesses as also the material parameters used by studies that simulated FSI and/or CSD). First, as already mentioned, almost all of them have used uniform wall thickness and uniform material properties for both arteries and aneurysms. In the light of the contents of Sections 2.3 and 2.5, it is striking the lack of studies that actually accounted for the aneurysm heterogeneous phenotypes, although it is important to note that each study in Table 3.1 gave its particular contribution despite the simplifying hypotheses used.

There are several reasons that possibly explain this. Numerical implementations of nonlinear solid models accounting for heterogeneous properties are not trivial and are even more complicated when FSI is numerically accounted for and involving such complex three-dimensional geometries such as patient-specific IAs. Additionally, the lack of available data. Most studies are from the last two decades, but comprehensible data on IA wall tissue properties were only published in the last decade. Finally, most studies performed comparative analyses which may not necessarily require a realistic model to be used for that particular purpose (for example, the main focus of the majority of the studies was hemodynamics, hence wall properties may not play a key role in this case, although they had to be accounted for in the modeling).

Second, it is also interesting to note that the majority of studies used the Hookean model, i.e. the small-strain linear elastic material law, even the most recent ones, probably due to its simplicity. However, it is known that deformation of arterial tissue occurs in the finite-strain

Table 3.1 – Aneurysm thickness, e_{ia}, artery thickness, e_w, and material constants, according to constitutive law used by the selected studies that performed FSI and/or CSD simulations with IAs geometries (interrogation marks were used when the study did not explicitly provided the parameter; brackets indicate that the study used a range of parameters for different geometries or a spatial varying model of thickness computed as a function of the lumen diameter, d_l. The studies for each model are organized from oldest to the newest.

Material Law	Publication	e_{ia} (mm)	e_w (mm)	Mechanical Properties		
				ρ^s (kg/m^3)	E (MPa)	ν^s
Hookean	Torii et al. (24)	0.30	0.30	?	1.0	0.49
	Valencia et al. (134)†	[0.20, 0.30]		1050	[5.0, 300.0]	0.45
	Torii et al. (126)	0.30	0.30	?	1.0	0.49
	Torii et al. (135)	0.30	0.30	?	1.0	0.45
	Torii et al. (127)	0.30	0.30	1000	1.0	0.49
	Valencia et al. (136)	[0.11 or 0.086]		1000	2.0	0.49
	Torii et al. (129)	0.30	0.30	1000	1.0	0.49
	Valencia et al. (137)	0.086	0.40	1050	7.0	0.49
	Sanchez et al. (138)	0.38	0.60	2300	3.0	0.49
	Lee et al. (117)	0.50	0.50	1100	5.0	0.49
	Lee et al. (125)	0.30	0.30	1000	[1.0, 2.0]	0.49
	Valencia et al. (139)	0.35	0.40	?	1.7742	?
	VoSS et al. (133)	0.30	0.30	1050	1.0	0.45
	Cho et al. (140)	<0.20	0.20	1050	2.6	0.45
Neo-Hookean	Bazilevs et al. (121)	0.018	0.018	1000	1.0	0.45
	Bazilevs et al. (131)	[0.2×$f(d_l)$]		1000	1.0	0.45
SVK	Torii et al. (127)	0.30	0.30	1000	1.0	0.49
				k_1 (MPa)	k_2	ν^s
Fung-type	Torii et al. (127)	0.30	0.30	0.3536	16.7	-
	Takizawa et al. (141)	[0.10, 0.67×$f(d_l)$]		0.0026	8.365	0.45
	Torii et al. (127)	0.05	0.30	0.3536	16.7	-
				c_{10} (MPa)	c_{01} (MPa)	c_{11} (MPa)
MR	Valencia et al. (134)*,†	[0.20, 0.30]		?	?	?
	Valencia et al. (137)*	0.086	0.086	−1.1314	2.3055	12.98
	Sanchez et al. (142)	0.38	0.60	0.39	0.0	22.14
		0.38	0.60	0.024	0.026	0.42
	Valencia et al. (139)*	0.35	0.40	0.385	−0.0891	0.512

† Used a single and virtual IA geometry; *These studies employed a five-parameters or nine-parameters MR laws with CSD and FSI numerical strategies; only the three first constants were given here for comparison with the three-parameter MR law.
Source: Prepared by the author.

regime and hyperelastic laws are the most suitable ones to represent their behavior, hence linear elasticity is a questionable modeling choice. The SVK model was less used possibly because it is an extension of the Hookean model to account for large rotations. The ones that employed traditional hyperelastic models for soft tissues — in the case, the neo-Hookean and MR models, and an isotropic exponential-like law named in this text “isotropic Fung” because it is similar

to Fung's models for arteries (41, 143) although originally proposed by Demiray (128) — were few and did not use mechanical properties of IAs. Most importantly, no clear indication of the most suitable law was given. Therefore, it currently remains unknown what is the impact of the use of different hyperelastic laws in the mechanics of IAs.

Overall, the focus of the studies in Table 3.1 was on the influence of different modeling choices on the hemodynamics only, i.e. most of them did not perform any comparison regarding the wall stresses. This would be important to assess in the context of searching for the likelihood of IA rupture, because since very early it is speculated that, from a mechanical point of view, the shape and thickness of the IA wall are more relevant to assess its rupture than size (56), the main indicator of rupture potential used by physicians.

Specific wall mechanics analyses were performed by another group of studies that took a different approach to simulate the behavior of the aneurysm wall. Very early studies of the IA wall mechanics were based on the equations for membranes of Laplace's law (Eq. (2.8)), which considers an infinitely thin membrane. Furthermore, the type of mechanical systems considered by Laplace's law are *statically determined* problems (144), i.e. the stress distribution is solely given by the load, BCs, and the geometry of the problem. Mechanical properties do not impact the overall mechanics of this type of problem (Eq. (2.8) exemplifies this). Ma et al. (145), for example, studied patient-specific IAs geometries assuming them to be statically determined and using an anisotropic Fung-like constitutive model. The authors compared the wall stresses and strains between ruptured and unruptured aneurysms, being able then to study the correlation between stress, strain, and surface curvature. However, they only studied the aneurysm sac, i.e. they removed the surrounding arteries portions that may have had an impact on the aneurysms sac stresses, and used a pressure-inflation model with static BCs. Moreover, they explain that the homogeneous wall thickness was a too strong hypothesis to be assumed and that the aneurysm problem may not be statically determined at all since this requires the membrane model to be suitable for aneurysms. Zhao et al. (144) used a similar technique but with the main goal of assessing how the material properties on the aneurysm wall were distributed. They successfully estimated it but argued that the technique may not work properly for high curvature regions, which are common in IA wall.

The same modeling used by Ma et al. (145) was also used by Ramachandran et al. (146), but these authors investigated the impact of different material laws on the wall stress and strains by numerically simulating the aneurysm sac. They used both anisotropic and isotropic versions of

Fung-like laws, the Yeoh law with three parameters, the SVK law, and the Hookean law too (only Torii et al. (127) studied different constitutive models, but as explained above solely focused on hemodynamics properties). Although their results suggest that the aneurysm sac may indeed be statically determined regarding different material laws, they also verified that Laplace's law was the worst method to estimate the stress. Finally, the authors highlighted that these conclusions may not withstand when the full vasculature is simulated with dynamical BCs that realistically reflect the cardiac cycle forces.

Therefore, statically determinacy is not a certainty when modeling IA wall tissue and further data is necessary to assess the impact of the material parameters heterogeneity and constitutive law in the mechanics of IAs. Additionally, the flow forces that drive the aneurysm wall mechanics must be accounted for in the model, be it in a full FSI simulation or in more simplified ways, such as the strategy called "one-way FSI" (147) or through a pressure-inflation model. One worthy question to ask is how useful these two latter models can be in the study of the IA wall mechanics. Finally, with increasingly better methods and more powerful computational resources, progress must be made by using numerical techniques that are able to gather realistic IA wall modeling, as performed by the wall mechanics studies mentioned in the two preceding paragraphs, with FSI techniques used by the studies in Table 3.1.

3.3 MAIN GOALS OF THIS WORK

The studies mentioned above show several advances, achieved in the last decade, in simulating the flow and the wall mechanics of an IA. Nonetheless, they have their limitations, normally due to simplified modeling choices that did not account for the overall complexity of the flow in an IA. This is probably explained by the lack of more powerful computational resources to deal with this complex problem, but also due to techniques that may not be suitable to solve such problems.

Perhaps one of the most important limitations was the poor choice of wall tissue modeling, without taking into account the finite strain regime at which the IA wall motion occurs and the nonlinearity of the constitutive behavior of an IA tissue. Additionally, the ones that did have not presented a more in-depth analysis of the wall stresses and strains. Only two studies (127, 146) explicitly investigated the impact of different constitutive laws on the IA wall mechanics. Nevertheless, some of their assumptions were restrictive, such as only simulating the aneurysm sac with static pressure BCs and assuming uniform IA wall thickness. Moreover, even the most

recent studies used simplifying hypotheses on the IA wall morphology, such as uniform wall thickness and uniform material properties, which are probably not the rule among IAs, as seen in Section 2.3.

Therefore, there is still a lack of overall understanding of the mechanical response of IAs, and how it is related to (or how could explain) the rupture event. This scenario forms the foundation of the goals of this work, described in general terms in Chapter 1, i.e. to assess the impact of the different wall modeling choices on the stresses and strains of an IA wall, more specifically, by testing different constitutive laws and wall morphology models. Additionally, the proposal here was to use ruptured and unruptured IA cases to further allow an investigation of the rupture event in terms of the wall mechanical response.

To accomplish this for patient-specific IAs, numerical simulations were the most obvious choice. *In-vivo* measurements of stress and strain are still hard to perform, which contrasts with the versatility of numerical techniques. The overall methodology will be presented in the three subsequent chapters, but, briefly, numerical simulations, using the library solids4foam, an open-source CSD library, were performed using geometries of patient-specific IAs. A partitioned technique implemented in solids4foam was used and realistic modeling of the blood flow and wall mechanics was developed, guided by the contents of Chapter 2. Finally, ruptured and unruptured geometries of IAs were used because this would allow a further assessment of which combination of modeling would most correctly predict the rupture — or whether all of them would.

Chapter 4

GEOMETRIES AND MORPHOLOGICAL CHARACTERIZATION

In this chapter, the extraction and computational analysis of the patient-specific intracranial aneurysm (IA) geometries selected for this study is presented in detail as also the morphological characterization of the IA sample.

4.1 GEOMETRY SEGMENTATION

The patient-specific IA geometries were obtained from digital subtraction angiography (DSA) examinations, collected retrospectively, provided by Dr. Carlos Eduardo Baccin, who collaborates in this work. The use of the examinations was approved by the Research Ethics Committee of the Faculty of Medicine of São Paulo State University (UNESP), Campus of Botucatu, and by Albert Einstein Israelite Hospital, São Paulo, where the images were taken. Some geometries were also obtained from the Aneurisk dataset repository (148), which provides a set of IAs geometries used during the Aneurisk project and available under the "CC BY-NC 3.0" license.

The geometries of the vessel network with IAs were segmented using the VMTK® library with the level-sets segmentation technique (149). According to its website (150), "VMTK® is a collection of libraries and tools for 3D reconstruction, geometric analysis, mesh generation and surface data analysis for image-based modeling of blood vessels".

The DSA file is a 3D pixelized image that is used to identify the brain vessels tree by an injection agent that highlights the lumen surface of the vessels during the angiography. The exams are normally presented as a DICOM file, commonly employed by the medical community. Figure 4.1 illustrates the process to extract a patient-specific vascular geometry with its surrounding

Figure 4.1 – Example of the steps of the IAs geometries segmentation using VMTK: starting with the (a) DSA image examination (shown in a volume-rendered view in ParaView®), (b) the VOI was selected and a raw surface was extracted (pink surface portion of the vasculature), which was then (c) "clipped" at the inlet and outlets of the domain containing an IA. The (d) final surface was then smoothed and freed of the artifacts on it due to the segmentation process, remaining only the portion containing the aneurysm geometry with a high-quality surface.

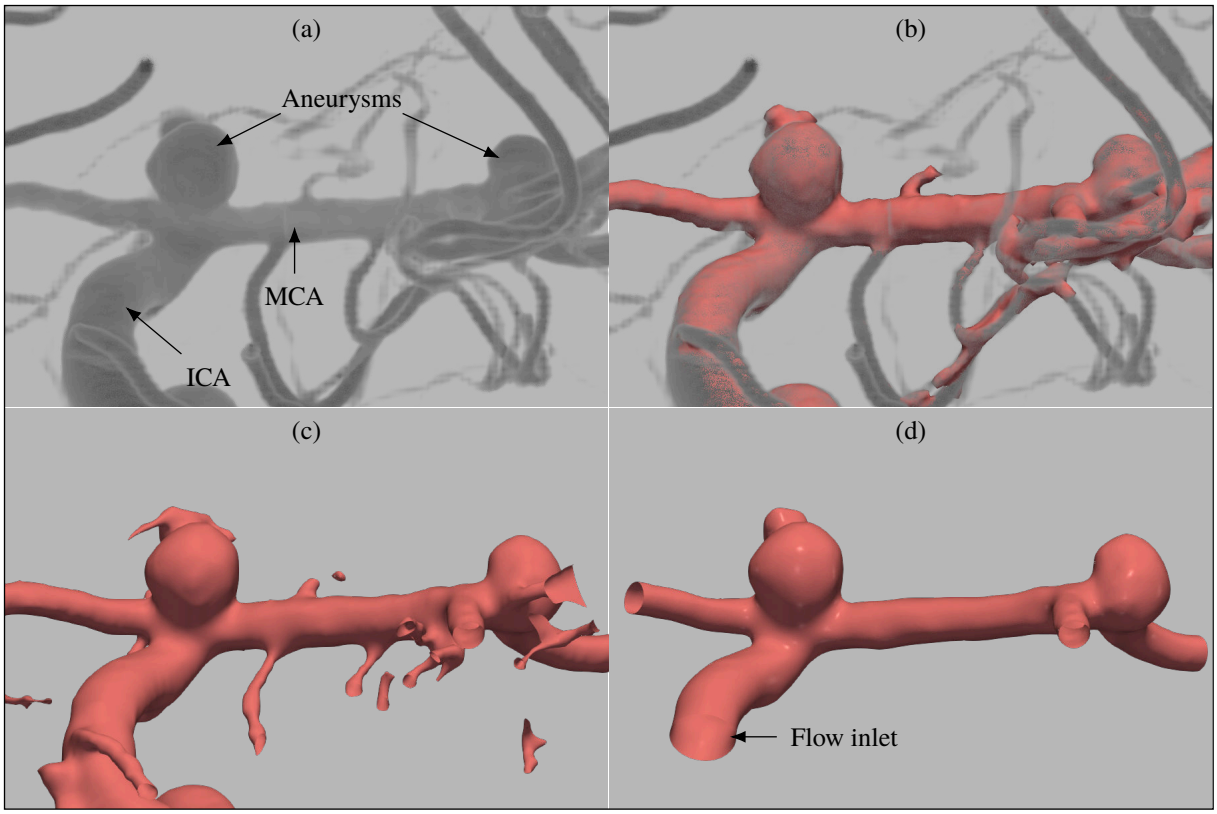

Source: Prepared by the author.

vessels. First, the VMTK's utility `vmtkimagevoiselector` was used to slice a cube out of the DSA image, known as the *volume of interest (VOI)*. In this procedure, the size of the VOI was not pre-defined but chosen large enough to ensure that it enclosures only the aneurysm and its closest surrounding vessels. Then, the utility `vmtklevelsetsegmentation` was employed to extract only the image of the aneurysm and its surrounding vessels from the VOI image. Finally, a triangulated surface was generated with the utility `vmtkmarchingcubes` (94, 151) (and stored as an STL file).

This raw surface generated by `vmtkmarchingcubes` had imperfections and several artifacts that can arise from the segmentation process, as also small patches originated from vessels in the surroundings of the domain of interest, but that are not part of it (Fig. 4.1c). These artifacts were removed and the surface quality was then improved with the utility `vmtksurfacesmoothing`. Finally, the inlets and outlets were "clipped" (152), i.e. the surrounding arteries were cut with `vmtksurfaceclipper` to correctly apply the inlet and outlets boundary conditions (BCs), yielding the final surface as an STL file (Fig. 4.1d).

4.2 MORPHOLOGICAL CHARACTERIZATION

Based on the goals of this work, which also depends on the comparison of ruptured and unruptured IA cases, a set of 12 vascular geometries, with 6 ruptured and 7 unruptured IAs, were selected. Figure 4.2 show them, geometrically scaled and grouped by rupture status (from now on, these two groups will be labeled "$\mathcal{R}$" for the ruptured sub-group and "$\mathcal{U}$" for the unruptured one), and ordered by their volume size, with their label, which will be used henceforth. These labels were defined by appending their rupture status, prefix "r" for ruptured and "ur" for unruptured, to their parent artery. For example, an unruptured case in the internal carotid artery (ICA) bifurcation is labeled "urICA", followed by a natural number in case of repetition. Cases rMCA1, rMCA2, and rICA1 were the ones selected from the Aneurisk database. Note that only the aneurysm sac surfaces, S_{ia}, are highlighted in the figure in a way that their *neck contour* can be clearly seen.

Theoretically, the neck contour, Γ_{ia}, is a 3D path that separates the aneurysm sac from the branches. Several works proposed different ways to compute it, from a "plane neck" (153) to a automatically-calculated 3D path using the Voronoi diagram of the vascular surface (154). Nevertheless, it is an inherently complex task primarily due to the variability of IAs' morphologies (Fig. 4.2 illustrates that), in which case no single technique is able to find a neck contour that would satisfy all the practical applications of such a geometrical entity. Therefore, in this work, Γ_{ia} was defined manually, by interactively marking the path on the vascular surface. This approach was motivated by the important use of Γ_{ia} in the physical model constructed to represent the IA wall thickness and mechanical properties, as will be presented Section 5.3.8.

Table 4.1 presents 1D and 3D size metrics of the IA sample's subjects and also the diameter of their respective parent artery, per rupture-status groups, all mathematically defined in Appendix A.1. It is important to note that these precise definitions of size metrics were used for consistency among the whole sample, although the 1D size shown in Fig. 2.1 are commonly employed in the medical practice. For a suitable comparison with the tables, Fig. 4.2 shows the IAs with their normal vector to neck ostium, $\boldsymbol{n}_o$, oriented along the vertical. The ostium surface, S_o was computationally created by joining the points lying on Γ_{ia} to the geometric center of it, $\boldsymbol{x}_o$, yielding a triangulated surface. Both ostium and all metrics were computed in an in-house library developed by the author in Python and using the VMTK® and the Visualization Toolkit (VTK)® libraries as its main components.

Apart from their rupture status, other factors were also accounted for their specific selection.

Figure 4.2 – Patient-specific IA geometries previously selected to be part of this work: 6 ruptured (left panel, group $\mathcal{R}$) and 7 unruptured (right panel, group $\mathcal{U}$) IAs at the ICA and middle cerebral artery (MCA) (the surfaces are scaled for intercomparison).

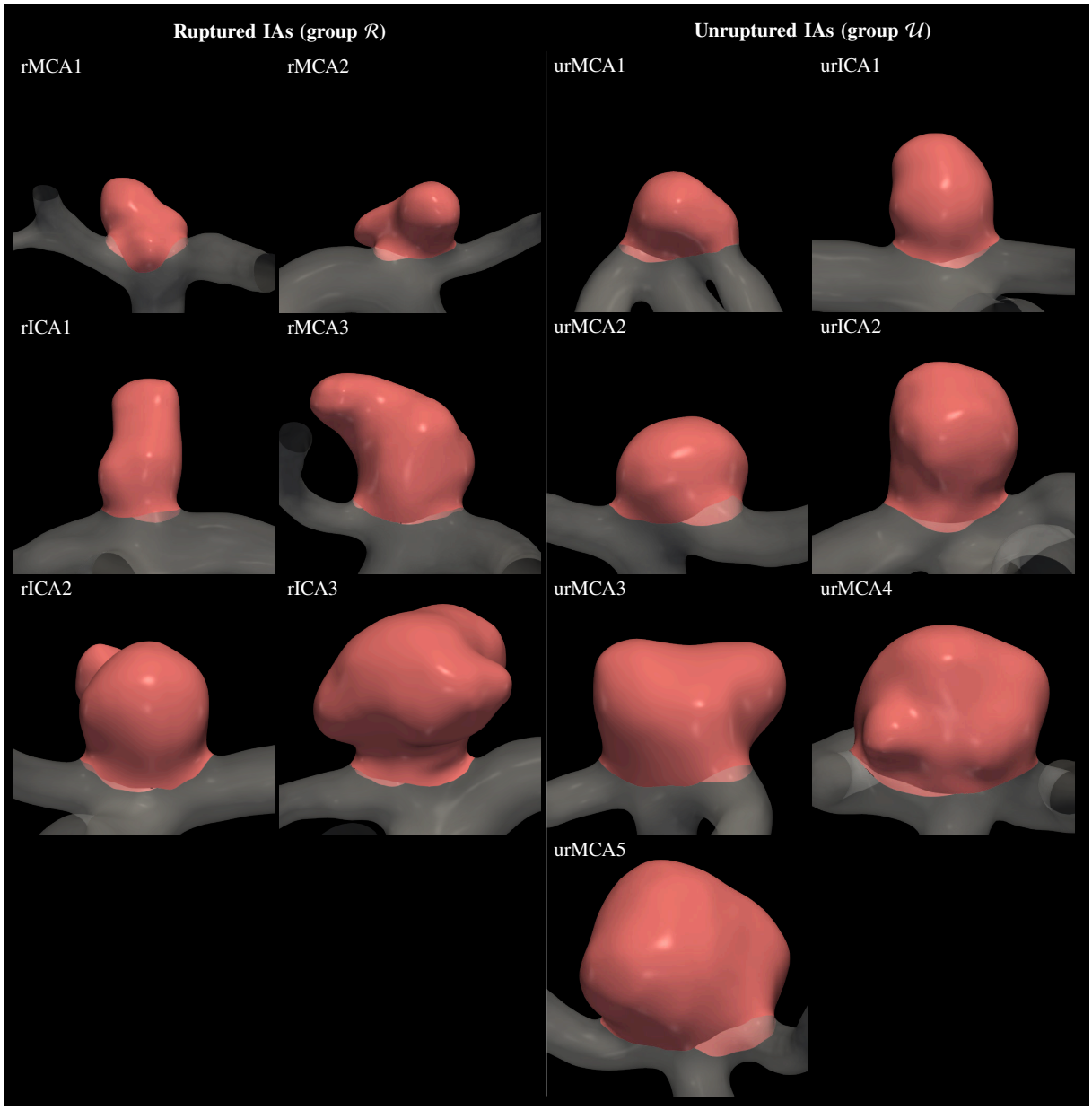

Source: Prepared by the author.

Firstly, their size, normally given by the maximum dome diameter, d_d and the maximum normal dome height, h_d. As can be seen in Table 4.1, the size range per rupture-status group are similar, ranging from, roughly, 3 mm to 7 mm, thus categorizing them as small- or medium-sized IAs (3 to 10 mm). As explained in Section 2.1, this fact is of particular importance in view of the trade-off between likelihood of rupture and likelihood of bad post-surgical outcome. The mean h_d for the rupture-status groups are also similar (ruptured: 5.14 mm, unruptured: 5.52 mm), although d_d is slightly different (ruptured: 4.93 mm, unruptured: 6.28 mm), which reflects in the

Table 4.1 – Size metrics of the IA sample and the respective parent artery diameter, d_{pa}, grouped by ruptured status and ordered by volume. The neck diameter, d_n, maximum dome diameter, d_d, and maximum normal dome height, h_d, are 1D size metrics, whereas both aneurysm sac surface area, A_{ia}, and sac volume, V_{ia} are 3D size metrics.

IA Case	d_{pa} (mm)	d_n (mm)	d_d (mm)	h_d (mm)	A_{ia} (mm^2)	V_{ia} (mm^3)
rMCA1	2.23	3.18	3.70	3.21	34.42	20.47
rMCA2	1.93	3.09	3.66	2.98	43.19	27.44
rICA1	2.08	3.35	3.43	5.83	61.27	42.54
rMCA3	2.68	3.92	5.51	5.90	100.9	95.29
rICA2	3.86	4.94	5.93	5.68	120.3	129.1
rICA3	3.62	4.37	7.38	7.23	186.1	226.2
Mean ± SD	3.08 ± 0.92	3.81 ± 0.74	4.93 ± 1.59	5.14 ± 1.68	91.04 ± 57.23	90.18 ± 78.89
urMCA1	2.60	3.62	5.29	3.42	51.43	41.71
urICA1	4.09	4.30	4.80	5.08	74.00	70.56
urMCA2	2.72	4.38	5.38	4.14	75.86	74.21
urICA2	3.90	4.73	5.78	6.42	114.5	125.5
urMCA3	3.17	5.11	6.75	5.76	139.8	168.8
urMCA4	3.06	6.18	7.98	6.38	163.5	228.5
urMCA5	2.88	5.54	7.97	7.44	191.1	275.2
Mean ± SD	3.20 ± 0.53	4.84 ± 0.85	6.28 ± 1.30	5.52 ± 1.40	115.74 ± 51.65	140.64 ± 87.52

Source: Prepared by the author.

surface area and volume of the IAs, making the subjects of the unruptured group more “bulky”.

Secondly, they originate only from the more common bifurcation spots of IA occurrences, the ICA and MCA, which, together, account for more than 60 % of all IAs occurrences (see Fig. 2.2), while only a few geometries of other arteries — such as the anterior communicating artery (ACoA) and basilar artery (BA) — were available to be used, thus it was preferred to exclude them. Only bifurcations IAs were included due to their prevalence in the cerebral arteries.

Finally, by visually inspecting the IA surfaces, it is straightforward to note that the ruptured cases have a much more irregular surface than the unruptured ones, due to large lobular regions (e.g. case rICA3) as also prominent blebs (e.g. case rICA2) present on their surface, which have already been associated with rupture (155, 156). On the other hand, all unruptured cases presented uniform, regular, and more spherical shapes. Quantitatively, this can be verified by comparing the 3D shape metrics per group, also defined in Appendix Section A.1 and given as means per group in Table 4.2. Briefly, both non-sphericity index, *NSI*, and ellipticity index, *EI*, measure how similar an IA shape is to a hemisphere (zero indicates a perfect hemisphere and

one a collapsed aneurysm), but *EI* uses the convex hull of the aneurysm in its definition to avoid distortions caused by blebs; the undulation index, *UI*, quantifies the presence of blebs or lobular regionn Raghavan et al. (33).

Table 4.2 – Means and standard deviation (SD) of 2D and 3D shape metrics for the ruptured ($\mathcal{R}$) and unruptured ($\mathcal{U}$) subgroups of the IA sample; aspect ratio, *AR*, is a 2D shape index, whereas the undulation index, *UI*, non-sphericity index, *NSI*, and ellipticity index, *EI*, are 3D shape metrics (157).

Index Type	Index	$\mathcal{R}$	$\mathcal{U}$
2D Shape Index	*AR*	1.34 ± 0.34	1.13 ± 0.17
3D Shape Indices	*UI*	0.140 ± 0.024	0.077 ± 0.015
	EI	0.140 ± 0.042	0.091 ± 0.030
	NSI	0.200 ± 0.028	0.130 ± 0.025

Source: Prepared by the author.

The mean of these indices for the ruptured group is roughly twice that for the unruptured group. To attest this difference, statistical tests were performed between the rupture (n = 6) and unruptured (n = 7) groups for all the metrics in Tables 4.1 and 4.2. The paired t-test for independent groups was employed (the Shapiro-Wilk test was used for normality assessment). All tests were performed with the SciPy library (158). The significance level was considered $\alpha = 0.05$ (95 % confidence interval).

Even with this relatively small sample, the difference between ruptured and unruptured cases was statistically significant for the *UI* ($p < 0.001$), *NSI* ($p < 0.001$), and *EI* ($p = 0.024$). The other metrics did not reach for statistical significance, even the aspect ratio that has already been used to categorize ruptured and unruptured aneurysms (30). Most importantly, this statistical test have shown that, regarding the IA size range, the ruptured and unruptured subgroups are statistically the same, whereas they differ in their shape.

When studying IAs, the sample selection is a crucial task and was performed with care in view of the specific goals of this work, as also by accounting for the randomness in the sample selection. The characterization presented here followed this line of thought, and it must be reinforced that the morphological characterization was performed *after* the sample selection, carried out exclusively by the IA rupture status and by accounting for aneurysms of small and medium-size, only.

Apart from that, other factors that motivated specific IA selection were based on technicalities involving the mesh creation process. For example, some aneurysms have high curvature regions that make it difficult to create a high-quality wall mesh, or have artery branches next to the

aneurysm surface, which would cause overlapping wall meshes, currently impossible to be solved by the software employed for this work. Nevertheless, these reasons do not add any bias to the sample selection, on the contrary, it only limits the possibilities of IA cases to be included in this work.

Chapter 5

PHYSICAL AND MATHEMATICAL MODELING OF IAs

As explained in Section 3.2, blood flow inside a vasculature with an IA is considered a Fluid-Solid Interaction (FSI) problem because the mechanical variables of the blood flow and the tissue motion are mutually dependent. Being in possession of patient-specific geometries, presented in Chapter 4, to numerically simulate this FSI phenomenon, mathematical models of the wall motion and the blood flow are needed, more especifically the *constitutive equations* of the materials involved and the *physical principles* governing them. This is the main focus of this chapter and the foundations of this modeling were given in Chapter 2.

Mathematically, the FSI problem of an IA is constituted by a 3D *moving* domain $\Omega(t)$, with boundary Λ, composed of the solid subdomain $\Omega^{s}(t)$ (the artery and IA walls) and the fluid subdomain $\Omega^{f}(t)$ (the blood flowing), i.e. $\Omega = \Omega^{s} \cup \Omega^{f}$, with boundaries indicated by Λ^{s} and Λ^{f}, respectively, as shown schematically in Fig. 5.1. The coupling between these two subdomains occurs through the physical interface called *fluid-solid interface*, defined as $\Lambda^{fs} = \Lambda^{f} \cap \Lambda^{s}$. Biologically, this interface corresponds to the lumen surface of the vascular wall — exactly the computational surface extracted with VMTK presented in Section 4.1. In the following sections, physical models for both Ω^{f} and Ω^{s} are developed.

Initially, a presentation of the strategy to couple both subdomain's physics is given. In the sequence, the specific physical and mathematical models, as also BCs, for the fluid and solid subdomains are presented.

Additionally, it is important to note that there are two foundational hypotheses assumed for both blood and vascular tissue. First, these materials can be represented as a continuum. This hypothesis is acceptable, in those cases, because the smallest material volumes in the domain of

Figure 5.1 – Schematic saccular IA in a bifurcation of a vessel, with clipped flow inlets and outlets, indicating the solid, Ω^{s}, and fluid subdomains, Ω^{f}, as also the fluid-solid interface Λ^{fs} and boundaries of each region.

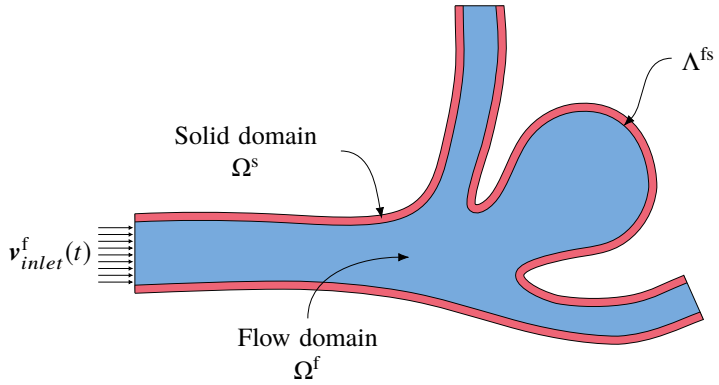

Source: Prepared by the author.

study contain a large number of molecules and atoms. Therefore, the material properties vary continuously, in the mathematical sense. Second, a purely mechanical view of the blood flow and vessel wall was assumed, i.e. all the biological processes occurring at a specific time in them were ignored because the aim of this work was to model a few cardiac cycles, whereas the time scale of the mechanobiological processes that take place on an IA wall are on the order of months or years. Moreover, any fast muscle contraction motion was ignored and all the processes assumed isothermal. In other words, the tissue was assumed to respond *passively*.

Finally, it is important to add that, throughout this section, integral versions of the governing equations were preferred, instead of differential versions, because they are more suitable to be used in presentations involving the Finite Volume Method (FVM), the numerical method used to solve both fluid and solid governing equations, as will be explained later in this text.

5.1 THE ONE-WAY FSI STRATEGY

In Section 3.2, works that have successfully solved the blood flow in patient-specific IAs geometries were discussed. Although the majority of those works used the monolithic strategy, some employed the *partitioned* one to solve for the FSI, in which, briefly, the fluid and solid problems are solved separately and sequentially and the coupling enforced through the FSI interface for *both sub-domains*, i.e. the flow-driven force is passed to the solid and the solid motion is informed to the flow domain in the course of the computations. Henceforth, in this text, this approach will be labeled two-way fluid-solid interaction (2WFSI).

Unfortunately, the 2WFSI strategy poses severe difficulties to solve for the motion of a large cohort of patient-specific IAs. As thoroughly explained in the specialized literature, partitioned

FSI techniques suffer from unconditionally numerical instabilities if incompressible flows and light structures are involved in the physics of the problem. More specifically, if the density ratio between the fluid and solid media, $\frac{\rho^{\mathrm{f}}}{\rho^{\mathrm{s}}}$, is greater than or close to the unity. This is the case for the IA FSI problem. The operator related to these instabilities is called the added-mass operator and a review of this subject can be found in Appendix B.

Additionally, a complex 3D geometry and nonlinear equations for both fluid and solid subdomains may further complicate the solution of it, leading to prohibitively computational solution times even for a single IA case (on the order of months) in case the solution converges for all time-steps. Therefore, because in this work the main goal involved an analysis of the mechanical response of an IA wall, and not necessarily an analysis of the hemodynamic changes caused by the wall motion, an alternative FSI strategy was chosen where the interaction is unidirectional, the so-called one-way fluid-solid interaction (1WFSI) approach.

In the 1WFSI strategy, the fluid forces are transferred from the fluid mesh interface, $\Lambda^{\mathrm{fs}}_{fluid}$, to the solid mesh interface $\Lambda^{\mathrm{fs}}_{solid}$, whereas the solid deformation is not transferred back to the fluid domain. Therefore, this can be viewed as a Computational Solid Dynamics (CSD) simulation with the traction due to the flow applied to the lumen surface at each time-step. Figure 5.2 shows a schematic two-dimensional drawing of the 1WFSI strategy and the BCs used for the other surfaces. In terms of BCs, the vessel walls for the fluid domain, i.e. $\Lambda^{\mathrm{fs}}_{fluid}$ because it is the fluid counterpart of the FSI interface, are assumed rigid with zero mass flux, zero pressure gradient, and no-slip. On the other hand, on the inner surface of the vessels, $\Lambda^{\mathrm{fs}}_{solid}$ (corresponding to the lumen surface), the traction BC was imposed with the traction being calculated from the flow solution at each time step, as follows:

$$\underbrace{\left(\boldsymbol{n}^{\mathrm{s}} \cdot \boldsymbol{\sigma}^{\mathrm{s}}\right)_{\Lambda^{\mathrm{fs}}_{solid}}}_{\boldsymbol{t}^{\mathrm{s}}} \coloneqq -\underbrace{\left(\boldsymbol{n}^{\mathrm{f}} \cdot \boldsymbol{\sigma}^{\mathrm{f}}\right)_{\Lambda^{\mathrm{fs}}_{fluid}}}_{\boldsymbol{t}^{\mathrm{f}}}, \tag{5.1}$$

(note the use of the assignment operator, typically used in computer science) where $\boldsymbol{\sigma}$ is the Cauchy stress tensor in each domain, and $\boldsymbol{n}^{\mathrm{s}}$ and $\boldsymbol{n}^{\mathrm{f}}$ are the normal vectors on Λ^{fs} pointing outwards, respectively, of the solid and fluid domains. It is important to highlight that the fluid forces are interpolated "on the fly", i.e. the flow simulation is carried out alongside the solid simulation and the interpolation of information to the solid wall performed at each time step.

Figure 5.2 – Schematic two-dimensional representation of the BCs applied in the aneurysms 1WFSI simulations with a detail illustrating the transfer of information on the Λ^{fs}: pressure and viscous traction from the flow are interpolated from the fluid mesh interface, $\Lambda^{\text{fs}}_{fluid}$, to the solid mesh interface, $\Lambda^{\text{fs}}_{solid}$.

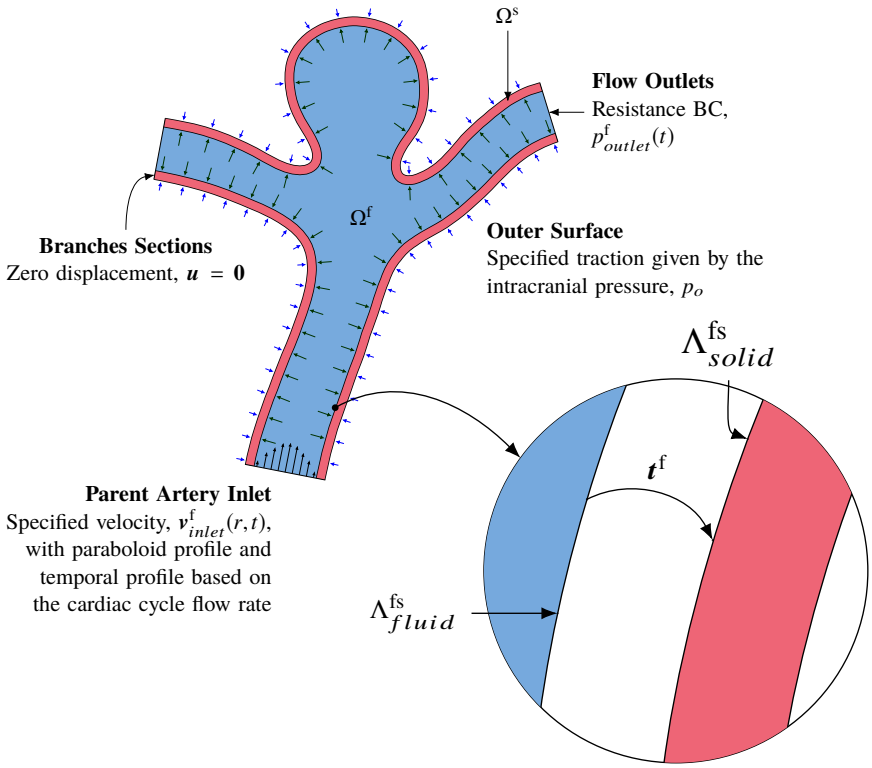

Source: Prepared by the author.

5.2 BLOOD FLOW MODELING

In the fluid domain, Ω^{f}, blood was assumed to be a compressible Newtonian fluid flowing in an isothermal laminar regime. The Reynolds number of the flow in the cerebral arteries varies between 300 and 1000 along the cardiac cycle, enough to assume laminar flow in these tubular-like structures. Furthermore, the discussion in Section 2.2 showed the current controversy on the constitutive assumption over blood in IAs and, nonetheless, the Newtonian law was still assumed because it is likely that the overall impact of different non-Newtonian laws on the wall mechanics is similar to the Newtonian effect. Finally, the compressibility of blood has been reported since early (159) and it is similar to water's compressibility.

5.2.1 Governing Equations of the Flow

In the context of the IA FSI problem and assuming an isothermal flow of a compressible fluid, the flow governing equations are the conservation of mass and the balance of linear momentum. Given that the assumption of FSI involves a moving fluid-solid interface, these principles must

be written, rigorously, for a moving frame of reference. The alternative used here was the so-called arbitrary Lagrangian-Eulerian (ALE) formulation (160), in which an extra coordinate system, indicated by $\boldsymbol{\chi}$, is considered. Computationally, this coordinate system is attached to the fluid flow computational mesh.

Therefore, by using the Reynolds transport theorem for a moving domain, $\Omega^{\mathrm{f}}(t)$, both governing equations can be written as:

$$\frac{\partial}{\partial t}\left(\int\limits_{\Omega^{\mathrm{f}}(t)} \rho^{\mathrm{f}} \mathrm{d}V\right)\Bigg|_{\boldsymbol{\chi}} + \oint\limits_{\Lambda^{\mathrm{f}}(t)} \rho^{\mathrm{f}} \left(\boldsymbol{v}^{\mathrm{f}} - \boldsymbol{\omega}\right) \cdot \boldsymbol{n} \mathrm{d}S = 0\,, \tag{5.2}$$

where $\boldsymbol{v}^{\mathrm{f}}$ is the flow velocity field, $\boldsymbol{\omega}$ is the velocity of the referential system of the ALE formulation, and $\boldsymbol{n}$ is the outward normal vector to the control surface Λ^{f}. The momentum equation in integral form is written as follows:

$$\frac{\partial}{\partial t}\left(\int\limits_{\Omega^{\mathrm{f}}(t)} \rho^{\mathrm{f}} \boldsymbol{v}^{\mathrm{f}} \mathrm{d}V\right)\Bigg|_{\boldsymbol{\chi}} + \oint\limits_{\Lambda^{\mathrm{f}}(t)} \rho^{\mathrm{f}} \boldsymbol{v}^{\mathrm{f}} \left(\boldsymbol{v}^{\mathrm{f}} - \boldsymbol{\omega}\right) \cdot \boldsymbol{n} \mathrm{d}S = \oint\limits_{\Lambda^{\mathrm{f}}(t)} \boldsymbol{\sigma}^{\mathrm{f}} \cdot \boldsymbol{n} \mathrm{d}S\,. \tag{5.3}$$

where $\boldsymbol{\sigma}^{\mathrm{f}}$ is the Cauchy stress tensor, defined based on the constitutive law for blood. Finally, note that, by using the 1WFSI, the mesh velocity is zero in Eqs. (5.2) and (5.3), i.e. $\boldsymbol{\omega} = \mathbf{0}$.

5.2.2 The Constitutive Law for Blood

For a compressible Newtonian fluid, the constitutive equation is given by:

$$\boldsymbol{\sigma}^{\mathrm{f}} = -p^{\mathrm{f}}\boldsymbol{I} + \mu^{\mathrm{f}}\left[\nabla \boldsymbol{v}^{\mathrm{f}} + (\nabla \boldsymbol{v}^{\mathrm{f}})^{\mathrm{T}}\right] - \frac{2}{3}\mu^{\mathrm{f}}\left(\nabla \cdot \boldsymbol{v}^{\mathrm{f}}\right)\boldsymbol{I}\,, \tag{5.4}$$

where $\boldsymbol{\sigma}^{\mathrm{f}}$ is the Cauchy stress tensor, p^{f} is the thermodynamic pressure in the blood flow and $\boldsymbol{I}$ is the second-order identity tensor. The dynamic viscoty of blood was assumed to be $\mu^{\mathrm{f}} = 3.3 \times 10^{-3}$ Pa s.

To close the system of equations for the flow problem, an equation of state must be provided to represent the compressibility of blood and a "weakly compressible liquid" law, also known as the barotropic equation of state, was chosen in this work. It has already been used to model blood behavior in FSI problems (38, 161, 162).

The weakly compressible law can be applied for liquids at "low pressures", normally considered to be the case when the variation in the fluid density is lower than 1 %. In this situation, the change in density is linearly related to the pressure change according to the definition of the

bulk modulus of the fluid, κ^{f}:

$$\kappa^{\mathrm{f}} = \rho^{\mathrm{f}} \frac{\partial p^{\mathrm{f}}}{\partial \rho^{\mathrm{f}}} \,. \tag{5.5}$$

where ρ^{f} is the density and p^{f} the thermodynamic pressure. Using Eq. (5.5), and assuming the aforementioned conditions, κ^{f} is approximately constant, hence:

$$\rho^{\mathrm{f}} = \rho_0^{\mathrm{f}} + \frac{\rho_0^{\mathrm{f}}}{\kappa^{\mathrm{f}}} \left(p^{\mathrm{f}} - p_0^{\mathrm{f}} \right) , \tag{5.6}$$

where the subscript "0" indicates a reference state of the fluid, assumed to be blood at an average cardiac cycle pressure, 100 mmHg, with $\rho_0^{\mathrm{f}} = 1000.0\,\mathrm{kg/m^3}$. The bulk modulus of blood was assumed to be 2.2×10^9 Pa (38).

The constant $\dfrac{\rho_0^{\mathrm{f}}}{\kappa^{\mathrm{f}}}$ can be identified as a measure of the isothermal compressibility of the fluid, defined as:

$$\psi^{\mathrm{f}} = \frac{1}{\rho^{\mathrm{f}}} \frac{\partial \rho^{\mathrm{f}}}{\partial p^{\mathrm{f}}} \,. \tag{5.7}$$

In view of this definition and to simplify Eq. (5.6), Eq. (5.6) is re-written as:

$$\rho^{\mathrm{f}} = \underbrace{\left[\rho_0^{\mathrm{f}} - \psi^{\mathrm{f}^*} p_0^{\mathrm{f}} \right]}_{\text{constant} \equiv \rho_{\mathrm{ref}}^{\mathrm{f}}} + \psi^{\mathrm{f}^*} p^{\mathrm{f}} \Rightarrow \rho^{\mathrm{f}} = \rho_{\mathrm{ref}}^{\mathrm{f}} + \psi^{\mathrm{f}^*} p^{\mathrm{f}} \tag{5.8}$$

where the modified isothermal compressibility, ψ^{f^*}, is defined as:

$$\psi^{\mathrm{f}^*} = \frac{\rho_0^{\mathrm{f}}}{\kappa^{\mathrm{f}}} \,, \tag{5.9}$$

and $\rho_{\mathrm{ref}}^{\mathrm{f}}$ is a modified density computed at the reference state and is a constant for the weakly compressible law. Note that the weakly compressible law should approach the incompressibility limit as $\kappa^{\mathrm{f}} \to \infty$, which is equivalent to $\psi^{\mathrm{f}^*} \to 0$.

It is important to note that not only the physics of blood was a motivation to choose this weakly compressible law. Numerical partitioned FSI techniques using incompressible laws for blood exhibit severe instabilities. But it has been recently shown that using compressible fluid laws in partitioned FSI applications may result in a more stable calculation due to reduced added-mass effects (163). In the early investigations of an 2WFSI solution during the course of this work, this model was then much preferred for computational reasons too. Although at the end a 1WFSI strategy was preferred, the choice of the weakly compressible law remained because it is more strongly supported by the physics of blood than a purely incompressible law.

5.2.3 Boundary Conditions

The fluid flow BCs are schematically depicted in Fig. 5.2. At the inlet, the parabolic velocity profile for a fully-developed laminar flow in a pipe was used for the spatial velocity distribution:

$$\boldsymbol{v}^{\mathrm{f}}_{inlet}(r,t) = 2\frac{q_a(t)}{A_{inlet}}\left[1 - \frac{4r^2}{{d_{pa}}^2}\right], \tag{5.10}$$

where A_{inlet} is the cross-sectional area of the inlet artery, d_{pa} is its diameter, and r is the radial coordinate of the circular inlet section — an artificial circular-section extension, with length equals to twice the diameter d_{pa}, was added to the artery inlet to impose this inlet flow condition. The time-varying pulsatile blood flow rate, $q_a(t)$, corresponding to the flow pulse from the beginning of systole until the end of the diastole, was obtained by multiplying the normalized flow rate reported by Hoi et al. (164), for older adults, by the mean blood flow rate in the respective IA parent artery reported by Zarrinkoob et al. (165). This average flow rate was used because the patient-specific blood flow rate waveform at the ICA was not available. Thus, for example, if the parent artery for a particular case was the ICA, the reported mean blood flow rate was $\bar{q}_a = 4.3\,\mathrm{ml/s}$, yielding the profile shown in Fig. 5.3a. Additionally, the pressure gradient was set to zero at the inlet.

At the flow outlets, a flux-corrected velocity with a resistance BC for pressure was imposed. The resistance BC is defined as a being proportional to the blood flow rate profile, but with

Figure 5.3 – (a) Flow rate profile waveform for older adults in a cardiac cycle from Hoi et al. (164) (nondimensional time axis by dividing per the cardiac period, $T_c = 0.94\,\mathrm{s}$) and (b) pressure waveform used at the flow outlets computed as being proportional to the flow rate and between the normal range 80 to 120 mmHg.

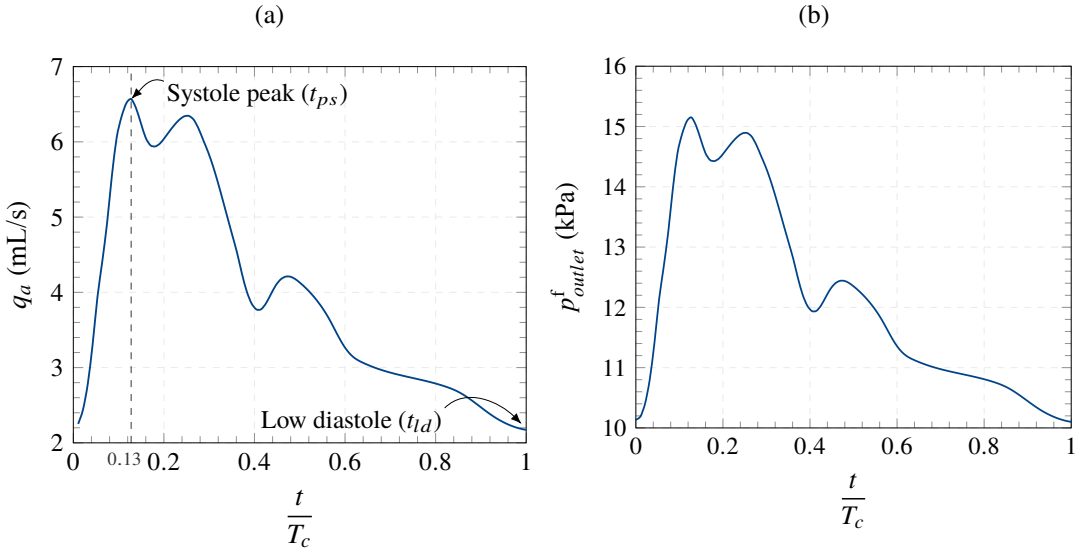

Source: Prepared by the author.

levels ranging between the normal cardiac cycle pressure levels, i.e. from 80 to 120 mmHg (approximately 10 to 16 kPa), shown in Fig. 5.3b. Since the distances between the outlets and the aneurysm were not sufficiently long, reports show that it is important to use this BC (166).

5.3 IA WALL TISSUE AND ITS MOTION

The solid domain Ω^s is constituted by the shell-like aneurysm and artery structures, with a thickness assumed heterogeneous and composed of a tissue assumed to be an isotropic nearly-incompressible prestressed hyperelastic material with heterogeneous material properties. Moreover, the physics of the motion of arteries and IA walls fits in the realm of *finite-deformation elasticity*. The following sections translate these hypotheses into the equations that needed to be solved. Complementary to this chapter, an overview of the basic concepts, such as stress, deformation, and strain definitions, in their most general multiaxial form in the finite-deformation regime is given in Appendix C. These concepts can also be found in detail in standard textbooks like Holzapfel (167) and Belytschko (160).

Furthermore, an important assumption made here for the constitutive behavior of artery and IA tissue was the so-called *pseudo-elastic approach* (41), by which traditional elastic models can be used to study biosolids. As presented in Section 2.4, arteries exhibit hysteresis upon loading and unloading and, additionally, must be preconditioned to guarantee a repeatable stress-strain curve for the material. In the preconditioned state, both loading and unloading curves are each unique, although together they still behave inelastically, and the material can be treated separately as one elastic material during the loading and another elastic material during the unloading process. This separate treatment of loading and unloading curves was named *pseudo-elasticity*. It is not a material property but a suitable way to treat the material and to use the elastic theory in its modeling.

5.3.1 Governing Equations of the Wall Motion

Given the mechanical hypotheses outlined above, the two sufficient principles employed to solve for the motion of arteries and IA wall are the conservation of mass and the balance of linear momentum. In Solid Mechanics, especially with elastic materials that by definition present a *natural undeformed state*, these principles are cast in reference to this configuration — normally associated with time zero, when there is no motion, i.e. the so-called Lagrangian description. In finite-deformation solid mechanics, this description can be split into two: the total and updated

Lagrangian formulations. In this presentation, the total Lagrangian formulation was employed and it uses the material coordinates, i.e. the Lagrangian coordinates, $\boldsymbol{\xi}$, as the reference to calculate the integrals and derivatives that appear in the governing equations. In general, the material coordinates coincide with the material at $t = 0$, i.e. the initial configuration, and that was the assumption in this work.

The principle of mass conservation states, as the name indicates, that the mass of a continuum system, m, which occupies a volume V_0 on the reference configuration, is constant. Therefore:

$$\frac{\mathrm{d}m}{\mathrm{d}t} = 0\,, \tag{5.11}$$

where the mass of the continuum is given by:

$$m = \int_{\Omega_0^{\mathrm{s}}} \rho_0^{\mathrm{s}}\left(\boldsymbol{\xi}, t\right) \mathrm{d}V_0\,, \tag{5.12}$$

where ρ_0^{s} is the specific mass of the material at the reference configuration. In the total Lagrangian description, Eq. (5.11) can be integrated and Eq. (5.12) can be used to write it as a function of the density of the current configuration ρ^{s}:

$$\int_{\Omega_0^{\mathrm{s}}} \rho_0^{\mathrm{s}}\left(\boldsymbol{\xi}, t\right) \mathrm{d}V_0 = \text{constant} = \int_{\Omega^{\mathrm{s}}} \rho^{\mathrm{s}}\left(\boldsymbol{x}, t\right) \mathrm{d}V\,. \tag{5.13}$$

By transforming the variable of the right-hand side integral to the reference configuration and introducing the Jacobian of the motion (see Appendix C), follows

$$\int_{\Omega_0^{\mathrm{s}}} \rho_0^{\mathrm{s}}\left(\boldsymbol{\xi}, t\right) \mathrm{d}V_0 = \int_{\Omega^{\mathrm{s}}} \rho^{\mathrm{s}}\left(\boldsymbol{\xi}, t\right) J \mathrm{d}V_0 \Rightarrow \int_{\Omega^{\mathrm{s}}} \left(\rho^{\mathrm{s}} J - \rho_0^{\mathrm{s}}\right) \mathrm{d}V_0 = 0\,. \tag{5.14}$$

Once the volume is arbitrary, the integrand must vanish, yielding:

$$\rho^{\mathrm{s}} J = \rho_0^{\mathrm{s}}\,, \tag{5.15}$$

the mass conservation principle written in the total Lagrangian formulation. One of the main consequences of Eq. (5.15) is the positiveness imposed to the Jacobian of the deformation gradient, $\boldsymbol{F}$. Since ρ_0^{s} and ρ^{s} are always positive, then $0 < J < \infty$.

The balance of linear momentum is written as follows:

$$\int_{\Omega_0^{\mathrm{s}}} \rho_0^{\mathrm{s}} \frac{\partial^2 \boldsymbol{u}}{\partial t^2}(\boldsymbol{\xi}, t) \mathrm{d}V_0 = \int_{\Omega_0^{\mathrm{s}}} \nabla_0 \bullet \boldsymbol{P} \mathrm{d}V_0\,, \tag{5.16}$$

where $\boldsymbol{u}$ is the solid displacement field of the material and $\boldsymbol{P}$ is the nominal stress tensor (the multiaxial counterpart of the classic uniaxial *engineering stress*).

By using the relations between the different forms of stresses presented in Appendix C, Eq. (5.16) can be changed to more suitable forms. For example, in terms of the second Piola-Kirchhoff stress tensor, $\boldsymbol{S}$, we obtain:

$$\int_{\Omega_0^s} \rho_0^s \frac{\partial^2 \boldsymbol{u}}{\partial t^2}(\boldsymbol{\xi}, t) \mathrm{d}V_0 = \int_{\Omega_0^s} \nabla_0 \cdot (\boldsymbol{F} \cdot \boldsymbol{S}) \mathrm{d}V_0 \,, \tag{5.17}$$

whereas in terms of the Cauchy stress tensor, we find:

$$\int_{\Omega_0^s} \rho_0^s \frac{\partial^2 \boldsymbol{u}}{\partial t^2}(\boldsymbol{\xi}, t) \mathrm{d}V_0 = \int_{\Omega_0^s} \nabla_0 \cdot \left(J \boldsymbol{F}^{-1} \cdot \boldsymbol{\sigma}^s \right) \mathrm{d}V_0 \,. \tag{5.18}$$

Similarly to the fluid case, a constitutive equation is necessary to complement Eq. (5.17) where the stress tensor must be related to the motion.

5.3.2 Hyperelasticity

As mentioned in Section 2.4, constitutive laws that typically represent the behavior of arteries and IAs tissues are within the class of *hyperelastic* laws. Hyperelastic materials are those that present deformation work independent of the path (160) and are characterized by the existence of a deformation work function, Ψ, or *strain-energy function* that depends on the components of a strain or deformation tensor. This strain-energy function acts as a constitutive equation for the hyperelastic material because the stresses can be derived from it by a potential relation. For some materials, this potential relationship can be derived, thus, originating naturally the deformation work function. However, the existence of Ψ is postulated for a hyperelastic material, independently of the type of process that the material undergoes. If $\Psi = \Psi(\boldsymbol{E})$, where $\boldsymbol{E}$ is the Green-Lagrange strain tensor, then the resulting stress is given by the second Piola-Kirchhoff stress:

$$\boldsymbol{S} = \frac{\partial \Psi}{\partial \boldsymbol{E}}(\boldsymbol{E}) = 2 \frac{\partial \Psi}{\partial \boldsymbol{C}}(\boldsymbol{C}) \,, \tag{5.19}$$

where the second equality stems from Eq. (C.13) (see Appendix C) and $\boldsymbol{C}$ is the right Cauchy-Green deformation tensor, defined as $\boldsymbol{C} = \boldsymbol{F}^{\mathrm{T}} \cdot \boldsymbol{F}$. Different functions $\Psi(\boldsymbol{E})$ characterize different hyperelastic behaviors. Note that the same notation for the strain-energy function was used independently of which variable is considered a function of. For the thermodynamical origins of Eq. (5.19), see Appendix D.

From Eq. (5.19), the Cauchy stress tensor is obtained by using Eq. (C.25), thus:

$$\boldsymbol{\sigma}^{\mathrm{s}} = 2J^{-1}\boldsymbol{F} \cdot \frac{\partial \Psi}{\partial \boldsymbol{C}} \cdot \boldsymbol{F}^{\mathrm{T}} \,. \tag{5.20}$$

5.3.3 Isotropic Hyperelasticity

For isotropic hyperelastic materials, it is possible to prove that the strain-energy function is only a function of the principal invariants of the right Cauchy-Green deformation tensor, $\boldsymbol{C}$, I_1, I_2, and I_3 (168), which are given by:

$$I_1 = \mathrm{tr}\,(\boldsymbol{C}) = C_{ii} \,, \tag{5.21}$$

$$I_2 = \frac{1}{2}\left[(\mathrm{tr}\,\boldsymbol{C})^2 - \mathrm{tr}\,(\boldsymbol{C}\cdot\boldsymbol{C})\right] = \frac{1}{2}\left[(C_{kk})^2 - C_{ij}C_{ji}\right] \,, \tag{5.22}$$

$$I_3 = \det(\boldsymbol{C}) = \varepsilon_{ijk} C_{i1} C_{j2} C_{k3} \,. \tag{5.23}$$

Then, if $\Psi = \Psi(I_1, I_2, I_3)$, the chain rule applied to Eq. (5.19) yields:

$$\boldsymbol{S} = 2\frac{\partial \Psi}{\partial \boldsymbol{C}} = 2\left(\frac{\partial \Psi}{\partial I_1}\frac{\partial I_1}{\partial \boldsymbol{C}} + \frac{\partial \Psi}{\partial I_2}\frac{\partial I_2}{\partial \boldsymbol{C}} + \frac{\partial \Psi}{\partial I_3}\frac{\partial I_3}{\partial \boldsymbol{C}}\right) \,. \tag{5.24}$$

By taking the derivatives of the principal invariants with respect to $\boldsymbol{C}$, given by (160):

$$\frac{\partial I_1}{\partial \boldsymbol{C}} = \boldsymbol{I} \qquad \frac{\partial I_1}{\partial C_{ij}} = \delta_{ij} \,, \tag{5.25}$$

$$\frac{\partial I_2}{\partial \boldsymbol{C}} = I_1 \boldsymbol{I} - \boldsymbol{C}^{\mathrm{T}} \qquad \frac{\partial I_2}{\partial C_{ij}} = I_1 \delta_{ij} - C_{ji} \,, \tag{5.26}$$

$$\frac{\partial I_3}{\partial \boldsymbol{C}} = I_3 \boldsymbol{C}^{-\mathrm{T}} \qquad \frac{\partial I_3}{\partial C_{ij}} = I_3 {C_{ji}}^{-1} \,, \tag{5.27}$$

and by substituting into Eq. (5.24), follows:

$$\boldsymbol{S} = 2\left(\frac{\partial \Psi}{\partial I_1} + I_1 \frac{\partial \Psi}{\partial I_2}\right)\boldsymbol{I} - 2\frac{\partial \Psi}{\partial I_2}\boldsymbol{C} + 2I_3 \frac{\partial \Psi}{\partial I_3}\boldsymbol{C}^{-1} \,. \tag{5.28}$$

This is the most general form of the constitutive equation for an isotropic hyperelastic material, given in terms of the second Piola-Kirchhoff stress. The form with the Cauchy stress, which will be preferred, can be obtained by using Eq. (C.25). Thus, by multiplying Eq. (5.28)

by the deformation gradient and its transpose, follows:

$$J\boldsymbol{\sigma}^{\mathrm{s}} = 2\left(\frac{\partial\Psi}{\partial I_1} + I_1\frac{\partial\Psi}{\partial I_2}\right)\boldsymbol{B} - 2\frac{\partial\Psi}{\partial I_2}\boldsymbol{B}\cdot\boldsymbol{B} + 2I_3\frac{\partial\Psi}{\partial I_3}\boldsymbol{I}\,, \tag{5.29}$$

where $\boldsymbol{B} = \boldsymbol{F}\cdot\boldsymbol{F}^{\mathrm{T}}$ is the *left Cauchy-Green deformation tensor* (168). An equivalent form of Eq. (5.29) can be obtained by using the Cayley-Hamilton theorem, by which a second-order tensor also satisfies its characteristic equation. In this case, it is possible to show that:

$$J\boldsymbol{\sigma}^{\mathrm{s}} = \left(I_2\frac{\partial\Psi}{\partial I_2} + I_3\frac{\partial\Psi}{\partial I_3}\right)\boldsymbol{I} + 2\frac{\partial\Psi}{\partial I_1}\boldsymbol{B} - 2I_3\frac{\partial\Psi}{\partial I_2}\boldsymbol{B}^{-1}\,. \tag{5.30}$$

Note that the tensorial character of an isotropic hyperelastic constitutive equation is given by either one of Eqs. (5.28) to (5.30), with the particular mechanical behavior restricted to the strain-energy function. Moreover, the equations above can be applied for general compressible hyperelastic materials.

5.3.4 Incompressible Hyperelasticity

As shown in Section 2.4, aneurysms and arteries in general must be modeled as incompressible or nearly-incompressible. In this work, the hypothesis of nearly-incompressibility was employed. Nevertheless, the concept of incompressibility is important in the development of a nearly-incompressible version of the constitutive laws used here.

If the material is incompressible, then by the conservation of mass, Eq. (5.15), $J = \det\boldsymbol{F} = 1$. Consequently, the third invariant of $\boldsymbol{C}$ is also equal to the unity — it can be proved that $I_3 = J^2$. Therefore, the strain-energy function looses its dependence on the third invariant and, consequently, Eqs. (5.28) to (5.30), loose their terms involving I_3. In this case, the incompressibility constraint must be accounted for in the constitutive law through the inclusion of the *hydrostatic pressure*, p^{s}. The physical foundations for this inclusion are explain in Appendix D.1, and yields the following modification to the generic constitutive law for hyperelastic materials, Eq. (5.19):

$$\boldsymbol{S} = -p^{\mathrm{s}}\boldsymbol{C}^{-1} + 2\frac{\partial\Psi}{\partial\boldsymbol{C}}\,, \tag{5.31}$$

where now $\Psi = \Psi(I_1, I_2)$ and must be obtained for an incompressible material. It is very important to note that the hydrostatic pressure, p^{s}, is an undefined scalar and can only be calculated through the boundary conditions of the problem and the equilibrium condition.

5.3.5 Examples of Ψ for Purely Incompressible Materials

As already explained, hyperelastic solid laws were classically the preferred choice in the biomechanics of soft tissues, from arteries, in general (55, 169–171), to IAs (81, 93, 79), specially because they are versatile enough to allow the inclusion of different mechanisms, such as inelastic ones (172) as also anisotropic behavior (145).

Several types of strain-energy functions exist and the ones that are suitable to model IA tissue are presented in this section. For example, most of them were used to fit mechanical data of IA tissue, as seen in Section 2.4, as also to numerically solve IA walls motion (see Table 3.1 and the content of Section 3.2).

Chagnon et al. (143) classified these hyperelastic laws into two groups, depending on their functional form: the exponential and polynomial types. The authors present several different strain-energy functions that appeared in the last decades to model hyperelasticity in soft tissues, most of them applied to model arteries' behavior. The classical model that represents the first group is due to Fung (173), which uses an exponential function of the Green-Lagrange strain components to model soft tissues with anisotropic behavior. Its most general form is given, in index notation, as follows (173):

$$\Psi = \frac{1}{2}\alpha_{ijkl}E_{ij}E_{kl} + \left(\beta_0 + \beta_{mnpq}E_{mn}E_{pq}\right)\mathrm{e}^{\gamma_{ij}E_{ij}+\kappa_{ijkl}E_{ij}E_{kl}+\ldots}, \tag{5.32}$$

where α_{ijkl}, β_0, β_{mnpq}, γ_{ij}, and κ_{ijkl} are material constants that must be determined empirically. Simplified versions of Eq. (5.32) are usually employed in practice to model the mechanical behavior of collagen. For example, Fung (41) shows that the cubic terms (and other high-order terms) in the exponential can be dropped and the constants γ_{ij} and β_{mnpq} can be set to zero. Furthermore, for stresses and strains in the physiological range and if high accuracy at lower strains is of no concern, the linear term can be omitted, leaving only a quadratic expression in the exponential argument:

$$\Psi = \beta_0\mathrm{e}^{\kappa_{ijkl}E_{ij}E_{kl}}. \tag{5.33}$$

Chagnon et al. (143), in their review, express Eq. (5.33) in a generic form, as follows:

$$\Psi = \frac{k}{2}\left(\mathrm{e}^{Q} - 1\right). \tag{5.34}$$

where Q is a generic function of the strain tensor components and several forms of it have already been proposed.

While the laws above assume the material is anisotropic, for isotropic tissues similar constitutive equations were proposed. Demiray (128), for example, proposed the following law for isotropic and incompressible rubber-like materials:

$$\Psi(I_1) = \frac{k_1}{k_2}\left[\mathrm{e}^{\frac{k_2}{2}(I_1-3)} - 1\right] ; \tag{5.35}$$

where k_1 and k_2 are material constants. A modified version with a quadratic argument in the exponential was also proposed by Demiray et al. (174) based on experiments with the abdominal aorta of rats, and given by:

$$\Psi(I_1) = \frac{k_1}{2k_2}\left[\mathrm{e}^{k_2(I_1-3)^2} - 1\right] . \tag{5.36}$$

In the polynomial class of hyperelastic laws, a classical one that has been shown to represent well the mechanical behavior of rubber is the model due to Ogden: its strain-energy function is postulated as dependent on the principal stretches, λ_a, $a = 1, 2, 3$, which are the eigenvalues of the deformation gradient tensor, $\boldsymbol{F}$. It has the form:

$$\Psi(\lambda_1, \lambda_2, \lambda_3) = \sum_{p=1}^{N} \frac{\mu_p}{\alpha_p}\left(\lambda_1^{\alpha_p} + \lambda_2^{\alpha_p} + \lambda_3^{\alpha_p} - 3\right), \tag{5.37}$$

where the material coefficients obey the consistency condition:

$$2G = \sum_{p=1}^{N} \mu_p \alpha_p \tag{5.38}$$

with $\mu_p \alpha_p > 0$, and G is the shear modulus of the material in the reference configuration, Eq. (C.28). Holzapfel (167) gave numerical examples of these material coefficients that were shown to yield good agreement with experimental data for vulcanized rubber in simple tension and equibiaxial experiments with $N = 3$.

Rivlin et al. (175) developed a hyperelastic model for incompressible materials which are initially isotropic. With the hypothesis of incompressibility, the strain-energy function can be written as $\Psi = \Psi(I_1, I_2)$ and can be expanded as a doubly-infinite series function of the terms $(I_1 - 3)$ and $(I_2 - 3)$ — note that, from Eqs. (5.21) and (5.22), in the undeformed configuration $I_1 = I_2 = 3$:

$$\Psi(I_1, I_2) = \sum_{i=0}^{\infty}\sum_{j=0}^{\infty} c_{ij}\,(I_1 - 3)^i\,(I_2 - 3)^j , \tag{5.39}$$

where c_{ij} are constants and $c_{00} = 0$. Mooney (176) then showed experimentally that the simple

two-parameters form:

$$\Psi\left(I_1, I_2\right) = c_{10}\left(I_1 - 3\right) + c_{01}\left(I_2 - 3\right) \tag{5.40}$$

is adequate for large deformations of rubber. Equation (5.40) is a particular form of the Ogden law, Eq. (5.37) for $N = 2$, $\alpha_1 = 2$, and $\alpha_2 = -2$. Using the definition of the right Cauchy-Green strain invariants as a function of its eigenvalues and the incompressibility condition, $J = 1$, written in this case as $I_3 = J^2 = \lambda_1^2\lambda_2^2\lambda_3^2 = 1$, follows

$$\begin{aligned}\Psi(I_1, I_2) &= c_{10}\left(\lambda_1^2 + \lambda_2^2 + \lambda_3^2 - 3\right) + c_{01}\left(\lambda_1^{-2} + \lambda_2^{-2} + \lambda_3^{-2} - 3\right) \\ &= c_{10}\left(I_1 - 3\right) + c_{01}\left(I_2 - 3\right) ,\end{aligned} \tag{5.41}$$

with constants $c_{10} = \frac{\mu_1}{2}$ and $c_{01} = \frac{\mu_2}{2}$.

The version mentioned in Section 2.4, used by Costalat et al. (81) in uniaxial extension experiments with IAs tissue, was the three-parameters version of the Mooney-Rivlin (MR) law, i.e. including a second-order term from Eq. (5.39), as follows:

$$\Psi(I_1, I_2) = c_{10}\left(I_1 - 3\right) + c_{01}\left(I_2 - 3\right) + c_{11}\left(I_1 - 3\right)\left(I_2 - 3\right) . \tag{5.42}$$

According to the author, the third material parameter, c_{11}, was shown to be essential to characterize the stress-strain curve of this type of material.

If in the Ogden law $N = 1$ is used and $\alpha_1 = 1$, then a common incompressible law known as the *neo-Hookean* law is found, which is considered an extension of the Hookean solid for finite deformations,

$$\Psi(I_1) = \frac{1}{2}\mu^{\mathrm{s}}\left(I_1 - 3\right) , \tag{5.43}$$

where μ^{s} is the first Lamé constant of the linearized theory, Eq. (C.28).

The Yeoh model has also been used to model IAs mechanical behavior (82). Its strain-energy function is given by:

$$\Psi(I_1) = c_{10}\left(I_1 - 3\right) + c_{20}\left(I_1 - 3\right)^2 + c_{30}\left(I_1 - 3\right)^3 . \tag{5.44}$$

where the material constants c_{i0}, $i = 1, 2, 3$, have to satisfy certain restrictions due to material stability and convexity.

5.3.6 Compressible Hyperelasticity and the Multiplicative Decomposition

Instead of directly using the incompressible version of the general hyperelastic law, Eq. (5.30), with the inclusion of the hydrostatic pressure and any of the strain-energy functions presented in Section 5.3.5, a compressible formulation of hyperelasticity was preferred. With this formulation, it is possible to model the hydrostatic pressure, p^{s}, which is indeterminate, and obtain the nearly-incompressible behavior through the selection of the bulk modulus of the material. To understand this formulation, the so-called multiplicative decomposition is first introduced (167).

The traditional additive decomposition of a second-order tensor $\boldsymbol{A}$ is defined by:

$$\boldsymbol{A} = \underbrace{\operatorname{dev}(\boldsymbol{A})}_{\text{deviatoric part}} + \underbrace{\frac{1}{3}\operatorname{tr}(\boldsymbol{A})\boldsymbol{I}}_{\text{isotropic part}}, \tag{5.45}$$

where "dev" is the deviatoric operator. Through this decomposition, the deviatoric part is defined as the tensor whose trace vanishes, i.e.:

$$\operatorname{tr}(\operatorname{dev}\boldsymbol{A}) = 0, \tag{5.46}$$

as can be easily demonstrated from Eq. (5.45). Hence, if $\boldsymbol{A}$ is identified with a linear deformation measurement, such as the linear strain tensor, $\boldsymbol{\varepsilon}$, the isotropic part of the decomposition holds all volumetric contribution to the deformation. On the other hand, the deviatoric part holds the distortional contribution.

However, in the finite-deformation regime, this decomposition loses its physical meaning and must be replaced by the *multiplicative decomposition* where both parts of the decomposition recover their significance. This can be viewed by applying the additive decomposition to the deformation gradient, $\boldsymbol{F}$. In this case, the isotropic part, $\frac{1}{3}\operatorname{tr}(\boldsymbol{F})\boldsymbol{I}$ does not represent the volumetric deformation and is not even related to it, because the volumetric deformation in finite deformation is given by the Jacobian of the deformation gradient:

$$J = \det\boldsymbol{F} = \frac{\mathrm{d}V}{\mathrm{d}V_0}, \tag{5.47}$$

where V and V_0 are the volumes of the body at the current and reference configurations, respectively.

To decompose the deformation gradient into a purely volumetric and a purely distortional parts, first it is assumed that a part of $\boldsymbol{F}$ is given by an isochoric motion and labeled $\boldsymbol{F}^*$, i.e. it

only represents the motion related to distortion. Rigorously, $\boldsymbol{F}^*$ is thus incompressible, hence:

$$\det \boldsymbol{F}^* = 1\,. \tag{5.48}$$

It can then be shown that $\boldsymbol{F}^*$ is given by:

$$\boldsymbol{F}^* = J^{-1/3}\boldsymbol{F}\,. \tag{5.49}$$

Hence, by rearranging Eq. (5.49), the correct deviatoric-volumetric decomposition for finite deformations follows:

$$\boldsymbol{F} = \underbrace{\left(J^{1/3}\boldsymbol{I}\right)}_{\text{volumetric part}} \cdot \underbrace{(\boldsymbol{F}^*)}_{\text{deviatoric part}}\,. \tag{5.50}$$

Based on Eq. (5.50), other deformation or strain measurements can be also decomposed in the same way. For example, the right Cauchy-Green deformation, $\boldsymbol{C}$, and Green-Lagrange strain, $\boldsymbol{E}$, tensors can be written as:

$$\boldsymbol{C} = \left(J^{2/3}\boldsymbol{I}\right) \cdot (\boldsymbol{C}^*) \tag{5.51}$$

and

$$\boldsymbol{E} = J^{2/3}\boldsymbol{E}^* + \frac{1}{2}\left(J^{2/3} - 1\right)\boldsymbol{I}\,, \tag{5.52}$$

respectively, where $\boldsymbol{C}^* = (\boldsymbol{F}^*)^{\mathrm{T}} \cdot \boldsymbol{F}^*$ and $\boldsymbol{E}^* = \frac{1}{2}(\boldsymbol{C}^* - \boldsymbol{I})$ are the volume-preserving portions of $\boldsymbol{C}$ and $\boldsymbol{E}$, respectively.

The volumetric-deviatoric decomposition can be also applied to hyperelastic laws. This a very useful approach because the incompressible strain-energy functions, presented in Section 5.3.5 can be "reused". To that end, the strain-energy function, Ψ, must be decomposed into the following form:

$$\Psi(\boldsymbol{C}) = \Psi_{vol}(J) + \Psi_{iso}(\boldsymbol{C}^*)\,, \tag{5.53}$$

where Ψ_{vol} is the contribution to the strain energy from the volumetric motion, whereas Ψ_{iso} is the contribution from the purely volume-preserving or isochoric motion. Rigorously, Ψ_{iso} can be modeled by one of the strain-energy functions for incompressible materials and the main task left to fully characterize the material is to find a model for Ψ_{vol}. This is the subject of the next section, but before, it is important to derive the constitutive equation in terms of the second Piola-Kirchhoff stress tensor, thus in the material description, and, then, in terms of the Cauchy stress tensor.

By substituting Eq. (5.53) into the version of Eq. (5.19) in terms of the right Cauchy-Green deformation tensor, follows:

$$\boldsymbol{S} = \underbrace{2\frac{\partial \Psi_{vol}}{\partial \boldsymbol{C}}(J)}_{\equiv \boldsymbol{S}_{vol}} + \underbrace{2\frac{\partial \Psi_{iso}}{\partial \boldsymbol{C}}(\boldsymbol{C}^*)}_{\equiv \boldsymbol{S}_{iso}} . \tag{5.54}$$

Each term expresses the contribution of the volumetric and isochoric motion in the second Piola-Kirchhoff tensor. They can be changed to a simpler and more elucidating form as shown below.

By taking the volumetric contribution, $\boldsymbol{S}_{vol}$, and by using the chain rule and Eq. (D.17) of Appendix D.1, $\frac{\partial J}{\partial \boldsymbol{C}} = \frac{1}{2} J \boldsymbol{C}^{-1}$, we find the following:

$$\boldsymbol{S}_{vol} = -J p^{\mathrm{s}}_{vol} \boldsymbol{C}^{-1} , \tag{5.55}$$

where p^{s}_{vol} is given by:

$$-p^{\mathrm{s}}_{vol} = \frac{\mathrm{d}\Psi_{vol}}{\mathrm{d}J} , \tag{5.56}$$

and can be identified as a hydrostatic pressure per unit of volume of the reference configuration, in this case (rigorously, this is related to the fact that the strain-energy function can be identified with the internal energy in isentropic processes or the Helmholtz free-energy in isothermal processes, and, since J is a volume change rate, the potential in Eq. (5.56) yields a thermodynamic pressure per unit volume. See Appendix D). Here, the notation p^{s}_{vol} was used to avoid confusion with the previously introduced p^{s}, in Section 5.3.4, which acts as a Lagrange multiplier enforcing the incompressibility constraint and is a constant, whereas p^{s}_{vol} must be modeled and is a sole consequence of the decomposition in Eq. (5.53).

By also applying the chain rule to the isochoric contribution to the second Piola-Kirchhoff stress, $\boldsymbol{S}_{iso}$, follows

$$\boldsymbol{S}_{iso} = 2\frac{\partial \Psi_{iso}}{\partial \boldsymbol{C}} = 2\frac{\partial \Psi_{iso}}{\partial \boldsymbol{C}^*} : \frac{\partial \boldsymbol{C}^*}{\partial \boldsymbol{C}} , \tag{5.57}$$

and it can be shown that the derivative $\frac{\partial \boldsymbol{C}^*}{\partial \boldsymbol{C}}$ is given by:

$$\frac{\partial \boldsymbol{C}^*}{\partial \boldsymbol{C}} = J^{-2/3} \underbrace{\left(\mathbb{I} - \frac{1}{3} \boldsymbol{C} \boldsymbol{C}^{-1} \right)}_{= \mathbb{P}^{\mathrm{T}}} , \tag{5.58}$$

where $\mathbb{I}$ is the fourth-order identity tensor and $\mathbb{P}$ is a fourth-order tensor defined as the expression between parentheses in the equation (its meaning will be evident below). After substituting

Eq. (5.58) into Eq. (5.57), follows

$$\boldsymbol{S}_{iso} = J^{-2/3}\left[\boldsymbol{S}^* - \frac{1}{3}\left(\boldsymbol{S}^* : \boldsymbol{C}\right)\boldsymbol{C}^{-1}\right] \equiv J^{-2/3}\mathbb{P} : \boldsymbol{S}^*, \tag{5.59}$$

where $\boldsymbol{S}^*$ is called "fictitious" second Piola-Kirchhoff stress tensor (167):

$$\boldsymbol{S}^* = 2\frac{\partial \Psi_{iso}}{\partial \boldsymbol{C}^*}. \tag{5.60}$$

Equation (5.59) gives the isochoric contribution to the "physical" second Piola-Kirchhoff stress tensor in a useful notation that highlights the meaning of the tensor $\mathbb{P}$: while $\boldsymbol{S}^*$ can be imagined as a stress defined in a "domain" of the volume-preserving motions, "$J^{-2/3}\mathbb{P}$" *projects* it back to the "physical domain". Furthermore, it also provides the correct deviatoric operator in Lagrangian coordinates because, as shown in Holzapfel (167), $(\mathbb{P} : \boldsymbol{S}) : \boldsymbol{C} = 0$.

Therefore, with the mechanical assumption of a decomposition of the form Eq. (5.50), and the postulation of a decoupled strain-energy function given by Eq. (5.53), the constitutive equation of a compressible hyperelastic material can be written as:

$$\boldsymbol{S} = -Jp^{\mathrm{s}}_{vol}\boldsymbol{C}^{-1} + J^{-2/3}\mathbb{P} : \boldsymbol{S}^*. \tag{5.61}$$

The decoupled form of the Cauchy stress tensor can be found by using Eq. (C.25), from Appendix C, with Eq. (5.61) leading to, after several manipulations:

$$\boldsymbol{\sigma}^{\mathrm{s}} = \underbrace{-p^{\mathrm{s}}_{vol}\boldsymbol{I}}_{\boldsymbol{\sigma}_{vol}} + \underbrace{\mathrm{dev}\left(\boldsymbol{\sigma}^{\mathrm{s}*}\right)}_{\boldsymbol{\sigma}_{iso}}, \tag{5.62}$$

where p^{s}_{vol} is given by Eq. (5.56), "dev" is the classical deviatoric operator defined in Eq. (5.45) and $\boldsymbol{\sigma}^{\mathrm{s}*}$ is the "fictitious" Cauchy stress tensor given by:

$$\boldsymbol{\sigma}^{\mathrm{s}*} = J^{-1}\boldsymbol{F} \cdot \boldsymbol{S}^* \cdot \boldsymbol{F}^{\mathrm{T}}. \tag{5.63}$$

With the definitions of $\boldsymbol{S}^*$ stress tensor given by Eq. (5.60) and Eq. (5.63), Eq. (5.62) can be written in the following form:

$$\boldsymbol{\sigma}^{\mathrm{s}} = -p^{\mathrm{s}}_{vol}\boldsymbol{I} + 2J^{-1}\,\mathrm{dev}\left(\boldsymbol{F} \cdot \frac{\partial \Psi_{iso}}{\partial \boldsymbol{C}^*} \cdot \boldsymbol{F}^{\mathrm{T}}\right). \tag{5.64}$$

Equation (5.64) can be compared with the constitutive equation derived in Appendix D.1 for incompressible hyperelastic materials Eq. (D.31), where it is clear the difference between p^{s} and p^{s}_{vol} mentioned above: the Lagrange multiplier appears acting as a hydrostatic pressure, whereas

in Eq. (5.64) the hydrostatic pressure must be modeled through the volumetric component of the strain-energy function, Ψ_{vol}, the subject of the next section.

Furthermore, with Eq. (5.64), the constitutive equation of a material can be found if its incompressible response is already available, since it can be identified with Ψ_{iso}. Therefore, Ψ_{iso} is substituted by one of the strain-energy functions already presented in Section 5.3.5, as follows:

- the MR model with 3 material parameters

$$\Psi_{iso}(I_1^*, I_2^*) = c_{10}\left(I_1^* - 3\right) + c_{01}\left(I_2^* - 3\right) + c_{11}\left(I_1^* - 3\right)\left(I_2^* - 3\right) \; ; \tag{5.65}$$

- the Yeoh model with 3 material parameters:

$$\Psi_{iso}(I_1^*) = c_{10}\left(I_1^* - 3\right) + c_{20}\left(I_1^* - 3\right)^2 + c_{30}\left(I_1^* - 3\right)^3 \; ; \tag{5.66}$$

- the "isotropic" version of the exponential Fung model (proposed by Demiray (128)):

$$\Psi_{iso}(I_1^*) = \frac{k_1}{k_2}\left[\mathrm{e}^{\frac{k_2}{2}\left(I_1^* - 3\right)} - 1\right] \; ; \tag{5.67}$$

- the "quadratic" version of the isotropic Fung model used for modeling the mechanical response of collagen:

$$\Psi_{iso}(I_1^*) = \frac{k_1}{2k_2}\left[\mathrm{e}^{k_2\left(I_1^* - 3\right)^2} - 1\right] \; . \tag{5.68}$$

Finally, it is important to note that, although the above demonstrations leading up to Eq. (5.64) can be used when anisotropy is assumed because the stress tensor depends on the complete set of components of the deformation tensor (see Eq. (5.60)), the same simplification of the general hyperelastic constitutive equation in the case of isotropy, i.e. using the principal invariants of the deformation tensor and presented in Section 5.3.3, can be applied to Eq. (5.60) or Eq. (5.63). Therefore, for isotropic compressible hyperelastic materials, one can write:

$$J\boldsymbol{\sigma}^{s*} = 2\left(\frac{\partial \Psi_{iso}}{\partial I_1^*} + I_1^* \frac{\partial \Psi_{iso}}{\partial I_2^*}\right)\boldsymbol{B}^* - 2\frac{\partial \Psi_{iso}}{\partial I_2^*}\boldsymbol{B}^* \boldsymbol{\cdot} \boldsymbol{B}^* \, , \tag{5.69}$$

where $\boldsymbol{B}^*$ is the volume-preserving portion of the left Cauchy-Green deformation tensor, defined similarly to Eq. (5.51) and I_i^*, $i = 1, 2$ are its principal invariants. Note, nevertheless, the lack of the compressible term dependent on the third principal invariant, $I_3 = J^2$. The equivalent form

of Eq. (5.69) obtained with the Cayley-Hamilton theorem is given by:

$$J\boldsymbol{\sigma}^{s*} = I_2^* \frac{\partial \Psi_{iso}}{\partial I_2^*} \boldsymbol{I} + 2\frac{\partial \Psi_{iso}}{\partial I_1^*} \boldsymbol{B}^* - 2\frac{\partial \Psi_{iso}}{\partial I_2^*} \boldsymbol{B}^{*-1} \,. \tag{5.70}$$

5.3.7 Modeling the Volumetric Motion

A general form for Ψ_{vol} was given in Holzapfel (167) and proposed originally by Ogden (177) which satisfies the restrictions that a strain-energy function has to obey regarding polyconvexity and can be applied for rubber-like materials. A particular version of it is written as:

$$\Psi_{vol}(J) = \frac{\kappa^s}{4}\left(-2\ln J + J^2 - 1\right) , \tag{5.71}$$

where κ^s is the bulk modulus. In this case, the hydrostatic pressure in Eq. (5.55) given by the potential Eq. (5.56) is:

$$-p^s_{vol} \equiv \frac{\mathrm{d}\Psi_{vol}}{\mathrm{d}J} = \frac{\kappa^s}{2J}\left(J^2 - 1\right) . \tag{5.72}$$

The bulk modulus was calculated using its linear elasticity definition as a function of Young's modulus, E, and the Poisson's ratio, ν^s, after employing the definitions of the first and second Lamé's constants:

$$\kappa^s \equiv \frac{2}{3}\mu^s + \lambda^s = \frac{E}{3(1-2\nu^s)} \,. \tag{5.73}$$

It is simpler to control the compressibility through Eq. (5.73) because the incompressible behavior is achieved as $\nu^s \to 0.5$, i.e. $\kappa^s \to \infty$, although rigorously Eq. (5.73) can only be applied to linear elasticity.

To calculate κ^s for any hyperelastic material defined via Ψ, it is important to calculate its elastic modulus, E, as a function of the actual material constants and in terms of the deformation since the materials handled in this work have nonlinear constitutive behavior. This can be accomplished by looking at the definition of the elastic modulus given by the simple extension problem. In this case, if one considers the Cauchy stress for the uniaxial extension of an incompressible hyperelastic material (given by Eq. (G.2) in Appendix E), the elastic modulus in the undeformed configuration is given by:

$$E = 6\left(\frac{\partial \Psi}{\partial I_1} + \frac{\partial \Psi}{\partial I_2}\right) . \tag{5.74}$$

In a similar way, its shear modulus, which will be used later in this work, is given by:

$$G = 2\left(\frac{\partial \Psi}{\partial I_1} + \frac{\partial \Psi}{\partial I_2}\right) . \tag{5.75}$$

5.3.8 Modeling the Heterogeneity of the IA Wall

As explained in Section 2.3, the wall of an IA most likely has heterogeneous thickness and mechanical properties, i.e. they vary locally throughout the sac surface. To model this heterogeneity is not an easy task, starting with the fact that they are rarely available on a patient-specific basis. Nevertheless, some reports correlated the local thickness and mechanical properties distributions with some hemodynamic wall parameters, allowing for the determination of the patient-specific IA wall heterogeneity. Based on that, a *hemodynamics-driven* modeling was employed to the aneurysm wall according to its local adjacent hemodynamics. Therefore, this assumption implies that the material constants of the hyperelastic laws introduced in Section 5.3.5, generically represented by c, vary continuously over S_v, the surface of the vasculature. Because the vascular surfaces, shown in Chapter 4, are considered the reference configuration, then $c = c(\boldsymbol{\xi})$, i.e. they depend on material coordinates. In addition, the thickness of the wall is also obtained and used to create the computational meshes of the solid domain, Ω^s (subject of the next chapter).

This heterogeneous model depends on the separation of the aneurysm sac and its surrounding arteries, being given by the *neck contour*, already introduced in Section 4.2. The neck contour separates the branches surface, S_b, and the aneurysm sac surface, S_{ia} — the vascular surface is clearly $S_v = S_{ia} \cup S_b$.

The thickness of S_b, e_b, was based on established evidence that arteries thickness is dependent on the vessel lumen diameter, as explained in Section 2.5. Thus, an approach based on the wall-to-lumen ratio (WLR) was used. The WLR is defined by Eq. (2.9), i.e.:

$$WLR \equiv \frac{\text{artery wall thickness}}{\text{artery lumen diameter}} = \frac{e_b}{d_l}, \tag{5.76}$$

where d_l is the artery lumen diameter at a specified position along the vasculature. Empirical values of the WLR in the cerebral arteries were reported by Nakagawa et al. (84) and given in Section 2.5.

By using Eq. (5.76), the local thickness of the *branches*, e_b, was computed as a function of the WLR and the *local* artery lumen diameter, $d_l(\boldsymbol{\xi})$:

$$e_b(\boldsymbol{\xi}) = WLR\ d_l(\boldsymbol{\xi}), \tag{5.77}$$

defined over S_b, and where d_l was calculated using the script `vmtkdistancetocenterlines` of the VMTK® library, which computes the distance between the vasculature *centerlines* and its surface (149). This procedure provides a measure of the local radius of the vasculature and, consequently, its local diameter.

The strict use of the two values of WLR for medium- and large-sized arteries given in Section 2.5 would lead to step-wise changes in e_b because the brain vasculatures have arteries of different diameters, thus leading to an unrealistic thickness distribution. To avoid this issue, the WLR in Eq. (5.77) was based on the local lumen diameter, according to the following linear relationship for lumen diameters between 2 to 3 mm, as follows:

$$WLR = \begin{cases} 0.070 & d_l < 2\,\text{mm} \\ 0.070 + 0.018\,(d_l - 2) & 2\,\text{mm} < d_l < 3\,\text{mm} \\ 0.088 & d_l > 3\,\text{mm} \end{cases} . \tag{5.78}$$

The aneurysm thickness, e_{ia}, cannot be computed using the above procedure because there is no meaningful definition of the aneurysm centerlines or of the aneurysm WLR. Therefore, e_{ia} was calculated as an average of the surrounding vasculature thickness field, $e_b(\boldsymbol{\xi})$. Thus, based on e_b computed using Eq. (5.77) by initially ignoring the aneurysm, e_{ia} was computed as follows:

$$e_{ia} = f_a \frac{\int_{S_b} g_n(\boldsymbol{\xi}) e_b(\boldsymbol{\xi}) \mathrm{d}S_b}{\int_{S_b} g_n(\boldsymbol{\xi}) \mathrm{d}S_b}, \tag{5.79}$$

where f_a is a factor to control how much thinner (or thicker) the aneurysm wall is compared to the vasculature; $f_a = 0.75$ was used consistently for all geometries so the aneurysm is slightly thinner than its surroundings and lies in the range that agrees with measured values available in the literature.

The variable g_n, serving as a weight function, is the minimum *geodesic* distance, i.e. the distance *along the vascular surface*, between each point of the surrounding branches, S_b, and the line that separates not only the aneurysm sac from the vasculature but also what was named the *region of aneurysm influence*. This line may not be coincident with the aneurysm *neck contour*, because, depending on its morphology and location, there might exist regions that are not originally from the vasculature but, also, are not normally characterized as a portion of the aneurysm sac. Therefore, this line may be imagined as a separation between the *hypothetical healthy vasculature* and the region of aneurysm influence, as schematically depicted as a dashed

Figure 5.4 – Modeling of the thickness and material constants of a vasculature with an IA: the branches surface, S_b, i.e. the surface geometrically similar to the hypothetical healthy vasculature, have a lumen-diameter-dependent thickness and uniform material constants whereas the aneurysm has a global thickness and material constants with abnormal patches of these properties that were modeled based on the local hemodynamics, in this case, the time-averaged wall shear stress (TAWSS) and the oscillatory shear index (OSI).

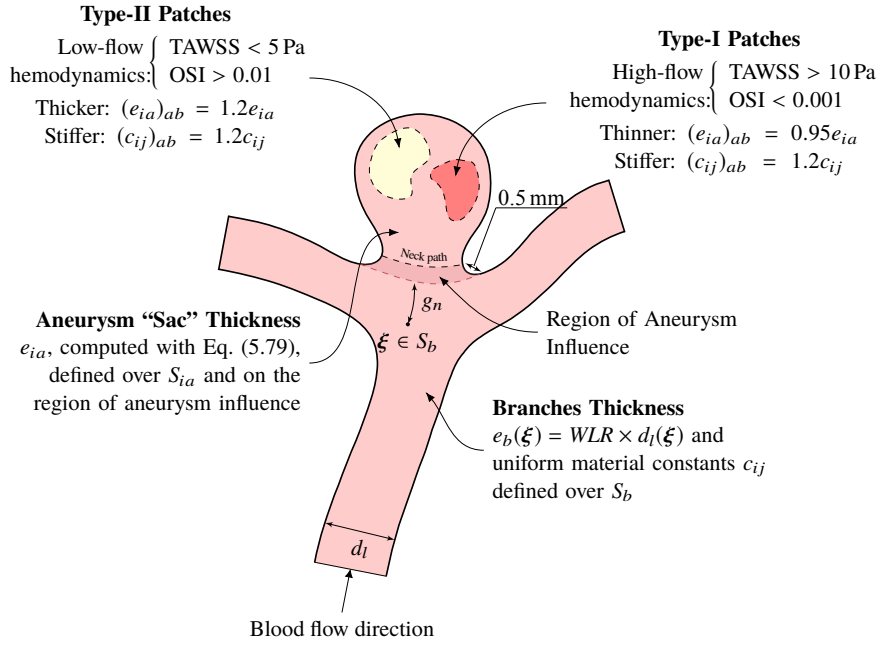

Source: Prepared by the author.

red line in Fig. 5.4 which also shows the aneurysm neck contour. This line was computed automatically based on the neck contour and, because an experimental measure of it could not be found, it was defined here as being at 0.5 mm from the neck contour consistently for all geometries.

Finally, the aneurysm thickness e_{ia} is set as the thickness on the aneurysm surface, S_{ia}. Computationally, this procedure created a discontinuity between the thickness on S_{ia} and the branches' thickness distribution defined over S_b. To correct this biologically unrealistic discontinuity, the resulting thickness was smoothed out using the script `vmtksurfacearraysmoothing` of VMTK® with 15 iterations.

The material constants of the constitutive laws presented in Section 5.3.5 that will be employed in this work, given by Eqs. (5.65) to (5.67), were selected separately for the branches and for the IAs according to their rupture status following the experimental works presented in Section 2.4. The constants used in this work are shown in Table 5.1. For the MR law, the averaged material constants according to rupture status provided by Costalat et al. (81) were used (Table 2.4). For the Yeoh law, Brunel et al. (82) provided the same averaged data for ruptured and unruptured aneurysms (Table 2.5). For both MR and Yeoh laws, the material constants for

the branches were chosen as the averaged value of the complete set of data provided by Costalat et al. (81) and Brunel et al. (82), respectively, because this yielded material constants that were not as soft as ruptured aneurysms, but also not stiffer as experiments suggested about unruptured aneurysms, hence they were intermediate values between ruptured and unruptured IAs.

The isotropic Fung law was also chosen because it has been classically used to model arteries and aneurysms, although no experimental study used it to fit aneurysm sample tissue data. Thus, the same constants used by Torii et al. (130) were employed here (see Table 3.1), $k_1 = 0.3536\,\text{MPa}$ and $k_2 = 16.7$, based on experiments with the porcine carotid artery, for the artery branches. In this case, for the aneurysms, the same value for k_2 was used, and double and halved k_1 for unruptured (stiffer) and ruptured (less stiff), respectively. A summary of the values used can be found in Table 5.1. Since the branches and the aneurysm have different material constants too, a field defined on the vascular surface for each material constant in Table 5.1 were created.

Table 5.1 – Material constants selected for arteries branches, S_b, and for the IA sac, S_{ia}, according to rupture status, for different constitutive laws and based on experimental works by Costalat et al. (81) and Brunel et al. (82).

Law	Constant	S_b	S_{ia}	
			$\mathcal{R}$	$\mathcal{U}$
MR	c_{10} (MPa)	0.1966	0.19	0.19
	c_{01} (MPa)	0.0163	0.026	0.023
	c_{11} (MPa)	7.837	1.377	11.780
Yeoh	c_{10} (MPa)	0.1067	0.07	0.12
	c_{20} (MPa)	5.1602	2.10	6.80
	c_{30} (MPa)	0.0	0.0	0.0
Fung	k_1 (MPa)	0.3536	0.1768	0.7072
	k_2	16.7	16.7	16.7

Source: Prepared by the author.

Note that, so far, this procedure is able to define both thickness and material constants separately on the surfaces S_{ia} and S_b, and, moreover, both properties are uniform on the aneurysm sac, although heterogeneous over the whole vascular surface. This model was labeled *uniform-wall model* and an example of the resulting fields for the IA case rICA2 is shown in the upper panel of Fig. 5.5a.

Subsequently, the aneurysm sac properties were altered to account for the intra-aneurysmal hemodynamics. Based on the discussion of Section 2.3, two "abnormal-hemodynamics" conditions adjacent to the aneurysm wall were selected that are associated with morphological

Figure 5.5 – Example of the wall morphology models construction for case rICA2: (a) The uniform thickness and material constant c_{10}, as example, fields defined initially on each IA; (b) the identification of abnormal-hemodynamics regions on the IA sac surface: TAWSS and OSI fields over the vasculature computed with Computational Fluid Dynamics (CFD) simulations of the blood flow (middle panel, left; the red-solid and white-dashed circles are examples of regions with high and low-flow hemodynamics, respectively), and identification of the aneurysm sac patches with abnormal hemodynamics (middle panel, right). (c) Finally, the thickness and c_{10} fields modified to account for abnormal intra-aneurysmal hemodynamics.

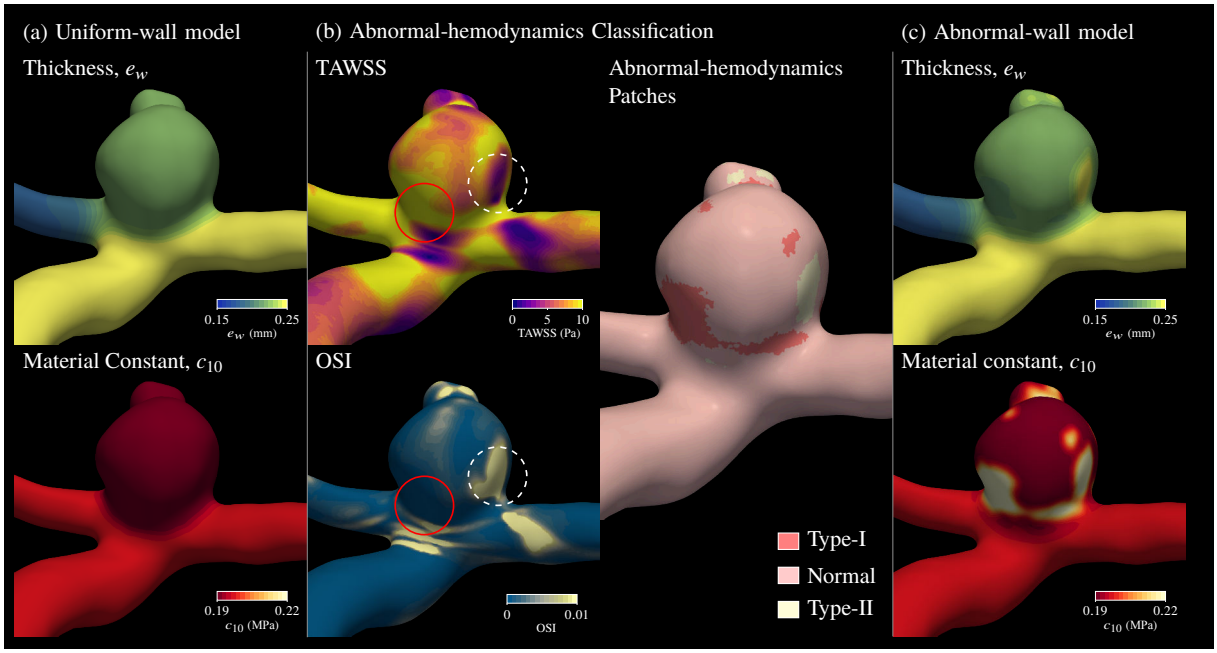

Source: Prepared by the author.

changes on the aneurysm wall, more specifically, with type-I and type-II regions as defined by Meng et al. (61) (see Fig. 2.7).

As explained in Section 2.5, regions of disturbed flow characterized by low TAWSS and high OSI, labeled "low-flow effects", were correlated with type-II regions of the aneurysm wall, i.e. atherosclerotic regions. On the other hand, regions of high TAWSS and low OSI, labeled "high-flow" effects were correlated with aneurysm wall thinning and represent the type-I "red-thin" aneurysm phenotype. The specific thresholds used here were given by $TAWSS < 5\,\text{Pa}$ and $OSI > 0.01\,\text{Pa}$ for low-flow hemodynamics and by $TAWSS > 10\,\text{Pa}$ and $OSI < 0.001\,\text{Pa}$ for high-flow hemodynamics (see Fig. 5.4). These were chosen after analysis of the averaged values found by Furukawa et al. (72) and Cebral et al. (73).

For each patient-specific IA geometry, these regions were identified by performing CFD simulations using the rigid-wall assumption for the sake of computational time. The specific methodology of these simulations can be found elsewhere (115). Nevertheless, it is important to mention that the commonly recommended steps to perform reliable CFD simulations in vascular geometries were employed.

With the CFD results of the local hemodynamics, the TAWSS and the OSI were calculated. An example can be seen in Fig. 5.5b, where red-solid and white-dashed circles indicate two abnormal-hemodynamics regions of type-I and type-II, respectively. The identification of these "abnormal hemodynamics" regions was performed automatically by using an in-house code implemented by the author in Python using the VTK® library and stored in a field defined on the aneurysm sac surface assuming discrete values, shown in the right portion of Fig. 5.5b, which identifies each region in white and dark red, respectively. The pink-colored regions indicate a "normal" wall type, i.e. with the absence of the characteristic hemodynamic conditions.

With the field defined over S_{ia} indicating the type of patch, the fields of aneurysm thickness, e_{ia}, and of each material constant on the aneurysm were "updated" according to the illustration in Fig. 5.4 and subsequently smoothed-out to avoid unrealistic discontinuities in the fields. If a portion of the aneurysm is identified as a type-I patch, the thickness was decreased by 5 % whereas the material constants were increased by 20 %. Similarly, if it is identified as a type-II patch, both thickness and constants were increased by 20 %. This procedure follows the mechanical and morphological characterization of type-I and II phenotypes discussed in Section 2.5. This abnormal-hemodynamics based morphology modeling of the IA wall will be labeled *abnormal-wall model*.

The values by which each property was changed were somewhat arbitrary because any quantitative measure of how much the abnormal hemodynamics conditions change the aneurysm wall was not found. For example, one could not find data on how thinner the red-looking or type-I regions are compared to normal walls, which would allow the selection of an appropriate factor to scale these patches. For atherosclerotic walls, hence type-II patches, data gathered in Holzapfel et al. (89), based on earlier studies, show that the thickness can be up to 1.5 times larger than the normal arteries whereas the artery elastic modulus can be 4 times larger in the later stages of development, in the presence of calcification, but much smaller than 1.5 times in early stages. Due to this lack of data, the factors that correctly represented the histological observation for each region were selected and used consistently among all geometries. Nevertheless, a parametric study was carried out by changing these factors to assess what is the impact of thickness and the material constants on the wall mechanics. These are described in detailed in Appendix I.3.

Examples of the resulting fields are shown in Fig. 5.5c, where it is possible to see the impact on the aneurysm thickness and on the material constant, here represented by c_{10}. Note that, once this aneurysm is ruptured, the aneurysm material constant in the uniform-wall model is

smaller than the branches, indicating a less stiff aneurysm, whereas the resulting field in the abnormal-wall model is higher than that of the branches on some portions of the wall (see Fig. 5.5a and c, respectively).

5.3.9 Boundary Conditions

The BCs on the solid domain Ω^s are indicated in Fig. 5.2. On the outer surface, a pressure of $p_o = 5$ mmHg, corresponding to the intracranial pressure, was imposed. This value was selected after discussion with Dr. Carlos Baccin, a collaborator in this research. Obviously, the reported values may vary, nonetheless, similar values were found in related studies (139, 142).

The selection of the BC on the arteries "sections" is more delicate. It is difficult to predict which BC can be realistically applied at these locations. The literature that has simulated CSD or FSI in vascular geometries commonly imposed a zero displacement (117, 139):

$$\boldsymbol{u} = \mathbf{0}\,. \tag{5.80}$$

However, few works (131) used a BC that allows the arterial branch to slide along its tangential, but constrains the displacement along its normal, thus a "zero-shear traction" BC. Mathematically:

$$\begin{aligned} \boldsymbol{n}^s \cdot \boldsymbol{u} &= 0 \\ \boldsymbol{t}^s - (\boldsymbol{n}^s \cdot \boldsymbol{t}^s)\, \boldsymbol{n}^s &= \mathbf{0}\,, \end{aligned} \tag{5.81}$$

where $\boldsymbol{n}^s$ is the outward normal to the boundary and $\boldsymbol{t}^s = \boldsymbol{n}^s \cdot \boldsymbol{\sigma}^s$ is the traction to the boundary. Apart from the controversy, the zero-shear BC requires a much larger computational time, thus, because both are implemented in the software used to run the simulations, a comparative study was carried out between these two BCs with the IAs geometries studied here to assess their influence on the mechanical response (see Appendix I.1). It was found that, although the displacement field was affected by different BCs, both the largest Cauchy stress and largest stretch were unaltered on the aneurysm sacs, with qualitative differences in these fields only near the locations of the sections, as expected. Furthermore, these sections should be made at least two local diameters away from the IAs neck contour to safely assume that the zero-displacement BC would not influence the stress and stretch distribution on the IA. Therefore, for all the geometries used here, this length was assured for all the branches, including the parent artery, and then the zero-displacement BC was employed.

5.3.10 Modeling the Tissue Prestress

The image that is taken from the patient's vasculature *in vivo*, and used to extract the patient-specific geometry shown in Chapter 4, is actually under the action of hemodynamic forces and, hence, the vascular geometry is at a stress state of equilibrium with these forces at the moment that the image was taken. This so-called *prestress* has to be accounted for in the solid model and, consequently, in the formulation of the momentum equation that needs to be solved for the solid domain, Eq. (5.17). The prestress formulation used in this work is similar to the one presented by Hsu et al. (132), who performed an analysis about the influence of prestress on the mechanics and hemodynamics of patient-specific IAs by using the total Lagrangian formulation to write the momentum equation.

In the momentum equation, the tissue prestress is included as a body force that is constantly acting on the body, i.e. throughout the cardiac cycle. It can also be viewed as an "extra stress" added up to the current stress. Thus, Eq. (5.17) can be re-written as:

$$\int_{\Omega_0^{\mathrm{s}}} \rho_0^{\mathrm{s}} \frac{\partial^2 \boldsymbol{u}}{\partial t^2}(\boldsymbol{\xi}, t)\mathrm{d}V_0 = \int_{\Omega_0^{\mathrm{s}}} \nabla_0 \cdot [\boldsymbol{F} \cdot (\boldsymbol{S} + \boldsymbol{S}_0)]\mathrm{d}V_0\,, \tag{5.82}$$

where $\boldsymbol{S}_0$ is the second Piola-Kirchhoff prestress and $\boldsymbol{S}$ is the current level of stress due to the BCs being applied at a particular instant of time, i.e. $\boldsymbol{S} = \boldsymbol{S}(\boldsymbol{\xi}, t)$ whereas $\boldsymbol{S}_0 = \boldsymbol{S}_0(\boldsymbol{\xi})$. The specification of the prestress as the second Piola-Kirchhoff prestress is important because it represents the prestress calculated with respect to the reference configuration that has the same geometry as the reference configuration implicit in Eq. (5.82).

Equation (5.82) was modified in such a way that the prestress be included in the hyperelastic constitutive law in terms of the Cauchy stress tensor. To this end, the second Piola-Kirchhoff stress tensor must be substituted by the Cauchy stress by using the inverse of Eq. (C.25), i.e.:

$$\boldsymbol{S} = J\boldsymbol{F}^{-1} \cdot \boldsymbol{\sigma}^{\mathrm{s}} \cdot \boldsymbol{F}^{-\mathrm{T}}\,. \tag{5.83}$$

By substituting Eq. (5.83) into Eq. (5.82) for both the actual stress and the prestress, follows:

$$\int_{\Omega_0^{\mathrm{s}}} \rho_0^{\mathrm{s}} \frac{\partial^2 \boldsymbol{u}}{\partial t^2}(\boldsymbol{\xi}, t)\mathrm{d}V_0 = \int_{\Omega_0^{\mathrm{s}}} \nabla_0 \cdot \left[J\boldsymbol{F}^{-1} \cdot \left(\boldsymbol{\sigma}^{\mathrm{s}} + \boldsymbol{\sigma}_0^{\mathrm{s}}\right)\right]\mathrm{d}V_0\,, \tag{5.84}$$

As will become clearer in the next chapter, this approach to include the prestress in terms of the Cauchy stress tensor is preferred due to the way the momentum equation is implemented in the

software used to solve the governing equations numerically, which separates the "solid model", i.e. the momentum equation for a particular mathematical formulation, from the "mechanical law", given in terms of the Cauchy stress tensor.

Additionally, it is important to provide the prestress through the second Piola-Kirchhoff stress tensor, $\boldsymbol{S}_0$, which is calculated separately, and hence its inclusion in Eq. (5.84) is made through the equation:

$$\boldsymbol{\sigma}_0^{\mathrm{s}} = J^{-1}\boldsymbol{F}\cdot\boldsymbol{S}_0\cdot\boldsymbol{F}^{\mathrm{T}}\,. \tag{5.85}$$

The actual calculation of $\boldsymbol{S}_0(\boldsymbol{\xi})$, for a single geometry must be performed separately because, rigorously, it is the result of a different problem. Several methods have been proposed to actually compute the prestress in arteries and IAs tissue (178, 179, 132).

The technique used in this work was based on the approach followed by Bazilevs et al. (131), who also simulated FSI with prestressed IAs geometries. The authors assumed that the prestress was obtained for the vascular geometry in equilibrium with the flow conditions at *the low-diastole instant* (see Fig. 5.3a). Therefore, the prestress would be the result of the solution of the momentum equation at equilibrium, in the total Lagrangian formulation. Hence, from Eq. (5.17) follows:

$$\int_{\Omega_0^{\mathrm{s}}} \nabla_0\cdot\left(J\boldsymbol{F}\cdot\boldsymbol{\sigma}_0^{\mathrm{s}}\right)\mathrm{d}V_0 = \boldsymbol{0}\,, \tag{5.86}$$

defined over the reference configuration, Ω_0^{s}. The stress in Eq. (5.86) must be computed with the same constitutive law used for the pulsatile computations. Hence, it is important to note that the Eq. (5.86) was solved for each combination between the hyperelastic laws and both uniform-wall model and abnormal-wall model presented, separately, because it is important to assure a model consistency between the prestress computation and the pulsatile simulations. Once solved, the prestress in terms of the second Piola-Kirchhoff tensor, $\boldsymbol{S}_0$, can be computed through Eq. (5.83), and inserted in Eq. (5.84) via Eq. (5.85).

The BCs for Eq. (5.86), as expected, were the same for the branch sections and the outer surface of Ω_0^{s} as shown in Section 5.3.9, i.e. zero-displacement and uniform traction given by the intracranial pressure $p_o = 5$ mmHg, respectively. The traction on the inner surface, however, was the traction of the steady-state flow with velocity conditions at the end of diastole, t_{ld}. For the cardiac cycle shown in Fig. 5.3a, t_{ld} was assumed to be at, approximately, 0.94 s, or $\dfrac{t_{ld}}{T_c} \approx 1$, in relation to the cardiac period.

5.4 SUMMARY AND CLOSING REMARKS

To conclude the presentation of the complete mathematical modeling of the blood flow and the wall motion of an IA wall, Fig. 5.6 provides a graphical summary of the systems of partial differential equationss (PDEs) that must be solved, presented in detail along this chapter.

Figure 5.6 – Summary of the systems of PDEs of the flow problem and the solid problem and through which condition the interaction takes place in the case of the 1WFSI strategy.

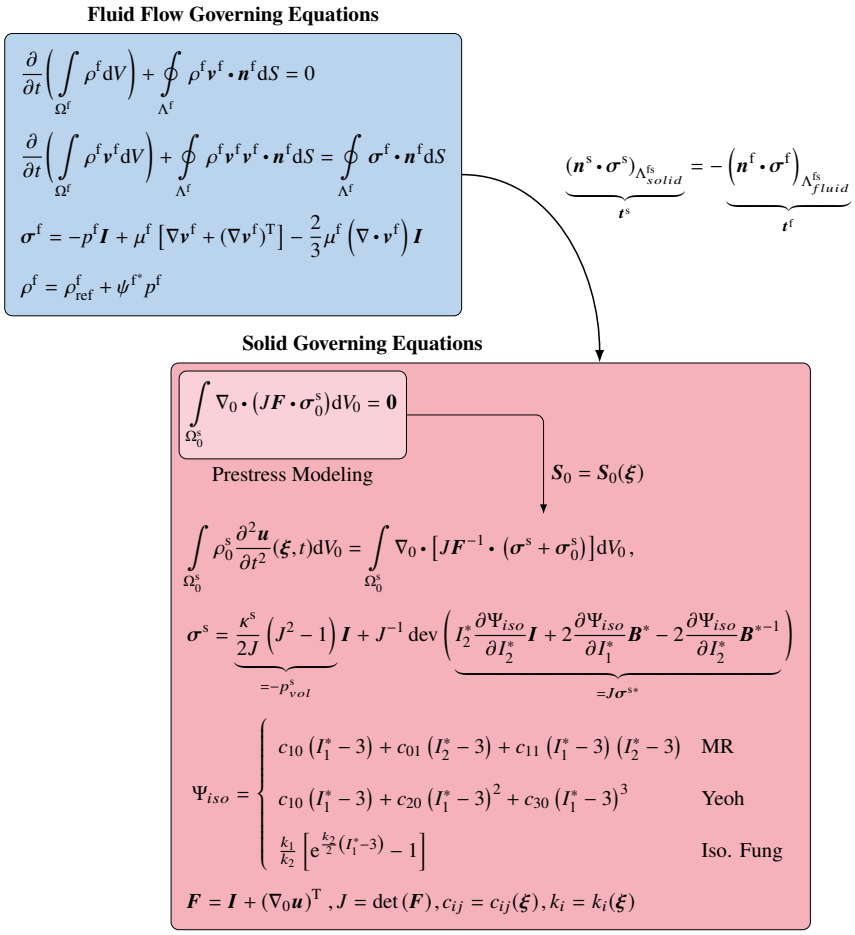

Source: Prepared by the author.

It is unnecessary to mention the complexity of this coupled system of PDEs, especially the solid sub-problem that accounts with geometric and material nonlinearities. Numerical techniques are, then, a natural choice to solve it. This option is even more obvious in light of the complex 3D geometries in which they must be solved. The numerical technicalities of its numerical solution are the subject of the next chapter.

Finally, one important note about the summary in Fig. 5.6 is the choice of the strain-energy function, Ψ_{iso}, where three laws were outlined — the MR, Yeoh, and isotropic Fung. Additionally, the functional form of the material constants, i.e. $c_{ij} = c_{ij}(\boldsymbol{\xi})$ and $k_i = k_i(\boldsymbol{\xi})$ was

used as a reference to the uniform-wall and abnormal-wall morphology models, indicating that the constants vary spatially over the wall geometries. This is to reinforce that the comparison among different modeling choices was performed among six different options by combining three constitutive laws and two morphology models.

Chapter 6

NUMERICAL METHODOLOGY

The numerical solution of the PDEs system presented in Chapter 5 was solved using solids4foam, an extension of OpenFOAM®, an open-source library for CFD and other problems in Continuum Mechanics. The solids4foam extension provides a suitable computational framework to include new materials laws for fluids and solids, to be solved in different formulations of the governing equations, and make these laws available in a FSI framework.

Like OpenFOAM®, solids4foam uses the FVM to discretize the PDEs that appear in Solid Mechanics. The mathematical details of the FVM and how it is implemented in OpenFOAM® because these can be found elsewhere (180), like standard textbooks (181, 182) or publications in the literature (183). However, a brief explanation of how the momentum equation in the total Lagrangian formulation, Eq. (5.18), is solved within solids4foam is given in Appendix F. This chapter focuses on the inclusion of the hyperelastic laws and the weakly compressible fluid model in solids4foam, as also their particular implementation to also include tissue prestress and heterogeneous material constants for the solid part. Finally, the discretization details for the fluid and solid sub-problems are outlined.

It is important to note that all newly implemented laws were verified against benchmark cases and analytical solutions to simpler problems. The verification assessment is included in Appendix G.

6.1 IMPLEMENTATION DETAILS IN SOLIDS4FOAM

Both the flow and solid problems, governed by the system of equations presented in Chapter 5, are inherently nonlinear, due to the advective terms in the flow momentum equation, the nonlinear measures of strain when the solid is deforming and also by the complex form of the hyperelastic

laws in Section 5.3.5. That is why discretization methods are classically used to solve these equations.

In solid mechanics, the Finite Element Method (FEM) is almost ubiquitous. It has been used for solving solid motion problems in linear elasticity since the early days of its development. However, it exhibits difficulties to solve nonlinear PDEs, due to instabilities that appear in the solution process when using interpolation techniques commonly used with the method. These difficulties have been addressed with different strategies. However, it has motivated the use of other methods that classically dealt with nonlinear equations, such as the FVM (184), which is almost dominant in CFD to handle the nonlinear terms that exist in the Navier-Stokes equations due to its capability to treat them in a simple manner and its strong conservativeness property. These properties have been proved to be helpful in certain areas of Solid Mechanics, for example, in the numerical solution of plasticity problems, which have strongly nonlinear PDEs and where conservativeness is also important to preserve numerically.

In this context, a package that has incorporated tools to deal with solid mechanics is OpenFOAM® and foam-extend[1]. OpenFOAM® and foam-extend are both a collection of libraries written in C++ to solve different physical problems with the FVM as its primary numerical method and traditionally used as a CFD tool (183, 180). Today, the extension of foam-extend called solids4foam, provides an extensive repertoire of solvers for solid mechanics including several constitutive material laws, contemplating both the small-strain theory and the finite-deformation theory of Continuum Mechanics, implemented in different formulations, including the total and updated Lagrangian formulations.

The design of solids4foam follows that of OpenFOAM® and foam-extend, i.e. based on *object-oriented programming* where the main programming structure is *classes* (185). While OpenFOAM® has different *solvers* for different models to solve a particular problem, solids4foam has a single solver, but the models are selected at run-time, allowing for more flexibility and the inclusion of new material laws, both for fluid and solids, as also for FSI solution strategies. The overall structure of the classes in solids4foam are illustrated in Fig. 6.1 by using a notation similar to the *unified modeling language* notation notation. Each box represents a class; open-base arrows represent an *association* between two classes, whereas closed-shape arrows represent an *inheritance relationship*.

[1]The original code was named FOAM (*Field Operation and Manipulation*), however, since it has been open-sourced, what was initially called *OpenFOAM* now is a trademark of the ESI group, while several branches of the original code exist, *foam-extend* being one of these.

Figure 6.1 – The class structure design of solids4foam with the newly implemented material laws under the class `biomechanicalLaw` that implements particular features of soft issues modeling. Other classes are also shown (based on Cardiff et al. (186)).

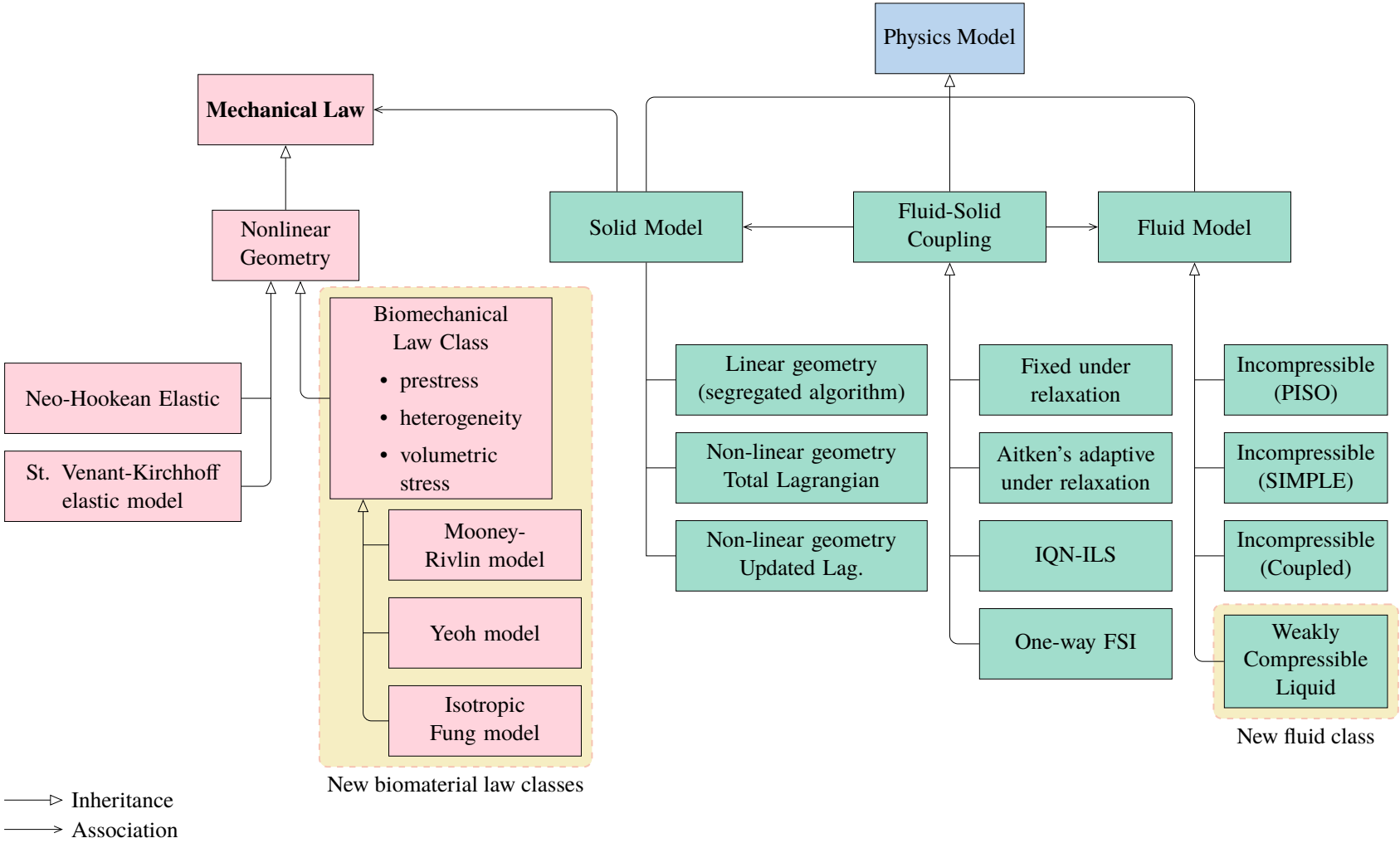

Source: Prepared by the author based on Cardiff et al. (186).

The `PhysicsModel` class yields objects that can be of three types so far: fluid or solid model, and fluid-solid coupling that has an associative relationship with a solid and fluid model, i.e. the `FluidSolidInteraction` class "knows" about the two other class. Each of the sub-classes implements a type of model of these three physics. Note, however, that the solid model is a parent class of different geometry descriptions, which differentiate between the small-strain and small-rotation theory and typical formulations in nonlinear solid mechanics, such as the total Lagrangian or updated Lagrangian formulations. Finally, the `mechanicalLaw` class implements different constitutive laws. This class provides the virtual function `sigma()`, which is implemented in each model sub-class. Therefore, to include a new constitutive law, one needs to include a new class derived from the `mechanicalLaw` class. It was under this class that the hyperelastic laws in Section 5.3.5 were implemented.

Finally, it is important to note that any new mechanical laws can be used with the different formulations of the momentum equation implemented as different "solid models" and also in the FSI framework. Computationally, the 1WFSI strategy was already implemented in solids4foam under the `fluidSolidInterface` class, which handles the FSI partitioned methods, as can be seen in Fig. 6.1.

6.2 IMPLEMENTATION OF BIOMECHANICAL LAWS

The hyperelastic laws used to model arteries have particular features that were not implemented natively in solids4foam for the nonlinear laws, such as tissue prestress and heterogeneity of the material constants. Hence, they were organized under a new class called `biomechanicalLaw`, derived from the `mechanicalLaw` class, as can be seen in the class diagram of Fig. 6.1.

The main reason to separate the implementation of the hyperelastic laws was the need to support the material constants to be scalar fields defined over the domain (a `volScalarField`, in the "language" of OpenFOAM®), allowing them to account for their heterogeneity without impacting the rest of the code where the material constants are assumed to be uniform fields overall (or `dimensionedScalars`). Therefore, all the fields presented in Section 5.3.8, created to represent all materials constants of the MR, Yeoh, and isotropic Fung laws, once converted to the OpenFOAM® format, can be used within the class.

Furthermore, `biomechanicalLaw` handles the variables involved with the prestress implementation and the inclusion of the volumetric modeling, discussed in Section 5.3.7, which are

the same for all hyperelastic laws. The equation implemented under `biomechanicalLaw` is the one given by Eq. (5.62). The prestress is added to this equation through the explicit inclusion of the prestress in the Cauchy stress form, Eq. (5.85). The volumetric modeling of the pressure term, $\boldsymbol{\sigma}_{vol} = -p^{s}_{vol}\boldsymbol{I}$ is also added explicitly to the material law through Eq. (5.72). Finally, the computation of the deviatoric part, $\boldsymbol{\sigma}_{iso} = \text{dev}\left(\boldsymbol{\sigma}^{*}\right)$ is delegated to the classes derived from `biomechanicalLaw`, indicated in Fig. 6.1, that implements the actual hyperelastic laws given in Section 5.3.6.

Given these implementation details, the discretized version of Eq. (5.84) with the different hyperelastic laws and morphology models was solved by using the *segregated* algorithm implemented in solids4foam (186) (see Appendix F). Second-order interpolation profiles were selected for the spatial discretization: the central differences scheme for any Laplacian terms with non-orthogonal and skewness corrections and the least-squares method for the gradients discretization (180). The temporal term was discretized by using the implicit first-order Euler approach. Finally, the normalized residual tolerance for the outer iterations of the momentum equation was 1×10^{-9},

The handling of the volumetric modeling deserves some further comments. When the Poisson's ratio tends to 0.5, i.e. towards the nearly-incompressible behavior, pressure field oscillations may occur in the solution, which could go unstable and cause divergence of the solution process (187). In order to smooth out these oscillations, a numerical technique originally proposed by Rhie et al. (188), and already implemented in solids4foam for some material laws, was applied by adding a third-order term that acts as a smoother to the solution, in the following manner:

$$-p^{s}_{vol} = \frac{1}{2J}\kappa^{s}\left(J^{2}-1\right) + \left[\underbrace{\gamma\nabla^{2}p^{s}_{vol}}_{\text{(I)}} - \underbrace{\nabla\bullet\left(\gamma\nabla p^{s}_{vol}\right)}_{\text{(II)}}\right], \tag{6.1}$$

where the term (I) is evaluated implicitly, i.e. it is discretized using the FVM discretization available in the OpenFOAM® framework and the term (II) is evaluated explicitly, i.e. using already computed values of the pressure field from the last time-step; γ is the diffusivity of this term and controls the amount of smoothing, defined as:

$$\gamma = \frac{1}{a^{\boldsymbol{u}}_{C}}\left(\frac{4}{3}G + \kappa\right), \tag{6.2}$$

where $a^{\boldsymbol{u}}_{C}$ are the diagonal coefficients of the discretized solid momentum equation in solids4foam (see Appendix F) and G is the shear modulus for the hyperelastic laws at the undeformed

configuration (167), Eq. (5.75). The term $\left(\frac{4}{3}G + \kappa\right)$ is used as an "implicit stiffness" of the momentum equation discretization (189).

Both terms (I) and (II) are mathematically the same, but their computational evaluation uses different stencils, hence, their difference adds an amount of numerical diffusion to the equation that minimizes the numerical oscillations of the pressure field, but as the cell size reduces, this correction tends to zero.

Equation (6.1) results in a system of equations and was solved by using the preconditioned Conjugate Gradient method with a normalized residual tolerance for of 1×10^{-9}. The BCs for Eq. (6.1) depend on the BCs for the momentum equation: on those boundaries where the displacement was specified, a zero-gradient Neumann BC was specified to the pressure, while when the traction is specified on a boundary, a Dirichlet BC was used for the pressure by extrapolating the interior value to the boundary.

Finally, the prestress calculation problem, defined by solving Eq. (5.86), with its BCs, was also solved numerically in solids4foam using the 1WFSI strategy, but with steady-state conditions. The steady-state regime was assumed and the flow at low-diastole conditions was solved using the SIMPLE algorithm and the same BCs for the flow domain outlined in Section 5.2.3. Normalized residual tolerances of 1×10^{-6} were used for both the pressure and velocity equations. Once finished, the traction on the wall was automatically imposed over the inner surface, and Eq. (5.86) solved with the total Lagrangian formulation with a normalized residual tolerance of 1×10^{-9}.

6.3 IMPLEMENTATION OF THE FLUID MODEL

On the fluid side, to solve the system formed by Eqs. (5.2), (5.3) and (5.8) the PISO algorithm (190) adapted for the flow of a compressible fluid, was used where the velocity and density fields are initially predicted according to Eqs. (5.2) and (5.3) for an initial pressure field, which is subsequently corrected to satisfy Eqs. (5.2) and (5.8), respectively, by using the pressure field computed with a pressure equation derived from the continuity equation, in a manner like it was originally proposed for incompressible flows.

As already known, in the segregated algorithms that are used to solve the governing equations of flows, like the SIMPLE and PISO, the construction of the pressure equation needs to be carefully carried out because part of the operators originate from the continuity equation while others from the momentum equation, which can have different discretization approaches. There-

fore, the pressure equation was found by combining the analytical equation of state, Eq. (5.8), with the continuity equation, Eq. (5.2), and the discretized form of the momentum equation, which takes the following form by the FVM (180):

$$\boldsymbol{v}^{\mathrm{f}} = \frac{1}{{a_C}^{\boldsymbol{v}}}\mathbf{H}(\boldsymbol{v}^{\mathrm{f}}) - \mathbf{D}^{\boldsymbol{v}}\nabla p^{\mathrm{f}}\,, \tag{6.3}$$

where $\mathbf{H}_C$ is a matrix operator that gather the discretization terms from the advective and diffusive terms of the momentum equation, $\mathbf{D}_C^{\boldsymbol{v}}$ is a measure of "pressure diffusivity", as will become clear when the pressure equation be derived, and ${a_C}^{\boldsymbol{v}}$ are the diagonal coefficients of the discretized momentum equation matrix. It was assumed that the only source term of the momentum equation comes from the pressure contribution, i.e. any influence of other body forces was neglected. Furthermore, it is important to note that the gradient operator in Eq. (6.3) must be viewed in a numerical way, i.e. it has been already discretized. More details on the explicit form of each term in Eq. (6.3) can be found in Jasak (180).

The pressure equation was derived by substituting the density given by Eq. (5.6) into Eq. (5.2). Next, the flow velocity in the resulting equation is substituted by Eq. (6.3). The result is a pressure integral equation given as follows:

$$\begin{aligned}\underbrace{\frac{\partial}{\partial t}\left(\int_{V(t)}\psi^{\mathrm{f}^*}p^{\mathrm{f}}\mathrm{d}V\right)\Big|_{\chi}}_{\text{Temporal term}} &+ \underbrace{\oint_{S(t)}\boldsymbol{n}\bullet\left\{\psi^{\mathrm{f}^*}\left[\frac{1}{{a_C}^{\boldsymbol{v}}}\mathbf{H}(\boldsymbol{v}^{\mathrm{f}})-\boldsymbol{\omega}\right]p^{\mathrm{f}}\right\}\mathrm{d}S}_{\text{Advective transport}} - \underbrace{\oint_{S(t)}\boldsymbol{n}\bullet\left(\rho^{\mathrm{f}}\mathbf{D}^{\boldsymbol{v}}\nabla p^{\mathrm{f}}\right)\mathrm{d}S}_{\text{Diffusive transport}} \\ &+ \underbrace{\oint_{S(t)}\rho^{\mathrm{f}}_{\mathrm{ref}}\boldsymbol{n}\bullet\left[\frac{1}{{a_C}^{\boldsymbol{v}}}\mathbf{H}(\boldsymbol{v}^{\mathrm{f}})-\boldsymbol{\omega}\right]\mathrm{d}S + \frac{\partial}{\partial t}\left(\int_{V(t)}\rho^{\mathrm{f}}_{\mathrm{ref}}\mathrm{d}V\right)\Big|_{\chi}}_{\text{Source terms}} = 0\,.\end{aligned} \tag{6.4}$$

The character of each term is indicated under it in Eq. (6.4), which is also discretized using the FVM. Compared to an incompressible flow, where the pressure presents a purely diffusive character with its information traveling with infinite speed across the entire domain, when the fluid is compressible, the presence of the temporal and the advective transport terms make the equation parabolic, thus pressure propagation occurs at a finite speed along time, which depends on the bulk modulus of the fluid. Furthermore, in the context of the numerical solution to this equation in a moving computational mesh, it is important to account for the second integral in the source terms because, even though $\rho^{\mathrm{f}}_{\mathrm{ref}}$ is constant, the volume of each cell may change, in general.

Finally, the complete PISO algorithm is shown in the flowchart of Fig. 6.2. This model

Figure 6.2 – Flowchart of the adapted PISO algorithm used to solve the governing equations of the weakly compressible fluid flow (we omitted the "f" superscript for the sake of simplicity); "n" indicates a time level and "m" indicates a PISO iteration.

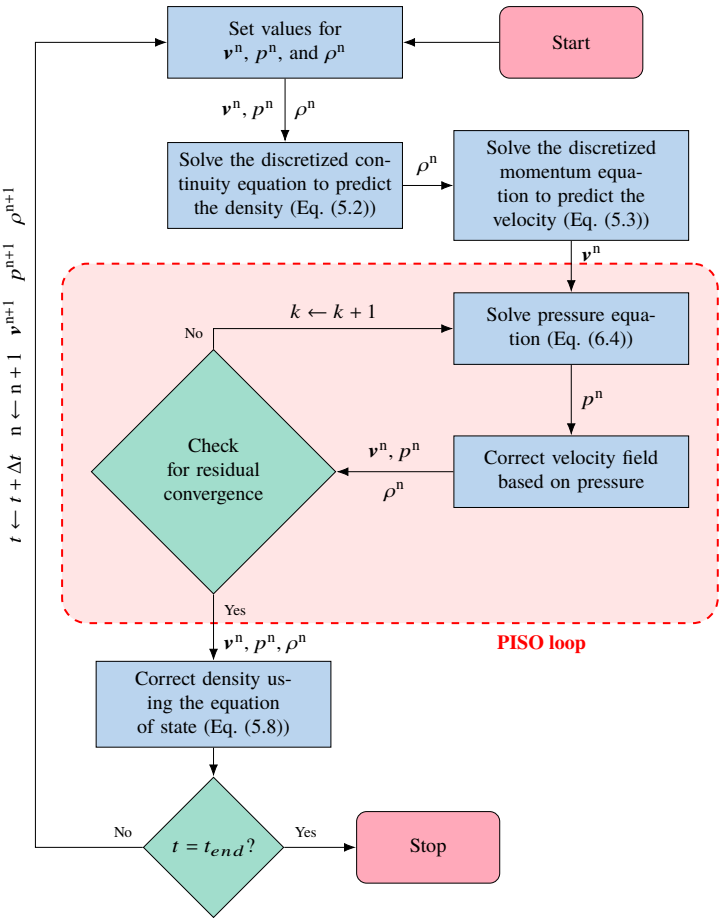

Source: Prepared by the author.

was implemented in solids4foam as a new fluid model class called `sonicLiquidFluid` (see Fig. 6.1 where the new class storing the model implementation was placed).

In terms of the discretization and interpolation schemes, to maintain the second-order accuracy level of the FVM, only second-order interpolation profiles were selected: the second-order upwind scheme for the advective term of both momentum and pressure equations, with the least-squares scheme for both velocity and pressure gradients discretizations and the second-order central differences for the surface-normal gradient in the diffusion terms with non-orthogonal and skewness corrections (180); finally, the temporal discretization was performed with the second-order (backward) Euler scheme. The normalized residual convergence criterion for each system was: 1×10^{-6} for the pressure equation and 1×10^{-8} for the momentum equation.

6.4 COMPUTATIONAL MESHES

The triangulated surfaces extracted with VMTK® (Section 4.1) were used to build the fluid and solid computational meshes. An example of the mesh of the vaculature harbouring cases rICA2 and urMCA2 is depicted in Fig. 6.3. The fluid mesh, i.e. the mesh of the volume region contained by the triangulated surface was generated by using the utility `cartesianMesh` provided by foam-extend as part of the cfMesh library. This utility automatically creates polyhedral meshes that are dominantly composed of hexahedral cells, i.e. the interior of the mesh consists of cells close in shape to hexahedra. To fit the curved boundary, the cells adjacent to the wall are, generically, polyhedra with a prismatic boundary-layer-refined region composed of five layers. The structure of the mesh was created to provide systematically finer cells closer to the wall, instead of only the prismatic layer adjacent to the wall. Thus, a cell size grading from the interior of the mesh towards the wall was created.

After the fluid mesh creation, the FSI interface of this fluid mesh, $\Lambda^{\mathrm{fs}}_{fluid}$, a quadrilateral surface, was "re-meshed", i.e. its structure of it was modified to only contain triangular faces by using VMTK's script `vmtksurfaceremeshing`. This re-meshing procedure was necessary

Figure 6.3 – Examples of the FSI meshes of the geometry of cases rICA2 and urMCA2 with a detail of a section of an artery showing the structure of the fluid mesh and the solid mesh.

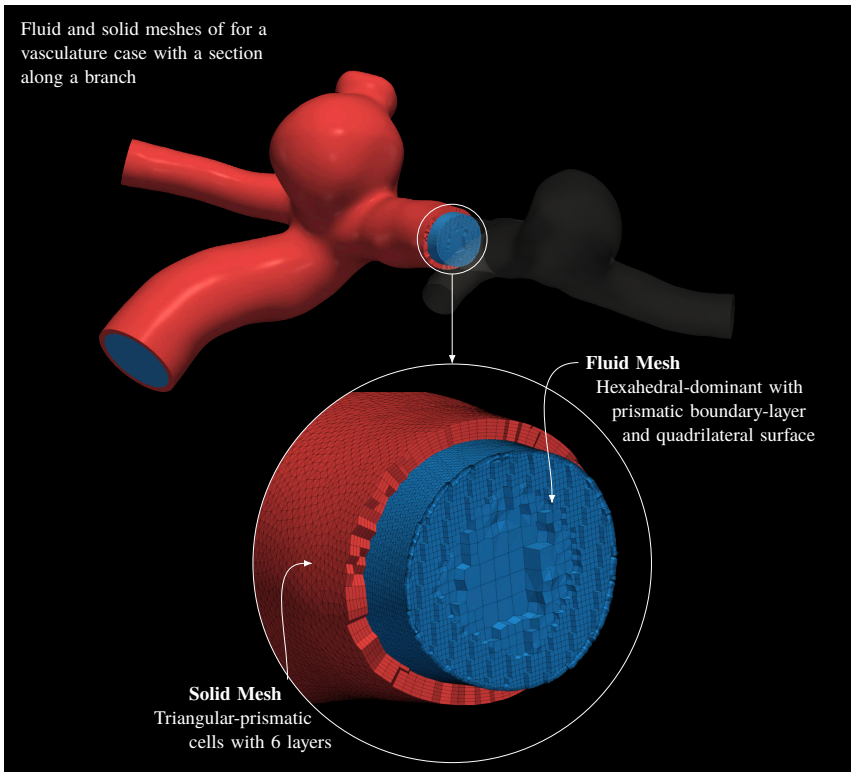

Source: Prepared by the author.

because of the possibility of pressure oscillations infecting the solid displacement solution when using quadrilateral cells with the segregated approach and the FVM (see Section H.2). The solid mesh was, then, created by extruding this remeshed surface of the fluid meshes in the outward direction with VMTK' script `vmtkboundarylayer`, which has support for a spatially-varying thickness field. The extrusion thicknesses were defined in Section 5.3.8, $e_w(\boldsymbol{\xi})$. Six layers were used in the extrusion. Clearly, the resulting "FSI mesh", i.e. the combination of the fluid and solid meshes, has a non-conformal interface at Λ^{fs}.

For each type of fluid meshes, mesh-sensitivity studies were carried out extensively with different IAs geometries and yielded a volume density of cells in the range of 3000 to 4000 cells/m^{3}m (an example of this study can be found in Oliveira et al. (115) and is reproduced in Appendix H), which was assured for all meshes used.

The mesh-independence study of the solid meshes was included in Appendix H and an extensive analysis was performed by also using Richardson's extrapolation to assess the discretization error. The simulations for this study were also done by using the 1WFSI strategy with three systematically-refined meshes and yielded a mesh with a surface-cells density of approximately 240.0 cells/mm^2, with 6 layers of cells along the thickness. A time-step refinement study was also carried out and the results are also in Appendix H. The test yielded a time-step of 1×10^{-4} s.

6.5 HARDWARE SUPPORT AND SIMULATION TIMES

The simulations were carried out in two high-performance computing clusters provided by the Center for Scientific Computing of UNESP and in the clusters labeled "Cedar", "Graham", "Béluga", and "Narval" provided by Compute Canada. In total, 72 simulations were carried out for the 12 geometries with 6 different models. The number of physical processors used per simulation was, on average, 118 (the specific number varied according to the mesh sizes).

The number of processors and the configuration of each cluster yielded simulations that ran for 62.7 h per cardiac cycle, on average. It is important to note, though, that the recorded computing times were different according to the hyperelastic law, as can be seen in Table 6.1 (the outer iterations showed in the table are the ones of the computation solution of the solid sub-problem. See Appendix F).

Table 6.1 – Averaged number of outer iterations of the solid sub-problem and computing times per cardiac cycle according to the hyperelastic law employed for the solid sub-problem.

Law	Avg. Number Outer Iter.	"Clock" Time/Cycle (h)
MR	846.55	69.70
Fung	831.24	68.72
Yeoh	586.71	49.29

Source: Prepared by the author.

Chapter 7

NUMERICAL RESULTS: COMPARING DIFFERENT MODELS

This chapter begins the presentation of the results of this work. Briefly, the thirteen vasculatures were simulated with the Mooney-Rivlin (MR), Yeoh, and isotropic Fung hyperelastic laws (indicated by "MR", "Y", and "F"), and each of them together with the *uniform* and the *abnormal* intracranial aneurysm (IA) morphology models. Note that the wall modeling of the branches was exactly the same for all modeling approaches on the IA. This chapter focuses on the assessment of the impact of these different combinations of modeling choices on the mechanical response, for the whole IA sample. First, how the simulation data were analyzed is presented in detail.

7.1 DATA ANALYSIS

Physical Variables of Analysis

The Cauchy stress tensor, $\boldsymbol{\sigma}^{\mathrm{s}}(\boldsymbol{x},t)$, and a deformation tensor chosen to be the right Cauchy-Green deformation tensor, $\boldsymbol{C}(\boldsymbol{x},t)$, were the main subject of investigation. Furthermore, the focus was on the aneurysmal region, i.e. with points $\boldsymbol{x} \in V_{ia}$, where V_{ia} is the volume of the wall of the aneurysm — it can be represented mathematically as $V_{ia} = S_{ia} \times e_{ia}(\boldsymbol{x})$ — and $t \in [0, T_c]$.

Metrics Employed

Due to the tensorial nature of $\boldsymbol{\sigma}^{\mathrm{s}}$ and $\boldsymbol{C}$, it is hard to investigate their six components (both are symmetric tensors). Instead, scalar quantities with an important physical meaning were chosen that are related to them: the largest principal Cauchy stress field, $\sigma_1^{\mathrm{s}}(\boldsymbol{x},t)$, and the

largest principal stretch, $\lambda_1(\boldsymbol{x}, t)$ — given by the square-root of the largest principal value of $\boldsymbol{C}$. Moreover, the preference for using the *normal* stress was based on evidence that, for IAs and also for arteries, the normal stresses are more important in failure criteria (56) than traditional shear-based stresses, such as the Von Mises stress, classically employed for metals, for example. Both fields were taken at the peak-systole instant, t_{ps} (see Fig. 5.3a), and the results shown in the *deformed* configuration, at t_{ps} (this was reinforced above by using the $\boldsymbol{x}$ in the functional forms). To ease the nomenclature, the following symbols will be used henceforth:

$$\sigma_1(\boldsymbol{x}) \equiv \sigma_1^{\mathrm{s}}(\boldsymbol{x}, t_{ps}), \tag{7.1}$$

and

$$\lambda_1(\boldsymbol{x}) \equiv \lambda_1(\boldsymbol{x}, t_{ps}). \tag{7.2}$$

Note, however, that σ_1 and λ_1 are scalar fields that vary over the wall volume V_{ia}. These were the subject of a qualitative comparison among the IA sample in the data analysis presented in this chapter by visualizing their fields with ParaView® (3). Nevertheless, to perform statistical analyses of the data for the whole IA sample, *metrics* of the σ_1 and λ_1 were calculated over the aneurysmal volume, V_{ia}. This approach allowed to map each IA case to a single value representing these fields, i.e. mathematically

$$IA_i \rightarrow \mathcal{M}\left\{\sigma_1(\boldsymbol{x})\right\}_i , \tag{7.3}$$

and

$$IA_i \rightarrow \mathcal{M}\left\{\lambda_1(\boldsymbol{x})\right\}_i , \tag{7.4}$$

where i represents each aneurysm case and $\mathcal{M}$ represent a particular metric. These were calculated over different portions of the volume V_{ia}: the inner and outer surfaces of the wall geometries. In biological terms, these are named luminal and abluminal surfaces of the vasculature, represented by S_{ia}^{l} and S_{ia}^{abl}, respectively. A "mid-thickness surface", S_{ia}^{m}, i.e. that lies at half-thickness from the lumen to the ablumen, was also analyzed.

Two metrics were computed. The first is the 99th percentile of each field, $(\sigma_1)_{99}$ and $(\lambda_1)_{99}$, used as a "proxy" of the fields maximum specifically for the statistical analysis, due to possible mesh-induced differences on the absolute maximum. The second metric is the surface-average

of a field over a surface, S, defined as follows, for σ_1:

$$\langle \sigma_1 \rangle_S = \frac{1}{A(S)} \int_S \sigma_1(\boldsymbol{x}) \mathrm{d}S, \quad \boldsymbol{x} \in S, \tag{7.5}$$

where $A()$ is the area operator and S is either S_{ia}^{l}, S_{ia}^{abl}, or S_{ia}^{m}. For σ_1, the surface-average metric gives a measure of the total traction on S caused by this stress. A similar physical meaning cannot be said about $\langle \lambda_1 \rangle$ although the same definition was used for regardless.

Computationally, the 99th percentile and the maximum were computed with the NumPy library (191), whereas the surface average was computed using an in-house code which computes the integral in Eq. (7.5) with first-order accuracy. Once these metrics were calculated for each aneurysm case, they were the subject of a statistical analysis and a comparison of their absolute values among the different models.

Statistical Analysis

Statistical tests were performed with n=13, for the 99th percentiles and the surface-averages, by using the SciPy library (158) with a significance level of $\alpha = 0.05$ (hence, 95 % confidence interval). All distributions were tested for normality by using the Shapiro-Wilk test.

To compare the two wall morphology models, for each hyperelastic law, the paired t-test and the Wilcoxon signed-rank tests were used for normal and non-normal distributions, respectively. Similarly, to compare the three distributions of the hyperelastic laws, the ANOVA test and the Kruskal-Wallis test were used *a priori* for normal and for non-normal distributions, respectively. Subsequently, pair-wise posthoc analyses were performed to test the distributions. The t-test and Dunn's posthoc methods were employed, in this case, for normal and non-normal distributions, respectively, via Python's library scikit-posthoc.

Relative Comparison Among Different Models

To quantify the differences among the metrics for each IA case, the *absolute* differences between each modeling choices were evaluated. If $\overline{\mathcal{M}}$ is the mean of the distribution of a metric $\mathcal{M}$, for a fixed hyperelastic law, the mean difference between the uniform and abnormal wall morphologies for a sample was defined as:

$$D_{\mathcal{M}}^{\mathrm{WM}} = \left| \overline{\mathcal{M}}_{AWM} - \overline{\mathcal{M}}_{UWM} \right|, \tag{7.6}$$

where the superscript "WM" stands for "wall morphology" and, consequentely, "UWM" and "AWM" indicate the uniform and abnormal-wall models.

Because three hyperelastic laws were employed and none can be assumed the "gold standard" to represent IA tissue, first, a difference similar to Eq. (7.6), but in a pair-wise manner between the three laws, MR, Yeoh, and isotropic Fung were computed. Then, the maximum of these values was found, or mathematically:

$$D_{\mathcal{M}}^{\mathrm{HL}} = \max_{i,j} \left(\left| \overline{\mathcal{M}}_i - \overline{\mathcal{M}}_j \right| \right), \tag{7.7}$$

where the superscript "HL" stands for "hyperelastic laws" and the pair (i, j) assumes the values in the set of permutations among the three hyperelastic laws.

7.2 COMPARISON OF THE MODELING APPROACHES

Hyperelastic Laws *vs.* Morphology Models

A preliminary qualitative analysis of σ_1 and λ_1 is shown in Figs. 7.1 and 7.2, respectively, both taken on S_{ia}^{l}, obtained with the uniform-wall and the abnormal-wall models and also with the different hyperelastic laws, for cases rMCA1 and urICA1 (upper and lower panels, respectively). First, it is clearly visible how the hyperelastic laws seem to more strongly affect λ_1 than the σ_1, irrespective of the morphology model. More specifically, the isotropic Fung and Yeoh laws produce higher levels of stretch in much larger areas than the MR, for example, whereas the σ_1 field is similar among all the laws, with small qualitative differences in the fields. Second, the overall levels of λ_1 are much larger for the ruptured case, rMCA1, than for the unruptured one, urICA1. Finally, both fields are similar in the two morphology models, indicating that the morphology model seems to have a smaller influence compared to different hyperelastic laws.

Cases rMCA1 and urICA1 seem to be representative of larger trends, as can be seen in Figs. 7.3 and 7.4 that show the distributions of the surface-average and 99th percentile of σ_1 and λ_1, over S_{ia}^{l}, respectively, for the IA sample through box-plots [1], separated by morphology models, and by the actual data points, segregated by rupture status. Additionally, the figures also depict, above and below the plots areas, the *p-value* resulting of hypothesis tests performed by

[1] Box-plots are a common way of showing statistical distributions, where the sample mean is depicted (here, as a diamond shape), and the actual box is delimited at the bottom and at the top by the 25th and 75th percentiles (first and third quartiles), respectively; the horizontal line inside the box marks the median. The upper and lower limits are called "whiskers" and are positioned, by definition, at 1.5 times the *inter-quartile range*, i.e., the distance between the first and third quartiles. The *outliers* lie outside the whiskers and were not depicted in the plots of the results presented here.

Figure 7.1 – Largest principal Cauchy stress, σ_1, field at the peak systole, on S^1_{ia}, for cases rMCA1 (top panel) and urICA1 (bottom panel), different hyperelastic laws (columns), and wall morphologies (rows).

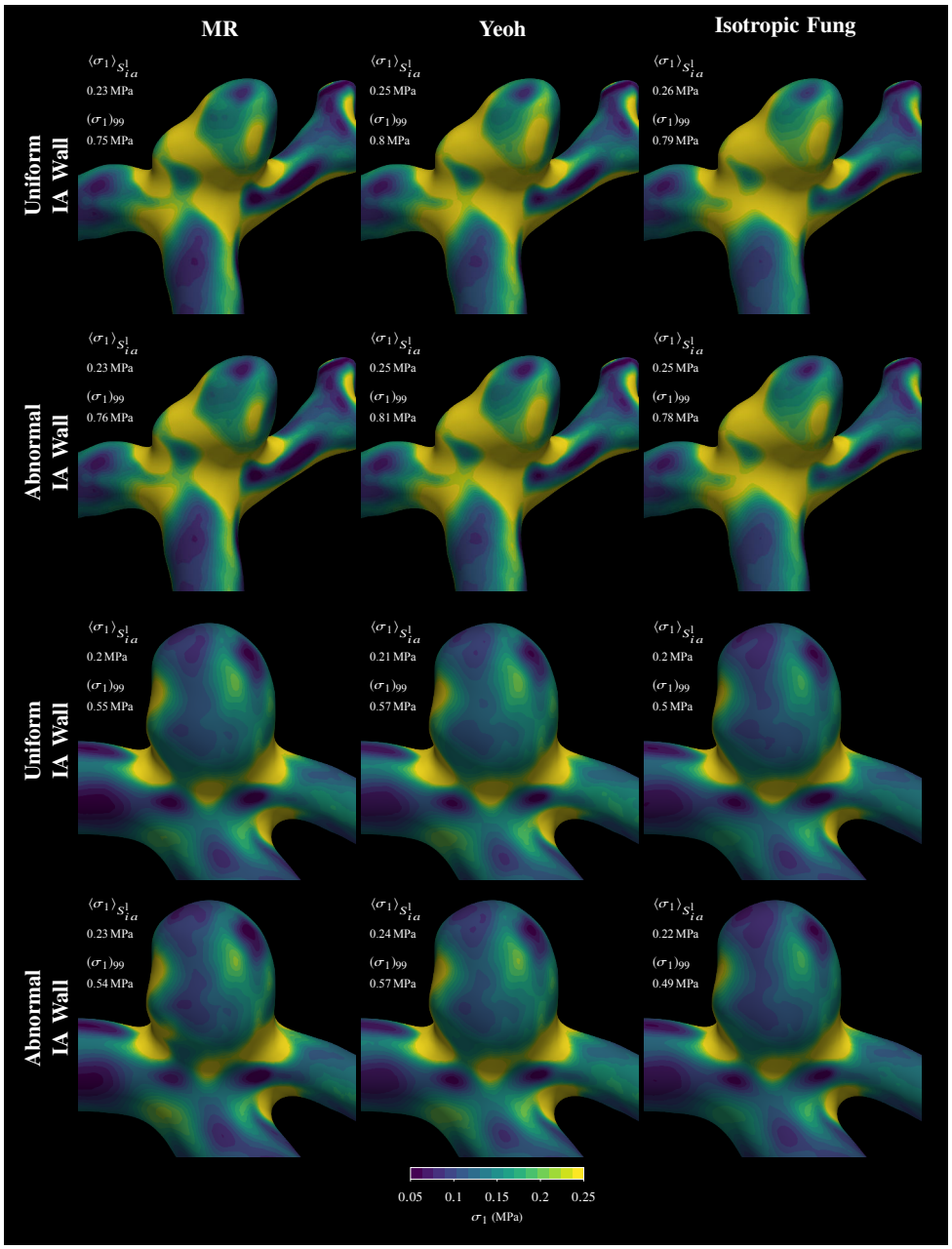

Source: Prepared by the author.

comparing the distributions through the special symbol "∘……p……∘", where the two circles visually indicate the two distributions that were compared and yielded the actual *p-value* shown above or below the symbol (this visual representation is used throughout this and the next chapter).

The distributions for the whole sample reflect the observations made about cases rMCA1 and urICA1 above. They indicate that the distributions of the metrics of σ_1 are more similar than the distributions of λ_1, by comparing the three laws, especially in terms of their means and medians, but also in terms of the spread. Second, the same can be told about the resulting distributions

Figure 7.2 – Largest principal stretch, λ_1, field at the peak systole, on S^1_{ia}, for cases rMCA1 (top panel) and urICA1 (bottom panel), different hyperelastic laws (columns), and wall morphologies (rows).

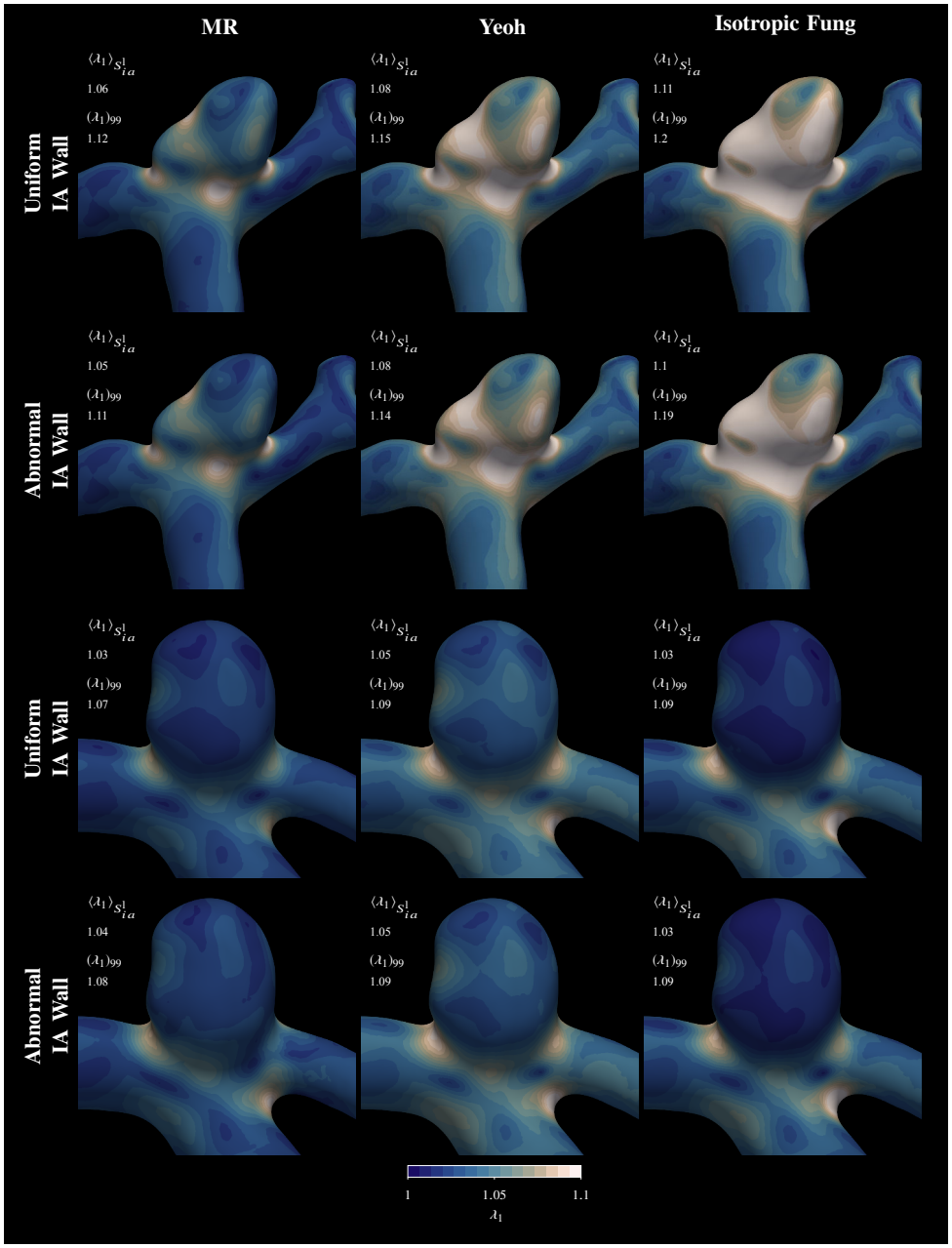

Source: Prepared by the author.

with the uniform-wall and abnormal-wall models for λ_1, although for σ_1 the uniform-wall model yield more dispersed distributions.

When comparing the three hyperelastic laws, the differences in the distributions of both σ_1 metrics did not reach statistical significance ($p = 0.73$ and $p = 0.57$ for the uniform-wall and abnormal-wall models, respectively, for $\langle\sigma_1\rangle_{S^1_{ia}}$; $p = 0.53$ and $p = 0.52$ for the uniform-wall model and abnormal-wall model, respectively, for $(\sigma_1)_{99}$). Furthermore, a post-hoc analysis using the t-test in a pair-wise manner yielded that the three distributions are not statistically

Figure 7.3 – Box-plots and data points (placed on top of their respective box-plot) of the distributions of (a) $\langle\sigma_1\rangle_{S^1_{ia}}$ and (b) $(\sigma_1)_{99}$ for the whole IA sample with the three hyperelastic laws (along the x-axis) and segregated by morphology model and rupture status. The diamond shape indicates the mean of each distribution. The p-values resulting from hypotheses tests comparing the three hyperelastic laws and the two morphology models distributions are shown below and above each plot area, respectively.

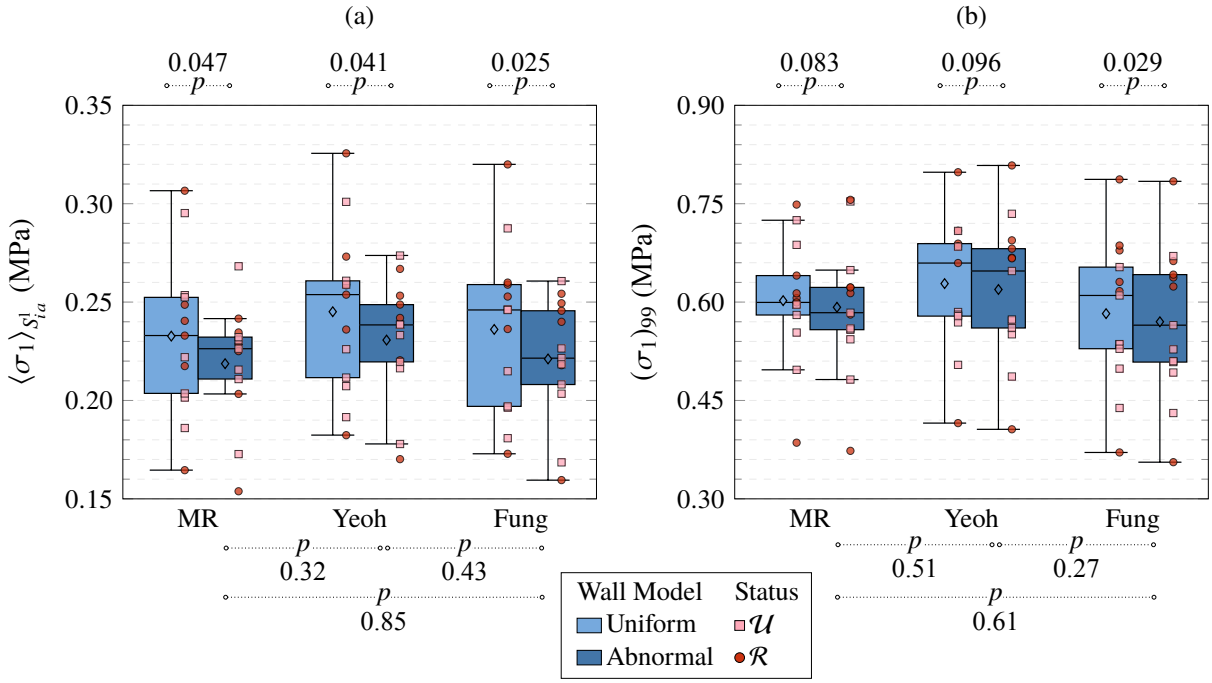

Source: Prepared by the author.

different (p-values depicted in Fig. 7.3 with the abnormal-wall model only; similar p-values were found with the uniform-wall model).

A different situation occurred with the distributions of λ_1. By comparing the three distributions, using in this case the ANOVA test for the surface-average and the Kruskal-Wallis test for the 99th percentile, it reached statistical significance for both metrics (for $\langle\lambda_1\rangle_{S^1_{ia}}$, $p = 0.033$ with the uniform-wall model and $p = 0.026$ with the abnormal-wall model, and for $(\lambda_1)_{99}$ $p = 0.030$ with the uniform-wall model and $p = 0.030$ with the abnormal-wall model). Post-hoc analyses showed different trends, though. For $\langle\lambda_1\rangle_{S^1_{ia}}$, the paired t-test indicated significant differences only between the pairs (MR, Yeoh) and (MR, Fung) (see Fig. 7.4a). For $(\lambda_1)_{99}$, Dunn's test with Holm's p-adjustment indicated that there was not significant differences for the three distributions, although the p-values by comparing (MR, Yeoh) and (MR, Fung) were close to the significance level (see Fig. 7.4b).

By comparing the distributions of the uniform-wall model and abnormal-wall model, they reached statistical significance for both λ_1 metrics, irrespective of the hyperelastic law (see the p-values above the plots of Fig. 7.4). Although the same did not occur for the σ_1, for which

Figure 7.4 – Box-plots and data points (placed on top of their respective box-plot) of the distributions of (a) $\langle\lambda_1\rangle_{S^1_{ia}}$ and (b) $(\lambda_1)_{99}$ for the whole IA sample with the three hyperelastic laws (along the x-axis) and segregated by morphology model and rupture status. The diamond shape indicates the mean of each distribution. The p-values resulting of hypotheses tests comparing the three hyperelastic laws and the two morphology models distributions are shown below and above each plot area, respectively.

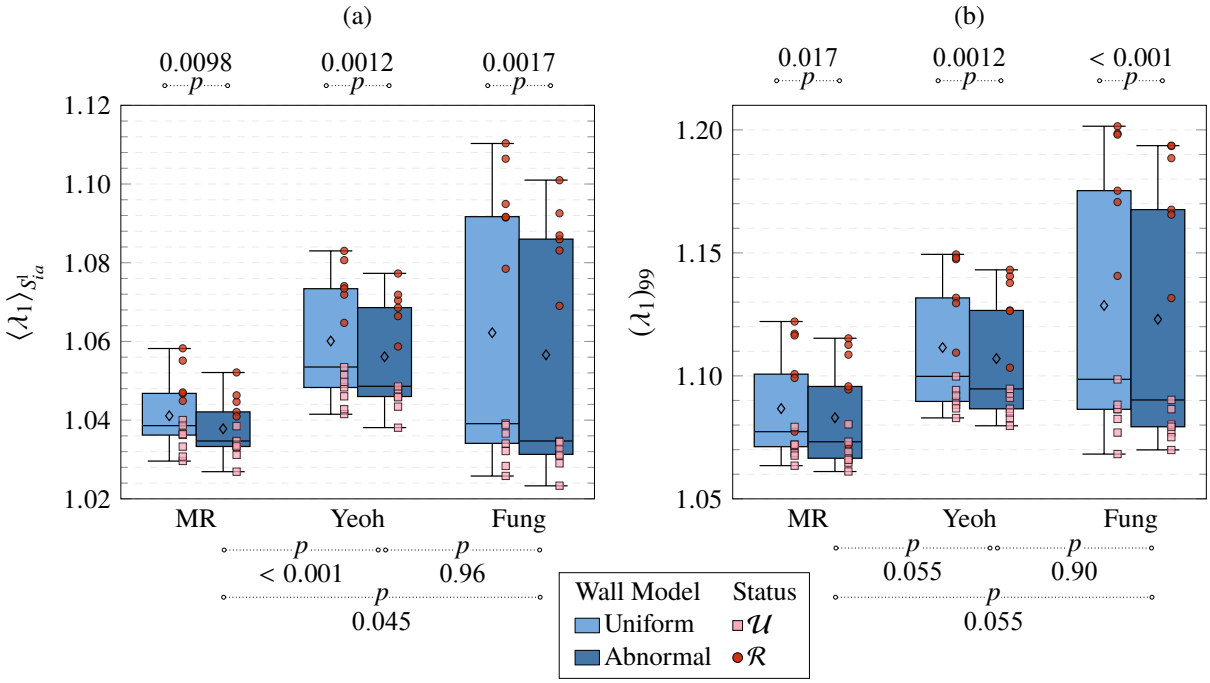

Source: Prepared by the author.

statistical significance was only reached by the distribution of $\langle\sigma_1\rangle$ with all laws, whereas the distribution of $(\sigma_1)_{99}$ only reached for the Fung law.

Quantitatively, the absolute difference between the means of σ_1 and λ_1 were larger when the hyperelastic laws were compared than when comparing the wall morphology models (Table 7.1), especially on the luminal surface and irrespective of the morphology model, confirming that the mechanical response is more sensitive to the choice of hyperelastic law. It is possible to note that the influence of the hyperelastic laws is more drastic for λ_1 and, furthermore, depends on the rupture status — note how the mean absolute difference is larger for the ruptured group than the unruptured one in Table 7.1. It is important to note though that only differences for λ_1 reached statistical significance, whereas that was not the case for σ_1.

These results suggest that the abnormal-wall model predicts a similar mechanical response than a model where the aneurysm wall has uniform thickness and material constants, the uniform-wall model, the most common alternative used in previous works that simulated IA wall mechanics as explained in Chapter 3, with absolute differences smaller than when different hyperelastic laws were compared. These findings indicate that the uniform-wall model may be

Table 7.1 – Maximal absolute difference for the selected metrics (surface-average and 99th percentile) of the σ_1 and λ_1 fields on the luminal and abluminal surfaces, among different hyperelastic laws and morphology models (Eqs. (7.6) and (7.7), respectively). The differences were averaged over each rupture-status group.

Side	Field Metric, $\mathcal{M}$	$D^{\mathrm{HL}}_{\mathcal{M}}$				$D^{\mathrm{WM}}_{\mathcal{M}}$					
		Abnormal		Uniform		MR		Yeoh		Fung	
		$\mathcal{R}$	$\mathcal{U}$	$\mathcal{R}$	$\mathcal{U}$	$\mathcal{R}$	$\mathcal{U}$	$\mathcal{R}$	$\mathcal{U}$	$\mathcal{R}$	$\mathcal{U}$
S^{l}_{ia}	$\langle\sigma_1\rangle$ (kPa)	19.1	12.9	19.8	12.6	20.6	8.25	21.3	8.49	22.4	8.79
	$(\sigma_1)_{99}$ (kPa)	59.3	60.6	60.4	61.9	4.23	15.1	5.28	12.2	10.8	13.7
	$\langle\lambda_1\rangle$ ($\times 10^{-3}$)	43.3	14.2	47.4	14.1	5.03	1.74	5.74	2.47	9.12	2.60
	$(\lambda_1)_{99}$ ($\times 10^{-3}$)	73.6	18.9	75.3	19.9	5.72	1.90	6.30	2.94	7.40	4.17
S^{abl}_{ia}	$\langle\sigma_1\rangle$ (kPa)	3.79	3.49	4.79	4.06	6.28	6.51	6.71	7.97	7.70	9.35
	$(\sigma_1)_{99}$ (kPa)	8.90	55.2	6.74	46.9	0.124	6.16	1.86	13.2	4.01	14.4
	$\langle\lambda_1\rangle$ ($\times 10^{-3}$)	37.1	12.2	40.3	12.3	3.06	1.47	4.07	2.24	6.27	2.17
	$(\lambda_1)_{99}$ ($\times 10^{-3}$)	62.6	14.8	64.9	17.1	4.45	0.647	5.05	2.93	6.82	3.87

Source: Prepared by the author.

used to find the mechanical response in populational studies of IAs. Care must be taken, though, depending on the particular application of the numerical results. Cebral et al. (93), for example, using a similar modeling to the abnormal-wall model to investigate the rupture site of IAs, found that a wall with both uniform thickness and stiffness was not able to predict the rupture site specifically, compared to models with focal properties changes.

The separation of λ_1 levels according to rupture status seen in Fig. 7.4 seems to be an important feature. The gap is largest for the isotropic Fung law, which explains the large dispersion of the distributions of λ_1, although the same can also be perceived with the Yeoh and MR models to a smaller extent. This particular feature did not occur for σ_1 metrics distributions, where they spread over a range between, approximately, 0.15 MPa to 0.30 MPa but not similarly segregated by rupture status. This feature explains the larger differences in λ_1' metrics for the ruptured group, in Table 7.1, clearly smaller for σ_1. This comparative behavior among each law is most likely to be related to the stiffer material properties of the unruptured group. Therefore, as stiffer an IA wall might be, all laws tend to yield the same, or at least similar, mechanical response, in terms of stretches, whereas as less stiff an IA wall is, i.e. closer to a ruptured condition, the MR deviated significantly from both Yeoh and Fung results.

Mechanical Response Along the Wall Thickness

Similar plots of Figs. 7.3 and 7.4 were inspected on the abluminal and mid-surfaces and similar conclusions were found on them, although not shown here for the sake of space. This reinforces that these comparative trends are robust and affect the whole field of σ_1 and λ_1 over V_{ia}.

Different, though, was the overall magnitude of σ_1 and λ_1 *along the thickness of the wall*, as also the field distributions over the aneurysms sacs, as can be seen in Fig. 7.5, which shows an example of these variables over the aneurysm case urMCA3 on the luminal, mid, and abluminal surfaces. Note how the fields change qualitatively from the luminal to the abluminal sides and, moreover, it is possible to see an increase of areas with relatively lower σ_1 and λ_1, suggesting an small decrease along the thickness (this is confirmed by inspecting the surface-average and 99th percentile annotated in the figure).

Figure 7.5 – Fields of σ_1 (top) and λ_1 (bottom) over the aneurysm sac of case urMCA3, with indication of both their surface-average and 99th percentile metrics over the luminal, mid, and abluminal surfaces of the wall (fields obtained with the MR law and the uniform-wall model).

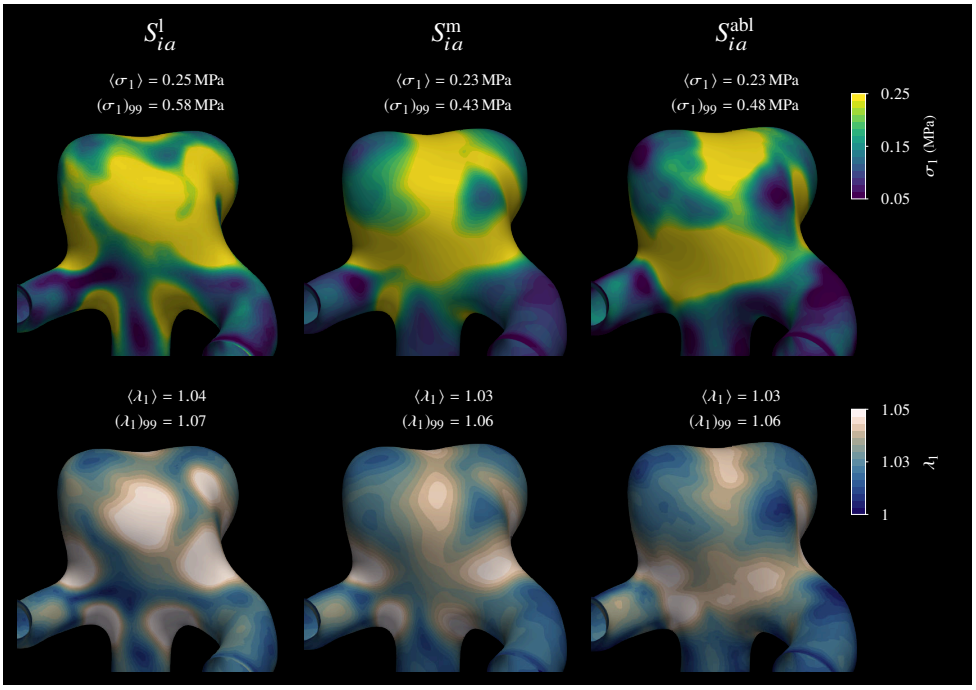

Source: Prepared by the author.

Additionally, the metrics over the mid and abluminal surfaces are similar, suggesting that the maximum level occurs on the lumen, tends to slightly decrease, and remains relatively constant between the mid-thickness and ablumen. Indeed this is the case for the whole IA sample, as shown by the box plots in Fig. 7.6. Although the figure shows the results of the MR with the

Figure 7.6 – Distributions of (a) $\langle \sigma_1 \rangle$ and (b) $\langle \lambda_1 \rangle$ over the luminal, mid, and abluminal surfaces for the IA sample (results obtained with the MR law and the uniform-wall model).

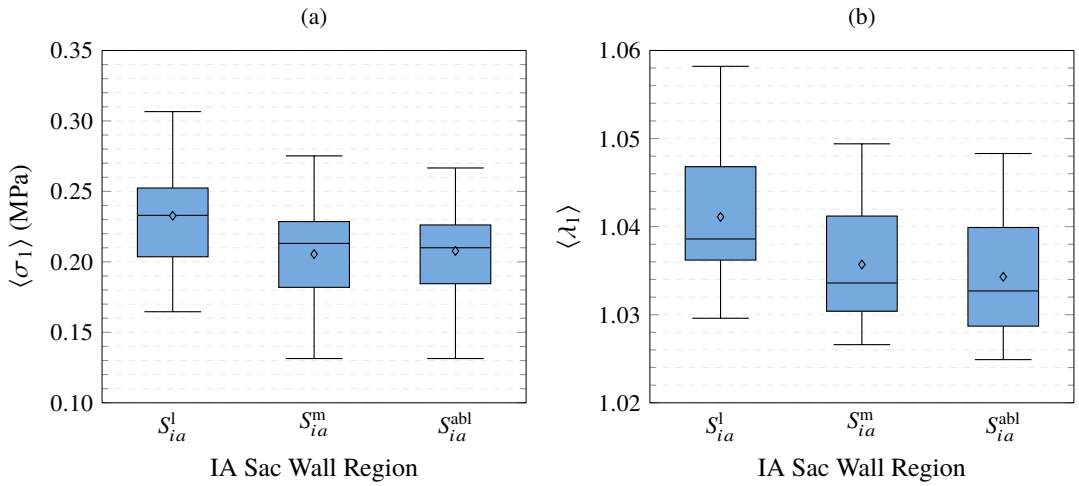

Source: Prepared by the author.

uniform-wall model only, the same behavior was found for the other modelings.

Variations of stress and stretch along the wall thickness are expected in this kind of geometry due to the boundary conditions applied on the inner and outer surfaces of the wall, i.e. relatively complex fields of wall shear stress (WSS) and pressure forces from the flow. Furthermore, although the variations along the thickness are relatively small, this behavior gives rise to normal and tangential gradients in the wall that could potentially have damaging effects on the structural integrity of the wall. These eventual effects remain currently unknown and deserve further investigations.

Nevertheless, no other works were found that have performed this kind of investigation. How the stress and stretch vary along the wall thickness is important because the wall is actually composed of different layers (see Fig. 2.6). In the simulations used here, a single-layer model was employed with a mechanical behavior expected to be the result of the combination of different structural elements, elastin and collagen mainly, that are not homogeneously distributed along the thickness. In Section 2.3, the different composition of each layer of an aneurysm and artery walls were presented and they may vary, thus potentially presenting different mechanical properties. Fung (41), for example, cited some early experimental works with samples of the thoracic aorta of pigs that found the modulus of Young of the intima and media layers, combined, to be as high as four times that of the adventitia. Therefore, the rupture event could result due to damage in one of the layers, serving as an initial fracture, which propagates, thus facilitating the complete wall failure.

Mechanical Response Along the Cardiac Cycle

While the conditions at the peak of the systole period present the harshest conditions during the cardiac cycle, it is important to assess whether the results shown held at the rest of the cardiac cycle. To this end, Fig. 7.7 shows central tendency plots (mean and confidence interval based on the 95 % percentile) of $\langle \sigma_1 \rangle_{S^{\mathrm{l}}_{ia}}$ and $\langle \lambda_1 \rangle_{S^{\mathrm{l}}_{ia}}$ of the IA sample resulted from the hyperelastic laws (only the abnormal-wall model is shown, but similar plots were found for the uniform-wall model).

Figure 7.7 – Central tendency plots (mean and confidence interval based on the 95-percentile) over time (shown in dimensionless form with respect to the cardiac cycle period, T_c) of (a) $\langle \sigma_1 \rangle$ and (b) $\langle \lambda_1 \rangle$, computed over S^{l}_{ia}, for the three hyperelastic laws and the abnormal-wall model.

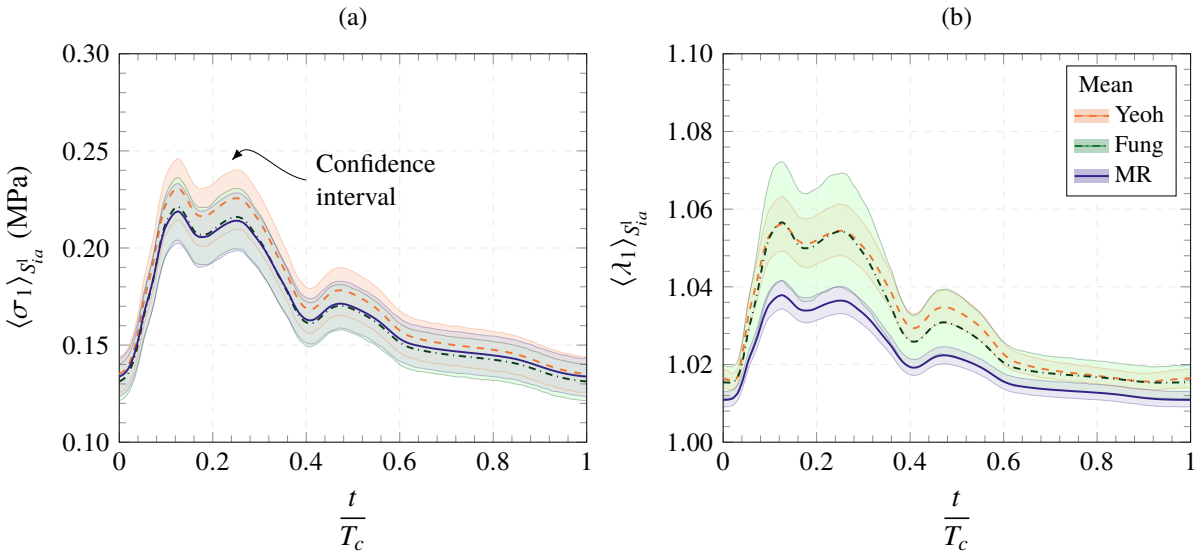

Source: Prepared by the author.

As expected, the largest differences among the models occur at the peak-systole and any difference tends to actually decrease after the systolic period towards the diastolic period. Thus, it is likely that all the results presented in the previous section still hold. For λ_1, the plots suggest that quantitative differences tend to decrease during the diastole too, whereas the differences among the models are much larger during the systole, probably as a manifestation of the nonlinearities of the laws depending on the level of forces driving the motion, higher during the systole.

This was confirmed by performing the statistical analysis presented with the results at the end of the diastole instant, t_{ld} (see Fig. 5.3a), and indeed the same conclusions still hold. The overall quantitative differences revealed the similar patterns seen in Table 7.1, although the magnitudes were indeed smaller.

7.3 FURTHER DISCUSSIONS AND CLOSING REMARKS

As discussed in Chapter 3, few studies were found to have also investigated the impact of different modeling choices on the mechanical response of IAs in the past two decades. Torii et al. (127) assessed the impact of different materials laws mainly on the hemodynamics, using a single IA geometry, thus limiting the possibility of comparison with our results (regarding the wall motion the authors only reported the maximum displacement on the IA sac and only used one law employed in this work, the Fung one). Ramachandran et al. (146) directly compared different material laws in patient-specific IA geometries, although they assumed static boundary conditions (BCs) and simulated only the IA sac, i.e. without the branches walls. They employed anisotropic and isotropic versions of the Fung law, the Yeoh law, and both small and finite strain versions of Hooke's law. Although the material constants they have employed were different, their conclusions broadly agree with the findings in this work, i.e. that the material laws predicted similar responses in terms of the wall stresses. Although, it is important to note that their study did not use the MR law, the one that presented the most divergent response compared to the Yeoh and Fung responses. The authors recognized, though, that their results could not hold as more patient-specific modeling features were added to the whole IA wall model in populational studies if these avoided the "uniform modeling choices applied across the patient population". The comparison performed here between the uniform-wall model and abnormal-wall model suitably addresses their concerns by showing that the absolute differences between a uniform wall IA and a realistic one, in terms of their mechanical response as given by σ_1 and λ_1, are actually smaller than by comparing different material laws.

The observed similarity of σ_1 among all the modeling choices further suggests that this field is indeed statically determined, one of the main questions raised by the work of Ramachandran et al. (146). This occurred irrespective of rupture status, hence further reinforcing that conclusion. On the other hand, λ_1 was more likely to be different according to the material law chosen, hence, using a similar language, stretch (and, more generally, strain) is not statically determined and was subject of a significant influence of the material constants. In this regard, the separation of λ_1 levels according to rupture status is also curious because it could potentially represent an important indicator of rupture. This will be further investigated in the next chapter.

The comparison between the uniform-wall and abnormal-wall models produced smaller absolute differences than by comparing the material laws, with statistical significance. Nevertheless, as explained in Section 5.3.8, the values by which thickness and material constants were

altered in the assumptions made for the abnormal-wall model (see Fig. 5.4) were somewhat arbitrary, even if based on scarce data available in the literature on this subject. To assess how these scaling factors would change the results, a parametric study was carried out by incrementally changing them, thus by altering both thickness and material constants locally and separately on type-I and type-II patches (see Section I.3 of Appendix I). By then computing $\langle \sigma_1 \rangle_{S^{\mathrm{l}}_{ia}}$ and $\langle \lambda_1 \rangle_{S^{\mathrm{l}}_{ia}}$, mean maximum absolute differences of 22.5 kPa and 4.13×10^{-3} were found, respectively, computed between the extremes of the parametric intervals, when the thickness of type-II patches was varied. All the others yielded smaller differences. Most importantly, the variation induced by focal changes in thickness and material constants were consistent among all IAs, as expected, therefore our main conclusions are most likely to withstand if other scale factors were chosen, although differences in the magnitudes of the fields could appear.

In practical terms, these findings may help future studies to choose a more suitable modeling to investigate other aspects of the mechanical response of IAs, which can further advance the understanding of the rupture event of an IA.

Chapter 8

LOCAL MECHANICAL RESPONSE AND PATHWAYS TO RUPTURE

In this chapter, the analysis of the simulations results continues with the focus on the differences in the mechanical response between ruptured and unruptured aneurysms, that were seen in the previous chapter, for the stretch mainly. Therefore, now that the effects of the material laws and morphology models were already assessed, other potential determinants of the mechanical response of IAs walls are the focus in this chapter. This was performed through two different analyses: an investigation of the maximum stress and stretch over the IAs walls and a search for the patches of IA sac with the largest stress and stretch, hence a local analysis.

8.1 DATA ANALYSIS

In view of the data presented in Chapter 7, the results of a single hyperelastic law and morphology model were selected. The MR law was chosen because, first, it yielded the smallest differences between the ruptured ("$\mathcal{R}$") and unruptured ("$\mathcal{U}$") groups compared to the Fung and Yeoh laws, thus any significant difference identified for that law is most likely to produce similar conclusions with the latter two. Second, the material properties used for the MR law were fitted from human IA tissue samples, a better choice compared with using the Fung law, for example, whose properties did not originate from IA tissue. Finally, the uniform-wall model was the chosen wall morphology model to eliminate the influence of the heterogeneous thickness and material properties on the mechanical response. In any case, it is important to mention that all the analyses presented below were also performed with the other hyperelastic laws and wall models and the conclusions were the same.

The data analysis followed closely the one explained in Section 7.1. The mechanical variables

chosen were the principal Cauchy stress and the principal stretch over the deformed configuration at peak-systole, i.e. $\sigma_1(\boldsymbol{x}) = \sigma^{\mathrm{s}}(\boldsymbol{x}, t_{ps})$ and $\lambda_1(\boldsymbol{x}) = \lambda_1(\boldsymbol{x}, t_{ps})$, respectively.

The two analyses performed used different metrics to quantify σ_1 and λ_1:

1. In Section 8.2, the absolute maximum stress and stretch over the wall sac *volume*, i.e. V_{ia}, was used, i.e.:

$$(\sigma_1)_{max} = \max_{\boldsymbol{x} \in V_{ia}} \sigma_1(\boldsymbol{x}), \tag{8.1}$$

$$(\lambda_1)_{max} = \max_{\boldsymbol{x} \in V_{ia}} \lambda_1(\boldsymbol{x}), \tag{8.2}$$

   because the largest stress and stretch potentially indicate the cases at the highest risk of rupture.

2. In Section 8.3, different patches of the sac surface were investigated. Therefore, it employed the surface-average metric (defined as in Eq. (7.5)) because this analysis had to be performed over a surface (it required the curvatures to be calculated), chosen to be the luminal surface, S^{l}_{ia}, because it exhibited the largest levels of both stretch and stress (see previous chapter).

Finally, for the statistical analysis between the distributions of the metrics above, the same tests presented in Section 7.1 were used accordingly to the type of data.

8.2 MAXIMUM STRESS AND STRETCH OVER THE SAC SURFACES

Figure 8.1 shows the distributions of $(\sigma_1)_{max}$ and $(\lambda_1)_{max}$ per rupture-status groups. The evident separation of $\langle\lambda_1\rangle$ seen in Fig. 7.3 and the lack of it for $\langle\sigma_1\rangle$ are both seen for the fields maxima, as expected. The maximum σ_1 is not significantly different between groups $\mathcal{R}$ and $\mathcal{U}$ ($p = 0.42$), although the contrary is true for the maximum λ_1 ($p = 0.037$). Furthermore, note that the unruptured group not only accounts with individual data points for which $(\sigma_1)_{max}$ are larger than the ruptured group (indicated by the whiskers of the box-plots), but also both the distributions means and medians are higher in the unruptured group. This is somewhat counter intuitive because higher stress have always been associated with increased risk of tissue failure.

The results then suggest that λ_1 is more likely to play a role as a rupture-indicator. This is not entirely surprising because, as explained in the previous chapter, the less stiff properties assumed for the ruptured IAs would obviously cause larger deformations in this group compared

Figure 8.1 – Distributions of (a) $(\sigma_1)_{max}$ and (b) $(\lambda_1)_{max}$ segregated by rupture-status groups (results obtained with the MR law and the uniform-wall model).

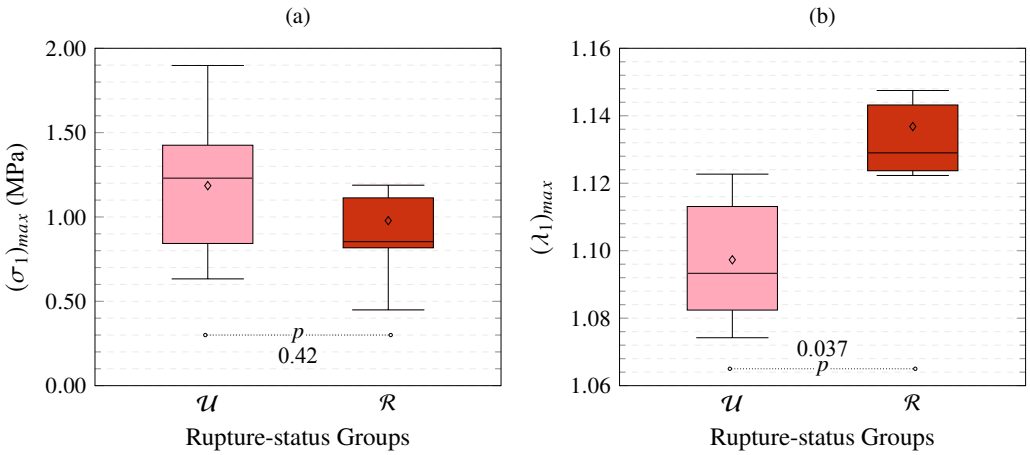

Source: Prepared by the author.

with the unruptured one. The biggest surprise is perhaps that the same behavior was not found to the stresses, i.e. σ_1 is less likely to act as a potential rupture-indicator or to indicate whether particular cases of IAs are imminently closer to rupture. More importantly, the maximum stress was, on average, higher in unruptured IAs than ruptured ones. To the author's knowledge, this has not been reported elsewhere in the literature in studies with a relatively large sample, only scarce data with only few aneurysms such as the numerical results provided by Lee et al. (125). The authors conducted an Fluid-Solid Interaction (FSI) numerical study and found one unruptured case that had higher effective stress — their IA sample was relatively smaller, with two ruptured and three unruptured IAs. Finally, it is not prudent, though, to also conclude that stresses do not *cause* the rupture. Comprehensively, stress has been classically targeted as the variable that also explains soft tissue failure, thus possibly explaining the rupture of IAs, although it is known that the *normal* component of the stress is more important in this respect (56), in contrast to classical metal theories where shearing-based effective stresses, such as the von Mises stress, are used.

That the deformations are higher in ruptured aneurysms was also supported by simulations performed by Sanchez et al. (142), who reported that aneurysmal pulsatility is a potential predictor of IA rupture. As defined in that study, the aneurysmal pulsatility, labeled here as δ_v, is given by:

$$\delta_v = \frac{V_{ps} - V_{ld}}{V_{ld}}, \tag{8.3}$$

where V_{ps} and V_{ld} are the luminal volume at the peak systole and low diastole, respectively. This variable was also analyzed for the IA sample used here and the results of its distribution are

Figure 8.2 – Box-plot of the distributions of δ_v for the IA sample segregated by rupture-status groups (results obtained with the MR law and the uniform-wall model).

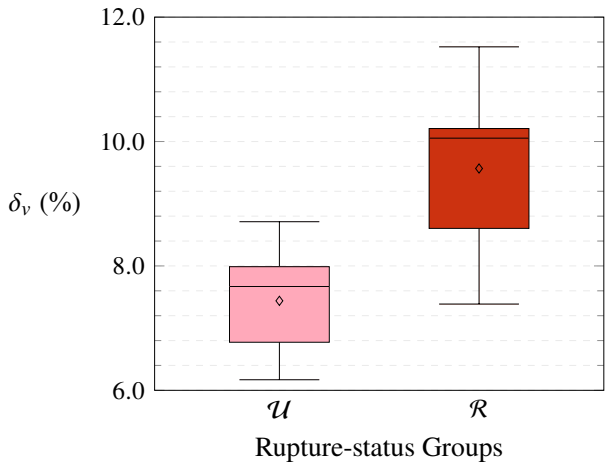

Source: Prepared by the author.

shown in Fig. 8.2. Clearly, δ_v follows the same trend than λ_1. Moreover, $(\delta_v)_{\mathcal{R}}$ was significantly higher than $(\delta_v)_{\mathcal{U}}$ ($p = 0.027$). Therefore, and in turn, the sample used in this work further support the results by Sanchez et al. (142).

The aneurysmal pulsatility is a measure of the volumetric deformation of an IA sac, hence it depends on the deformation of the wall. The same is true of the largest principal stretch and other strain measures, rigorously, because they all ultimately depend on the wall displacement, $\boldsymbol{u}$. Therefore, the trends found for λ_1 and δ_v are physically related. Still, δ_v is easier to calculate for a single aneurysm case, as the authors of Sanchez et al. (142) promptly pointed out, than $(\lambda_1)_{max}$, or any other metric of it, since the latter would depend on the whole λ_1 field.

An assessment of rupture likelihood based on the mechanical response computed for this work is not entirely complete without considering the failure properties of IAs tissue. In Section 2.4, experimental data reported by other works were presented, although all of the works performed uniaxial tests to failure, which probably under-characterizes the failure properties of those samples. Robertson et al. (79) measured the ultimate Cauchy stress of IAs samples and found a mean of 1.39 MPa (see Fig. 2.9a and Table 2.3) for the whole sample studied. Thus, based on the plots of Fig. 8.1, the unruptured group contains cases that would be effectively closer to rupture than the ruptured group. The large variability of the disease is what possibly explain, then, this seemingly confounding role of the stress. Robertson et al. (79) further divided their sample in "low strength" and "high strength" aneurysms with a mean ultimate Cauchy stress of 0.68 ± 0.08 MPa and of 1.60 ± 0.36 MPa, respectively. High-strength tissue was more prevalent in their sample, hence the unruptured cases here could be all high-strength cases,

whereas the ruptured ones could be all low-strength cases.

Additionally, Robertson et al. (79) also measured the ultimate stretch of their sample and found an average of 1.31 (see Table 2.3). Similarly, Brunel et al. (82), who experimentally investigated the failure properties of IA tissue, reported an average ultimate stretch of 1.190 ± 0.069 and 1.210 ± 0.071 for ruptured and unruptured groups, respectively. By also considering the variability of the disease, these values could roughly explain the ruptured cases in the sample used here (see Fig. 8.1b), especially in view of the fact, seen in the previous chapter, that both Yeoh and Fung laws overestimated the stretch compared to the MR law. Interestingly, Brunel et al. (82) also found a more consistent ultimate strain limit, of about $20.0 \pm 6.0\,\%$ of uniaxial deformation, than an ultimate stress limit, of about $0.38 \pm 0.24\,\mathrm{MPa}$ of uniaxial engineering stress, for their sample. The authors concluded that a "notion of strain limit is more relevant than one of stress limit". They highlight, though, that this was true only for the strain, instead of stretch. In the triaxial case, principal stretch and principal strains are related through a non-linear relationship given by $E_i = \lambda_i^2 - 1$, $i = 1, 2, 3$ (where here the principal values of the Green-Lagrange strain tensor, E_i, were employed). Their values were also estimated for the sample used in this work and, regardless, the strain measurements were still significantly higher for ruptured compared to unruptured aneurysms.

Ultimately, this section at least exemplifies the relative complexity of an IA wall regarding its failure properties because, not only the inter-aneurysm variability is important, but it is most likely that the failure limits also vary spatially on an aneurysm sac. Therefore, more detailed data of the failure properties of IAs tissue is necessary for further assessment of the likelihood of rupture based on the mechanical response of a patient-specific IA. But determining both ultimate stress and ultimate stretch of a patient-specific aneurysm is currently almost impossible without invasive techniques and, probably, much more difficult than to obtain its thickness and material constants distributions over S_{ia}. Nevertheless, the fact that the stretch plays a more prominent role as an indicator of the rupture of an IA may also indicate that it could be an important physical variable related to the mechanisms behind the rupture event, i.e. it could point to the regions of an IA wall that are in danger.

8.3 LOCAL STRESS AND STRETCH

The exact location of the rupture site in a patient-specific IA has intrigued researchers since early. Medical observations suggest that the majority of them occur on the dome of the

sac, although ruptures on the neck have also been reported (192). Clearly, the rupture site is probably co-localized with the sites of largest stress and stretch that, in turn, depends on the intrinsic heterogeneity of the wall, but also by local characteristics of the sac, such as its shape, intrinsically related to the wall curvature. The investigation of these sites is presented in this section and was accomplished through "patching" of the IAs luminal surface.

8.3.1 Patching of an IA Sac Surface

Three different patchings were performed to investigate the distributions of $\langle\sigma_1\rangle$ and $\langle\lambda_1\rangle$ over different surfaces.

1. By the abnormal-hemodynamics patches that based the abnormal-wall model model: type-I ("red" patches), type-II (atherosclerotic), and "normal" ones (see Section 5.3.8, and Fig. 8.3a for an example with the resulting patches of case urICA1). Each patch was indicated by S_I, S_{II}, and S_R, respectively.

2. By an artificial classification typically employed by physicians to split an IA sac into "neck", "body", and "dome". Although commonly employed in the medical practice, no formal mathematical definition exists of this classification, therefore, the one proposed and used by Salimi Ashkezari et al. (193) was employed in this work. First, the contours of geodesic distance from the neck contour were computed over each IA sac surface, S^{l}_{ia}, g_n, using VTK®. Then, the sac was split into the three patches named for the neck, S_N, body, S_B, and dome, S_D, based on the maximum geodesic distance to the neck contour, $(g_n)_{max}$:

$$S_N \equiv \left\{\boldsymbol{x} \in S^{\mathrm{l}}_{ia} \mid 0 < g_n \leq 0.20(g_n)_{max}\right\} , \tag{8.4a}$$

$$S_B \equiv \left\{\boldsymbol{x} \in S^{\mathrm{l}}_{ia} \mid 0.20(g_n)_{max} < g_n \leq 0.60(g_n)_{max}\right\} , \tag{8.4b}$$

$$S_D \equiv \left\{\boldsymbol{x} \in S^{\mathrm{l}}_{ia} \mid 0.60(g_n)_{max} < g_n \leq (g_n)_{max}\right\} . \tag{8.4c}$$

   An example of the resulting patching is shown in Fig. 8.3b.

3. Finally, a "local-shape" patching based on the principal curvatures of the luminal surface, κ_1 and κ_2, which are related to its fundamental forms. Based on them, more commonly used measures of curvatures are the Gaussian and mean curvatures, defined as follows:

$$K = \kappa_1\kappa_2 \tag{8.5}$$

Figure 8.3 – Examples of the three types of patching used to locally analyze the mechanical response of IAs walls for case urICA1: (a) the phenotypic classification used to base the abnormal-hemodynamics wall model; (b) the "physician-oriented" patching into "neck", "body", "dome" as defined by Salimi Ashkezari et al. (193); (c) based on the Gaussian, K, and mean, H, curvature fields of the lumen surface, a "local shape characterization" based on the one proposed by Ma et al. (157).

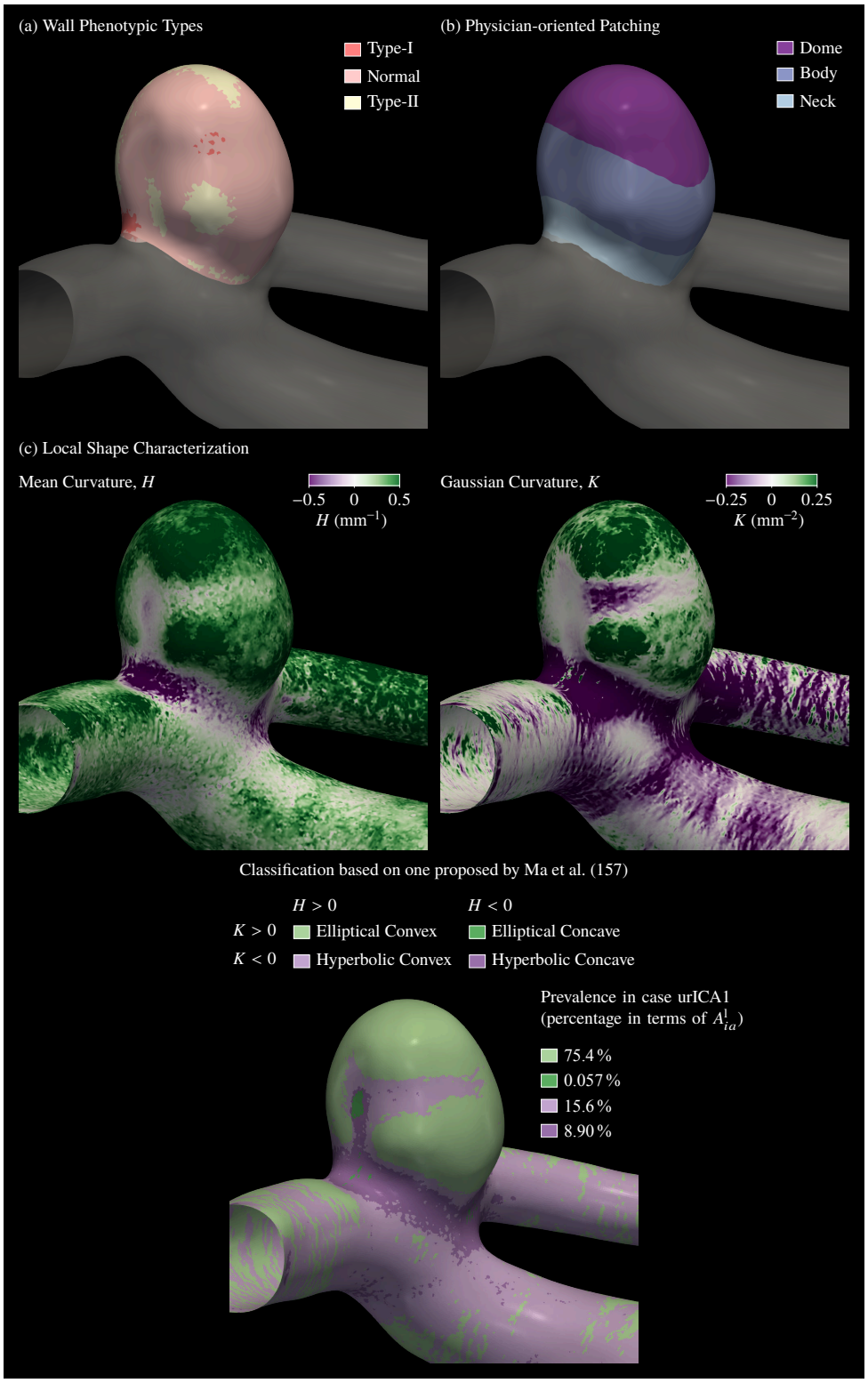

Source: Prepared by the author.

and

$$H = \kappa_1 + \kappa_2\,, \tag{8.6}$$

respectively. The Gaussian curvature, given in mm^{-2}, is used to characterize the points of a surface as elliptic ($K > 0$), parabolic ($K = 0$), or hyperbolic ($K < 0$). Elliptic points are localized on patches that look like a sphere or ellipsoid, whereas examples of a surface with parabolic points everywhere are cylindrical surfaces. Hyperbolic points are commonly known as "saddle" or "goose-neck" points. The mean curvature, given in mm^{-1}, is used to characterize local convexity $H > 0$ indicates convex portions, whereas $H < 0$ is a marker of a more concave portion. The fields of K and H are shown in Fig. 8.3c (middle panel) for case urICA1, calculated using the VTK® library, that accounts with a native filter to compute them. Based on them, Ma et al. (157) proposed a local shape classification, shown at the bottom of Fig. 8.3c. Note that only the classes that were found on the vascular surfaces were included, although others are possible, such as parabolic and planar surfaces. This classification yielded a map of the types of regions spanning the vascular surface, including the aneurysms (shown at the bottom of Fig. 8.3c). For the subsequente analysis, elliptical and hyperbolic patches are indicated as S_E and S_H, respectively.

It is important to note that the abnormal-hemodynamics patches were defined based on *a priori* Computational Fluid Dynamics (CFD) simulations performed with the rigid-wall model to create the abnormal-wall model used here, and not on the deformed configuration of the wall, as similarly done for the construction of the abnormal-wall model. Unfortunately, that was not possible due to the one-way fluid-solid interaction (1WFSI) numerical strategy used, which does not deform the fluid domain, nonetheless the abnormal-hemodynamics patches were built based on temporal-averaged quantities (time-averaged wall shear stress (TAWSS) and oscillatory shear index (OSI)). Hence, it is unlikely that the artery deformation would substantially change these patches.

Additionally, as can be seen in Fig. 8.3c, both K and H fields have a "noisy" behavior. As explained in Ma et al. (157), curvatures are second-order quantities in nature that depend on the points of the surface. Hence, their computation for discretized surfaces lead to these noisy fields and, more important, the level of surface mesh refinement may affect the evaluation of the curvatures. To avoid any impact on the analysis performed here, both H and K were computed on highly-refined versions of the luminal surface and, subsequently, interpolated to the surfaces

where the wall mechanics results were stored. This procedure avoided any discrepancy produced if the curvatures would have been calculated separately for each surface.

As can be seen in the Fig. 8.3c, an aneurysm sac contains four types of patches with different shape types. By comparing the shapes with Fig. 8.3b, the neck patch is dominated by saddle points ($K < 0$) whereas the dome and body patches are more spherical and, hence, dominated by elliptical regions ($K > 0$), although on the body and dome, hyperbolic points can exist depending on the aneurysm shape. Ruptured aneurysms, for example, tend to have blebs and lobular regions that enriches their curvatures distributions (this can be qualitatively assessed in Fig. 4.2).

The importance of investigating the abnormal-hemodynamics patches lies in their connection with the underlying local hemodynamics and, regarding the local-shape patches, to investigate the connection of local curvature with the mechanical response. Thus, note that the abnormal-hemodynamics and local-shape patchings are physically based, whereas the physician-oriented patching is an artificially created subdivision with applications in the medical practice — medical observations suggest that the majority often ruptures on the dome (192). Hence, to physically characterize the first two, their areas were measured for the IA sample and its distribution, as a percentage of the sac area, A^{l}_{ia}, shown as box-plots in Fig. 8.4, respectively, by rupture-status groups. In the plots of the local shape patches prevalence, both convex and concave patches were added and included under the elliptic and hyperbolic points only. That was based on the fact that, although elliptical concave regions were identified, they accounted for less than 0.1 % of the sac area, on average.

First, it is clear that type-II patches (atherosclerotic) tend to be more prevalent than type-I ones, based on the hemodynamic classification used in this work (with statistical significance, $p < 0.001$). In view of the sample taken that encompasses IAs in different sites and a large range of sizes, implying different hemodynamics, it is striking how rare type-I patches seem to be — note in Fig. 8.4a that some unruptured cases did not have these patches. Furthermore, that occurred independently of rupture status, with both ruptured and unruptured groups presenting statistically the same differences (see p-values in Fig. 8.4a).

Second, elliptic patches are more prevalent on IAs, with hyperbolic patches occupying a range of 30 to 40 % of an IA sac surface area. Furthermore, hyperbolic patches are significantly larger in ruptured IAs than unruptured ones (mean ± standard deviation (SD) = 34.6 ± 4.3 % *versus* 24.4 ± 4.3 %, respectively; see p-values in Fig. 8.4b).

Figure 8.4 – Distribution of area of the (a) abnormal-hemodynamics patches of type I, II, and also "normal" — neither type-I nor type-II — and (b) the local-shape type, as defined in Fig. 8.3c, grouped by convexity, for the IA sample. Values are given by the ratio between the respective patch area, generically indicated by A, and the aneurysm sac surface area, A^{I}_{ia}.

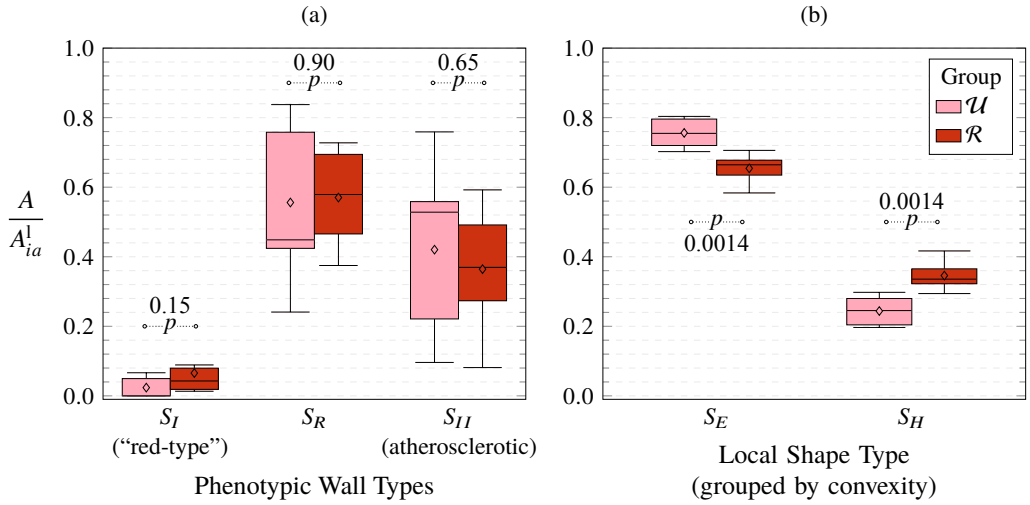

Source: Prepared by the author.

8.3.2 Local Mechanical Response on Different Wall Patches

As can be seen in Fig. 8.5, hyperbolic patches have $\langle\sigma_1\rangle$ as high as twice than elliptic ones, although no significant differences were found between the $\mathcal{R}$ and $\mathcal{U}$ groups (see plots for p-values). Significant differences also occur for $\langle\lambda_1\rangle$ between elliptic and hyperbolic patches. Furthermore, and most interestingly, the largest levels of $\langle\lambda_1\rangle$ are found on hyperbolic patches of the ruptured group, with statistical significance, whereas no statistically significant differences between $\mathcal{R}$ and $\mathcal{U}$ were found for elliptic ones.

Figure 8.5 – Distributions of (a) $\langle\sigma_1\rangle$ and (b) $\langle\lambda_1\rangle$ over the surface patches of elliptic and hyperbolic types, segregated by rupture-status groups (results obtained with the MR law and the uniform-wall model).

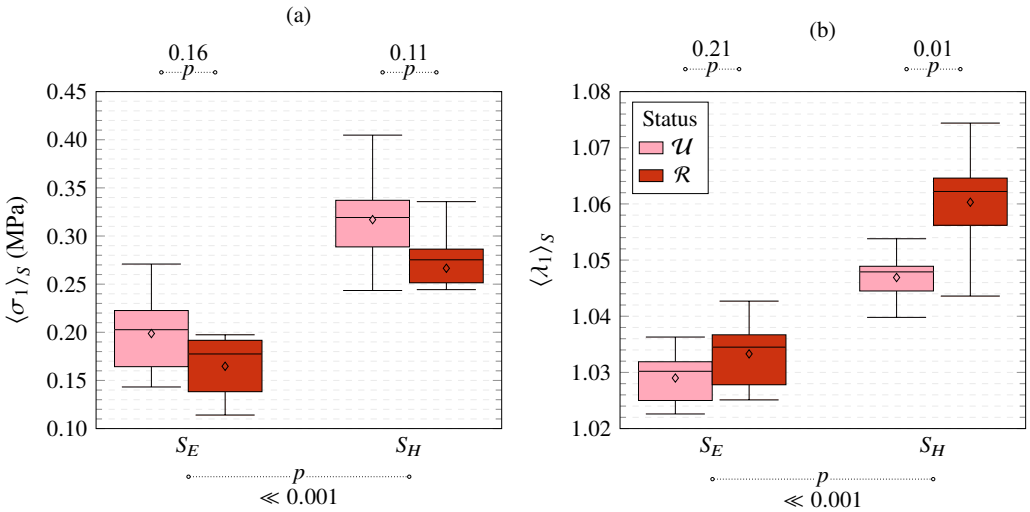

Source: Prepared by the author.

Figure 8.6 shows the same distributions but averaged over the patches defined by the abnormal-hemodynamics and physician-oriented patchings. Both $\langle\sigma_1\rangle$ and $\langle\lambda_1\rangle$ tend to be higher on S_I, by as much as twice on S_{II}, while intermediate levels of such variables were found on S_R. Statistical tests confirmed that there were significant differences between the three patch types for both $\langle\sigma_1\rangle$ and $\langle\lambda_1\rangle$ ($p = 0.0019$ and $p < 0.001$, respectively), although a post-hoc pair-wise analysis showed that the two variables are not significantly different between S_R and S_{II}.

Regarding the physician-oriented patching analysis, S_N exhibits the highest levels of both $\langle\sigma_1\rangle$ and $\langle\lambda_1\rangle$, with the statistical test confirming that there is significant differences between the three patches types for both $\langle\sigma_1\rangle$ and $\langle\lambda_1\rangle$ ($p < 0.001$ for both variables). Post-hoc pair-wise analysis showed that there was no significant differences for both variables between S_B and S_D.

Similarly to what was found for the whole sac, $\langle\sigma_1\rangle$ was not significantly different between groups $\mathcal{R}$ and $\mathcal{U}$, irrespective of the patching (see p-values Fig. 8.6a and b). A more interesting situation occurred for $\langle\lambda_1\rangle$. It was found to be significantly higher for $\mathcal{R}$ than $\mathcal{U}$ on patches S_I and S_R, in the abnormal-hemodynamics patching, and also on S_N and S_B, in the physician-oriented patching (see p-values in Fig. 8.6c and d) — note, however, that the largest differences occurred on the former of each. Whereas no differences were found on S_{II} and S_D.

Nevertheless, by inspecting the plots in Fig. 8.6e and f, which shows the distributions of $\langle K\rangle$ for the abnormal-hemodynamics and physician-oriented patchings (suitably split into elliptic, $K > 0$, and hyperbolic, $K < 0$, regions), both S_I and S_N are, on average, entirely in negative Gaussian curvature region, showing that they are characterized as hyperbolic patches, whereas S_{II} and S_D by elliptic patches. Intermediate situations occur for S_R and S_B. As seen in Fig. 8.5, hyperbolic patches present intrinsically higher $\langle\sigma_1\rangle$ and $\langle\lambda_1\rangle$. Therefore, the largest $\langle\sigma_1\rangle$ and $\langle\lambda_1\rangle$ seen on S_N and S_I are probably explained by the curvature of these patches, instead of any other intrinsic characteristic of them.

Further support for this seemingly important relationship between the mechanical variables and the curvature is provided by the plots shown in Fig. 8.7, where $\langle\sigma_1\rangle$ and $\langle\lambda_1\rangle$ are plotted against $\langle K\rangle$ and $\langle H\rangle$ over elliptic and hyperbolic patches. Using a surface-average metric for the curvatures too as a form of showing an eventual relationship between λ_1 and σ_1 and the curvature was preferred because the curvature fields are very noisy, as explained in the previous section, hence point-wise correlations would probably reproduce this noise. All the plots show a significant negative correlation between both mechanical variables and the curvatures — see

Figure 8.6 – Distributions of $\langle \sigma_1 \rangle$ (a and b), $\langle \lambda_1 \rangle$ (c and d), and $\langle K \rangle$ (e and f) over the abnormal-hemodynamics patches (S_I, S_{II}, and S_R; left column) and over the physician-oriented patches (S_N, S_B, and S_D; right column), segregated by rupture-status groups (results obtained with the MR law and the uniform-wall model).

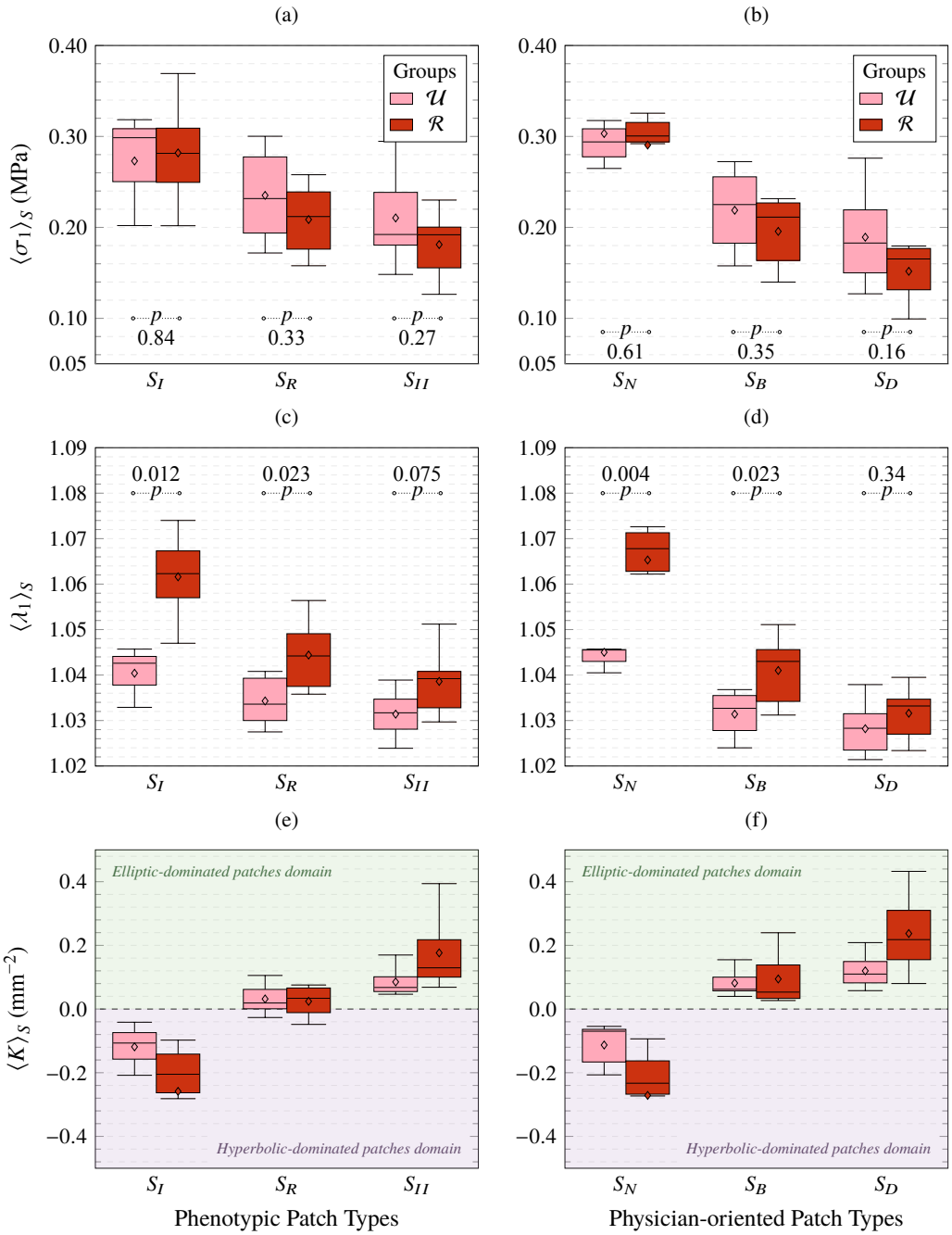

Source: Prepared by the author.

Pearson's correlation coefficient, ρ_{P}, on top of each plot.

Although a continuous relationship between mechanical variables and the wall curvature could not be found, the plots in Fig. 8.7 suggest that such a relationship may exist for the wall of IAs and is most likely to be similar to Laplace's law, i.e. both stress and stretch inversely proportional to the curvatures. Furthermore, and most importantly, this local analysis suggests

Figure 8.7 – Correlation plots between $\langle\sigma_1\rangle$ (a and b) and $\langle\lambda_1\rangle$ (c and d) *versus* $\langle K\rangle$ and $\langle H\rangle$ over the surface patches of elliptic and hyperbolic types, segregated by rupture-status groups (results obtained with the MR law and the uniform-wall model). The hyperbolic and elliptic patches "regions" on each plot are marked as different colors. The regression lines were computed with linear regression using Python's library SciPy.

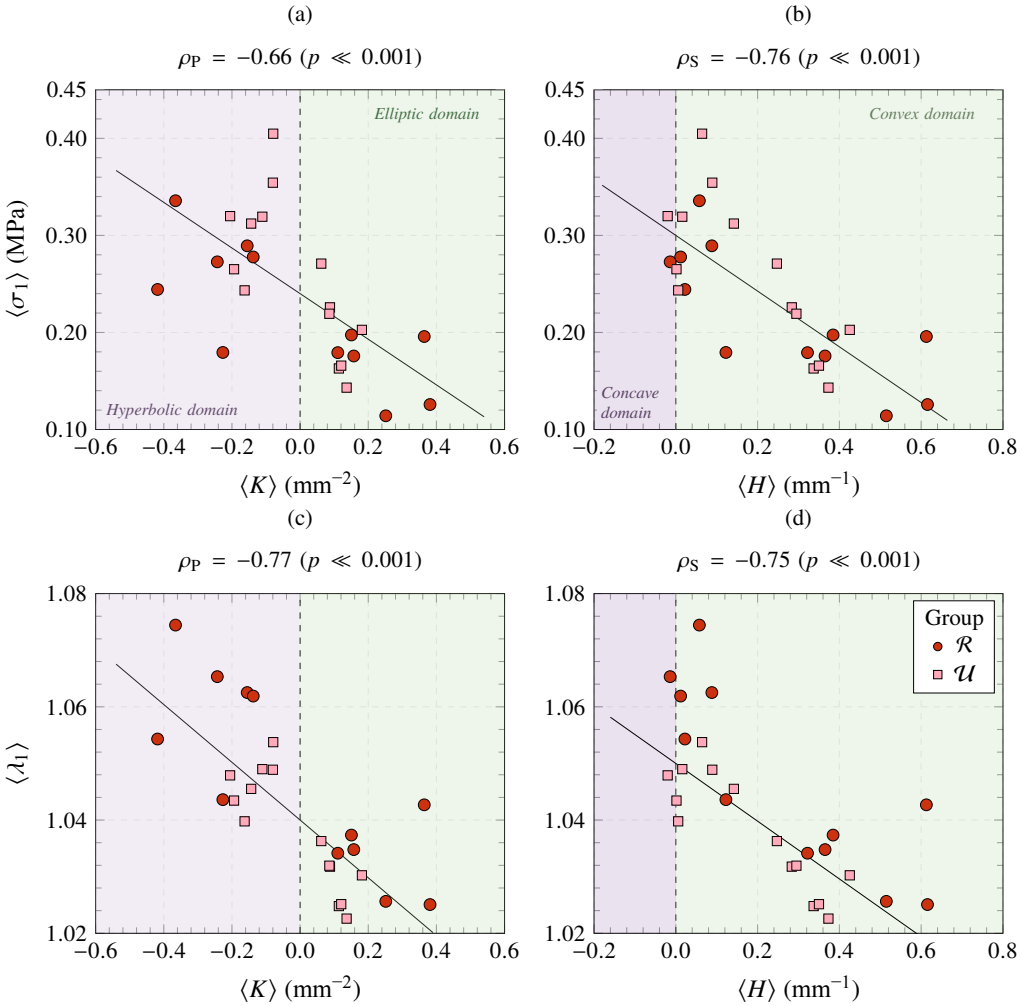

Source: Prepared by the author.

that one of the most important determinants of the largest σ_1 and λ_1 in IAs walls is their wall curvature(s).

Curvature is an intrinsic property of any surface and, consequently, of shells, and it plays an important role in determining the mechanical response of such structures. Laplace's law of membranes, for example, predicts that the tension induced on a membrane is inversely proportional to its principal curvatures and consequently, to their Gaussian and mean curvatures. For thick shells, though, Laplace's laws do not hold (41). IAs walls may be assumed as a thick shell as arteries as well, and, since very early, it has already been argued, based on this fundamental role of curvature in membrane and shell mechanics, that the sac shape — a property intrinsically related to local curvature — could play a more crucial role in the rupture of an IA

than its overall size (56). Nevertheless, and perhaps surprisingly, the sac curvature has been the subject of a small part of all the works related to the disease. A query in the Web of Science® database for published papers with terms related to "intracranial aneurysms" and "numerical simulation" found a percentage of only 2.5 % of items that also mentioned "surface curvature" or "surface shape" as their main topic. This was even smaller, of about 0.32 %, when comparing papers that investigated IAs in general, i.e. not with numerical simulations.

Ma et al. (145) performed a similar analysis than above, although with numerical results based on simulations with static BCs (an uniform pressure applied on the luminal surface) and using as geometry only the IA sac, i.e. without the branches walls. They employed an anisotropic Fung-like material law and found no statistically significant differences for stress and strain between ruptured and unruptured IAs, although they show that their levels in the former group were generally higher, which overall agrees with the findings presented in the previous section, although significant differences were found. More important, the authors also investigated the maximum and minimum curvatures fields and found strong correlations between stress and strain and the curvature. In their discussions, the authors point out that "the nature of the precise geometrical characteristics that correlate to elevated stress levels" need to be further assessed in large studies.

Although the study sample in this work is relatively small compared to general medical studies though (the sample is actually large if compared with numerical studies of IAs wall mechanics) the significant results presented in this chapter directly answer the questions raised by Ma et al. (145) by strongly indicating that the regions of dangerously-high levels of stretch and stress can be identified by looking at the local wall curvature. More specifically, by the regions identified as hyperbolic, i.e. with negative Gaussian curvature. Moreover, in those patches, the largest stretch was significantly higher in ruptured IAs than in unruptured ones. This is probably explained by the fact that ruptured IAs have more lobular regions and blebs (Section 4.2), which by their geometry increases the area of hyperbolic patches locally — the higher prevalence of hyperbolic patches in the $\mathcal{R}$ groups can be seen Fig. 8.4b —, hence further increasing the stretch levels overall on the sac.

The wall curvature also explained the corresponding high levels of σ_1 and λ_1 on the abnormal-hemodynamics and physician-oriented patchings. Clinical observations show that the majority of rupture sites of IAs occur at their dome, although there is a small incidence of rupture at their base, i.e. closer to the neck (192). The dome patch of an IAs is dominated by

elliptic points and most likely to be composed of type-II patches, i.e. with an atherosclerotic phenotype (see Fig. 8.6e and f). By their curvature, these patches are more likely to have relatively low λ_1 and σ_1 levels and, moreover, due to their natural development, be thicker and stiffer, further decreasing the overall values of these variables (see Section I.3). Therefore, other factors may play a role to explain the high prevalence of ruptures on the dome, either related to mechanical or failure properties of the wall. For example, it could be that other mechanical variables played a role in those ruptures, other than stress or stretch. Alternatively, the ultimate stress and ultimate strain at the dome could be smaller, compared to the rest of the sac, due to the natural development of the IA, although no research was found suggesting that. Nevertheless, a realistic scenario that would explain this high incidence of dome ruptures is caused by calcification, which is highly prevalent in human IAs as recent findings suggest (90), especially in atherosclerotic regions of their wall. Further studies show that calcification regions in IAs walls concentrate stress and significantly influence the mechanics locally (91). Unfortunately, to assess this hypothesis, mechanical and imaging analysis of the walls of the IAs used within this work would be necessary to assess calcified zones, but they were not available.

On the other hand, although the incidence of rupture sites on the neck is smaller than on the dome, the mechanical data collected here satisfactorily explains the rupture in these sites based on the local mechanical response. Both λ_1 and σ_1 were comparatively higher on the neck, which is more likely to be dominated by type-I patches, i.e. "red-patches" that are thinner and stiffer, thus slightly increasing both σ_1 and λ_1 (see Section I.3). Nonetheless, failure properties should also be assessed to confirm the likelihood of rupture in that situation. Cebral et al. (80) investigated failure mechanics and the hemodynamics of a sample of eight unruptured IAs and found that the tissue ultimate strain is negatively correlated with time and surface-averaged WSS on the sac lumen. Although their study did not investigated local properties of each IA wall, that trend suggests that, as areas of high WSS get bigger in an IA lumen, smaller will be its tissue ultimate strain. Moreover, with large areas of high WSS, it is also more likely that type-I patches will exist (defined by $TAWSS > 10\,\text{MPa}$ and $OSI < 0.001$), which in turn tend to concentrate hyperbolic areas, inducing the highest stresses and stretches already mentioned. With a small ultimate strain, this situation could well explain a rupture on the neck.

Finally, it is very important to note that, according to the pathways to rupture proposed by Meng et al. (61) (see Fig. 2.7), red-type and atherosclerotic regions may eventually lead to a bleb and/or a thrombus on the IA wall, respectively. Both focal manifestations effectively create

local hyperbolic regions that probably act as stress (and stretch) concentrators in both cases. Two examples are shown in Fig. 8.8 with IA cases of the sample used here. Therefore, further increasing the likelihood of rupture in those situations. Nevertheless, it is important to reinforce that those two mechanisms depend on particularities of an IA failure properties, thus future studies should investigate that.

Figure 8.8 – Examples of (a) an unruptured IA, case urMCA4, with a thrombus or bleb near the neck patch that introduces new local hyperbolic patches on the neck (and, in this case, on the body patch too); and (b) a ruptured IA, case rICA2, harbouring a clear bleb on its dome patch, that also creates new local hyperbolic patches (the white line marks the neck contour and the yellow lines mark the contours between the S_N, S_B, and the S_D patches).

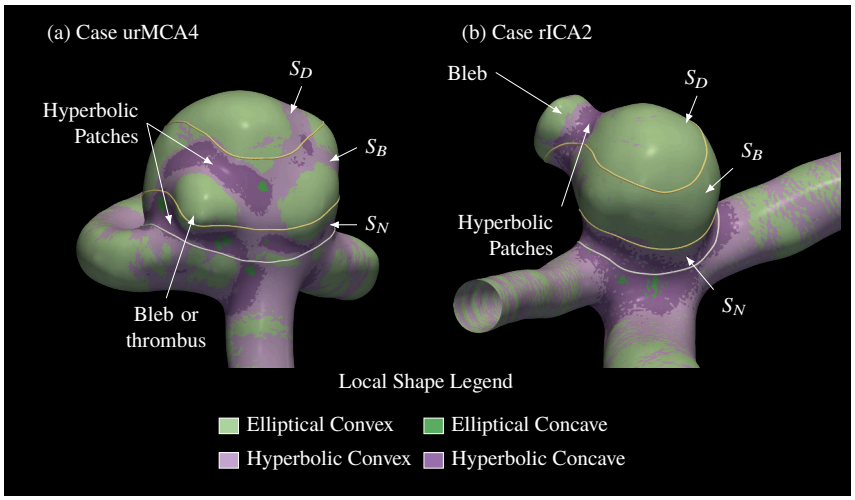

Source: Prepared by the author.

Interestingly too is the curious relationship between the local shape and the abnormal-hemodynamics patches. The data show that, in the sample used here, type-I and type-II patches have larger areas of hyperbolic and elliptic patches, respectively (see Fig. 8.6e and f). Because type-I and type-II patches were defined based on particular hemodynamic environments, this suggests that the local lumen curvature could be a determinant of local hemodynamics. From the fluid mechanics perspective, this is likely because the curvature of a surface is an important parameter that determines the dynamics of the boundary layer adjacent to it. But whether this specifically causes the low-flow and high-flow hemodynamics is harder to assess due to the temporal and spatial complexity of the flow inside an IA. By the time of this writing, no specific study on cardiovascular fluid mechanics was found that investigated this eventual relationship — although there are studies that assessed the influence of arterial path curvature on the WSS of coronary arteries (194), this does not help with intra-aneurysmal local flow. Nevertheless, a recent line of research into the near-wall cardiovascular flows may help in understanding this connection, because it explores the liaison between local wall properties and the WSS field (195). Unfortunately, such an investigation would be beyond the scope of this work. In any

case, a quick analysis of the hemodynamics data of the IA sample used here was performed by computing the surface average of TAWSS and OSI (among others hemodynamic wall parameter (HWP)), and elliptical and hyperbolic patches. The box-plots of such distributions are shown in Fig. 8.9.

Figure 8.9 – Distributions of (a) $\langle TAWSS \rangle$ and (b) $\langle OSI \rangle$ (right) over the surface patches of elliptic and hyperbolic types, for the IA sample segregated by rupture-status groups.

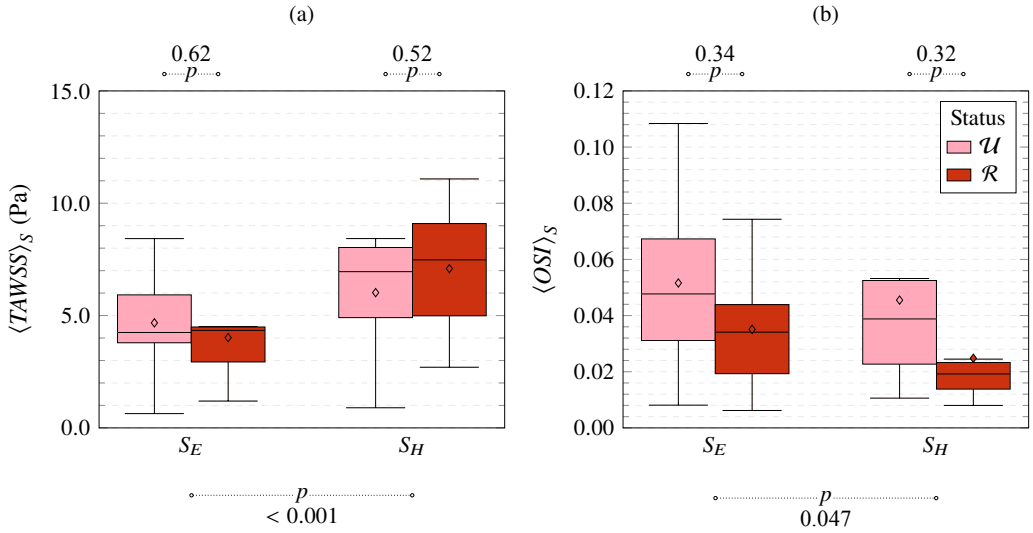

Source: Prepared by the author.

Indeed, the TAWSS was significantly higher on hyperbolic patches than on elliptic ones, whereas the contrary is the case for the OSI. Moreover, no significant differences were found for either $\langle TAWSS \rangle$ or $\langle OSI \rangle$ between groups $\mathcal{R}$ and $\mathcal{U}$. This explains the higher prevalence of type-I patches on hyperbolic patches, although it is important to insist that a causal explanation for this relationship must be the subject of future investigations.

8.4 FURTHER DISCUSSIONS AND SUMMARY

The connections between the mechanical response of IAs walls, their shape and geometry, hemodynamics, and biomechanical and failure properties, described and exemplified in the previous paragraphs, are graphically summarized in the diagrams shown in Fig. 8.10. It embeds the mechanobiological pathways proposed by Meng et al. (61) too, that based the abnormal-wall model of this work. To the author's knowledge, this is the first attempt to categorize IA rupture events based on the actual mechanical response of an IA sample, although unfortunately a relatively small one. It attempts to clarify the role that curvature plays on the mechanics of this disease and, although it does not provide definitive answers, it also helps to find the next questions.

Figure 8.10 – Pathways that could potentially explain the rupture of IAs based on the mechanical response on (a) hyperbolic patches and (b) elliptic patches. The geometrical and biological connections between the different regions and phenotypes of the IA wall are also depicted.

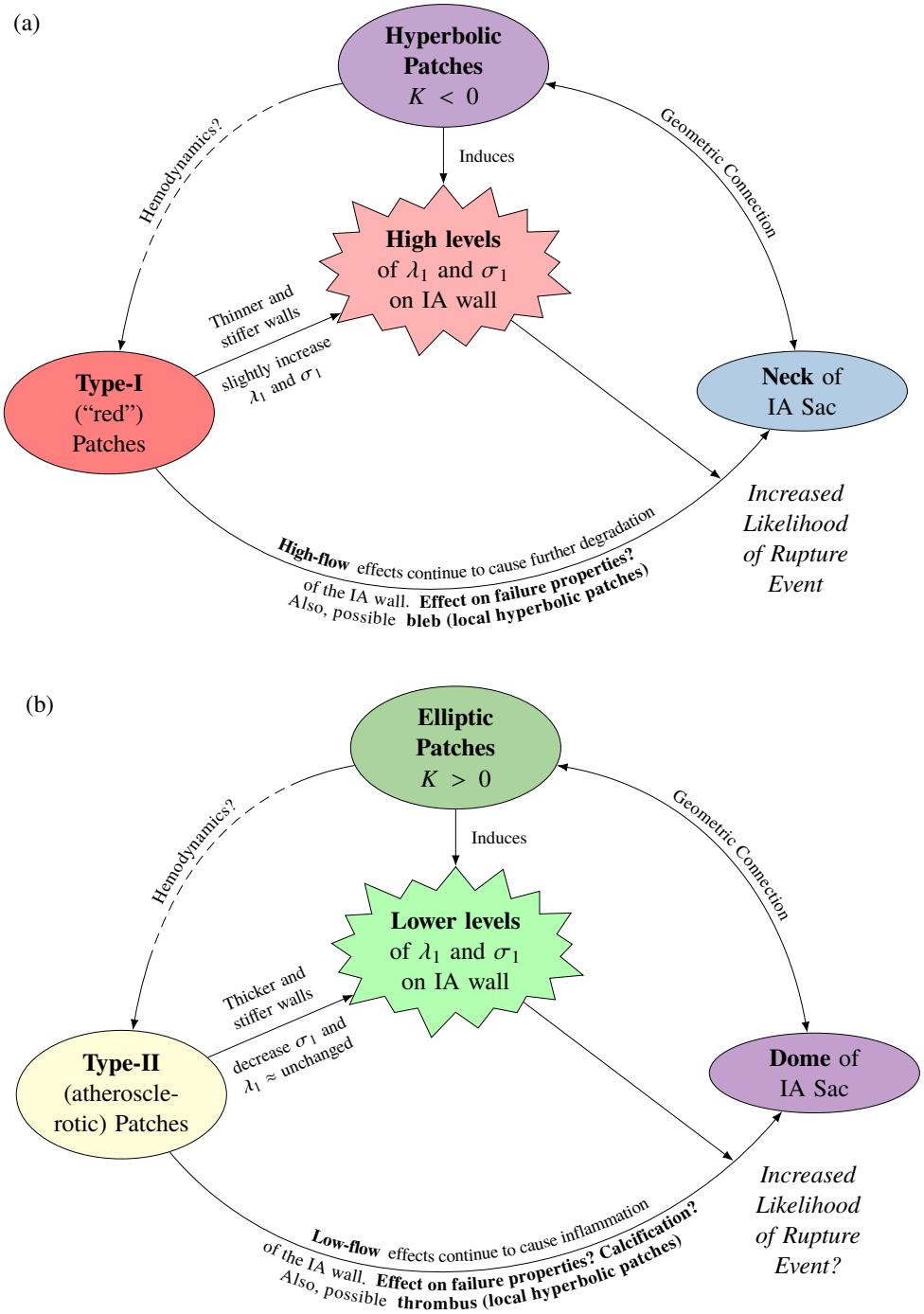

Source: Prepared by the author.

Perhaps one of the most pressing issues is to gather more data on the failure mechanics of IAs, which could well bridge the gap between the mechanical response and more definitive explanations on the rupture of IAs.

Moreover, it is extremely important to highlight that the mechanisms summarized in Fig. 8.10

must not be regarded in a static way, i.e. for an instant in time. On the contrary, due to the evolving nature of an IA, these mechanisms are certainly acting constantly in different regions of the sac wall.

As highlighted in the introduction of this work, one of the most intriguing facts about IAs is that they can rupture while still small — they account for approximately 50 % of the ruptured cases according to reports (25). The important action of the curvature in determining the mechanical response provides an explanation for this fact, because the hyperbolic patches may occur at any time of the natural history of an IA, independently of its size. Indeed, note that hyperbolic patches are dominant on the neck of the IA and, rigorously, the neck is the first indication of the IA inception. Therefore since early in an IA history, the local level of stretch and stress may already be high on the neck, compared to its surrounding arteries.

Chapter 9

CONCLUSIONS AND FUTURE DIRECTIONS

9.1 OVERVIEW

In summary, the main findings reported in the previous two chapters are:

- Changing the hyperelastic laws or the wall morphology models had a relatively negligible effect on the stress field compared to the stretch fields, for which significant differences were found according to different hyperelastic laws. This may indicate that, although stresses are indeed statically determined to a certain point, stretches may not be in the sense that the deformations are more affected by different modelings. More specifically, the large differences in stretch were found mainly on ruptured aneurysms and, in part, related to the softer mechanical properties used for ruptured aneurysms, that clearly affected the stretch levels.

- The largest levels of stress and stretch were found near the lumen side and further decreased along the thickness of the wall from the luminal to the abluminal surfaces.

- Ruptured IAs had a significantly higher maximum stretch compared to unruptured ones, whereas the stress levels were not significantly different between the two groups — although, surprisingly, the stress levels were slightly higher on unruptured aneurysms. This indicates that deformation-related properties of the wall may indicate rupture.

- The curvature of the sac luminal surface was the most significant determinant of local stress and stretch. Moreover, the higher stretch levels reported in the previous chapter were located on hyperbolic (negative Gaussian curvature) patches only, although the same was not the case on elliptic ones, suggesting that hyperbolic patches of an IA wall are probable regions where rupture is more likely to occur.

- The lumen curvature was also connected with abnormal-hemodynamics conditions that are responsible for affecting the mechanical integrity of the wall, further increasing, in certain situations, the likelihood of rupture.

The main sources of the potential usefulness of each of these were discussed in the previous two chapters and are related to both a more complete understanding of the fundamental physics behind the motion of IAs walls, thus into a better understanding of their rupture, but also into stimulating further and larger computational studies with IA geometries. These results can be of use to biomedical engineers and, most probably, to physicians who research and treat this disease. Regarding the latter group, it is not only important to improve the understanding of the mechanics of IAs, but also in how to translate those very specific findings into ways to predict the likelihood of rupture of a single IA. Furthermore, important questions that needed answers were also identified, some connected with limitations of this work. These issues are addressed in the following sections.

9.2 NUMERICAL SIMULATIONS AND IAs

The flexibility and reliability of numerical techniques have made it a tool of widespread use to study IAs, in general. It definitely helped to further understand the disease, although it also raised some concerns, further becoming a debatable topic in the clinical practice (101, 100). Clearly, numerical techniques have their limitations and the cure for it is further researches and incrementally gathering more data on the subject. The findings of this work goes in that direction by ultimately showing that numerical simulations are a source of powerful information on an IA wall mechanics.

From a practical perspective, assessing the impact of different hyperelastic laws, wall thickness and material properties modeling allow that a suitable and simpler modelings be chosen for large cohort studies in view of the difficulties of modeling the wall tissue and its motion. This simplified modeling could be reliably used to investigate average quantities over the IAs sacs. Moreover, this would keep the computational times small by selecting a model with smaller computating times (see Table 6.1, for example). It is important to note, though, that because numerical simulations are not used by the medical community directly, these findings should be more relevant for researchers that use numerical methods in future studies of the IA wall.

9.3 RELEVANCE OF THE FINDINGS TO THE MEDICAL COMMUNITY

The fact that stretches were significantly higher in ruptured cases is probably more directly important to the medical practice. It suggests at looking on displacements, strains, and stretch patterns for qualitative assessments of the likelihood of rupture. Time-resolved 3D imaging techniques, such as four-dimensional (4D) computational tomography angiography (CTA), were recently used to measure the displacement and pulsatility of IAs walls *in-vivo* (196, 197). This could lead to assessing the likelihood of rupture from these examinations, as they become more common in the medical practice.

Perhaps the most important finding for the medical community is the essential role played by the curvature in locating the patches with higher stress and stretch. The curvature of the wall can be readily calculated from medical imaging examinations routinely performed in the diagnostics of IAs. Therefore, physicians should be aware of this important relationship and take this into consideration in their prognostics, although, obviously, combined with other clinical information that they already use. Currently, this is somewhat accounted for based on the known observation that aneurysms with lobular regions or blebs are more likely to rupture (155, 156). But, more importantly, this finding also points to identifying curvature-based IA sac metrics to help predict the rupture.

As pointed out in the previous chapter, few attempts have been made in this direction. Curvature-based metrics were introduced, in the context of saccular IAs, primarily by Ma et al. (157) with four indices computed as surface-averages and L2-norms of K and H — labeled *GAA*, *MAA*, *GLN*, and *MLN* (the "AA" and "LN" stand for "area-average" and "L2-norm", respectively. See Section A.1 of Appendix A for their mathematical definitions). All of them give an overall measure of the curvature of an IA sac, but the *MAA* and *GAA* depend on both size and shape, whereas *MLN* and *GLN* depend only on the shape. For completeness with the morphological characterization presented in Section 4.2, they were also computed for the sample used here (see Table 9.1).

As pointed out by Ma et al. (157), these values are easier to interpret only in a relative basis. For example, the *GLN* was defined so that it is equal to the unity for a sphere, hence the means in Table 9.1 indicate that the unruptured IAs are more similar to a sphere compared to the ruptured ones, i.e. the latter have more saddle patches, as already suggested by inspecting other shape metrics. The differences between the means of groups $\mathcal{R}$ and $\mathcal{U}$, though, were only statistically significant for the *MLN* ($p = 0.02$), whereas for *GLN* it was not ($p = 0.091$). Similar results

Table 9.1 – Means and SD of curvature-based metrics introduced by Ma et al. (157) for the ruptured ($\mathcal{R}$) and unruptured ($\mathcal{U}$) subgroups.

Index	$\mathcal{R}$	$\mathcal{U}$
MAA (mm^{-1})	0.33 ± 0.09	0.270 ± 0.057
GAA (mm^{-2})	0.059 ± 0.037	0.052 ± 0.029
GLN	2.98 ± 1.07	2.080 ± 0.678
MLN	0.340 ± 0.038	0.290 ± 0.025

Source: Prepared by the author.

were reported by Raghavan et al. (33), who assessed the potential to discriminate ruptured IAs by size, shape, and curvature-based indices, including the *MLN* and *GLN*. The authors found that the *UI*, *EI*, *NSI*, *AR*, and *MLN* were statistically significantly different between their sample's $\mathcal{R}$ and $\mathcal{U}$ groups — in the sample used here, only the aspect ratio was not significantly different between groups $\mathcal{R}$ and $\mathcal{U}$. The authors conclude that shape is probably more effective than size alone in indicating rupture potential.

How are these indices connected to the actual mechanics of an IA wall? No assessment of the correlations between the curvature-based metrics (or the shape ones) and the mechanical variables have been found in the literature. By investigating the relationship between all the size, shape, and curvature-based metrics and the σ_{1max} and λ_{1max} over S^{l}_{ia} of the sample used here, statistically significant correlations were only found between λ_{1max} and both *GLN* and *MLN*, and , surprisingly, between σ_{1max} and the maximum dome diameter, d_d (see Fig. 9.1). Therefore, although previous works and the current one found that shape indices statistically identified ruptured aneurysms, the actual stretches were significantly correlated with the curvature-based metrics only. The same was not the case for the stress, although interestingly σ_{1max} increased with the overall size of the aneurysm. Therefore, curvature-based metrics are more likely to bridge the geometry of a patient-specific IAs and its motion mechanics, hence potentially acting as an indicator of rupture.

The correlation between stretch and *MLN* and *GLN* can be explained by the high stretch levels found in hyperbolic patches, and thus connected to the correlations found between surface-average stretch and the Gaussian and mean curvatures (see Fig. 8.7c and d). In larger areas of the sac with negative, and high in absolute terms, Gaussian curvature tends to increase *GLN* and, mechanically, produce large stretch levels, explaining the correlations. Although it is important to highlight that significant correlations were only found for the maximum over the IA lumen, and not other metrics. Nevertheless, this finding further reinforces the potential use

Figure 9.1 – Correlation plots between λ_{1max} in S^{l}_{ia} and (a) *GLN* and (b) *MLN*, and (c) between the σ_{1max} and maximum dome diameter, d_d. Pearson's correlation coefficient and the p-values are shown above each plot. The regression lines were computed with linear regression using Python's library SciPy.

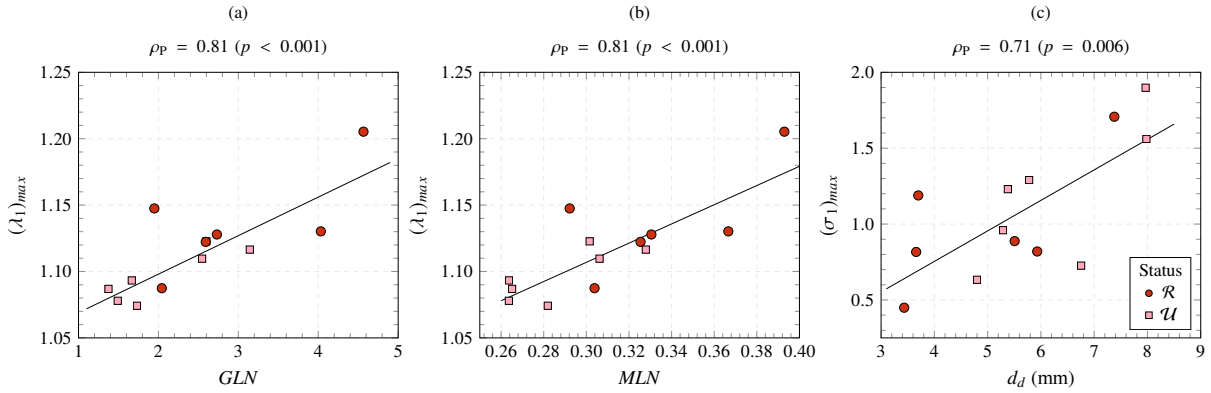

Source: Prepared by the author.

of curvature-based metrics for rupture assessment. The lack of significant correlations between the stretch levels and the other shape metrics should be further investigated, though. It could be that the shape metrics, like the undulation index, are not directly influenced by the hyperbolic patches as the curvature-based ones are, hence not leading to significant correlations with the maximum stretch. It could also be explained by the relatively small sample size used, thus the other shape metrics should be further investigated in larger studies.

Interestingly enough was the increase in σ_{1max} with the maximum diameter. This relationship should be further explored in larger studies too once the mechanisms behind failure are further understood because it could also indicate an IA near a ruptured state, although, as seen in the previous chapter, an indication of larger stresses on the wall was not directly connected with ruptured aneurysms. Furthermore, this relationship is probably a manifestation of the statically determined nature of σ_1 for IAs, suggested by the results in Chapter 7, where the stresses on a membrane are proportional to the diameter of the membrane.

Finally, if sac metrics are to be used to predict the likelihood of rupture of an IA, the curvature-based ones, more specifically, *MLN* and *GLN*, should be the subjects of further studies in the future. They could be added, for example, to the group of metrics used in those studies that searched for a "score" that would predict the likelihood of rupture, such as the ones mentioned in Section 2.1.1 (see Eq. (2.1), for example). Additionally, other metrics could also be proposed that more directly reflected the larger levels of stress and stretch on highly-curved hyperbolic patches.

9.4 LIMITATIONS OF THIS STUDY AND FUTURE DIRECTIONS

The use of the 1WFSI numerical strategy, instead of the two-way fluid-solid interaction (2WFSI), is a clear limitation of this study because it eliminates the full couple between the wall motion and the flow domain. As can be seen in the discussion in Appendix B, partitioned FSI techniques are improving and thus more robust numerical solvers capable of robustly solving strongly coupled problems may emerge in the near future. These could be used to solve larger cohorts of IA geometries. Having said that, the actual impact of the volumetric change of the flow domain is hard to assess without actually simulating 2WFSI for at least a few geometries. A comparison with other studies revealed that the magnitudes of stress and stretch found here are similar. But is important to mention that there are no common choices of BCs and other modeling aspects among works with IAs, therefore these comparisons are limited in what they can tell. Furthermore, as mentioned in Section 3.2, those studies focused on the impact of the wall flexibility on the hemodynamics, and not the other way around.

Additionally, using a fully-coupled FSI strategy would also allow to investigate the connections between wall curvature and near-wall hemodynamics in IAs. Different blood modeling should be investigated too after reports suggesting the occurrence of transitional flow (198) or flow instabilities (199) at much smaller Reynolds number inside the sac of IAs, although there is still controversy in the literature about such phenomena in IAs flow. Transitional or turbulent flow inside an IA sac would likely to alter the motion patterns of its sac wall.

The relatively small number of IA geometries simulated also limits the generality of the main conclusions, nonetheless, the sample was large enough to obtain statistically significant results for the main findings. Also, it is important to note that the sample size was actually small compared to large cohort studies that rarely involved numerical simulations of the wall motion. Compared to the latter case, the sample size was actually large. Nevertheless, the reproduction of this work in other studies with larger samples is encouraged due to the intrinsic variability of the disease.

Despite this work has been partly about the assessment of different modeling aspects of IAs walls, a few other considerations on the wall modeling needed careful treatment or extreme simplification. For example, the peri-aneurysmal environment was completely ignored for lack of information on the IAs surrounding tissue in the images used — specific examinations would have to be taken to identify those structures. Furthermore, if the peri-aneurysmal environment was to be accounted for in the simulations, it would further pose its own difficulties because, as is

the case with arteries and IA tissue, the mechanical properties of peri-aneurysmal environment tissues are just as unknown as IAs ones. Because the effect of the peri-aneurysmal environments in the mechanics of IAs is still poorly understood, the best alternative found was to use a consistent BC among all cases on the outer wall surface.

Other important modeling aspects are the incompressibility of the solid wall and the BC applied at the artificial branch sections BCs that were addressed here by means of parametric studies (presented in Appendix I). Regarding the tissue incompressibility, the values of the Jacobian, J, recorded in the simulations, independently of the model chosen, ranged from 0.97 to 1.09 l along the cardiac cycle, characterizing the motion as nearly-incompressible (these extremes occurred with the MR and Yeoh laws, respectively, both with the abnormal-wall model model). Nevertheless, based on the results of the parametric study with a higher Poisson ratio, further approaching the incompressibility limit would change stress and stretch by approximately, or less, than 2 %, thus hardly changing our main conclusions. To deal with the incompressibility of soft tissues, in general, more robust and faster solvers should be used in the future.

Additionally, only isotropic hyperelastic laws were employed based on evidence that anisotropic laws yield similar mechanical responses compared to their isotropic versions (146). Nevertheless, the tissue of arteries and IAs are anisotropic, and this feature should be included in future works to further assess its influence on the wall mechanics.

Finally, another probable relevant effect on the tissue properties would come from fatigue due to the cyclical nature of the forces acting on the wall. Its effect on soft tissues, though, is still poorly understood and few models of it exists (200), especially for IAs, although some reports argued that it could be the dominant cause of their failure. This should also be addressed in future works. Fatigue would also have an effect on the failure mechanics of IAs, although before understanding this effect, it is more pressing to actually measure these failure properties because, as argued in this work, further understanding the rupture by modeling and computing the complete mechanical response of patient-specific IA also requires the failure properties of the wall, but scarce experimental (and numerical) data exist on it. It is hard to measure the failure properties of tissue *in-vivo*, but future studies should further investigate possible ways to perform it.

9.5 CONCLUDING REMARKS

First, this work provides perhaps one of the first attempts to more thoroughly understand the impact of several modeling choices on the mechanical response of the wall of patient-specific IAs via numerical techniques. Second, that mechanical response was the subject of further investigations by comparing ruptured and unruptured aneurysms, shedding light on the patches of their wall that could be nearing a state of rupture. This led to findings that could potentially guide future studies into a better understanding of the rupture event and, furthermore, suggestions for metrics to be used in that endeavor were also presented, hence bridging the gap between physics and medical practice.

Finally, although of foremost importance, this work is yet another example of how numerical techniques are tools that can help in further understanding the physics of this dangerous, silent, and often fatal disease. They should continue to be used to that end and gradually in the future could be included in the medical practice, but of course with warnings of its limitations, simplifications, and complexities, specially because these could be overcome.

Chapter 10

THESIS OUTCOME

PENDING JOURNAL PAPERS

- OLIVEIRA, I. L. et al. **A Numerical Investigation of the Mechanics of Intracranial Aneurysms Walls: Assessing the Influence of Tissue Hyperelastic Laws and Heterogeneous Properties on the Stress and Stretch Fields**. May 2022 (based on Chapter 7; submitted to *Journal of the Mechanical Behavior of Biomedical Materials* and currently under review).

- Chapter 8 also presents relevant findings that should be submitted to the scientific community. A manuscript based on it was being written by the author at the time of writing this document.

PUBLISHED JOURNAL PAPERS

- OLIVEIRA, I. L. et al. A Longitudinal Study of a Lateral Intracranial Aneurysm: Identifying the Hemodynamic Parameters behind Its Inception and Growth Using Computational Fluid Dynamics. **Journal of the Brazilian Society of Mechanical Sciences and Engineering**, Heidelberg, v. 43, p. 138, 2021. DOI: 10.1007/s40430-021-02836-6

- OLIVEIRA, I. L. et al. Non-Newtonian Blood Modeling in Intracranial Aneurysm Hemodynamics: Impact on the Wall Shear Stress and Oscillatory Shear Index Metrics for Ruptured and Unruptured Cases. **Journal of Biomechanical Engineering**, New York, v. 143, n. 7, p. 071006, 2021. DOI: 10.1115/1.4050539

CONFERENCES

- OLIVEIRA, I. L. et al. Effect of Blood Rheology Model on Hemodynamic Parameters Related to Intracranial Aneurysm Rupture. In: 17TH Brazilian Congress of Thermal Sciences and Engineering. Águas de Lindóia, SP, Brazil: ABCM, 2018. DOI: 10.26678/ABCM.ENCIT2018.CIT18-0761

- OLIVEIRA, I. L. et al. Hemodynamic and Morphological Case Study of an Intracranial Aneurysm Initiation and Evolution. In: ABCM INTERNATIONAL CONGRESS of Mechanical Engineering. Uberlândia, MG, Brazil, 2019. DOI: 10.26678/ABCM.COBEM2019.COB2019-0516

- OLIVEIRA, I. L. et al. Implementation and Numerical Verification of an Incompressible Three-Parameter Mooney-Rivlin Model for Large Deformation of Soft Tissues. In: 15TH OpenFOAM Workshop. Washington, DC, USA, 2020

- OLIVEIRA, I. et al. Semicoupled Numerical Strategy to Solve Large-Strain Motion of Incompressible Hyperelastic Materials. In: 16TH OpenFOAM Workshop. Dublin, Ireland, 2021. p. 2

- OLIVEIRA, I. L. et al. On the Influence of the Wall Thickness Heterogeneity in the Mechanics of Intracranial Aneurysms. In: PROCEEDINGS of the 26th International Congress of Mechanical Engineering. ABCM, 2021. DOI: 10.26678/ABCM.COBEM2021.COB2021-0451

COMPUTATIONAL CODES

Apart from the new models implemented and currently available in solids4foam (see Section 6.2 and Fig. 6.1), all the pre and post-processing of the data used in this work were performed in the code developed by the author and openly available in GitHub https://github.com/iagolessa/vmtk4aneurysms under the GNU General Public License v3.0 (207).

REFERENCES

1 WALT, S. van der; SMITH, N. **MPL Colormaps**. 2020. https://bids.github.io/colormap/.

2 CRAMERI, F. **Scientific colour maps**. 2021. www.fabiocrameri.ch/colourmaps/.

3 PARAVIEW. **ParaView Website**. 2017. https://www.paraview.org/. [Accessed 26-June-2017].

4 CYNTHIA BREWER MARK HARROWER, P. S. U. **Color Brewer**. 2022. https://colorbrewer2.org.

5 TOL, P. **Paul Tol's Notes: Colour schemes and templates**. 2022. https://personal.sron.nl/~pault/.

6 CRAMERI, F.; SHEPHARD, G. E.; HERON, P. J. The Misuse of Colour in Science Communication. **Nature Communications**, London, v. 11, n. 1, p. 5444, Dec. 2020. DOI: 10.1038/s41467-020-19160-7.

7 THYNG, K. M.; COMBA, J. The Importance of Colormaps. **Computing in Science & Engineering**, Piscataway, v. 22, n. 5, p. 96–102, Sept. 2020. DOI: 10.1109/MCSE.2020.3006946.

8 DIAGBOUGA, M. R. et al. Role of Hemodynamics in Initiation/Growth of Intracranial Aneurysms. **European Journal of Clinical Investigation**, Chichester, v. 48, p. 1–12, 2018. DOI: 10.1111/eci.12992.

9 CEBRAL, J. R.; RASCHI, M. Suggested Connections between Risk Factors of Intracranial Aneurysms: A Review. **Annals of Biomedical Engineering**, New York, v. 41, n. 7, p. 1366–1383, 2013. DOI: 10.1007/s10439-012-0723-0.

10 THE INTERNATIONAL STUDY OF UNRUPTURED INTRACRANIAL ANEURYSMS INVESTIGATORS. Unruptured Intracranial Aneurysms: Natural History, Clinical Outcome, and Risks of Surgical and Endovascular Treatment. **Lancet**, London, v. 362, p. 103–110, 2003.

11 KENHUB. **KenHub Website**. 2017. https://www.kenhub.com/. [Accessed 16-June-2017].

12 VLAK, M. H. M. et al. Risk of Rupture of an Intracranial Aneurysm Based on Patient Characteristics: A Case-Control Study. **Stroke**, Philadelphia, v. 44, n. 5, p. 1256–1259, 2013. DOI: 10.1161/STROKEAHA.111.000679.

13 SAQR, K. M. et al. What Does Computational Fluid Dynamics Tell Us about Intracranial Aneurysms? A Meta-Analysis and Critical Review. **Journal of Cerebral Blood Flow and Metabolism**, London, v. 0, n. 0, p. 1–19, 2019. DOI: 10.1177/0271678X19854640.

14 MALMIVAARA, K. et al. Health-Related Quality of Life and Cost-Effectiveness of Treatment in Subarachnoid Haemorrhage. **European Journal of Neurology**, Chichester, v. 19, n. 11, p. 1455–1461, 2012. DOI: 10.1111/j.1468-1331.2012.03744.x.

15 QURESHI, A. I. et al. Comparison of Endovascular and Surgical Treatments for Intracranial Aneurysms: An Evidence-Based Review. **Lancet**, London, v. 6, n. 9, p. 816–825, 2007. DOI: 10.1016/S1474-4422(07)70217-X.

16 THE INTERNATIONAL STUDY OF UNRUPTURED INTRACRANIAL ANEURYSMS INVESTIGATORS. Unruptured Intracranial Aneurysms - Risk of Rupture and Risks of Surgical Intervention. **The New England Journal of Medicine**, Waltham, v. 339, n. 24, p. 1725–1733, 1998.

17 FRÖSEN, J. Smooth Muscle Cells and the Formation, Degeneration, and Rupture of Saccular Intracranial Aneurysm Walla Review of Current Pathophysiological Knowledge. **Translational Stroke Research**, New York, v. 5, n. 3, p. 347–356, June 2014. DOI: 10.1007/s12975-014-0340-3.

18 VAN GIJN, J. et al. Subarachnoid Haemorrhage: Diagnosis, Causes and Management. **Brain: a journal of neurology**, Oxford, v. 124, Pt 2, p. 249–78, 2001. DOI: 10.1093/brain/124.2.249.

19 VAN GIJN, J. et al. Subarachnoid Haemorrhage. **Lancet**, London, v. 369, n. 9558, p. 306–318, 2007. DOI: 10.1016/S0140-6736(07)60153-6.

20 ZACHARIA, B. E. et al. Epidemiology of Aneurysmal Subarachnoid Hemorrhage. **Neurosurgery Clinics of North America**, Philadelphia, v. 21, p. 221–233, 2010. DOI: 10.1016/j.nec.2009.10.002.

21 HOP, J. W. et al. Case-Fatality Rates and Functional Outcome after Subarachnoid Hemorrhage: A Systematic Review. **Stroke**, Philadelphia, v. 28, n. 3, p. 660–664, Mar. 1997. DOI: 10.1161/01.STR.28.3.660.

22 FORBES, G. et al. Interobserver Variability in Angiographic Measurement and Morphologic Characterization of Intracranial Aneurysms: A Report from the International Study of Unruptured Intracranial Aneurysms. **American Journal of Neuroradiology**, Oak Brook, v. 17, p. 1407–1415, 1996.

23 WONG, G. K. C.; POON, W. S.; WONG, G. K. C. Current Status of Computational Fluid Dynamics for Cerebral Aneurysms: The Clinician's Perspective. **Journal of Clinical Neuroscience**, Oxford, v. 18, p. 1285–1288, 2011. DOI: 10.1016/j.jocn.2011.02.014.

24 TORII, R. et al. Fluid-Structure Interaction Modeling of Aneurysmal Conditions with High and Normal Blood Pressures. **Computational Mechanics**, Heidelberg, v. 38, p. 482–490, 2006. DOI: 10.1007/s00466-006-0065-6.

25 ZHENG, J. et al. Small Ruptured Intracranial Aneurysms: The Risk of Massive Bleeding and Rebleeding. **Neurological Research**, Abingdon, v. 41, n. 4, p. 312–318, Apr. 2019. DOI: 10.1080/01616412.2018.1563737.

26 LEEMANS, E. L. et al. Intracranial Aneurysm Growth: Consistency of Morphological Changes. **Neurosurgical Focus**, Meadows, v. 47, p. 1–9, 2019. DOI: 10.3171/2019.4.focus19332.

27 LEVITT, M. R. et al. One Way to Get There. **Journal of NeuroInterventional Surgery**, London, v. 13, n. 5, p. 401–402, 2021.

28 ETMINAN, N. et al. The Unruptured Intracranial Aneurysm Treatment Score: A Multidisciplinary Consensus. **Neurology**, Philadelphia, v. 85, n. 10, p. 881–889, Sept. 2015. DOI: 10.1212/WNL.0000000000001891.

29 RAJABZADEH-OGHAZ, H. et al. A Data-Driven Model to Identify High-Risk Aneurysms and Guide Management Decisions: The Rupture Resemblance Score. **Journal of Neurosurgery**, Meadows, v. 135, n. 1, p. 9–16, Sept. 2020. DOI: 10.3171/2020.5.JNS193264.

30 WEIR, B. et al. The Aspect Ratio (Dome/Neck) of Ruptured and Unruptured Aneurysms. **Journal of neurosurgery**, Meadows, v. 99, n. 3, p. 447–451, 2003. DOI: 10.3171/jns.2003.99.3.0447.

31 JUVELA, S.; KORJA, M. Intracranial Aneurysm Parameters for Predicting a Future Subarachnoid Hemorrhage: A Long-Term Follow-up Study. **Neurosurgery**, Cary, v. 81, n. 3, p. 432–440, 2017. DOI: 10.1093/neuros/nyw049.

32 RAHMAN, M. et al. Size Ratio Correlates with Intracranial Aneurysm Rupture Status: A Prospective Study. **Stroke**, Philadelphia, v. 41, p. 916–920, 2010. DOI: 10.1161/STROKEAHA.109.574244.

33 RAGHAVAN, M. L.; MA, B.; HARBAUGH, R. E. Quantified Aneurysm Shape and Rupture Risk. **Journal of Neurosurgery**, Meadows, v. 102, n. 2, p. 355–362, 2005. DOI: 10.3171/jns.2005.102.2.0355.

34 GREVING, J. P. et al. Development of the PHASES Score for Prediction of Risk of Rupture of Intracranial Aneurysms: A Pooled Analysis of Six Prospective Cohort Studies. **Lancet**, London, v. 13, p. 59–66, 2014. DOI: 10.1016/S1474-4422(13)70263-1.

35 FUNG, Y. C. **Biomechanics: Mechanical Properties of Living Tissues**. 2nd: Springer, 1998. p. 568. DOI: 10.1097/00024382-199802000-00018.

36 SOCHI, T. **Non-Newtonian Rheology in Blood Circulation**. 2013. p. 1–26. arXiv: 1306.2067.

37 CAMPO-DEAÑO, L.; OLIVEIRA, M. S. N.; PINHO, F. T. A Review of Computational Hemodynamics in Middle Cerebral Aneurysms and Rheological Models for Blood Flow. **Applied Mechanics Reviews**, New York, v. 67, 2015. DOI: 10.1115/1.4028946.

38 KANYANTA, V. **Towards Early Diagnosis of Atherosclerosis: Accurate Prediction of Wall Shear Stress**. 2009. PhD thesis.

39 COKELET, G. R. et al. The Rheology of Human BloodMeasurement near and at Zero Shear Rate. **Journal of Rheology**, Pennsylvania, v. 7, n. 1, p. 303, 1963. DOI: 10.1122/1.548959.

40 ROBERTSON, A. M.; SEQUEIRA, A.; OWENS, R. G. Rheological Models for Blood. In: CARDIOVASCULAR Mathematics. Modeling and Simulation of the Circulatory System. Springer, 2009. p. 211–241.

41 FUNG, Y.-C. **Biomechanics - Mechanical Properties of Living Tissues**. New York, NY: Springer New York, 1993. DOI: 10.1007/978-1-4757-2257-4.

42 FISHER, C.; ROSSMANN, J. S. Effect of Non-Newtonian Behavior on Hemodynamics of Cerebral Aneurysms. **Journal of Biomechanical Engineering**, New York, v. 131, p. 091004/1–9, 2009. DOI: 10.1115/1.3148470.

43 SHIBESHI, S. S.; COLLINS, W. E. The Rheology of Blood Flow in a Branched Arterial System with Three-Dimensional Model: A Numerical Study. **Applied Rheology**, Berlin, v. 15, n. 6, p. 398–405, 2005. DOI: 10.1017/S1727719100002951.

44 THURSTON, G. B. Rheological Parameters for the Viscosity, Viscoelasticity and Thixotropy of Blood. **Biorheology**, Amsterdam, v. 16, p. 149–162, 1979.

45 GIJSEN, F. J. H.; VAN DE VOSSE, F. N.; JANSSEN, J. D. The Influence of the Non-Newtonian Properties of Blood on the Flow in Large Arteries: Steady Flow in a Carotid Bifurcation Model. **Journal of Biomechanics**, Oxford, v. 32, n. 6, p. 601–8, 1999. DOI: 10.1016/S0021-9290(99)00015-9.

46 CHEN, J.; LU, X. Y. Numerical Investigation of the Non-Newtonian Blood Flow in a Bifurcation Model with a Non-Planar Branch. **Journal of Biomechanics**, Oxford, v. 37, n. 12, p. 1899–1911, 2004. DOI: 10.1016/j.jbiomech.2004.02.030.

47 BERNSDORF, J.; WANG, D. Non-Newtonian Blood Flow Simulation in Cerebral Aneurysms. **Computers and Mathematics with Applications**, Oxford, v. 58, n. 5, p. 1024–1029, 2009. DOI: 10.1016/j.camwa.2009.02.019.

48 PERKTOLD, K.; RESCH, M.; FLORIAN, H. Pulsatile Non-Newtonian Flow Characteristics in a Three-Dimensional Human Carotid Bifurcation Model. **Journal of Biomechanical Engineering**, New York, v. 113, n. 4, p. 464–75, 1991. DOI: 10.1115/1.2895428.

49 VALENCIA, A. et al. Non-Newtonian Blood Flow Dynamics in a Right Internal Carotid Artery with a Saccular Aneurysm. **International Journal for Numerical Methods in Fluids**, Oxford, v. 50, July 2005, p. 751–764, 2006. DOI: 10.1002//d.1078.

50 XIANG, J. et al. Newtonian Viscosity Model Could Overestimate Wall Shear Stress in Intracranial Aneurysm Domes and Underestimate Rupture Risk. **Journal of NeuroInterventional Surgery**, London, v. 4, p. 351–357, 2012. DOI: 10.1136/neurintsurg-2011-010089.

51 EVJU, O.; VALEN-SENDSTAD, K.; MARDAL, K.-A. A Study of Wall Shear Stress in 12 Aneurysms with Respect to Different Viscosity Models and Flow Conditions. **Journal of Biomechanics**, Oxford, v. 46, p. 2802–2808, 2013. DOI: 10.1016/j.jbiomech.2013.09.004.

52 CASTRO, M. A. et al. Unsteady Wall Shear Stress Analysis from Image-Based Computational Fluid Dynamic Aneurysm Models under Newtonian and Casson Rheological Models. **Medical and Biological Engineering and Computing**, Heidelberg, v. 52, p. 827–839, 2014. DOI: 10.1007/s11517-014-1189-z.

53 HIPPELHEUSER, J. E. et al. Realistic Non-Newtonian Viscosity Modelling Highlights Hemodynamic Differences between Intracranial Aneurysms with and without Surface Blebs. **Journal of Biomechanics**, Oxford, v. 47, p. 3695–3703, 2014. DOI: 10.1016/j.jbiomech.2014.09.027.

54 OLIVEIRA, I. L. et al. Non-Newtonian Blood Modeling in Intracranial Aneurysm Hemodynamics: Impact on the Wall Shear Stress and Oscillatory Shear Index Metrics for Ruptured and Unruptured Cases. **Journal of Biomechanical Engineering**, New York, v. 143, n. 7, p. 071006, 2021. DOI: 10.1115/1.4050539.

55 HOLZAPFEL, G. A.; GASSER, T. C.; OGDEN, R. W. A New Constitutive Framework for Arterial Wall Mechanics and a Comparative Study of Material Models. **Journal of Elasticity**, Dordretch, v. 61, n. 1-3, p. 1–48, 2000. DOI: 10.1023/A:1010835316564.

56 HUMPHREY, J. D.; CANHAM, P. B. Structure, Mechanical Properties, and Mechanics of Intracranial Saccular Aneurysms. **Journal of Elasticity**, Dordretch, v. 61, p. 49–81, 2000.

57 FRÖSEN, J. et al. Flow-Induced, Inflammation-Mediated Arterial Wall Remodeling in the Formation and Progression of Intracranial Aneurysms. **Neurosurgical Focus**, Meadows, v. 47, n. 1, e21, July 2019. DOI: 10.3171/2019.5.FOCUS19234.

58 SFORZA, D. M.; PUTMAN, C. M.; CEBRAL, J. R. Hemodynamics of Cerebral Aneurysms. **Annual Review of Fluid Mechanics**, Palo Alto, v. 41, n. 1, p. 91–107, 2009. DOI: 10.1146/annurev.fluid.40.111406.102126.

59 MALEK, A. M.; ALPER, S. L.; IZUMO, S. Hemodynamic Shear Stress and Its Role in Atherosclerosis. **Journal of the American Medical Association**, Chicago, v. 282, December, p. 2035–2042, 1999.

60 SHOJIMA, M. et al. Magnitude and Role of Wall Shear Stress on Cerebral Aneurysm. Computational Fluid Dynamic Study of 20 Middle Cerebral Artery Aneurysms. **Stroke**, Philadelphia, v. 35, n. 11, p. 2500–2505, 2004. DOI: 10.1161/01.STR.0000144648.89172.of.

61 MENG, H. et al. High WSS or Low WSS? Complex Interactions of Hemodynamics with Intracranial Aneurysm Initiation, Growth, and Rupture: Toward a Unifying Hypothesis. **American Journal of Neuroradiology**, Oak Brook, v. 35, n. 7, p. 1254–1262, 2014. DOI: 10.3174/ajnr.A3558.

62 DOLAN, J. M.; KOLEGA, J.; MENG, H. High Wall Shear Stress and Spatial Gradients in Vascular Pathology: A Review. **Annals of Biomedical Engineering**, New York, v. 41, July, p. 1411–1427, 2013. DOI: 10.1007/s10439-012-0695-0.

63 MENG, H. et al. Complex Hemodynamics at the Apex of an Arterial Bifurcation Induces Vascular Remodeling Resembling Cerebral Aneurysm Initiation. **Stroke**, Philadelphia, v. 38, p. 1924–1931, 2007. DOI: 10.1161/STROKEAHA.106.481234.

64 LAURIC, A. et al. Curvature Effect on Hemodynamic Conditions at the Inner Bend of the Carotid Siphon and Its Relation to Aneurysm Formation. **Journal of Biomechanics**, Oxford, v. 47, n. 12, p. 3018–3027, 2014. DOI: 10.1016/j.jbiomech.2014.06.042.

65 PENN, D. L.; KOMOTAR, R. J.; SANDER CONNOLLY, E. Hemodynamic Mechanisms Underlying Cerebral Aneurysm Pathogenesis. **Journal of Clinical Neuroscience**, Oxford, v. 18, n. 11, p. 1435–1438, 2011. DOI: 10.1016/j.jocn.2011.05.001.

66 FRÖSEN, J. et al. Saccular Intracranial Aneurysm: Pathology and Mechanisms. **Acta Neuropathologica**, Heidelberg, v. 123, p. 773–786, 2012. DOI: 10.1007/s00401-011-0939-3.

67 HUMPHREY, J. D. Coupling Haemodynamics with Vascular Wall Mechanics and Mechanobiology to Understand Intracranial Aneurysms. **International Journal of Computational Fluid Dynamics**, Abingdon, v. 23, n. 8, p. 569–581, Sept. 2009. DOI: 10.1080/10618560902832712.

68 SCOTT, S.; FERGUSON, G. G.; ROACH, M. R. Comparison of the Elastic Properties of Human Intracranial Arteries and Aneurysms. **Canadian Journal of Physiology and Pharmacology**, Ottawa, v. 50, n. 4, p. 328–332, 1972. DOI: 10.1139/y72-049.

69 HE, X. et al. Pulsatile Flow in the Human Left Coronary Artery Bifurcation: Average Conditions. **Journal of Biomechanical Engineering**, New York, v. 118, February 2016, p. 74–82, 1996. DOI: 10.1115/1.2795948.

70 KADASI, L. M.; DENT, W. C.; MALEK, A. M. Cerebral Aneurysm Wall Thickness Analysis Using Intraoperative Microscopy: Effect of Size and Gender on Thin Translucent Regions. **Journal of NeuroInterventional Surgery**, London, v. 5, n. 3, p. 201–206, May 2013. DOI: 10.1136/neurintsurg-2012-010285.

71 SUZUKI, J.; OHARA, H. Clinicopathological Study of Cerebral Aneurysms. **Journal of Neurosurgery**, Meadows, v. 48, p. 505–514, 1978. DOI: 10.3171/jns.1978.48.4.0505.

72 FURUKAWA, K. et al. Hemodynamic Characteristics of Hyperplastic Remodeling Lesions in Cerebral Aneurysms. Ed. by Stephan Meckel. **PLOS ONE**, San Francisco, v. 13, p. 1–11, Jan. 2018. DOI: 10.1371/journal.pone.0191287.

73 CEBRAL, J. R. et al. Local Hemodynamic Conditions Associated with Focal Changes in the Intracranial Aneurysm Wall. **American Journal of Neuroradiology**, American Society of Neuroradiology, Oak Brook, v. 40, n. 3, p. 510–516, 2019. DOI: 10.3174/ajnr.A5970.

74 KADASI, L. M.; DENT, W. C.; MALEK, A. M. Colocalization of Thin-Walled Dome Regions with Low Hemodynamic Wall Shear Stress in Unruptured Cerebral Aneurysms. **Journal of Neurosurgery**, Meadows, v. 119, n. 1, p. 172–179, Mar. 2013. DOI: 10.3171/2013.2.jns12968.

75 RUÍZ, D. S. M. et al. The Perianeurysmal Environment: Influence on Saccular Aneurysm Shape and Rupture. **American Journal of Neuroradiology**, Oak Brook, v. 27, p. 504–512, 2006.

76 HARKNESS, R. D. Biological Functions of Collagen. **Biological Reviews**, Oxford, v. 36, n. 4, p. 399–455, Nov. 1961. DOI: 10.1111/j.1469-185X.1961.tb01596.x.

77 CAREW, T. E. et al. Compressibilty of the Arterial Wall. **Circulation Research**, Heidelberg, v. 23, p. 61–68, 1968.

78 STEIGER, H. J. et al. Strength, Elasticity and Viscoelastic Properties of Cerebral Aneurysms. **Heart and Vessels**, Tokyo, v. 5, n. 1, p. 41–46, Mar. 1989. DOI: 10.1007/BF02058357.

79 ROBERTSON, A. M. et al. Diversity in the Strength and Structure of Unruptured Cerebral Aneurysms. **Annals of Biomedical Engineering**, New York, v. 43, n. 7, p. 1502–1515, 2015. DOI: 10.1007/s10439-015-1252-4.

80 CEBRAL, J. R. et al. Wall Mechanical Properties and Hemodynamics of Unruptured Intracranial Aneurysms. **American Journal of Neuroradiology**, Oak Brook, v. 36, n. 9, p. 1695–1703, 2015. DOI: 10.3174/ajnr.A4358.

81 COSTALAT, V. et al. Biomechanical Wall Properties of Human Intracranial Aneurysms Resected Following Surgical Clipping (IRRAs Project). **Journal of Biomechanics**, Oxford, v. 44, n. 15, p. 2685–2691, 2011. DOI: 10.1016/j.jbiomech.2011.07.026.

82 BRUNEL, H. et al. Rupture Limit Evaluation of Human Cerebral Aneurysms Wall: Experimental Study. **Journal of Biomechanics**, Oxford, v. 77, p. 76–82, Aug. 2018. DOI: 10.1016/j.jbiomech.2018.06.016.

83 ABRUZZO, T. et al. Histologic and Morphologic Comparison of Experimental Aneurysms with Human Intracranial Aneurysms. **American Journal of Neuroradiology**, Oak Brook, v. 19, p. 1309–1314, 1998.

84 NAKAGAWA, D. et al. Wall-to-lumen Ratio of Intracranial Arteries Measured by Indocyanine Green Angiography. **Asian Journal of Neurosurgery**, Meadows, v. 11, p. 361–364, 2016. DOI: 10.4103/1793-5482.175637.

85 KLEINLOOG, R. et al. Visualization of the Aneurysm Wall: A 7.0-Tesla Magnetic Resonance Imaging Study. **Neurosurgery**, Cary, v. 75, December, p. 614–622, 2014. DOI: 10.1227/NEU.0000000000000559.

86 SAMANIEGO, E. A.; ROA, J. A.; HASAN, D. Vessel Wall Imaging in Intracranial Aneurysms. **Journal of NeuroInterventional Surgery**, London, v. 11, n. 11, p. 1105–1112, Nov. 2019. DOI: 10.1136/neurintsurg-2019-014938.

87 SIGNORELLI, F. et al. Biomechanical Characterization of Intracranial Aneurysm Wall: A Multiscale Study. **World Neurosurgery**, Philadelphia, v. 119, e882–e889, Nov. 2018. DOI: 10.1016/j.wneu.2018.07.290.

88 HOLZAPFEL, G. A.; SOMMER, G.; REGITNIG, P. Anisotropic Mechanical Properties of Tissue Components in Human Atherosclerotic Plaques. **Journal of Biomechanical Engineering**, New York, v. 126, n. 5, p. 657–665, Oct. 2004. DOI: 10.1115/1.1800557.

89 HOLZAPFEL, G. A.; OGDEN, R. W. (Eds.). **Biomechanics of Soft Tissue in Cardiovascular Systems**. Vienna: Springer Vienna, 2003. DOI: 10.1007/978-3-7091-2736-0.

90 GADE, P. S. et al. Calcification in Human Intracranial Aneurysms Is Highly Prevalent and Displays Both Atherosclerotic and Nonatherosclerotic Types. **Arteriosclerosis, Thrombosis, and Vascular Biology**, Dallas, v. 39, n. 10, p. 2157–2167, Oct. 2019. DOI: 10.1161/ATVBAHA.119.312922.

91 FORTUNATO, R. N. et al. Effect of Macro-calcification on the Failure Mechanics of Intracranial Aneurysmal Wall Tissue. **Experimental Mechanics**, New York, v. 61, n. 1, p. 5–18, Jan. 2021. DOI: 10.1007/s11340-020-00657-7.

92 KIMURA, H. et al. Clear Detection of Thin-Walled Regions in Unruptured Cerebral Aneurysms by Using Computational Fluid Dynamics. **World Neurosurgery**, Philadelphia, v. 121, e287–e295, 2019. DOI: 10.1016/j.wneu.2018.09.098.

93 CEBRAL, J. R. et al. Analysis of Hemodynamics and Wall Mechanics at Sites of Cerebral Aneurysm Rupture. **Journal of NeuroInterventional Surgery**, London, v. 7, n. 7, 2015. DOI: 10.1136/neurintsurg-2014-011247.

94 ANTIGA, L. et al. Geometric Reconstruction for Computational Mesh Generation of Arterial Bifurcations from CT Angiography. **Computerized Medical Imaging and Graphics**, London, v. 26, p. 227–235, 2002.

95 VIGNON-CLEMENTEL, I. E. et al. Outflow Boundary Conditions for Three-Dimensional Finite Element Modeling of Blood Flow and Pressure in Arteries. **Computer Methods in Applied Mechanics and Engineering**, Amsterdam, v. 195, n. 29-32, p. 3776–3796, 2006. DOI: 10.1016/j.cma.2005.04.014. arXiv: 1012.0736.

96 KARMONIK, C. et al. Intra-Aneurysmal Flow Patterns and Wall Shear Stresses Calculated with Computational Flow Dynamics in an Anterior Communicating Artery Aneurysm Depend on Knowledge of Patient-Specific Inflow Rates. **Acta Neurochirurgica**, Wien, v. 151, n. 5, p. 479–485, 2009. DOI: 10.1007/s00701-009-0247-z.

97 UGRON, Á.; PAÁL, G. On the Boundary Conditions of Cerebral Aneurysm Simulations. **Periodica Polytechnica Mechanical Engineering**, Budapest, v. 58, n. 1, p. 37–45, 2014. DOI: 10.3311/PPme.7392.

98 USMANI, A. Y.; MURALIDHAR, K. Flow in an Intracranial Aneurysm Model: Effect of Parent Artery Orientation. **Journal of Visualization**, Heidelberg, p. 1–24, 2018. DOI: 10.1007/s12650-018-0491-5.

99 KARMONIK, C. et al. Quantitative Comparison of Hemodynamic Parameters from Steady and Transient CFD Simulations in Cerebral Aneurysms with Focus on the Aneurysm Ostium. **Journal of NeuroInterventional Surgery**, London, p. 1–6, 2014. DOI: 10.1136/neurintsurg-2014-011182.

100 CEBRAL, J. R.; MENG, H. **Counterpoint: Realizing the Clinical Utility of Computational Fluid DynamicsClosing the Gap**. Oak Brook, 2012. p. 397–398. DOI: 10.3174/ajnr.a2993.

101 KALLMES, D. F. Point: CFDComputational Fluid Dynamics or Confounding Factor Dissemination. **American Journal of Neuroradiology**, Oak Brook, v. 33, p. 393–398, 2012. DOI: 10.3174/ajnr.A2993.

102 CEBRAL, J. R. et al. Characterization of Cerebral Aneurysms for Assessing Risk of Rupture by Using Patient-Specific Computational Hemodynamics Models. **American Journal of Neuroradiology**, Oak Brook, v. 26, n. 10, p. 2550–2559, 2005. DOI: 10.1016/S0098-1672(08)70473-9.

103 CEBRAL, J. R. et al. Efficient Pipeline for Image-Based Patient-Specific Analysis of Cerebral Aneurysm Hemodynamies Technique and Sensitivity. **IEEE Transactions on Medical Imaging**, Piscataway, v. 24, n. 4, p. 457–467, 2005. DOI: 10.1109/TMI.2005.844159.

104 SHIMOGONYA, Y. et al. Can Temporal Fluctuation in Spatial Wall Shear Stress Gradient Initiate a Cerebral Aneurysm? A Proposed Novel Hemodynamic Index, the Gradient Oscillatory Number (GON). **Journal of Biomechanics**, Oxford, v. 42, p. 550–554, 2009.

105 XIANG, J. et al. Hemodynamic-Morphologic Discriminants for Intracranial Aneurysm Rupture. **Stroke**, Philadelphia, v. 42, n. 1, p. 144–152, 2011. DOI: 10.1161/STROKEAHA.110.592923.

106 BYRNE, G.; MUT, F.; CEBRAL, J. Quantifying the Large-Scale Hemodynamics of Intracranial Aneurysms. **American Journal of Neuroradiology**, Oak Brook, v. 35, n. 2, p. 333–338, 2014. DOI: 10.3174/ajnr.A3678.

107 JING, L. et al. Morphologic and Hemodynamic Analysis in the Patients with Multiple Intracranial Aneurysms: Ruptured versus Unruptured. **PLOS ONE**, San Francisco, v. 10, n. 7, 2015. DOI: 10.1371/journal.pone.0132494.

108 XIANG, J. et al. CFD: Computational Fluid Dynamics or Confounding Factor Dissemination? The Role of Hemodynamics in Intracranial Aneurysm Rupture Risk Assessment. **American Journal of Neuroradiology**, Oak Brook, v. 35, p. 1849–1857, 2014. DOI: 10.3174/ajnr.A3710.

109 CEBRAL, J. R. et al. Association of Hemodynamic Characteristics and Cerebral Aneurysm Rupture. **American Journal of Neuroradiology**, Oak Brook, v. 32, p. 264–270, 2011. DOI: 10.3174/ajnr.A2274.

110 CEBRAL, J. R. et al. Quantitative Characterization of the Hemodynamic Environment in Ruptured and Unruptured Brain Aneurysms. **American Journal of Neuroradiology**, Oak Brook, v. 32, p. 145–151, 2011. DOI: 10.3174/ajnr.A2419.

111 LONGO, M. et al. Role of Hemodynamic Forces in Unruptured Intracranial Aneurysms: An Overview of a Complex Scenario. **World Neurosurgery**, Philadelphia, v. 105, 2017. DOI: 10.1016/j.wneu.2017.06.035.

112 MANTHA, A. et al. Hemodynamics in a Cerebral Artery before and after the Formation of an Aneurysm. **American Journal of Neuroradiology**, Oak Brook, v. 27, May, p. 1113–1118, 2006.

113 CHEN, H. et al. Investigating the Influence of Haemodynamic Stimuli on Intracranial Aneurysm Inception. **Annals of Biomedical Engineering**, New York, v. 41, July, p. 1492–1504, 2013. DOI: 10.1007/s10439-013-0794-6.

114 GEERS, A. J. et al. Wall Shear Stress at the Initiation Site of Cerebral Aneurysms. **Biomechanics and Modeling in Mechanobiology**, Heidelberg, v. 16, p. 97–115, 2017. DOI: 10.1007/s10237-016-0804-3.

115 OLIVEIRA, I. L. et al. A Longitudinal Study of a Lateral Intracranial Aneurysm: Identifying the Hemodynamic Parameters behind Its Inception and Growth Using Computational Fluid Dynamics. **Journal of the Brazilian Society of Mechanical Sciences and Engineering**, Heidelberg, v. 43, p. 138, 2021. DOI: 10.1007/s40430-021-02836-6.

116 BAZILEVS, Y. et al. Isogeometric Fluid-Structure Interaction: Theory, Algorithms, and Computations. **Computational Mechanics**, Heidelberg, v. 43, n. 1, p. 3–37, 2008. DOI: 10.1007/s00466-008-0315-x.

117 LEE, C. J. et al. The Influence of Elastic Upstream Artery Length on Fluid-Structure Interaction Modeling: A Comparative Study Using Patient-Specific Cerebral Aneurysm. **Medical Engineering and Physics**, London, v. 35, n. 9, p. 1377–1384, 2013. DOI: 10.1016/j.medengphy.2013.03.009.

118 TRICERRI, P. et al. Fluid-Structure Interaction Simulations of Cerebral Arteries Modeled by Isotropic and Anisotropic Constitutive Laws. **Computational Mechanics**, Heidelberg, v. 55, n. 3, p. 479–498, 2015. DOI: 10.1007/s00466-014-1117-y.

119 FELIPPA, C. A.; PARK, K. C.; FARHAT, C. Partitioned Analysis of Coupled Mechanical Systems. **Computer Methods in Applied Mechanical Engineering**, Amsterdam, v. 190, p. 3247–3270, 2001.

120 HOU, G.; WANG, J.; LAYTON, A. Numerical Methods for Fluid-Structure Interaction - A Review. **Communications in Computational Physics**, Hong Kong, v. 12, n. 2, p. 337–377, 2012. DOI: 10.4208/cicp.291210.290411s.

121 BAZILEVS, Y. et al. A Fully-Coupled Fluid-Structure Interaction Simulation of Cerebral Aneurysms. **Computational Mechanics**, Heidelberg, v. 46, p. 3–16, 2010. DOI: 10.1007/s00466-009-0421-4.

122 BAZILEVS, Y. et al. Computational Fluid-Structure Interaction: Methods and Application to a Total Cavopulmonary Connection. **Computational Mechanics**, Heidelberg, v. 45, n. 1, p. 77–89, 2009. DOI: 10.1007/s00466-009-0419-y.

123 BAZILEVS, Y. et al. Isogeometric Fluid-Structure Interaction Analysis with Applications to Arterial Blood Flow. **Computational Mechanics**, Heidelberg, v. 38, n. 4-5, p. 310–322, 2006. DOI: 10.1007/s00466-006-0084-3.

124 EKEN, A.; SAHIN, M. A Parallel Monolithic Approach for Fluid-Structure Interaction in a Cerebral Aneurysm. **Computers and Fluids**, Oxford, v. 153, p. 61–75, 2017. DOI: 10.1016/j.compfluid.2017.05.005.

125 LEE, C. J. et al. A Fluid-Structure Interaction Study Using Patient-Specific Ruptured and Unruptured Aneurysm: The Effect of Aneurysm Morphology, Hypertension and Elasticity. **Journal of Biomechanics**, Oxford, v. 46, n. 14, p. 2402–2410, 2013. DOI: 10.1016/j.jbiomech.2013.07.016.

126 TORII, R. et al. Influence of Wall Elasticity in Patient-Specific Hemodynamic Simulations. **Computers and Fluids**, Oxford, v. 36, p. 160–168, 2007. DOI: 10.1016/j.compfluid.2005.07.014.

127 TORII, R. et al. Fluid-Structure Interaction Modeling of a Patient-Specific Cerebral Aneurysm: Influence of Structural Modeling. **Computational Mechanics**, Heidelberg, v. 43, p. 151–159, 2008. DOI: 10.1007/s00466-008-0325-8.

128 DEMIRAY, H. A Note on the Elasticity of Soft Biological Tissues. **Journal of Biomechanics**, Oxford, v. 5, p. 309–311, 1972. DOI: 10.1016/0021-9290(72)90047-4.

129 TORII, R. et al. Fluid-Structure Interaction Modeling of Blood Flow and Cerebral Aneurysm: Significance of Artery and Aneurysm Shapes. **Computer Methods in Applied Mechanics and Engineering**, Amsterdam, v. 198, p. 3613–3621, 2009. DOI: 10.1016/j.cma.2008.08.020.

130 TORII, R. et al. Influence of Wall Thickness on FluidStructure Interaction Computations of Cerebral Aneurysms. **International Journal for Numerical Methods in Biomedical Engineering**, Oxford, v. 26, p. 336–347, 2010. DOI: 10.1002/cnm.

131 BAZILEVS, Y. et al. Computational Vascular Fluid-Structure Interaction: Methodology and Application to Cerebral Aneurysms. **Biomechanics and Modeling in Mechanobiology**, Heidelberg, v. 9, p. 481–498, 2010. DOI: 10.1007/s10237-010-0189-7.

132 HSU, M.-C.; BAZILEVS, Y. Blood Vessel Tissue Prestress Modeling for Vascular Fluid-Structure Interaction Simulation. **Finite Elements in Analysis and Design**, v. 47, p. 593–599, 2011. DOI: 10.1016/j.finel.2010.12.015.

133 VOSS, S. et al. Fluid-Structure Simulations of a Ruptured Intracranial Aneurysm: Constant versus Patient-Specific Wall Thickness. **Computational and Mathematical Methods in Medicine**, London, v. 2016, 2016. DOI: 10.1155/2016/9854539.

134 VALENCIA, A.; SOLIS, F. Blood Flow Dynamics and Arterial Wall Interaction in a Saccular Aneurysm Model of the Basilar Artery. **Computers and Structures**, Oxford, v. 84, p. 1326–1337, 2006. DOI: 10.1016/j.compstruc.2006.03.008.

135 TORII, R. et al. Numerical Investigation of the Effect of Hypertensive Blood Pressure on Cerebral Aneurysm - Dependence of the Effect on the Aneurysm Shape. **International Journal for Numerical Methods in Fluids**, Oxford, v. 54, p. 995–1009, 2007. DOI: 10.1002/fld.1497.

136 VALENCIA, A. et al. Blood Flow Dynamics and Fluid-Structure Interaction in Patient-Specific Bifurcating Cerebral Aneurysms. **International Journal for Numerical Methods in Fluids**, Oxford, v. 58, n. 10, p. 1081–1100, 2008. DOI: 10.1002/fld.1786.

137 VALENCIA, A. et al. Comparison between Computational Fluid Dynamics, Fluid-Structure Interaction and Computational Structural Dynamics Predictions of Flow-Induced Wall Mechanics in an Anatomically Realistic Cerebral Aneurysm Model. **International Journal of Computational Fluid Dynamics**, Abingdon, v. 23, n. 9, p. 649–666, 2009. DOI: 10.1080/10618560903476386.

138 SANCHEZ, M. et al. Biomechanical Assessment of the Individual Risk of Rupture of Cerebral Aneurysms: A Proof of Concept. **Annals of Biomedical Engineering**, New York, v. 41, n. 1, p. 28–40, Jan. 2013. DOI: 10.1007/s10439-012-0632-2.

139 VALENCIA, A. et al. Fluid Structural Analysis of Human Cerebral Aneurysm Using Their Own Wall Mechanical Properties. **Computational and Mathematical Methods in Medicine**, London, v. 2013, p. 1–18, 2013. DOI: 10.1155/2013/293128.

140 CHO, K.-C. et al. Prediction of Rupture Risk in Cerebral Aneurysms by Comparing Clinical Cases with FluidStructure Interaction Analyses. **Scientific Reports**, London, v. 10, n. 1, p. 18237, Dec. 2020. DOI: 10.1038/s41598-020-75362-5.

141 TAKIZAWA, K. et al. Wall Shear Stress Calculations in Space-Time Finite Element Computation of Arterial Fluid-Structure Interactions. **Computational Mechanics**, Heidelberg, v. 46, p. 31–41, 2010. DOI: 10.1007/s00466-009-0425-0.

142 SANCHEZ, M. et al. Intracranial Aneurysmal Pulsatility as a New Individual Criterion for Rupture Risk Evaluation: Biomechanical and Numeric Approach (IRRAs Project). **American Journal of Neuroradiology**, Oak Brook, v. 35, p. 1765–1771, 2014. DOI: 10.3174/ajnr.A3949.

143 CHAGNON, G.; REBOUAH, M.; FAVIER, D. Hyperelastic Energy Densities for Soft Biological Tissues: A Review. **Journal of Elasticity**, Dordretch, v. 120, n. 2, p. 129–160, 2015. DOI: 10.1007/s10659-014-9508-z.

144 ZHAO, X.; RAGHAVAN, M. L.; LU, J. Identifying Heterogeneous Anisotropic Properties in Cerebral Aneurysms: A Pointwise Approach. **Biomechanics and Modeling in Mechanobiology**, Heidelberg, v. 10, n. 2, p. 177–189, Apr. 2011. DOI: 10.1007/s10237-010-0225-7.

145 MA, B. et al. Nonlinear Anisotropic Stress Analysis of Anatomically Realistic Cerebral Aneurysms. **Journal of Biomechanical Engineering**, New York, v. 129, n. 1, p. 88–96, Feb. 2007. DOI: 10.1115/1.2401187.

146 RAMACHANDRAN, M. et al. On the Role of Modeling Choices in Estimation of Cerebral Aneurysm Wall Tension. **Journal of Biomechanics**, Oxford, v. 45, n. 16, p. 2914–2919, Nov. 2012. DOI: 10.1016/j.jbiomech.2012.07.029.

147 HIRSCHHORN, M. et al. Fluid-structure Interaction Modeling in Cardiovascular Medicine - A Systematic Review 2017 - 2019. **Medical Engineering & Physics**, London, v. 78, p. 1–13, Apr. 2020. DOI: 10.1016/j.medengphy.2020.01.008.

148 T. PASSERINI, M. PICCINELLI, A. VENEZIANI AND L. ANTIGA. **aneurisk**. 2021. http://ecm2.mathcs.emory.edu/aneuriskweb/index.

149 PICCINELLI, M. et al. A Framework for Geometric Analysis of Vascular Structures: Application to Cerebral Aneurysms. **IEEE Transactions on Medical Imaging**, Piscataway, v. 28, n. 8, p. 1141–1155, Aug. 2009. DOI: 10.1109/TMI.2009.2021652.

150 VMTK. **VMTK Website**. 2017. http://www.vmtk.org/. [Accessed 19-June-2022].

151 ANTIGA, L. et al. An Image-Based Modeling Framework for Patient-Specific Computational Hemodynamics. **Medical and Biological Engineering and Computing**, Heidelberg, v. 46, p. 1097–1112, 2008. DOI: 10.1007/s11517-008-0420-1.

152 ANTIGA, L.; ENE-IORDACHE, B.; REMUZZI, A. Computational Geometry for Patient-Specific Reconstruction and Meshing of Blood Vessels from MR and CT Angiography. **IEEE Transactions on Medical Imaging**, Piscataway, v. 22, n. 5, p. 674–684, 2003. DOI: 10.1109/TMI.2003.812261.

153 PICCINELLI, M. et al. Automatic Neck Plane Detection and 3d Geometric Characterization of Aneurysmal Sacs. **Annals of Biomedical Engineering**, New York, v. 40, n. 10, p. 2188–2211, 2012. DOI: 10.1007/s10439-012-0577-5.

154 CARDENES, R. et al. Automatic Aneurysm Neck Detection Using Surface Voronoi Diagrams. **IEEE Transactions on Medical Imaging**, Piscataway, v. 30, n. 10, p. 1863–1876, Oct. 2011. DOI: 10.1109/TMI.2011.2157698.

155 LINDGREN, A. et al. Irregular Shape of Intracranial Aneurysm Indicates Rupture Risk Irrespective of Size in a Population-Based Cohort. **Stroke**, Philadelphia, v. 47, p. 1219–1226, 2016. DOI: 10.1161/STROKEAHA.115.012404.

156 ABBOUD, T. et al. Morphology of Ruptured and Unruptured Intracranial Aneurysms. **World Neurosurgery**, Philadelphia, v. 99, p. 610–617, 2017. DOI: 10.1097/GOX.0000000000000736.

157 MA, B.; HARBAUGH, R. E.; RAGHAVAN, M. L. Three-Dimensional Geometrical Characterization of Cerebral Aneurysms. **Annals of Biomedical Engineering**, New York, v. 32, n. 2, p. 264–273, 2004.

158 SCIPY. **SciPy Website**. 2017. https://www.scipy.org. [Accessed 05-May-2022].

159 SACKS, A. H.; TICKNER, E. G. The Compressibility of Blood. **Biorheology**, Amsterdam, v. 5, n. 4, p. 271–274, Dec. 1968. DOI: 10.3233/BIR-1968-5403.

160 BELYTSCHKO, T. **Nonlinear Finite Elements for Continua and Structures**. Second: Wiley, 2014.

161 KANYANTA, V.; IVANKOVIC, A.; KARAC, A. Validation of a Fluid-Structure Interaction Numerical Model for Predicting Flow Transients in Arteries. **Journal of Biomechanics**, Oxford, v. 42, n. 11, p. 1705–1712, Aug. 2009. DOI: 10.1016/j.jbiomech.2009.04.023.

162 TANDIS, E.; ASHRAFIZADEH, A. A Numerical Study on the Fluid Compressibility Effects in Strongly Coupled FluidSolid Interaction Problems. **Engineering with Computers**, London, 2019. DOI: 10.1007/s00366-019-00880-4.

163 LA SPINA, A. et al. On the Role of (Weak) Compressibility for Fluid-Structure Interaction Solvers. **International Journal for Numerical Methods in Fluids**, Oxford, 2019. DOI: 10.1002/fld.4776.

164 HOI, Y. et al. Characterization of Volumetric Flow Rate Waveforms at the Carotid Bifurcations of Older Adults. **Physiological Measurement**, Bristol, v. 31, n. 3, p. 291–302, 2010. DOI: 10.1088/0967-3334/31/3/002.

165 ZARRINKOOB, L. et al. Blood Flow Distribution in Cerebral Arteries. **Journal of Cerebral Blood Flow and Metabolism**, London, v. 35, p. 648–654, 2015. DOI: 10.1038/jcbfm.2014.241.

166 CHNAFA, X. C. et al. Better Than Nothing: A Rational Approach for Minimizing the Impact of Outflow Strategy on Cerebrovascular Simulations. **American Journal of Neuroradiology**, Oak Brook, v. 39, p. 337–343, 2018. DOI: 10.3174/ajnr.A5484.

167 HOLZAPFEL, G. A. **Nonlinear Solid Mechanics**. Chichester: John Wiley & Sons, Inc., 2000.

168 MALVERN, L. E. **Introduction to the Mechanics of a Continuous Medium**. New Jersey: Prentice Hall, 1969.

169 HUMPHREY, J. Continuum Biomechanics of Soft Biological Tissues. **Proceedings of the Royal Society of London**, London, v. 459, p. 3–46, 2002. DOI: 10.1098/.

170 GASSER, T. C.; OGDEN, R. W.; HOLZAPFEL, G. A. Hyperelastic Modelling of Arterial Layers with Distributed Collagen Fibre Orientations. **Journal of the Royal Society Interface**, London, v. 3, n. 6, p. 15–35, 2006. DOI: 10.1098/rsif.2005.0073.

171 HOLZAPFEL, G. A.; OGDEN, R. W.; OLZAPFEL, B. Y. G. E. A. H. Constitutive Modelling of Arteries. **Proceedings of the Royal Society A: Mathematical, Physical and Engineering Sciences**, London, v. 466, n. 2118, p. 1551–1597, 2010. DOI: 10.1098/rspa.2010.0058.

172 WULANDANA, R.; ROBERTSON, A. M. An Inelastic Multi-Mechanism Constitutive Equation for Cerebral Arterial Tissue. **Biomechanics and Modeling in Mechanobiology**, Heidelberg, v. 4, n. 4, p. 235–248, Dec. 2005. DOI: 10.1007/s10237-005-0004-z.

173 FUNG, Y.-C. B. Biorheology of Soft Tissues. **Biorheology**, Amsterdam, v. 10, n. 2, p. 139–155, June 1973. DOI: 10.3233/BIR-1973-10208.

174 DEMIRAY, H. et al. A Stress-Strain Relation for a Rat Abdominal Aorta. **Journal of Biomechanics**, Oxford, v. 21, n. 5, p. 369–374, 1988.

175 RIVLIN, R. S.; SAUNDERS, D. W. Large Elastic Deformations of Isotropic Materials VII. Experiments on the Deformation of Rubber. **Philosophical Transactions of the Royal Society of London A: Mathematical, Physical and Engineering Sciences**, London, v. 243, n. 865, p. 251–289, 1951.

176 MOONEY, M. A Theory of Large Elastic Deformation. **Journal of Applied Physics**, Melville, v. 11, n. 153, 1940. DOI: 10.1063/1.1713863.

177 OGDEN, R. W. Large Deformation Isotropic Elasticity: On the Correlation of Theory and Experiment for Compressible Rubberlike Solids. **Proceedings of the Royal Society of London. A. Mathematical and Physical Sciences**, London, v. 328, p. 567–583, 1972. DOI: 10.1098/rspa.1972.0096.

178 ZHAO, X.; RAGHAVAN, M. L.; LU, J. Characterizing Heterogeneous Properties of Cerebral Aneurysms With Unknown Stress-Free Geometry: A Precursor to In Vivo Identification. **Journal of Biomechanical Engineering**, New York, v. 133, n. 5, p. 051008, May 2011. DOI: 10.1115/1.4003872.

179 NAMA, N. et al. A Nonlinear Rotation-Free Shell Formulation with Prestressing for Vascular Biomechanics. **Scientific Reports**, London, v. 10, n. 1, p. 17528, Dec. 2020. DOI: 10.1038/s41598-020-74277-5.

180 JASAK, H. **Error Analysis and Estimation for the Finite Volume Method with Applications to Fluid Flows**. 1996. PhD thesis – Imperial College.

181 VERSTEEG, H. K.; MALALASEKERA, W. **An Introduction to Computational Fluid Dynamics: The Finite Volume Method**. 2nd ed. Harlow, England ; New York: Pearson Education Ltd, 2007.

182 MOUKALLED, F.; MANGANI, L.; DARWISH, M. **The Finite Volume Method in Computational Fluid Dynamics: An Advanced Introduction with OpenFOAMő and Matlab**. Cham: Springer International Publishing, 2016. v. 113. (Fluid Mechanics and Its Applications). DOI: 10.1007/978-3-319-16874-6.

183 WELLER, H. G. et al. A Tensorial Approach to Computational Continuum Mechanics Using Object-Oriented Techniques. **Computers in Physics**, v. 12, p. 620–631, 1998.

184 CARDIFF, P.; DEMIRDI, I. Thirty Years of the Finite Volume Method for Solid Mechanics. **Archives of Computational Methods in Engineering**, Dordrecht, Feb. 2021. DOI: 10.1007/s11831-020-09523-0.

185 STROUSTRUP, B. **The C++ Programming Language**. Fourth edition. Upper Saddle River, NJ: Addison-Wesley, 2013.

186 CARDIFF, P. et al. **An Open-Source Finite Volume Toolbox for Solid Mechanics and Fluid-Solid Interaction Simulations**. v. 00. 2018. p. 1–45. arXiv: 1808.10736.

187 CARDIFF, P. et al. A Lagrangian Cell-Centred Finite Volume Method for Metal Forming Simulation. **International Journal for Numerical Methods in Engineering**, Oxford, v. 109, n. 13, p. 1777–1803, 2017. DOI: 10.1002/nme.5345.

188 RHIE, C. M.; CHOW, W. L. Numerical Study of the Turbulent Flow Past an Airfoil with Trailing Edge Separation. **AIAA Journal**, Reston, v. 21, n. 11, p. 1525–1532, 1983. DOI: 10.2514/3.8284.

189 JASAK, H.; WELLER, H. G. Application of the Finite Volume Method and Unstructured Meshes to Linear Elasticity. **International Journal for Numerical Methods in Engineering**, Oxford, v. 48, p. 267–287, 2000. DOI: 10.1002/(SICI)1097-0207(20000520)48.

190 ISSA, R. I. Solution of the Implicitly Discretised Fluid Flow Equations by Operator-Splitting. **Journal of Computational Physics**, Maryland, v. 62, n. 1, p. 40–65, 1986. DOI: 10.1016/0021-9991(86)90099-9. arXiv: gr-qc/9809069v1.

191 NUMPY. **NumPy Website**. 2017. https://numpy.org/. [Accessed 05-May-2022].

192 PARK, J. et al. Ruptured Intracranial Aneurysms With Small Basal Outpouching. **Neurosurgery**, Cary, v. 71, n. 5, p. 994–1002, Nov. 2012. DOI: 10.1227/NEU.0b013e31826cde9f.

193 SALIMI ASHKEZARI, S. F. et al. Blebs in Intracranial Aneurysms: Prevalence and General Characteristics. **Journal of NeuroInterventional Surgery**, London, v. 13, n. 3, p. 226–230, Mar. 2021. DOI: 10.1136/neurintsurg-2020-016274.

194 JOHNSTON, B. M.; JOHNSTON, P. R. The Relative Effects of Arterial Curvature and Lumen Diameter on Wall Shear Stress Distributions in Human Right Coronary Arteries. **Physics in Medicine and Biology**, Bristol, v. 52, n. 9, p. 2531–2544, May 2007. DOI: 10.1088/0031-9155/52/9/013.

195 ARZANI, A.; SHADDEN, S. C. Wall Shear Stress Fixed Points in Cardiovascular Fluid Mechanics. **Journal of Biomechanics**, Oxford, v. 73, p. 145–152, May 2018. DOI: 10.1016/j.jbiomech.2018.03.034.

196 ZHANG, C. et al. Morphodynamic Analysis of Cerebral Aneurysm Pulsation From Time-Resolved Rotational Angiography. **IEEE Transactions on Medical Imaging**, Piscataway, v. 28, n. 7, p. 1105–1116, July 2009. DOI: 10.1109/TMI.2009.2012405.

197 FERRARI, F. et al. Wall Motion at 4D-CT Angiography and Surgical Correlation in Unruptured Intracranial Aneurysms: A Pilot Study. **Journal of Neurosurgical Sciences**, Turin, v. 63, n. 5, Oct. 2019. DOI: 10.23736/S0390-5616.16.03640-7.

198 JAIN, K.; ROLLER, S.; MARDAL, K. A. Transitional Flow in Intracranial Aneurysms - A Space and Time Refinement Study below the Kolmogorov Scales Using Lattice Boltzmann Method. **Computers and Fluids**, Oxford, v. 127, p. 36–46, Mar. 2016. DOI: 10.1016/j.compfluid.2015.12.011. arXiv: 1512.02504.

199 KHAN, M. et al. On the Prevalence of Flow Instabilities from High-Fidelity Computational Fluid Dynamics of Intracranial Bifurcation Aneurysms. **Journal of Biomechanics**, Oxford, v. 127, p. 110683, Oct. 2021. DOI: 10.1016/j.jbiomech.2021.110683.

200 MARTIN, C.; SUN, W. Fatigue Damage of Collagenous Tissues: Experiment, Modeling and Simulation Studies. **Journal of Long-Term Effects of Medical Implants**, Danbury, v. 25, n. 1-2, p. 55–73, 2015. DOI: 10.1615/JLongTermEffMedImplants.2015011749.

201 OLIVEIRA, I. L. et al. **A Numerical Investigation of the Mechanics of Intracranial Aneurysms Walls: Assessing the Influence of Tissue Hyperelastic Laws and Heterogeneous Properties on the Stress and Stretch Fields**. May 2022.

202 OLIVEIRA, I. L. et al. Effect of Blood Rheology Model on Hemodynamic Parameters Related to Intracranial Aneurysm Rupture. In: 17TH Brazilian Congress of Thermal Sciences and Engineering. Águas de Lindóia, SP, Brazil: ABCM, 2018. DOI: 10.26678/ABCM.ENCIT2018.CIT18-0761.

203 OLIVEIRA, I. L. et al. Hemodynamic and Morphological Case Study of an Intracranial Aneurysm Initiation and Evolution. In: ABCM INTERNATIONAL CONGRESS of Mechanical Engineering. Uberlândia, MG, Brazil, 2019. DOI: 10.26678/ABCM.COBEM2019.COB2019-0516.

204 OLIVEIRA, I. L.; GASCHE, J. L.; CARDIFF, P. Implementation and Numerical Verification of an Incompressible Three-Parameter Mooney-Rivlin Model for Large Deformation of Soft Tissues. In: 15TH OpenFOAM Workshop. Washington, DC, USA, 2020.

205 OLIVEIRA, I. et al. Semicoupled Numerical Strategy to Solve Large-Strain Motion of Incompressible Hyperelastic Materials. In: 16TH OpenFOAM Workshop. Dublin, Ireland, 2021. p. 2.

206 OLIVEIRA, I. L. et al. On the Influence of the Wall Thickness Heterogeneity in the Mechanics of Intracranial Aneurysms. In: PROCEEDINGS of the 26th International Congress of Mechanical Engineering. ABCM, 2021. DOI: 10.26678/ABCM.COBEM2021.COB2021-0451.

207 OLIVEIRA, I. L. **vmtk4aneurysms**. Zenodo, June 2022. DOI: 10.5281/zenodo.6675879.

208 DHAR, S. et al. Morphology Parameters for Intracranial Aneurysm Rupture Risk Assessment. **Neurosurgery**, Cary, v. 63, n. 2, p. 185–196, 2008. DOI: 10.1227/01.NEU.0000316847.64140.81.

209 LEE, S. W.; ANTIGA, L.; STEINMAN, D. A. Correlations among Indicators of Disturbed Flow at the Normal Carotid Bifurcation. **Journal of Biomechanical Engineering**, New York, v. 131, n. 6, p. 1–7, 2009. DOI: 10.1115/1.3127252.

210 PEIFFER, V.; SHERWIN, S. J.; WEINBERG, P. D. Computation in the Rabbit Aorta of a New Metric - the Transverse Wall Shear Stress - to Quantify the Multidirectional Character of Disturbed Blood Flow. **Journal of Biomechanics**, Oxford, v. 46, n. 15, p. 2651–2658, 2013. DOI: 10.1016/j.jbiomech.2013.08.003.

211 WALL, W. A.; MOK, D. P.; RAMM, E. Iterative Substructering Schemes for Fluid Structure Interaction. In: ANALYSIS and Simulation of Multifield Problems. 2003. p. 349–369.

212 MATTHIES, H. G.; STEINDORF, J. Partitioned but Strongly Coupled Iteration Schemes for Nonlinear Fluid-Structure Interaction. **Computers and Structures**, Oxford, v. 80, n. 27-30, p. 1991–1999, 2002. DOI: 10.1016/S0045-7949(02)00259-6.

213 MATTHIES, H. G.; STEINDORF, J. Partitioned Strong Coupling Algorithms for Fluid-Structure Interaction. **Computers and Structures**, Oxford, v. 81, n. 8-11, p. 805–812, 2003. DOI: 10.1016/S0045-7949(02)00409-1.

214 FERNÁNDEZ, M. A.; MOUBACHIR, M. A Newton Method Using Exact Jacobians for Solving Fluid-Structure Coupling. **Computers and Structures**, Oxford, v. 83, n. 2-3, p. 127–142, 2005. DOI: 10.1016/j.compstruc.2004.04.021.

215 MATTHIES, H. G.; NIEKAMP, R.; STEINDORF, J. Algorithms for Strong Coupling Procedures. **Computer Methods in Applied Mechanics and Engineering**, Amsterdam, v. 195, n. 17-18, p. 2028–2049, 2006. DOI: 10.1016/j.cma.2004.11.032.

216 KÜTTLER, U.; WALL, W. A. Fixed-Point Fluid-Structure Interaction Solvers with Dynamic Relaxation. **Computational Mechanics**, Heidelberg, v. 43, n. 1, p. 61–72, 2008. DOI: 10.1007/s00466-008-0255-5.

217 DEGROOTE, J.; BATHE, K. J.; VIERENDEELS, J. Performance of a New Partitioned Procedure versus a Monolithic Procedure in Fluid-Structure Interaction. **Computers and Structures**, Oxford, v. 87, n. 11-12, p. 793–801, 2009. DOI: 10.1016/j.compstruc.2008.11.013.

218 VIERENDEELS, J. et al. Implicit Coupling of Partitioned Fluid-Structure Interaction Problems with Reduced Order Models. **Computers and Structures**, Oxford, v. 85, n. 11-14, p. 970–976, 2007. DOI: 10.1016/j.compstruc.2006.11.006.

219 CAUSIN, P.; GERBEAU, J. F.; NOBILE, F. Added-Mass Effect in the Design of Partitioned Algorithms for Fluid-Structure Problems. **Computer Methods in Applied Mechanical Engineering**, Amsterdam, v. 194, n. 42-44, p. 4506–4527, 2005. DOI: 10.1016/j.cma.2004.12.005.

220 FÖRSTER, C.; WALL, W. A.; RAMM, E. Artificial Added Mass Instabilities in Sequential Staggered Coupling of Nonlinear Structures and Incompressible Viscous Flows. **Computer Methods in Applied Mechanics and Engineering**, Amsterdam, v. 196, n. 7, p. 1278–1293, 2007. DOI: 10.1016/j.cma.2006.09.002.

221 FERNÁNDEZ, M. A.; MULLAERT, J.; VIDRASCU, M. Explicit Robin-Neumann Schemes for the Coupling of Incompressible Fluids with Thin-Walled Structures. **Computer Methods in Applied Mechanics and Engineering**, Amsterdam, v. 267, p. 566–593, 2013. DOI: 10.1016/j.cma.2013.09.020.

222 BANKS, J. W.; HENSHAW, W. D.; SCHWENDEMAN, D. W. An Analysis of a New Stable Partitioned Algorithm for FSI Problems. Part I: Incompressible Flow and Elastic Solids. **Journal of Computational Physics**, Maryland, v. 269, p. 108–137, 2014. DOI: 10.1016/j.jcp.2014.03.006.

223 TUKOVI,. et al. Added Mass Partitioned FluidStructure Interaction Solver Based on a Robin Boundary Condition for Pressure. **OpenFOAM**, p. 1–22, 2019. DOI: 10.1007/978-3-319-60846-4_1.

224 RUTHERFORD, A. **Vectors, Tensors and the Basic Equations of Fluid Mechanics**. Dover Publications, 1962. p. 314.

225 TRUESDELL, C. **The Non-Linear Field Theories of Mechanics.** Springer, 2004.

226 FERZIGER, J. H.; PERI, M. **Computational Methods for Fluid Dynamics**. 3rd, rev. ed. Berlin ; New York: Springer, 2002.

227 CARDIFF, P.; KARA, A.; IVANKOVI, A. A Large Strain Finite Volume Method for Orthotropic Bodies with General Material Orientations. **Computer Methods in Applied Mechanics and Engineering**, Amsterdam, v. 268, p. 318–335, 2014. DOI: 10.1016/j.cma.2013.09.008.

228 TANG, T.; HEDEDAL, O.; CARDIFF, P. On Finite Volume Method Implementation of Poro-Elasto-Plasticity Soil Model. **International Journal for Numerical and Analytical Methods in Geomechanics**, Oxford, v. 39, n. 13, p. 1410–1430, 2015. DOI: 10.1002/nag.

229 SUSSMAN, T.; BATHE, K.-J. A Finite Element Formulation for Nonlinear Incompresible Elastic and Inelastic Analysis. **Computers and Structures**, Oxford, v. 26, p. 357–409, 1987.

230 BIJELONJA, I.; DEMIRDI, I.; MUZAFERIJA, S. A Finite Volume Method for Large Strain Analysis of Incompressible Hyperelastic Materials. **International Journal for Numerical Methods in Engineering**, Oxford, v. 64, p. 1594–1609, Nov. 2005. DOI: 10.1002/nme.1413.

231 FORMAGGIA, L. et al. On the Coupling of 3D and 1D Navier-Stokes Equations for Flow Problems in Compliant Vessels. **Computer Methods in Applied Mechanical Engineering**, Amsterdam, v. 191, p. 561–582, 2001.

232 LOZOVSKIY, A.; OLSHANSKII, M. A.; VASSILEVSKI, Y. V. Analysis and Assessment of a Monolithic FSI Finite Element Method. **Computers and Fluids**, Oxford, v. 179, p. 277–288, 2019. DOI: 10.1016/j.compfluid.2018.11.004.

233 COOMBS, W. M. et al. Overcoming Volumetric Locking in Material Point Methods. **Computer Methods in Applied Mechanics and Engineering**, Amsterdam, v. 333, p. 1–21, May 2018. DOI: 10.1016/j.cma.2018.01.010.

234 WHEEL, M. A. A Mixed Finite Volume Formulation for Determining the Small Strain Deformation of Incompressible Materials. **International Journal for Numerical Methods in Engineering**, Oxford, v. 44, p. 1843–1861, 1999.

235 ROACHE, P. J. Quantification of Uncertainty in Computational Fluid Dynamics. **Annual Review of Fluid Mechanics**, Palo Alto, v. 29, n. 1, p. 123–160, 1997. DOI: 10.1146/annurev.fluid.29.1.123.

236 OBERKAMPF, W. L.; TRUCANO, T. G. Verification and Validation in Computational Fluid Dynamics. **Progress in Aerospace Sciences**, Oxford, v. 38, n. 3, p. 209–272, 2002. DOI: 10.1016/S0376-0421(02)00005-2.

APPENDICES

Appendix A

MORPHOLOGICAL AND HEMODYNAMIC PARAMETERS

A.1 MORPHOLOGICAL PARAMETERS

The variability in shape and size of IAs sac surface make a challenge to characterize it morphologically. Commonly, physicians employ 1D metrics based on measurements performed on 2D projections of medical images. Several works, however, already proposed 3D size and shape parameters to study this disease (157, 33, 208).

In the sequence, the methodology proposed by Ma et al. (157) and Raghavan et al. (33) is briefly presented. Both works proposed several size and shape metrics of different dimensionaly, some of them interrelated. Fundamentally, their definition depend on the delineation of the *aneurysm neck* contour, Γ_{ia}, the 3D path that separates the aneurysm sac surface, S_{ia}, from the branches surface, S_b (153, 154). Ideally, a *plane* would be the most simple way to separate them, but a plane is almost impossible to find for all types of saccular IAs (154). Hence, several works already tried to delineate Γ_{ia} either automatically or manually.

Ma et al. (157) and Raghavan et al. (33) proposed their metrics based on a plane neck. Here, the definitions proposed by the authors were extended and based on a generic 3D Γ_{ia} defined as the boundary of S_{ia}, i.e. not necessarily one lying on a plane, as schematically shown in Fig. A.1. This approach was motivated by the use of a 3D Γ_{ia} in the phisical modeling of the thickness and material properties of an IA wall, as discussed in the main text. Nonetheless, they are still suitable for a relative comparison among the metrics in a single sample, which is the case here.

The contour Γ_{ia} is also the boundary of an imaginary surface that "closes" the orifice of the aneurysm lumen, called *ostium surface*, S_o, which, clearly, S_o is not a plane (110). Nevertheless,

a *global* normal directionl to this surface, $\boldsymbol{n}_o$, was defined as the area-average normal vector, i.e., $\boldsymbol{n}_o = \frac{1}{A_o}\int_{S_o} \boldsymbol{n}(\boldsymbol{x})\mathrm{d}A_o$. This approach broadly provides a direction line that transpasses the aneurysm sac in its longitudinal direction (see Fig. A.1).

Figure A.1 – Geometrical definitions of 1D size metrics used to characterize the sac surface of an IA, S_{ia}.

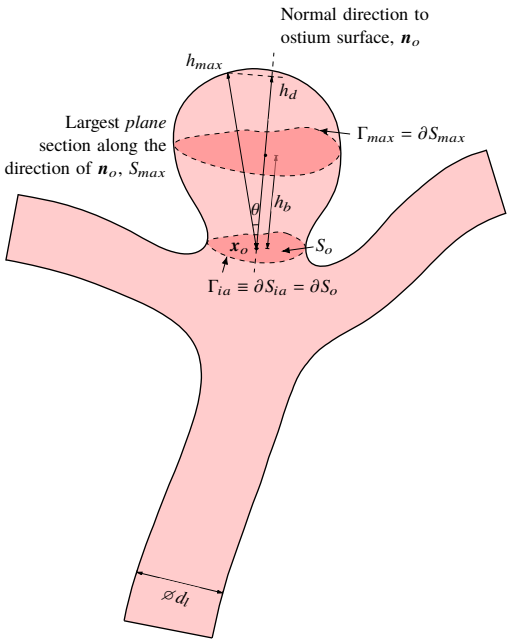

Source: Prepared by the author.

From the geometric center of S_o, $\boldsymbol{x}_o$, and its normal direction, three important 1D size metrics can be defined for any IA: the neck diameter and the sac's height and diameter.

The aneurysm neck diameter, d_n, was defined based on the definition of the *hydraulic diameter*, commonly used Fluid Mechanics, in which case:

$$d_n = \frac{4A_o}{P_o}, \tag{A.1}$$

where A_o and P_o are the surface area and perimeter of S_o, respectively.

The aneurysm height, h_d, was defined as the maximum perpendicular distance from $\boldsymbol{x}_o$ to S_{ia} points. It was calculated by, first, finding the maximum aneurysm height, h_{max}, and then projecting it into the direction of $\boldsymbol{n}_o$, as follows:

$$h_{max} = \max_{\boldsymbol{x}\in S_{ia}}(\|\boldsymbol{x} - \boldsymbol{x}_o\|) \rightarrow h_d = h_{max}\cos(\theta), \tag{A.2}$$

where θ is the angle between the direction of h_{max} and $\boldsymbol{n}_o$.

The diameter of the IA sac, d_d, was defined as the hydraulic diameter of the largest plane section, measured by its area, of S_{ia}, perpendicular to $\boldsymbol{n}_o$ and along its direction, labeled S_{max},

with area given by A_{max}. Being P_{max} the perimeter of its boundary contour, $\Gamma_{max} = \partial S_{max}$, d_d is then defined as follows:

$$d_d = \frac{4A_{max}}{P_{max}}\,. \tag{A.3}$$

Moreover, the height of S_{max} measured from $\boldsymbol{x}_o$ is known as the *bulge height*, h_b.

Two important 3D size metrics are the area of the sac surface, A_{ia}, and the volume enclosured by it and the ostium surface, V_{ia}. Moreover, an important entity in the 3D characterization of IAs is its *convex hull* (157). This can be imagined as the smallest convex surface that encompasses S_{ia} (literally, imagine an "elastic membrane" that covers the aneurysm surface), with surface area S_{ch} and volume V_{ch}. The convex hull was employed to charaterize the shape of an IA.

Based on these 1D and 3D size metrics, 1D and 3D *shape* metrics were defined and are listed in Table A.1, which also provides a short explanation of the meaning of the index or parameter and its range of definition.

Table A.1 – Mathematical definition, meaning, and range of 2D and 3D shape metrics proposed by different authors to characterize a saccular IA surface.

Index or Parameter	Mathematical Formulation	Meaning	Range
Aspect Ratio, *AR*	$\frac{h_d}{d_n}$	Elongated or more "bulky" IAs	$[0, \infty[$
Undulation Index, *UI*	$1 - \frac{V_{ia}}{V_{ch}}$	Quantifies the presence of blebs or lobular regions on the aneurysm surface (33)	$[0, 1]$
Non-sphericity Index, *NSI*	$1 - (18\pi)^{1/3}\frac{V_{ia}^{2/3}}{A_{ia}}$	Measures how close the aneurysm morphology is to a hemisphere (zero indicates a perfect hemisphere and one a collapsed aneurysm) (33)	$[0, 1]$
Ellipticity Index, *EI*	$1 - (18\pi)^{1/3}\frac{V_{ch}^{2/3}}{A_{ch}}$	Measures the ellipticity of S_{ia}; similar to the non-sphericity index, but uses the convex hull to avoid distortions caused by blebs (33)	$[0, 1]$

Source: Prepared by the author.

All metrics given above and in Table A.1 are rigorously *zeroth-order*, because they depend solely on the definition of the points of S — this is still true for discrete surfaces, the case here. Ma et al. (157) also defined curvature-based or *second-order* metrics of an IA surface, shown in Table A.2, because they depend on the curvature fields of the surface: the Gaussian and the mean curvature, defined in terms of second-order derivatives of the points on the surface. Note that the definitions presented in Table A.2 were given in terms of the points of a discrete S_{ia}, as

orignally proposed by Ma et al. (157).

Table A.2 – Mathematical definition, meaning, and range of 3D curvature-based shape metrics proposed by Ma et al. (157) to characterize a saccular IA surface.

Index or Parameter	Mathematical Formulation	Meaning	Range
Area-average Gaussian Curvature, *GAA*	$\sum_{i \in S_{ia}} K_i A_i \Big/ \sum_{i \in S_{ia}} A_i$	Area-average metric of the Gaussian curvature field, K, over the sac surface (157)	$]-\infty, \infty[$
Area-average Mean Curvature, *MAA*	$\sum_{i \in S_{ia}} H_i A_i \Big/ \sum_{i \in S_{ia}} A_i$	Area-average metric of the mean curvature field, H, over the sac surface (157)	$]-\infty, \infty[$
L2-norm Gaussian Curvature, *GLN*	$\frac{1}{4\pi}\sqrt{\sum_{i \in S_{ia}} A_i \left(\sum_{i \in S_{ia}} K_i^2 A_i \right)}$	Measures the degree of irregularities over the sac surface (157)	$[0, \infty[$
L2-norm Mean Curvature, *MLN*	$\frac{1}{4\pi}\sqrt{\sum_{i \in S_{ia}} H_i^2 A_i}$	Measures the degree of irregularities (157) over S_{ia}	$[0, \infty[$

Source: Prepared by the author.

A.2 HEMODYNAMIC WALL PARAMETERS

The physical and mathematical definitions of the WSS, $\boldsymbol{\tau}_w$, were given in the main text (Eq. (2.7)). However, as mentioned there, several other HWP are associated with other functions in the artery and aneurysms walls. A summary of the most relevant parameters that have already been associated with aneurysm growth or rupture is given in Table A.3, with also their mathematical definition and physical meaning.

Table A.3 – Hemodynamic wall parameters defined from the WSS and their physical meaning. Some of these parameters have been associated with aneurysm growth or rupture.

Name	Symbol	Mathematical Definiton	Physical Meaning
Time-averaged WSS	$TAWSS(\boldsymbol{x})$	$= \overline{\tau_w}(\boldsymbol{x}) = \frac{1}{T_c}\int_0^{T_c} \|\boldsymbol{\tau}_w\| \mathrm{d}t$	Averaged WSS over the cardiac cycle
Average Shear Direction	$\boldsymbol{p}$	$= \frac{\int_0^{T_c} \boldsymbol{\tau}_w(\boldsymbol{x},t)\mathrm{d}t}{\left\|\int_0^{T_c} \boldsymbol{\tau}_w(\boldsymbol{x},t)\mathrm{d}t\right\|}.$	Average direction of the $\boldsymbol{\tau}_w$ over the cardiac cycle
Transverse Shear Direction	$\boldsymbol{q}$	$= \boldsymbol{p} \times \boldsymbol{n}$	Orthogonal vector to $\boldsymbol{p}$ that is also tangent to the vascular surface (with normal $\boldsymbol{n}$)
Oscillatory Shear Index (OSI)	$OSI(\boldsymbol{x})$	$= \frac{1}{2}\left(1 - \frac{\left\|\frac{1}{T_c}\int_0^{T_c} \boldsymbol{\tau}_w \mathrm{d}t\right\|}{\frac{1}{T_c}\int_0^{T_c} \|\boldsymbol{\tau}_w\| \mathrm{d}t}\right)$	Quantifies the change in direction of $\boldsymbol{\tau}_w$ over time
WSS Pulsatility Index	$WSSPI(\boldsymbol{x})$	$= \frac{\max_{t\in[0,T_c]} \tau_w - \min_{t\in[0,T_c]} \tau_w}{TAWSS(\boldsymbol{x})}$	Quantifies the largest variations in τ_w over the cardiac cycle
Maximum WSS Temporal Gradient	$WSSTG(\boldsymbol{x})$	$= \max_{t\in[0,t]}\left(\frac{\partial \tau_w}{\partial t}\right)$	Maximum local temporal derivative of the WSS field (209)
Relative Residence Time (RRT)	$RRT(\boldsymbol{x})$	$= \left\|\frac{1}{T_c}\int_0^{T_c} \boldsymbol{\tau}_w(\boldsymbol{x},t)\mathrm{d}t\right\|^{-1}$	Quantify the state of disturbed flow adjacent to an artery wall
Surface Gradient of WSS	$\boldsymbol{G}(\boldsymbol{x},t)$	$= \left(\frac{\partial}{\partial \boldsymbol{p}}(\boldsymbol{\tau}_w \cdot \boldsymbol{p}), \frac{\partial}{\partial \boldsymbol{q}}(\boldsymbol{\tau}_w \cdot \boldsymbol{q})\right)$	Measures the tangetial gradient of $\boldsymbol{\tau}_w$ over time (209)
Surface Gradient of TAWSS	$TAWSSG(\boldsymbol{x})$	$= \boldsymbol{p} \cdot \nabla_t(TAWSS)$	Measures the tangential gradient of the TAWSS
Transversal WSS	$transWSS(\boldsymbol{x})$	$= \frac{1}{T_c}\int_0^{T_c} \|\boldsymbol{\tau}_w \cdot \boldsymbol{q}\| \mathrm{d}t$	Quantifies the component of $\boldsymbol{\tau}_w$ transversal to the average flow direction (210)
Aneurysm Formation Indicator (AFI)	$AFI(\boldsymbol{x},t)$	$= \frac{\boldsymbol{\tau}_w(\boldsymbol{x},t)}{\|\boldsymbol{\tau}_w\|} \cdot \boldsymbol{p}$	Potential indicator of aneurysm formation proposed by Mantha et al. (112)
Gradient Oscillatory Number (GON)	$GON(\boldsymbol{x})$	$= 1 - \frac{\left\|\int_0^{T_c} \boldsymbol{G}(\boldsymbol{x},t)\mathrm{d}t\right\|}{\int_0^{T_c} \|\boldsymbol{G}(\boldsymbol{x},t)\| \mathrm{d}t}$	Potential indicator of aneurysm formation proposed by Shimogonya et al. (104)

Source: Prepared by the author.

Appendix B

INSTABILITIES AND THE ADDED-MASS EFFECT IN FSI

As briefly explained at the beginning of Section 3.2, the two groups of methods to deal with coupled problems governed by partial differential equationss (PDEs) are divided in monolithic and partitioned strategies. The former consists of discretizing each PDE of the fluid, solid, and FSI interface together, in the same algebraic system, whereas the latter consists of solving the flow problem, the solid problem, separately and sequentially with the conditions at the fluid-solid interface obtained by interpolating each solution there.

The most classic formulation of this condition is called the *Dirichlet-Neumann formulation*, in which the BC at the "fluid side" of the FSI interface is a specified velocity field and at the "solid side" of the FSI interface a specified traction field, hence a Dirichlet and a Neumann-type BCs, respectively. On Λ^{fs}, the Dirichlet BC applied for the fluid domain is mathematically written after the kinematical condition that assures the continuity of the velocity field on this boundary, thus if $\boldsymbol{v}^{\mathrm{f}}$ is the blood flow velocity field and $\boldsymbol{u}$ the solid displacement field, the kinematical conditions reads:

$$(\boldsymbol{v}^{\mathrm{f}})_{\Lambda^{\mathrm{fs}}} = (\boldsymbol{v}^{\mathrm{s}})_{\Lambda^{\mathrm{fs}}} \equiv \left(\frac{\mathrm{d}\boldsymbol{u}}{\mathrm{d}t}\right)_{\Lambda^{\mathrm{fs}}} . \tag{B.1}$$

The Neumann BC at Λ^{fs} for the momentum equation of the solid domain consists in an imposed traction, $\boldsymbol{t}$, due to the dynamic condition of traction continuity at the interface, expressed as:

$$\underbrace{\left(\boldsymbol{\sigma}^{\mathrm{f}} \cdot \boldsymbol{n}^{\mathrm{f}}\right)_{\Lambda^{\mathrm{fs}}}}_{\boldsymbol{t}^{\mathrm{f}}} + \underbrace{(\boldsymbol{\sigma}^{\mathrm{s}} \cdot \boldsymbol{n}^{\mathrm{s}})_{\Lambda^{\mathrm{fs}}}}_{\boldsymbol{t}^{\mathrm{s}}} = \boldsymbol{0}, \tag{B.2}$$

where $\boldsymbol{\sigma}^{\mathrm{f}}$ and $\boldsymbol{\sigma}^{\mathrm{s}}$ are the Cauchy stress tensors of the fluid and solid domains, respectively (we

use the superscripts “f” and “s” from here on to indicate fluid and solid variables, respectively). In Eq. (B.2), $\boldsymbol{n}^{\mathrm{f}}$ and $\boldsymbol{n}^{\mathrm{s}}$ are the outwards normal vectors on Λ^{fs} of the solid and fluid domains, respectively.

Partitioned strategies are very appealing because they allow the reuse of already implemented algorithms, which are possibly optimized, to solve the different “partitions” of the coupled system (where partition in this case was defined by Felippa et al. (119) and indicates the different physics models that are present in the coupled problem, in this case the fluid and solid). Hence, the remaining work to be done would be to couple the discretized system of equations for each partition, i.e. roughly to make each sub-problem aware of the other but seeking to achieve an equilibrium between the solutions in each partition.

FSI problems are naturally unsteady or have a transient followed by a steady state, hence the time-advancing techniques must be used for them. If partitioned algorithms will be used, the simplest idea to solve these problems would be a *staggered solution* approach, in which the fluid and solid sub-problems are solved sequentially by using already computed values, i.e. explicitly once per time-step, a definition given early by Wall et al. (211). The success of this type of algorithm depends on the physics of the FSI problem, for example, if the solid is much heavier and/or stiffer than the fluid. Thus, this technique can be successfully applied in aeroelasticity problems. However, for some specific FSI problems, as it was early noted, they may suffer from instabilities and, hence, several sub-iterations were needed to achieve the equilibrium of the FSI interface by performing interpolations, or mappings, of the mechanical variables involved in Eqs. (B.1) and (B.2) between the FSI interface of each computational mesh. In general, the former is called “loosely” or “weakly coupled” approach, whereas the latter “strongly coupled” approach.

Early works tried to enhance this strategy by formulating the FSI coupled system with a fixed-point formulation, using thus Picard iterations to sub-iterate in each time-step, or block-Newton techniques to solve the system, even if the Jacobian of each sub-problem was not known, due to “black-box” solvers, for example (212–215). Others tried to use fixed- or dynamic- relaxation approaches to couple the fluid and solid sub-problems, as thoroughly explained by Küttler et al. (216). One of the most common approaches is the so-called “Aitken’s dynamic relaxation”. In this line of works, more advanced techniques were proposed in the beginning of the last decade based primarily on Newton or quasi-Newton methods (214). Degroote et al. (217), for example, proposed a robust technique called Interface Quasi-Newton-Implicit Jacobian Least-Squares

(IQN-ILS) to effectively solve the discretized nonlinear system of equations written for the FSI interface nodes and, hence, predicting the equilibrium position of the FSI interface per time-step using a quasi-Newton method and an approximation of the inverse Jacobian of the system with a technique developed by Vierendeels et al. (218).

Deeper investigations into the numerical nature of the FSI coupling revealed the sources of the instabilities that may arise even when strongly coupled techniques are used. Early reports from numerical experiments (219) identified the occurrence of instabilities depending on the physical parameters of the problem and irrespective of the time-step used in the time-marching schemes — this behavior was considered abnormal because, as the time-step is reduced in explicit time-marching techniques, the instabilities were expected to disappear.

Causin et al. (219) investigated the sources of this instability for incompressible fluid flows coupled with light structures using the common Dirichlet-Neumann formulation. They showed that the interaction of the fluid on the structure occurs through the so-called "added-mass operator" (the name stems from the fact that the operator effectively acts as an extra mass on the solid deformation equations). They subsequently showed that the stability of explicit and implicit time-marching schemes depends upon the eigenvalues of the added-mass operator, which is purely geometrical, and the ratio of the fluid and solid densities. While Causin et al. (219) used a simplified linear coupled problem, a later work by Förster et al. (220) derived the added-mass operator for an incompressible viscous fluid flow with a structure modeled as a nonlinear material under large displacements. Their derivations were performed in a generic spatial discretization framework by separating the degrees of freedom of the interior domain and those of the FSI interface. The authors found an explicit form of the added-mass operator:

$$\boldsymbol{f}_{\Lambda^{\mathrm{fs}}} = m^{\mathrm{f}} \boldsymbol{\mathcal{M}}_{\mathbf{a}} \frac{\mathrm{d}\boldsymbol{v}^{\mathrm{f}}_{\Lambda^{\mathrm{fs}}}}{\mathrm{d}t}, \tag{B.3}$$

where $\boldsymbol{f}_{\Lambda^{\mathrm{fs}}}$ is the force on the FSI interface that is going to be transferred to the solid partition, $\frac{\mathrm{d}\boldsymbol{v}^{\mathrm{f}}_{\Lambda^{\mathrm{fs}}}}{\mathrm{d}t}$ is the acceleration of the FSI interface, m^{f} is the mass of the fluid, and $\boldsymbol{\mathcal{M}}_{\mathbf{a}}$ is the added-mass operator. The force $\boldsymbol{f}_{\Lambda^{\mathrm{fs}}}$ is the one effectively passed to the solid interface in the course of the sequential procedure and, hence, we can see that the operator $\boldsymbol{\mathcal{M}}_{\mathbf{a}}$ can act as an amplifier.

The authors go further and investigate the influence of the temporal discretization schemes on the onset of the instability, concluding with the following condition for the procedure to be unstable:

$$\frac{m^{\mathrm{f}}}{m^{\mathrm{s}}} \max_i \left(\mu_{\mathrm{a}}\right)_i > C_{inst}, \tag{B.4}$$

where μ_{a} are the eigenvalues of $\boldsymbol{\mathcal{M}}_{\mathbf{a}}$, m^{s} is the mass of the solid part, and C_{inst} is a constant that depends on the time-discretization approach for the fluid and solid problems, but also on the solid predictor discretization. It is important to highlight that their analysis was independent of the spatial discretization. More importantly, the aforementioned works show the existence of cases that are unconditionally unstable depending on the combination of physical, geometric, and time-marching parameters.

While strongly coupled approaches may be appropriate to solve FSI problems with a "large" added-mass operator, current studies on the subject have also turned attention to the continuous formulation of the FSI coupling condition. Most of the studies based their techniques on the Dirichlet-Neumann formulation, nevertheless others are possible. Some works used both Robin-Neumann and Robin-Robin formulations of the FSI problem, which employs a Robin, or BC of third type, on the FSI interface for the flow pressure. Some works showed that these formulations can be more stable, yielding to smaller added-mass instabilities due to the increased level of coupling they cause on the FSI interface (221–223).

As noted before, the instabilities that arise in FSI in flexible tubes are also related to the incompressibility of the fluid. A recent work by La Spina et al. (163) showed that compressible fluid models have better properties with respect to the added-mass operator. They showed that the form of the $\boldsymbol{\mathcal{M}}_{\mathbf{a}}$ for a weakly compressible fluid model has smaller eigenvalues, μ_{a}, therefore increasing the range of solvable FSI problems, as can be seen by Eq. (B.4).

Appendix C

CONCEPTS OF FINITE-DEFORMATION CONTINUUM MECHANICS

C.1 MOTION AND DEFORMATION

Consider a material body domain, Ω, with boundary surface $\Lambda \equiv \partial\Omega$, moving in space — the word "material" is used here because the description presented in this appendix applies to the motion of materials typically characterized either as solids or fluids.

The most common approaches to describe the motion of this body are (224, 168):

- the *material description*, which identify each "material particle", ξ, and describe its motion over time t;
- the *referential description*, which requires the definition of an arbitrary reference configuration of the material where the particle ξ occupies the position $\boldsymbol{\xi}$. The coordinate system associated with $\boldsymbol{\xi}$ is used to describe the motion. For example, in Elasticity, it is natural to chose the undeformed state of an elastic solid as the reference configuration, because the solid will return to this state when unloaded. If the reference is the solid at $t = 0$, this description is then called *Lagrangian description*;
- the *spatial description* uses the spatial coordinates system, $\boldsymbol{x}$, to identify the particle motion, i.e. the independent variable are the spatial coordinates of the particle ξ. This is the so-called *Eulerian description*, mainly used in Fluid Mechanics and Plasticity theories.

The material and Lagrangian descriptions are usually used interchangeably, because the coordinates $\boldsymbol{\xi}$ are used as labels for material particles, identifying each point in the body. Mathematically, $\boldsymbol{\xi}$ can be seen as a coordinate system attached to the body at time $t = 0$. The

material coordinate system can be viewed as "attached" to the body, and, hence, each coordinate $\boldsymbol{\xi}$ identifies the particle ξ at the instant t. In this text, we assume that $\boldsymbol{\xi}$ is the system attached to the *initial configuration* of the body.

The body's motion is characterized, then, by the function:

$$\boldsymbol{x} = \boldsymbol{x}(\boldsymbol{\xi}, t)\,. \tag{C.1}$$

Equation (C.1) expresses that the material particle, ξ, identified with the coordinate $\boldsymbol{\xi}$ at the time zero occupies the spatial position $\boldsymbol{x}$ at time t. Figure C.1 shows an example of a bar deformed by an external force $\boldsymbol{f}$ with its initial configuration defined by a set of Cartesian coordinates as $\boldsymbol{\xi} = \boldsymbol{x}(\boldsymbol{\xi}, 0)$ and the current configuration, i.e. the solid deformed at instant t, showing that the isolines of the system $\boldsymbol{\xi}$ are also deformed with the solid.

In Solid Mechanics, the Lagrangian description has been classically used. Therefore, all the differential operators in the equations derived below were calculated as functions of the material coordinates, $\boldsymbol{\xi}$. This approach is also called *total Lagrangian* by some authors (160), where all mechanical variables, such as stresses and deformations, are referred to the initial configuration of the solid. We will see below the different forms of expressing these quantities in terms of the undeformed and deformed configuration. When the stresses, strains, and all other mechanical variables are calculated with respect to the current configuration, the description is named *updated Lagrangian* (160).

Figure C.1 – Motion of a solid bar deformed by an external force $\boldsymbol{f}$, showing the initial (reference) configuration (left) with isolines of the coordinate system $\boldsymbol{\xi}$ attached to the solid and the current configuration (right) with the system $\boldsymbol{\xi}$ also deformed.

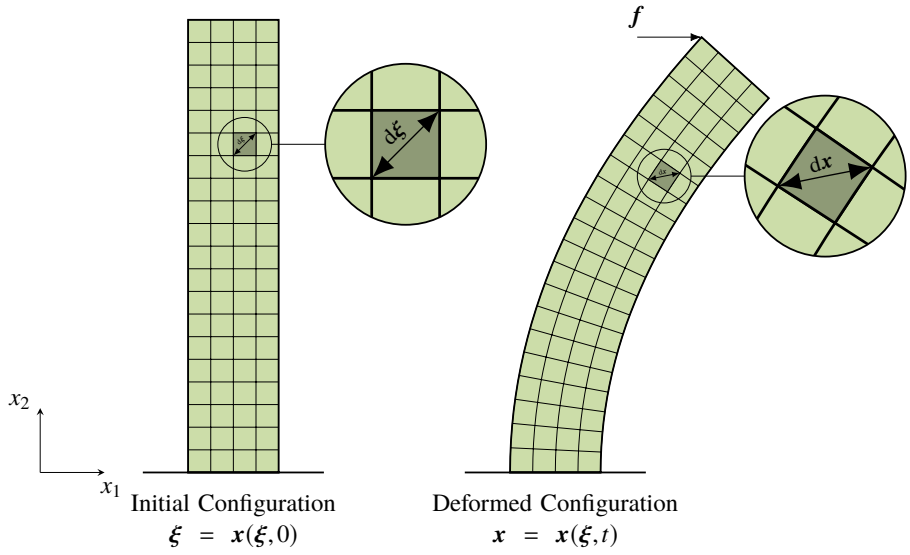

Source: Prepared by the author.

A fundamental measure of deformation, i.e. changes in size and shape of Ω, in the neighborhood of a point, as described by Eq. (C.1), is the *deformation gradient tensor*, $\boldsymbol{F}$ (225), a second-order tensor with components given by the components of the Jacobian matrix of the motion function:

$$\boldsymbol{F} = \frac{\partial \boldsymbol{x}}{\partial \boldsymbol{\xi}}(\boldsymbol{\xi}, t) = \nabla_0 \boldsymbol{x}\,, \tag{C.2}$$

where the subscript "0" is used to represent differential operators evaluated with reference to the initial material configuration. Hence, by using Einstein's index notation:

$$\nabla_0(\bullet) \equiv \boldsymbol{e}_{(i)} \frac{\partial(\bullet)}{\partial \xi_i}\,, \tag{C.3}$$

if a Cartesian coordinate system is used for the initial configuration with basis vector $\boldsymbol{e}_{(i)}$. The components of $\boldsymbol{F}$ are then given by:

$$F_{ij} = \frac{\partial x_i}{\partial \xi_j}(\xi_j, t)\,, \tag{C.4}$$

if $\boldsymbol{x}$ and $\boldsymbol{\xi}$ are both Cartesian coordinates systems — for a rigorous proof of its tensorial character, see Malvern (168).

The deformation gradient associates an arbitrary material line element at the initial configuration, $\mathrm{d}\boldsymbol{\xi}$, to the same line element at the current configuration (see Fig. C.1) as follows:

$$\mathrm{d}\boldsymbol{x} = \boldsymbol{F} \cdot \mathrm{d}\boldsymbol{\xi}\,. \tag{C.5}$$

Additionally, the determinant of $\boldsymbol{F}$ is known as the Jacobian of the motion, $J = \det(\boldsymbol{F})$ and gives the rate of change of an infinitesimal volume element.

The displacement field, $\boldsymbol{u}$, is defined as:

$$\boldsymbol{u} = \boldsymbol{x}(\boldsymbol{\xi}, t) - \boldsymbol{x}(\boldsymbol{\xi}, 0) \equiv \boldsymbol{x} - \boldsymbol{\xi}\,. \tag{C.6}$$

By using Eq. (C.2), from Eq. (C.6), follows:

$$\boldsymbol{F} = \frac{\partial(\boldsymbol{u} + \boldsymbol{\xi})}{\partial \boldsymbol{\xi}} = \nabla_0 \boldsymbol{u} + \boldsymbol{I}\,, \tag{C.7}$$

where $\boldsymbol{I}$ is the second-order identity tensor $\boldsymbol{I} = \delta_{ij}\boldsymbol{e}_i\boldsymbol{e}_j$, in dyadic notation, with δ_{ij} the Kronecker's delta.

The deformation gradient is one of the tensors that can be used as a deformation measurement in the theory of constitutive equations, for example. Even being one of the most fundamentals,

it is not the most suitable one (225). As Malvern (168) and other authors highlight, caution is necessary when using it, because it includes complete information of the deformation, i.e. strains and rotations. Since pure rotation does not induce any stresses on the material, a proper strain measurement to be used in constitutive theories — i.e. a relationship between strain and stresses — should vanish in rigid-body rotation. The deformation gradient does not possess this property and, thus, more appropriate strain measurements must be defined. Nevertheless, it is important to note that rotations play a prominent role in nonlinear solid mechanics since this particular type of motion may be responsible for a significant part of the deformation.

Figure C.1 shows the line segments vectors at the initial and current configurations, $\mathrm{d}\boldsymbol{\xi}$ and $\mathrm{d}\boldsymbol{x}$, respectively. Based on these segments, the Green — or Green-Lagrange — strain tensor is defined as follows (160):

$$2\mathrm{d}\boldsymbol{\xi}\cdot\boldsymbol{E}\cdot\mathrm{d}\boldsymbol{\xi} = \underbrace{\mathrm{d}\boldsymbol{x}\cdot\mathrm{d}\boldsymbol{x}}_{\substack{\text{Squared length,}\\ (\mathrm{d}L)^2\text{, in the}\\ \text{deformed}\\ \text{configuration}}} - \underbrace{\mathrm{d}\boldsymbol{\xi}\cdot\mathrm{d}\boldsymbol{\xi}}_{\substack{\text{Squared length,}\\ (\mathrm{d}L_0)^2\text{, in the}\\ \text{initial}\\ \text{configuration}}} , \tag{C.8}$$

which, as indicated, measures the change in the squared length of a material line vector, $(\mathrm{d}L_0)^2 = \mathrm{d}\boldsymbol{\xi}\cdot\mathrm{d}\boldsymbol{\xi}$, to the current length of the same line segment, $(\mathrm{d}L)^2 = \mathrm{d}\boldsymbol{x}\cdot\mathrm{d}\boldsymbol{x}$. By substituting Eq. (C.5) in Eq. (C.8), after some manipulations, follows:

$$\boldsymbol{E} = \frac{1}{2}\left(\boldsymbol{F}^{\mathrm{T}}\cdot\boldsymbol{F} - \boldsymbol{I}\right) . \tag{C.9}$$

From Eq. (C.9), it is immediate to verify that $\boldsymbol{E}$ is a symmetric second-order tensor. Moreover, in rigid-body motion, in which by definition the distance between two particles is preserved, the deformation gradient reduces to the so-called *rotation tensor*, $\boldsymbol{R}$, an orthogonal tensor (167). Hence, $\boldsymbol{F}^{\mathrm{T}}\cdot\boldsymbol{F} = \boldsymbol{I}$, which leads to $\boldsymbol{E} = \boldsymbol{0}$. Due to this property, $\boldsymbol{E}$ is commonly employed in constitutive theories.

It is possible to find a relationship between the Green strain tensor to the displacement $\boldsymbol{u}$ by substituting Eqs. (C.2) and (C.6) into Eq. (C.9), which yields:

$$\boldsymbol{E} = \frac{1}{2}\left[\nabla_0\boldsymbol{u} + (\nabla_0\boldsymbol{u})^{\mathrm{T}} + \nabla_0\boldsymbol{u}\cdot(\nabla_0\boldsymbol{u})^{\mathrm{T}}\right] . \tag{C.10}$$

In Eq. (C.10), it is easy to note the intrinsic nonlinear characteristic of finite-deformation strain measurements, mentioned in the main text, but implicit in the equations. This is referred as *geometric nonlinearity*, to avoid confusion with *material nonlinearity*, i.e. when a particular

constitutive equation is also nonlinear, but written in terms of $\boldsymbol{E}$, or other finite-deformation measurement.

While the Green strain tensor measures the *change* in the length of a material line segment, the so-called *right Cauchy-Green deformation tensor*, $\boldsymbol{C}$ measures the *new length*, $(\mathrm{d}L)^2 = \mathrm{d}\boldsymbol{x} \cdot \mathrm{d}\boldsymbol{x}$, in terms of the material coordinates $\boldsymbol{\xi}$:

$$(\mathrm{d}L)^2 = \mathrm{d}\boldsymbol{\xi} \cdot \boldsymbol{C} \cdot \mathrm{d}\boldsymbol{\xi} \,, \tag{C.11}$$

from which follows:

$$\boldsymbol{C} = \boldsymbol{F}^{\mathrm{T}} \cdot \boldsymbol{F} \,. \tag{C.12}$$

Therefore, comparing Eq. (C.9) with Eq. (C.12), one finds:

$$2\boldsymbol{E} = \boldsymbol{C} - \boldsymbol{I} \,. \tag{C.13}$$

Similar to the right Cauchy-Green deformation tensor, there is also the *left* Cauchy-Green deformation tensor, $\boldsymbol{B}$, defined as follows:

$$\boldsymbol{B} = \boldsymbol{F} \cdot \boldsymbol{F}^{\mathrm{T}} \,. \tag{C.14}$$

Both $\boldsymbol{C}$ and $\boldsymbol{B}$ are important measurements of deformation and their difference lies on the different coordinates where they are defined: a closer inspection of Eqs. (C.12) and (C.14) shows that $\boldsymbol{C}$ is defined in terms of material coordinates whereas $\boldsymbol{B}$ in terms of spatial coordinates (167).

Small-strain Formulation

It is very instructive to relate the quantities defined above to the more classical strain and deformation measurements commonly employed in Solid Mechanics, such as the *engineering strain tensor*, $\boldsymbol{\varepsilon}$, and the *true or logarithmic strain tensor*, $\boldsymbol{e}$. The correct use of these measurements resides in the hypothesis that the displacements and displacement gradients are very small or, rigorously, infinitesimal. In metal elasticity, for example, this is a good approximation, hence the "small-strain" theory, as it is normally called, can be used with enough accuracy.

If the components of the displacement gradient tensor are sufficiently smaller than the unity, the quadratic term in Eq. (C.10) is much smaller then its linear counterpart. In this case, the

Green strain tensor reduces to:

$$\boldsymbol{E} \approx \frac{1}{2}\left(\nabla_0 \boldsymbol{u} + \nabla_0^{\mathrm{T}} \boldsymbol{u}\right), \tag{C.15}$$

which is precisely the definition of the engineering strain tensor:

$$\boldsymbol{\varepsilon} = \frac{1}{2}\left(\nabla_0 \boldsymbol{u} + \nabla_0^{\mathrm{T}} \boldsymbol{u}\right). \tag{C.16}$$

It is interesting to note that, for the small-strain theory, the hypothesis of small gradient displacements yield $\boldsymbol{F} \approx \boldsymbol{I}$ by Eq. (C.7), and hence, by Eq. (C.5), $\mathrm{d}\boldsymbol{x} \approx \mathrm{d}\boldsymbol{\xi}$, i.e. the material and spatial coordinates coincide. Furthermore, note that small displacement gradient implies small strains and small *rotations*, which is not always the case.

C.2 STRESS

Consider the undeformed configuration of the body's domain, Ω_0, given in Fig. C.2, under the action of external forces on its boundary, Λ_0, that deform it to the current configuration, Ω. The figure shows an internal cross section of the body, with area $\mathrm{d}S$ and outward unit normal $\boldsymbol{n}$, where the resulting internal force is $\mathrm{d}\boldsymbol{f}$.

Figure C.2 – Generic deformation of a material domain at the undeformed configuration, Ω_0, and the deformed one, Ω, by external forces, with the detail of the resulting internal force on a section with initial area $\mathrm{d}S_0$ and outwards unit normal $\boldsymbol{n}_0$.

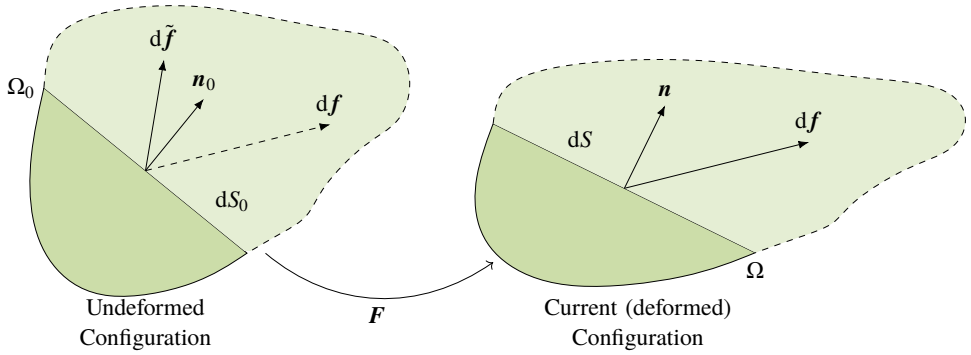

Source: Prepared by the author.

By definition, the traction, $\boldsymbol{t}_0$, applied on section $\mathrm{d}S_0$, and the traction on the current area, $\boldsymbol{t}$, are related to $\mathrm{d}\boldsymbol{f}$ as follows:

$$\mathrm{d}\boldsymbol{f} = \boldsymbol{t}_0 \mathrm{d}S_0 = \boldsymbol{t}\,\mathrm{d}S\,. \tag{C.17}$$

According to the Cauchy hypothesis, if $\boldsymbol{\sigma}$ is the Cauchy stress tensor, or true stress, in that

infinitesimal section dS, then (224, 168):

$$\boldsymbol{t} = \boldsymbol{n} \cdot \boldsymbol{\sigma} \,. \tag{C.18}$$

By combining Eqs. (C.17) and (C.18), follows:

$$\mathrm{d}\boldsymbol{f} = \boldsymbol{t}\mathrm{d}S = \boldsymbol{n} \cdot \boldsymbol{\sigma}\mathrm{d}S \,. \tag{C.19}$$

Equation (C.19) shows that the Cauchy stress tensor measures the stress state with reference to the current configuration of the material, since it depends on the current area dS and current traction.

Another important stress measurement is the *nominal stress*, $\boldsymbol{P}$, a multiaxial extension of the engineering stress in the small-strain theory. It is defined similarly to Eq. (C.19), however it yields the actual force d$\boldsymbol{f}$ on the *undeformed infinitesimal area*, S_0:

$$\mathrm{d}\boldsymbol{f} = \boldsymbol{t}_0\mathrm{d}S_0 = \boldsymbol{n}_0 \cdot \boldsymbol{P}\mathrm{d}S_0 \,. \tag{C.20}$$

The nominal stress tensor is very useful to be employed with the governing equations for a material motion when they are written in terms of the initial undeformed configuration. Nevertheless, it is not a symmetric tensor, thus it is not traditionally used to construct constitutive equations when symmetric strain measures are preferred. The transpose of the nominal stress is also know as the *first Piola-Kirchhoff stress tensor*.

The *second Piola-Kirchhoff stress tensor*, $\boldsymbol{S}$, is commonly used in finite-deformation solid mechanics and is also defined in terms of the undeformed configuration, thus useful to represent the motion in terms of the material coordinates, and it is a symmetric tensor. By definition, $\boldsymbol{S}$ is based on a *transformed force*, d$\tilde{\boldsymbol{f}}$, acting on the undeformed infinitesimal area:

$$\mathrm{d}\tilde{\boldsymbol{f}} \equiv \boldsymbol{F}^{-1} \cdot \mathrm{d}\boldsymbol{f} = \boldsymbol{F}^{-1} \cdot \boldsymbol{t}_0\mathrm{d}S_0 = \boldsymbol{n}_0 \cdot \boldsymbol{S}\mathrm{d}S_0 \,, \tag{C.21}$$

where $\boldsymbol{F}^{-1}$ is the inverse of the deformation gradient tensor. Therefore, the second-order tensor $\boldsymbol{S}$ relates the force d$\tilde{\boldsymbol{f}} = \boldsymbol{F}^{-1} \cdot \mathrm{d}\boldsymbol{f}$ (see Fig. C.2) to the undeformed area. Note that the "fictitious" force, d$\tilde{\boldsymbol{f}}$, depends on the material motion, i.e. it "follows" the material motion. As a consequence, the second Piola-Kirchhoff stress tensor remains "frozen" on the material in a rigid-body rotation.

When deriving the governing equations of motion and constitutive equations, it is usually useful to transform the different forms of stress. To this end, Nanson's formula is essential

because it relates an infinitesimal undeformed section area, $\mathrm{d}S_0$, of the material with the corresponding deformed one, $\mathrm{d}S$ (168):

$$\boldsymbol{n}\mathrm{d}S = J\boldsymbol{n}\cdot\boldsymbol{F}^{-1}\mathrm{d}S_0\,, \tag{C.22}$$

where $J = \det(\boldsymbol{F})$. By identifying Eqs. (C.19) and (C.20) and using Eq. (C.22), follows the relation between $\boldsymbol{\sigma}$ and $\boldsymbol{P}$:

$$\boldsymbol{\sigma} = \frac{1}{J}\boldsymbol{F}\cdot\boldsymbol{P}\,. \tag{C.23}$$

Similarly, the relationship between $\boldsymbol{S}$ and $\boldsymbol{P}$ can be found based on their definition and Nanson's equation, leading to:

$$\boldsymbol{P} = \boldsymbol{S}\cdot\boldsymbol{F}^{\mathrm{T}}\,. \tag{C.24}$$

Finally, by combining Eqs. (C.23) and (C.24), $\boldsymbol{S}$ is related to the Cauchy stress through the equation:

$$\boldsymbol{\sigma} = \frac{1}{J}\boldsymbol{F}\cdot\boldsymbol{S}\cdot\boldsymbol{F}^{\mathrm{T}}\,. \tag{C.25}$$

C.3 CONSTITUTIVE LAWS

Although one of the main subjects in this work are hyperelastic constitutive laws, it is important to put this subject into context by presenting typical elastic constitutive laws for large-strain motion — especially those that were already used to study IAs.

An *ideal* elastic solid, by definition, recovers its original undeformed state, or *natural state*, when unloaded. Moreover, the loading on the body induces a stress state distribution that depends *only on the current strain state and not on the history of deformation*. Thus, an ideally elastic solid is *path-independent*. Furthermore, the loading and unloading curves of its stress-strain relationship, for uniaxial loading, coincide, implying that the deformation process is *reversible*, in a purely mechanical sense.

The classic ideal constitutive relation for an elastic response is a linear relationship between a stress and a strain measure, usually taken with reference to the natural or undeformed configuration. In finite-deformation elasticity, the usual chosen ones are the Green-Lagrange strain, $\boldsymbol{E}$, and the second Piola-Kirchhoff stress, $\boldsymbol{S}$, tensors, with a relationship given by:

$$\boldsymbol{S} = \mathbb{C}\colon\boldsymbol{E}\,, \tag{C.26}$$

where $\mathbb{C}$ is a fourth-order tensor of elastic moduli with its components depending on the material

properties and "$:$" represents a tensorial double contraction.

A solid that obeys Eq. (C.26) when loaded is called a *Kirchhoff or Saint Venant-Kirchhoff solid* (160) and this form of equation describes a fully anisotropic representation of the solid, characterized by the $3^4 = 81$ components of $\mathbb{C}$, which are all constants in this case. Under the *elastic symmetry* hypothesis applied to the material (168, 167), the number of constants can be reduced. For example, since $\boldsymbol{S}$ and $\boldsymbol{E}$ are symmetric tensors, C exhibits *minor symmetries* reducing to 36 constants. If the material has one plane of symmetry, then this number is further reduced to 21 independent constants. If the material is *orthotropic* — three mutually orthogonal planes of symmetry, for example, a laminated steel — then there are only 9 independent constants.

By assuming that the material is isotropic, i.e. when there are no preferred directions, it can be shown that Eq. (C.26) reduces to:

$$\boldsymbol{S} = 2\mu^{\mathrm{s}}\boldsymbol{E} + \lambda^{\mathrm{s}}\,\mathrm{tr}\,(\boldsymbol{E})\boldsymbol{I}\,, \tag{C.27}$$

where the constants μ^{s} and λ^{s} are known as the Lamé's constants of the solid and are related to the Young's modulus and Poisson's ratio:

$$\mu^{\mathrm{s}} \equiv G = \frac{E}{2(1+\nu^{\mathrm{s}})} \tag{C.28}$$

$$\lambda^{\mathrm{s}} = \begin{cases} \dfrac{\nu^{\mathrm{s}}E}{(1+\nu^{\mathrm{s}})(1-\nu^{\mathrm{s}})} & \text{plane stress state} \\ \dfrac{\nu^{\mathrm{s}}E}{(1+\nu^{\mathrm{s}})(1-2\nu^{\mathrm{s}})} & \text{plane strain and 3D cases} \end{cases} \tag{C.29}$$

Note that the first Lamé constant is identified with the shear modulus, G, of the solid and the second one depends on the stress and strain states on the solid.

The Kirchhoff law is a generalization of Hooke's law for large deformations and large rotations. The Green strain tensor is suitable for any measure of strain and it vanishes for pure rigid-body rotations and the second Piola-Kirchhoff stress tensor is frozen on the material when it executes a pure rotation. Therefore, they are suitable for large deformations of a solid body.

In the small-strain regime, whose conditions were outlined above, the Green strain tensor reduces to the engineering strain tensor and, from Eq. (C.7), follows that the deformation gradient is approximately equal to the second-order identity tensor, hence from Eq. (C.5) it follows that there is no difference between the current and material coordinates and $\boldsymbol{S}$ can be replaced by the Cauchy stress — this also follows from Eq. (C.25) — in Eq. (C.27) to find the constitutive equation for an isotropic elastic solid for small strain and small rotations, which is the traditional

form known as Hooke's law:

$$\boldsymbol{\sigma}^{s} = 2\mu^{s}\boldsymbol{\varepsilon} + \lambda^{s}\,\mathrm{tr}(\boldsymbol{\varepsilon})\boldsymbol{I}\ . \tag{C.30}$$

This theory have been classically used to study metals deformation, but cannot be assumed *a priori* about the deformation of an IA wall.

Appendix D

THERMODYNAMICAL FOUNDATIONS OF HYPERELASTICITY

Assume again the same material body domain Ω used in Appendix C, performing a motion characterized by Eq. (C.1). This chapter presents an analysis of the motion from a Thermodynamics point of view. The procedure closely follows the one explained in Malvern (168). First, it is postulated that a fundamental relationship for the intensive specific internal energy, u, of the body is given as the following functional form:

$$u = u(s, \upsilon_j)\,, \tag{D.1}$$

with $j = 1, 2, ..., m$, where s is the specific entropy and υ_j is called a *thermodynamic substate* (168).

In Classical Thermodynamics, when viewed in terms of basic postulates, one of the most fundamental ones says that the internal energy of a system — here, the continuum body Ω —, U, is a function of its entropy, S, the volume, V, and the quantity of matter, which can be given in moles per chemical species, N_i, in the system, for example. Thus, the thermodynamic state of this system is fully specified by $n + 2$ independent quantities, with n the number of chemical species in the system. For the body Ω, we assume only one pure substance, i.e. $n = 1$. Consequently, the fundamental equation can be transformed to the intensive base, as follows:

$$U = U\,(S, V, N_i) \quad \Rightarrow \quad u = u\,(s, v)\ . \tag{D.2}$$

Note the similarity between Eq. (D.2) and the one postulated for a continuum body, Eq. (D.1). Their comparison helps to clarify what is the meaning of the thermodynamic substates υ_j: general mechanical quantities — in a broader sense, electromagnetic quantities too — that can

change the internal energy of the system. The specific volume can be one of them: the volume is a geometric parameter that, when changed due to an internal pressure, produces work. We left υ_j generic in Eq. (D.1) because they can be identified with different quantities depending on the problem being studied.

Equation (D.1) can be found by extending Eq. (D.5) to account for different *generalized displacements*, Υ_j, where j is the index of different sources of those displacements. These can be associated with different sources of work transfer when conjugated with *thermodynamic tensions*, τ_j. In this case, the fundamental relation for any system assumes the following functional form:

$$U = U\left(S, \Upsilon_j, N_i\right) \qquad i = 1, 2, \ldots n \;\; j = 1, 2, \ldots m\,, \tag{D.3}$$

which is the general form of the fundamental equation of Thermodynamics in energy representation. It can be shown that the changes in internal energy are then given by:

$$\mathrm{d}U = T\mathrm{d}S + \sum_j \tau_j \delta\Upsilon_j + \sum_i \mu_i \delta N_i\,. \tag{D.4}$$

For a single pure substance, Eq. (D.3) can be written in intensive base, as follows:

$$u = u\left(s, \upsilon_j\right) \qquad i = 1 \;\; j = 1, 2, \ldots m\,, \tag{D.5}$$

where $\upsilon_j = \dfrac{\Upsilon_j}{m}$ are the thermodynamic substates that can be interpreted as generalized displacements, per unit of the system mass, m, that are related to the work interactions through the system boundaries.

In this case, Eq. (D.4) yields:

$$\mathrm{d}u = T\mathrm{d}s + \sum_j \tau_j \delta\upsilon_j\,. \tag{D.6}$$

Note that τ_j is a potential that produces work, per unit mass, associated with its conjugate variable υ_j. Therefore, it follows that:

$$T = \left(\frac{\partial u}{\partial s}\right)_{\upsilon_j} \tag{D.7}$$

and

$$\tau_j = \left(\frac{\partial u}{\partial \upsilon_j}\right)_s\,. \tag{D.8}$$

If a continuous body is deforming according to Eq. (C.1), then any measurement of deformation can be used in Eq. (D.8) as the thermodynamic substate. For example, it can be shown

(168) that, if υ_j is chosen to be the components of the Green-Lagrange strain tensor defined in Eq. (C.8), then the thermodynamic tensions conjugate to it depend on the components of the second Piola-Kirchhoff stress tensor, i.e.:

$$\upsilon_j \equiv E_{ik} \quad \Rightarrow \quad \tau_j \equiv \frac{S_{ik}}{\rho_0}\,, \tag{D.9}$$

where ρ_0 is the body specific mass at the reference configuration and we employed the index notation for the second-order tensors. Therefore, we can conclude that, for an isentropic process, by using Eq. (D.8):

$$\begin{aligned} \frac{S_{ik}}{\rho_0} &= \left(\frac{\partial u}{\partial E_{ik}}\right)_s \Rightarrow \\ \Rightarrow S_{ik} &= \left[\frac{\partial\left(\rho_0 u\right)}{\partial E_{ik}}\right]_s \Rightarrow \\ \Rightarrow S_{ik} &= \left(\frac{\partial \Psi}{\partial E_{ik}}\right)_s\,, \end{aligned} \tag{D.10}$$

or, in vector notation:

$$\boldsymbol{S} = \left(\frac{\partial \Psi}{\partial \boldsymbol{E}}\right)_s\,, \tag{D.11}$$

where $\Psi = \rho_0 u$ is the strain-energy potential or deformation-work function. Equation (D.10) is valid only for a body under an isentropic process. Equation (D.10) still holds for isothermal processes too, but the deformation-work function is then replaced by: $\Psi = \rho_0 f$, where f is the specific Helmholtz free-energy function.

Equation (D.10) is the fundamental equation in hyperelasticity and the most general form of constitutive equation for hyperelastic materials, based on general assumptions of Thermodynamics. As explained in the main text, for a hyperelastic material, the existence of Ψ is postulated and gives the mechanical behavior of the material.

Finally, it is important to note that the definition that hyperelastic materials are independent of the path is embodied on Eq. (D.11). If Ψ exists, then the deformation work is zero in a cycle of deformation and, therefore, the deformation work per unit reference volume, w_{int}, in a process from a deformation state $\boldsymbol{E}_1$ to $\boldsymbol{E}_2$, since $\boldsymbol{S}$ and $\boldsymbol{E}$ are conjugate in power (168), is given by:

$$\rho_0 w_{int} \equiv \int_{\boldsymbol{E}_1}^{\boldsymbol{E}_2} \boldsymbol{S} : \mathrm{d}\boldsymbol{E} = \int_{\boldsymbol{E}_1}^{\boldsymbol{E}_2} \frac{\partial \Psi}{\partial \boldsymbol{E}} : \mathrm{d}\boldsymbol{E} = \Psi(\boldsymbol{E}_2) - \Psi(\boldsymbol{E}_1) \equiv \Psi(\boldsymbol{C}_2) - \Psi(\boldsymbol{C}_1)\,. \tag{D.12}$$

Hence, for hyperelastic materials, the deformation work depends only on the initial and final states.

D.1 THE INCOMPRESSIBILITY CONSTRAINT

While Eq. (D.11) is the most general form of the constitutive equation for a *compressible* hyperelastic material, the assumption of incompressibility changes the form of it. This new form will be found here, also with the help of Thermodynamics, but with an alternative procedure known as the *Coleman-Noll procedure* (167), by which the general Eq. (D.11) can also be found.

The incompressibility constraint, an *internal constraint*, is a property of certain materials that do not exhibit change of volume when deformed. In the realm of Solid Mechanics, rubber is a typical example. Soft tissues, such as arteries, are also considered incompressible due to the large amount of water in their composition. Water and, more generally, liquids are incompressible fluids.

This mechanical constraint imposes a restriction in every possible deformation of the material. Mathematically, we can write the incompressibility constraint in the following form: if a material particle of a continuum body in the reference configuration, Ω^0, has volume $\mathrm{d}V_0$ and, after a motion given by Eq. (C.1), its volume changes to $\mathrm{d}V$, then, the incompressibility condition implies:

$$\mathrm{d}V_0 = \mathrm{d}V \,. \tag{D.13}$$

The change in volume of material particles is given by the determinant of the deformation gradient tensor, $\boldsymbol{F}$, i.e. by its Jacobian $J = \det \boldsymbol{F}$. Therefore, Eq. (D.13) yields for incompressible materials:

$$J = 1 \,. \tag{D.14}$$

This condition can be written in several forms, but a very useful one for the purposes of this text is the one in rate form, given by:

$$\frac{\mathrm{d}J}{\mathrm{d}t} = 0 \,. \tag{D.15}$$

From Eq. (D.15), another useful form specifically in nonlinear Solid Mechanics, because it depends deformation measurements such as the right Cauchy-Green deformation tensor, $\boldsymbol{C}$. By using the chain rule, Eq. (D.15) can be written as:

$$\frac{\partial J}{\partial \boldsymbol{C}} : \frac{\mathrm{d}\boldsymbol{C}}{\mathrm{d}t} \,. \tag{D.16}$$

The determinant of the right Cauchy-Green deformation tensor, due to its definition, is J^2. Hence, it is possible to show that the derivative of J with respect to $\boldsymbol{C}$ is given by Holzapfel

(167):

$$\frac{\partial J}{\partial \boldsymbol{C}} = \frac{1}{2} J \boldsymbol{C}^{-1} \tag{D.17}$$

Therefore, Eq. (D.15) becomes:

$$J\boldsymbol{C}^{-1} : \frac{\mathrm{d}\boldsymbol{C}}{\mathrm{d}t} = 0\,. \tag{D.18}$$

Besides the kinematical consequences of the incompressibility constraint, it also impacts the constitutive behavior of the material. This can be showed by using the Second Law of Thermodynamics that will be written here for a closed system composed of a continuum material, with density ρ in the current configuration, in rate-form, with intensive thermodynamic properties and per unit material volume. In this case, by further assuming that the heat transfer interaction occurs through the heat flux vector, $\boldsymbol{q}$, we have:

$$\rho \dot{s}_{ger} = \rho \frac{\mathrm{d}s}{\mathrm{d}t} + \nabla \cdot \left(\frac{\boldsymbol{q}}{T} \right) \geq 0\,, \tag{D.19}$$

where s and s_{ger} are the intensive entropy and the intensive generated entropy, and T is the absolute temperature where the heat transfer interaction occurs. The particular form of the Second Law, Eq. (D.19), for a continuum body, is also referred to as the *Clausius-Duhem inequality* (167).

By using vector identities, the heat flux term can be decomposed into two terms, in such a way that Eq. (D.19) can be written as:

$$\rho \dot{s}_{ger} = \rho \frac{\mathrm{d}s}{\mathrm{d}t} + \frac{1}{T} \nabla \cdot \boldsymbol{q} + \frac{1}{T^2} \boldsymbol{q} \cdot \nabla T \geq 0\,. \tag{D.20}$$

For this same system, the First Law of Thermodynamics can be written for the continuum system, with the assumptions outlined above, as:

$$\rho \frac{\mathrm{d}u}{\mathrm{d}t} = \rho \dot{w}_{int} - \nabla \cdot \boldsymbol{q}\,, \tag{D.21}$$

where u is the intensive internal energy, $\dot{w}_{int}$ is the internal work rate caused by the deformation and stresses — we assume no other work interactions in this case —, and $\nabla \cdot \boldsymbol{q}$ is the total heat transfer interaction.

The internal mechanical power, in this case, is given by the thermodynamic tension and thermodynamics substates given in the previous section, and that are referred to as being *conjugate in power*. One example was shown in the previous section where the second Piola-Kirchhoff tensor, $\boldsymbol{S}$, and the rate of the Green strain tensor, $\frac{\mathrm{d}\boldsymbol{E}}{\mathrm{d}t}$, are conjugate in power (see

Eq. (D.12)), implying that:

$$\rho_0 \dot{w}_{int} = \boldsymbol{S} : \frac{\mathrm{d}\boldsymbol{E}}{\mathrm{d}t} = \frac{\mathrm{d}\boldsymbol{E}}{\mathrm{d}t} : \boldsymbol{S} \,. \tag{D.22}$$

where ρ_0 is the density at the reference configuration. This form is typically employed in Lagrangian formulations.

By assuming incompressibility and, moreover, that the motion is isothermal, by substituting the heat transfer term in Eq. (D.21) into Eq. (D.20), similarly to what we did in the previous section, after manipulating the resulting equation, we find:

$$\rho \dot{s}_{ger} = -\frac{\rho}{T}\frac{\mathrm{d}}{\mathrm{d}t}(u - Ts) + \frac{1}{T}\rho \dot{w}_{int} \geq 0 \,. \tag{D.23}$$

By using Eq. (D.22) and the mass conservation principle written in Lagrangian coordinates given by Eq. (5.15), $\rho_0 = J\rho$ for $J = 1$, we find:

$$\rho \dot{s}_{ger} = -\frac{\rho}{T}\frac{\mathrm{d}}{\mathrm{d}t}(u - Ts) + \frac{1}{T}\boldsymbol{S} : \frac{\mathrm{d}\boldsymbol{E}}{\mathrm{d}t} \geq 0 \,. \tag{D.24}$$

where the term in parenthesis is the intensive Helmholtz free-energy, $f \equiv u - Ts$.

As mentioned above, in isothermal processes, the strain-energy function is given by the Helmholtz free-energy per unit reference configuration volume, i.e. $\Psi \equiv \rho_0 f$. Therefore, in view of the mass conservation principle, Eq. (D.24) becomes:

$$\rho T \dot{s}_{ger} = \boldsymbol{S} : \frac{\mathrm{d}\boldsymbol{E}}{\mathrm{d}t} - \frac{\mathrm{d}\Psi}{\mathrm{d}t} \geq 0 \,. \tag{D.25}$$

Note that Eq. (D.25) is a particular form of the exergy balance for the closed system considered here and, hence, it gives the available work that the system can yield; $\rho T \dot{s}_{ger}$ is the *irreversibility rate* of the deformation process that, in this case, equals the balance between internal mechanical power and the rate of change of the strain-energy function.

Equation (D.25) can be written in terms of the right Cauchy-Green deformation tensor by using its relation with the Green-Lagrange strain tensor, $2\boldsymbol{E} = \boldsymbol{C} - \boldsymbol{I}$, and the chain rule. We use the same symbol for the strain-energy function independently of the strain tensor that it depends on. This equivalency between the strain-energy function for the different strain measurements is well presented elsewhere (167).

Finally, Eq. (D.25) becomes:

$$\rho T \dot{s}_{ger} = \frac{1}{2}\left(\boldsymbol{S} - 2\frac{\partial \Psi}{\partial \boldsymbol{C}}\right) : \frac{\mathrm{d}\boldsymbol{C}}{\mathrm{d}t} \geq 0 \,. \tag{D.26}$$

Equation (D.26) provides a functional relationship between the irreversibility function (or

dissipation) occurring in the deformation process and the rate of deformation. The irreversibility is zero in the reversible case, where the equality sign holds.

Because elastic deformations were assumed, the deformation process is reversible by definition and, hence, the equality can be used in Eq. (D.26). Note that, since the deformation is arbitrary, the term between parenthesis in Eq. (D.26) is zero, yielding the potential relation between the second Piola-Kirchhoff tensor and the strain-energy function that we found above:

$$\boldsymbol{S} = 2\frac{\partial \Psi}{\partial \boldsymbol{C}}\,. \tag{D.27}$$

However, the material was assumed to be incompressible. In this case, the minimization of Eq. (D.26) must be performed under a constraint that can also be expressed as a function m in terms of the right Cauchy-Green deformation tensor in Eq. (D.18):

$$m(\boldsymbol{C}) = J\boldsymbol{C}^{-1} : \frac{\mathrm{d}\boldsymbol{C}}{\mathrm{d}t} = 0\,. \tag{D.28}$$

By employing Lagrange multipliers, the minimum of the sum of $\rho T \dot{s}_{ger}$ and the constraint function, m, is sought:

$$\tilde{I}(\boldsymbol{C}) \equiv \frac{1}{2}\boldsymbol{S} : \frac{\mathrm{d}\boldsymbol{C}}{\mathrm{d}t} - \frac{\partial \Psi}{\partial \boldsymbol{C}} : \frac{\mathrm{d}\boldsymbol{C}}{\mathrm{d}t} + \frac{p}{2}\boldsymbol{C}^{-1} : \frac{\mathrm{d}\boldsymbol{C}}{\mathrm{d}t} \geq 0\,, \tag{D.29}$$

where $\dfrac{p}{2}$ is a Lagrange multiplier. For the reversible case, the new function $\tilde{I}(\boldsymbol{C})$ is zero, and the last equation yields:

$$\boldsymbol{S} = -p\boldsymbol{C}^{-1} + 2\frac{\partial \Psi}{\partial \boldsymbol{C}}\,, \tag{D.30}$$

which is the constitutive equation of an incompressible hyperelastic material. It is important to note that, in this case, the strain-energy function, Ψ, is defined for the incompressible material. The Lagrange multiplier, p, can be identified in this case with a hydrostatic pressure: it is a reaction to the motion that makes it keep the volume unchanged and that produces no work. Finally, we find the equivalent equation for the Cauchy stress tensor by applying a push-forward to Eq. (5.31):

$$\boldsymbol{\sigma} = -p\boldsymbol{I} + 2\boldsymbol{F} \cdot \frac{\partial \Psi}{\partial \boldsymbol{C}} \cdot \boldsymbol{F}^{\mathrm{T}}\,. \tag{D.31}$$

Appendix E

UNIAXIAL EXTENSION WITH HYPERELASTIC MATERIALS

In this appendix, the one-dimensional form of the constitutive equations for the hyperelastic materials discussed in the main text is outlined. They can be found by solving the simple extension problem with an incompressible hyperelastic material. Imagine a homogeneous cube, with sides along the Cartesian coordinates axes, made of an incompressible hyperelastic material with strain-energy function Ψ under an uniaxial load applied along the x-axis. In this case, the stress state is free of shear stress and the normal stresses are given by $\sigma_{xx} \equiv \sigma$ and $\sigma_{yy} = \sigma_{zz} = 0$. If the stretch along x is indicated by λ, then the incompressibility and the symmetry of the problem yield: $\lambda_y = \lambda_z = \lambda^{-1/2}$. Therefore, the deformation gradient of the uniaxial extension problem is:

$$\boldsymbol{F} = \begin{bmatrix} \lambda & 0 & 0 \\ 0 & \lambda^{-\frac{1}{2}} & 0 \\ 0 & 0 & \lambda^{-\frac{1}{2}} \end{bmatrix} . \tag{E.1}$$

The analytical solution of it can then be shown to be given by:

$$\sigma = 2\left(\lambda^2 - \frac{1}{\lambda}\right)\left(\frac{\partial \Psi}{\partial I_1} + \frac{1}{\lambda}\frac{\partial \Psi}{\partial I_2}\right) , \tag{E.2}$$

where I_1 and I_2 are the first and second principal invariants of the left Cauchy-Green deformation tensor. Due to the boundary conditions, the hydrostatic pressure can also be calculated analytically:

$$p = 2\left[\frac{1}{\lambda}\frac{\partial \Psi}{\partial I_1} + \left(\lambda + \frac{1}{\lambda^2}\right)\frac{\partial \Psi}{\partial I_2}\right] . \tag{E.3}$$

After using their triaxial definitions, the first and second invariants of the left Cauchy-Green

deformation tensor are given by:

$$I_1 = \lambda^2 + \frac{2}{\lambda} \tag{E.4}$$

and

$$I_2 = 2\lambda + \frac{1}{\lambda^2}\,. \tag{E.5}$$

Finally, after substitution of the particular strain-energy function of the materials mentioned in the main text and accounting for Eqs. (E.4) and (E.5), the following uniaxial stress-stretch relationships for the selected laws follow:

- neo-Hookean law:

$$\sigma = 2c_{10}\left(\lambda^2 - \frac{1}{\lambda}\right)\,; \tag{E.6}$$

- Mooney-Rivlin law:

$$\sigma = 2\left(\lambda^2 - \frac{1}{\lambda}\right)\left[c_{10} + c_{11}\,(I_2 - 3) + \frac{c_{01}}{\lambda} + \frac{c_{11}}{\lambda}\,(I_1 - 3)\right]\,; \tag{E.7}$$

- Yeoh law:

$$\sigma = 2\left(\lambda^2 - \frac{1}{\lambda}\right)\left[c_{10} + 2c_{20}\,(I_1 - 3) + 2c_{30}\,(I_1 - 3)^2\right]\,; \tag{E.8}$$

- isotropic Fung law:

$$\sigma = k_1 \mathrm{e}^{\frac{k_2}{2}(I_1 - 3)}\left(\lambda^2 - \frac{1}{\lambda}\right)\,; \tag{E.9}$$

- isotropic quadratic Fung law:

$$\sigma = 2k_1\,(I_1 - 3)\,\mathrm{e}^{k_2(I_1 - 3)^2}\left(\lambda^2 - \frac{1}{\lambda}\right)\,; \tag{E.10}$$

Appendix F

THE FINITE VOLUME METHOD IN SOLIDS4FOAM

In this chapter, an overview of how solids4foam solves the momentum equation that governs the motion of a solid material, written in the total Lagrangian formulation, using the Finite Volume Method (FVM). In solids4foam, the different formulations of the momentum equation and the different algorithms that are employed to solve it are implemented under the class `solidModel`, as can be seen in Fig. 6.1. Separately, the specific constitutive laws are implemented under the class `materialLaw`, as was explained in Section 6.1. Therefore, the implementation of the `solidModels` is performed in terms of a generic Cauchy stress tensor, as a virtual function `sigma()`, computationally.

As explained in Section 5.3.1, in the total Lagrangian approach, the momentum equation written with respect to the reference configuration was given by Eq. (5.18) (here, the superscript for the solid part, "s", was dropped to simplify the notation):

$$\int_{V_0} \rho_0^{\mathrm{s}} \frac{\partial^2 \boldsymbol{u}}{\partial t^2}(\boldsymbol{\xi}, t) \mathrm{d}V_0 = \int_{V_0} \nabla_0 \cdot \left(J \boldsymbol{F}^{-1} \cdot \boldsymbol{\sigma} \right) \mathrm{d}V_0 + \int_{V_0} \rho_0^{\mathrm{s}} \boldsymbol{b} \mathrm{d}V_0 \,. \tag{F.1}$$

For greater generality, here it was assumed that there are body forces acting on the solid, $\boldsymbol{b}$, and that they are known. Moreover, it is assumed that the relationship between the Cauchy stress and the solid displacement, $\boldsymbol{u}$, is also already defined by any constitutive law. Once BCs are specified for Eq. (F.1), it can be assumed that the problem is mathematically closed and that a solution can be found for the displacement field, $\boldsymbol{u}$.

To discretize the resulting equation with the FVM, the reference domain, Ω_0^{s}, must already have been discretized into non-overlapping control-volumes of generic polyhedral shape, as supported by OpenFOAM®, with flat polygonal faces, as shown in Fig. F.1, with volume V_0,

Figure F.1 – Polyhedral control volume, V_0, with its geometric parameters used on the finite-volume discretization; N is the centroid of a neighbor cell.

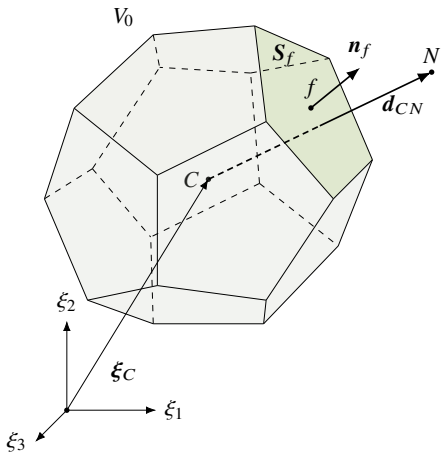

Source: Prepared by the author.

control surface S_0, and centroid C.

The term with the Cauchy stress, which resulted from the balance of surface forces on the domain, is usually the most problematic, because its discretization would depend on the particular form of the constitutive equation and this one may be fairly complex with several nonlinear terms. As discussed in Appendix C, this is actually the rule if a finite-deformation regime is assumed. One way to deal with this complexity would be to discretize the whole term in an explicit manner, i.e. estimate it based on already known values of the fields involved — from the last time-step, for example, computationally speaking. However, this approach would lead to a large source term in the resulting algebraic system, because it contains too much information, causing the iterative procedure to have a slow convergence rate. As explained in Jasak et al. (189) for the linear elastic case, an alternative approach is to split this term into a purely diffusive part, treated implicitly, i.e. which will aggregate to the coefficients of the discretized algebraic system, and the rest of it is computed explicitly. This explicitly-treated part normally contains the terms that depend on the inter-coupling between the different displacement components and other nonlinear terms.

In solids4foam, this is accomplished, for a generic $\boldsymbol{\sigma}$, by using a deferred-correction approach

as follows (226):

$$\begin{aligned}\int_{V_0}\rho_0^{\mathrm{s}}\frac{\partial^2\boldsymbol{u}}{\partial t^2}(\boldsymbol{\xi},t)\mathrm{d}V_0 = \underbrace{\int_{V_0}\nabla_0\bullet\left[\left(\frac{4}{3}\mu^{\mathrm{s}}+\kappa^{\mathrm{s}}\right)\nabla_0\boldsymbol{u}\right]\mathrm{d}V_0}_{\text{Evaluated implicitly}} + \int_{V_0}\rho_0^{\mathrm{s}}\boldsymbol{b}\mathrm{d}V_0 + \\ + \underbrace{\int_{V_0}\nabla_0\bullet\left(J\boldsymbol{F}^{-1}\bullet\boldsymbol{\sigma}\right)\mathrm{d}V_0 - \int_{V_0}\nabla_0\bullet\left[\left(\frac{4}{3}\mu^{\mathrm{s}}+\kappa^{\mathrm{s}}\right)\nabla_0\boldsymbol{u}\right]\mathrm{d}V_0}_{\text{Evaluated explicitly}}\,.\end{aligned} \tag{F.2}$$

The Laplacian term used in the deferred correction, with diffusivity $\frac{4}{3}\mu^{\mathrm{s}}+\kappa^{\mathrm{s}} = 2\mu^{\mathrm{s}}+\lambda^{\mathrm{s}}$ — computationally, this "property" is called *implicit stiffness* —, was used because the term $\nabla_0\bullet[(2\mu^{\mathrm{s}}+\lambda^{\mathrm{s}})\nabla_0\boldsymbol{u}]$ is the maximum consistent contribution of the surface forces to the implicit discretization (189). Furthermore, it is exactly this diffusive term that renders the matrix of coefficients diagonally-dominant, well suited for iterative procedures.

By applying Gauss' divergence theorem to it, yields:

$$\begin{aligned}\int_{V_0}\rho_0^{\mathrm{s}}\frac{\partial^2\boldsymbol{u}}{\partial t^2}(\boldsymbol{\xi},t)\mathrm{d}V_0 - \oint_{S_0}\left(\frac{4}{3}\mu^{\mathrm{s}}+\kappa^{\mathrm{s}}\right)\boldsymbol{n}_0\bullet\nabla_0\boldsymbol{u}\mathrm{d}S_0 = \int_{V_0}\rho_0^{\mathrm{s}}\boldsymbol{b}\mathrm{d}V_0 + \\ + \int_{V_0}\nabla_0\bullet\left(J\boldsymbol{F}^{-1}\bullet\boldsymbol{\sigma}\right)\mathrm{d}V_0 - \int_{V_0}\nabla_0\bullet\left[\left(\frac{4}{3}\mu^{\mathrm{s}}+\kappa^{\mathrm{s}}\right)\nabla_0\boldsymbol{u}\right]\mathrm{d}V_0\,.\end{aligned} \tag{F.3}$$

By proceeding with the finite-volume discretization, the order of the temporal derivative can be inverted because V_0 is a material control volume and $\frac{\partial^2\boldsymbol{u}}{\partial t^2}$ is evaluated by keeping the material coordinates constant. Hence, by using the mid-point rule to evaluate the integral with second-order accuracy follows:

$$\int_{V_0}\rho_0^{\mathrm{s}}\frac{\partial^2\boldsymbol{u}}{\partial t^2}(\boldsymbol{\xi},t)\mathrm{d}V_0 = \left(\rho_0^{\mathrm{s}}\right)_C\frac{\partial^2}{\partial t^2}\underbrace{\left(\int_{V_C}\boldsymbol{u}\mathrm{d}V\right)}_{\equiv\boldsymbol{u}_C V_C} = (\rho_0^{\mathrm{s}})_C V_C\frac{\partial^2\boldsymbol{u}_C}{\partial t^2}\,. \tag{F.4}$$

Finally, by using the notation $\frac{\Delta^2(\,)}{\Delta t^2}$ to indicate the discretized operator of the temporal term and decomposing the surface integral to the polyhedral cell of Fig. F.1, Eq. (F.3) (180, 226), follows:

$$\begin{aligned}(\rho_0^{\mathrm{s}})_C V_C\left(\frac{\Delta^2\boldsymbol{u}_C}{\Delta t^2}\right)^{\mathrm{n}} - \sum_f\left(\frac{4}{3}\mu^{\mathrm{s}}+\kappa^{\mathrm{s}}\right)_f(\nabla_0\boldsymbol{u})_f^{\mathrm{n}}\bullet\boldsymbol{S}_f = \int_{V_0}\rho_0^{\mathrm{s}}\boldsymbol{b}\mathrm{d}V_0 + \\ + \left[\int_{V_0}\nabla_0\bullet\left(J\boldsymbol{F}^{-1}\bullet\boldsymbol{\sigma}\right)\mathrm{d}V_0 - \int_{V_0}\nabla_0\bullet\left[\left(\frac{4}{3}\mu^{\mathrm{s}}+\kappa^{\mathrm{s}}\right)\nabla_0\boldsymbol{u}\right]\mathrm{d}V_0\right]^{\mathrm{old}}\,,\end{aligned} \tag{F.5}$$

where the superscript "old" in the last term of the right-hand side indicates that it is evaluated

directly with available values from the last iteration. The normal gradient in the second term of the left side of Eq. (F.5) was interpolated using a non-orthogonal and skewness-corrected scheme. Any further detail regarding the finite-volume discretization can be found in more specific literature (226, 182).

Finishing the discretizations of each term, the typical linearized algebraic equation for a control volume V_0 of the computational mesh in the finite-volume discretization follows, given in vector form in this case:

$$a_C^{\boldsymbol{u}} \boldsymbol{u}_C^{\mathrm{n}} + \sum_N a_N^{\boldsymbol{u}} \boldsymbol{u}_N^{\mathrm{n}} = \boldsymbol{b}_C^{\boldsymbol{u}}, \tag{F.6}$$

where the superscript "n" indicates a time-step level and N indicates a sum over all the neighboring cells to the cell with centroid C. The source term on the right-hand side contains all the information about the term evaluated explicitly in Eq. (F.5).

Because in solids4foam, the variables are defined in the Cartesian system, thus $\boldsymbol{u}$ can be written as: $\boldsymbol{u} = u_x \boldsymbol{i} + u_y \boldsymbol{j} + u_z \boldsymbol{k}$, where $\boldsymbol{i}$, $\boldsymbol{j}$ and $\boldsymbol{k}$ are vectors of the Cartesian canonical basis, Eq. (F.6) can be decomposed as follows:

$$\begin{aligned}
a_C^{u_x} (u_x)_C^{\mathrm{n}} + \sum_N a_N^{u_x} (u_x)_N^{\mathrm{n}} &= b_C^{u_x}, \\
a_C^{u_y} (u_y)_C^{\mathrm{n}} + \sum_N a_N^{u_y} (u_y)_N^{\mathrm{n}} &= b_C^{u_y}, \\
a_C^{u_z} (u_z)_C^{\mathrm{n}} + \sum_N a_N^{u_y} (u_z)_N^{\mathrm{n}} &= b_C^{u_z}.
\end{aligned} \tag{F.7}$$

Finally, by assembling each equation in Eq. (F.7) for all control volumes in the solid mesh, yields three systems of algebraic linearized equations:

$$\begin{aligned}
\mathbf{A}^{u_x} (\mathbf{u_x})^{\mathrm{n}} &= \mathbf{b}^{u_x}, \\
\mathbf{A}^{u_y} (\mathbf{u_y})^{\mathrm{n}} &= \mathbf{b}^{u_y}, \\
\mathbf{A}^{u_z} (\mathbf{u_z})^{\mathrm{n}} &= \mathbf{b}^{u_z}.
\end{aligned} \tag{F.8}$$

The segregated solution mentioned in the main text consists in solving the linearized systems in Eq. (F.8) sequentially and separately. Each system can be solved with any traditional iterative method for solving linear systems. The selected method to solve each system performs *inner iterations*. However, to deal with the explicitness of the inter-component and other nonlinear terms that were included in the coefficients of the matrix system, *outer iterations* are performed in a Picard/fixed-point approach, i.e. after solving each system separately, the result is used to

feed a new outer iteration over the systems (227, 228).

According to Jasak et al. (189) and Cardiff et al. (227), the segregated method is much more memory-efficient because, instead of one large sparse matrix, only three smaller ones are created. Furthermore, the matrices are well-structured and diagonally-dominant, which is ideal for iterative solvers. Nevertheless, one of the drawbacks of this approach is its first-order convergence rate (228), which may be improved with under-relaxation, but for some problems, the convergence may still be too slow.

In the "language" of foam-extend and OpenFOAM®, the discretized system, Eq. (F.8), is assembled computationally with the following computational code:

```
DEqn
(
      rho()*fvm::d2dt2(D())
  == fvm::laplacian(impK, D())
  -  fvc::laplacian(impK, D())
  +  fvc::div(J*Finv \& sigma())
  +  rho()*g()
  +  mechanical.RhieChowCorrection()
);
```

symbolically similar to the original PDE being solved, Eq. (F.2), where the variable `D()` is the solid displacement vector solution. In the equation above, `fvm` and `fvc` are C++ *namespaces* (185) which include *discretization operators* and *calculus operators*, respectively, i.e. all operations in front of `fvm` will generate a computational matrix of the algebraic system with coefficients adding to the final matrix $\mathbf{A}^{\boldsymbol{u}}$, whereas all operations in front of `fvc` evaluates the fields with already known values — therefore, explicitly; `impK` is the variable attributed to the implicit stiffness. Moreover, note that the function `sigma()` encapsulates the evaluation of the Cauchy stress tensor depending on the chosen constitutive material law, thus the computational equation above can be used with different constitutive models implemented separately as C++ classes in solids4foam.

Appendix G

NUMERICAL VERIFICATION

G.1 NEW HYPERELASTIC LAWS IMPLEMENTED

To verify the implementation of the biomechanical laws, the analytical solution of the uniaxial extension problem was used and also three benchmarks cases (Fig. G.1) employed by Sussman et al. (229) and Bijelonja et al. (230), who worked on the implementation of a two-parameter incompressible MR model (therefore, $c_{11} = 0.0$ was set for these cases).

Because both the total Lagrangian and updated Lagrangian formulations were available in solids4foam to solve the momentum equation for the solid motion, both of them were used for these benchmarks, but the results of both approaches were presented only when they yielded different solutions.

Benchmark 1: Long Wall

This benchmark consists in a wall with 1 m × 2 m (width × height) and assumed infinitely long in length, i.e. along the z axis (Fig. G.1a). Hence, due to symmetry, it can be assumed to be in a biaxial state of deformation. A compressing load of 50 MPa is applied on the right surface and a traction of 100 MPa on the upper surface. The left and bottom surfaces are free to slide along its tangential, but constrained of movement along their normal. The material was assumed isotropic and incompressible, with material parameters $c_{10} = 80$ MPa and $c_{01} = 20$ MPa, under plane-strain conditions.

The mesh used had 20 × 20 volumes, and both total and updated Lagrangian approaches yielded the same results. The boundary conditions were applied in 100 equal incremental steps and a normalized residual tolerance for the momentum equation of 1×10^{-9} was used. The results are compared in Table G.1.

Figure G.1 – (a) Long wall, with loads and boundary conditions, assumed infinitely along the z direction; (b) cylindrical pressurized vessel with inner and outer radius R_i and R_o, respectively, and applied uniform pressure of $p = 100\,\text{MPa}$; and (c) cylinder with diameter D between rigid plates: the upper plate is displaced in the negative y direction under the action of a displacement force F while the bottom plate is kept fixed. The area marked with a pattern was the portion effectively simulated due to symmetry of the problem.

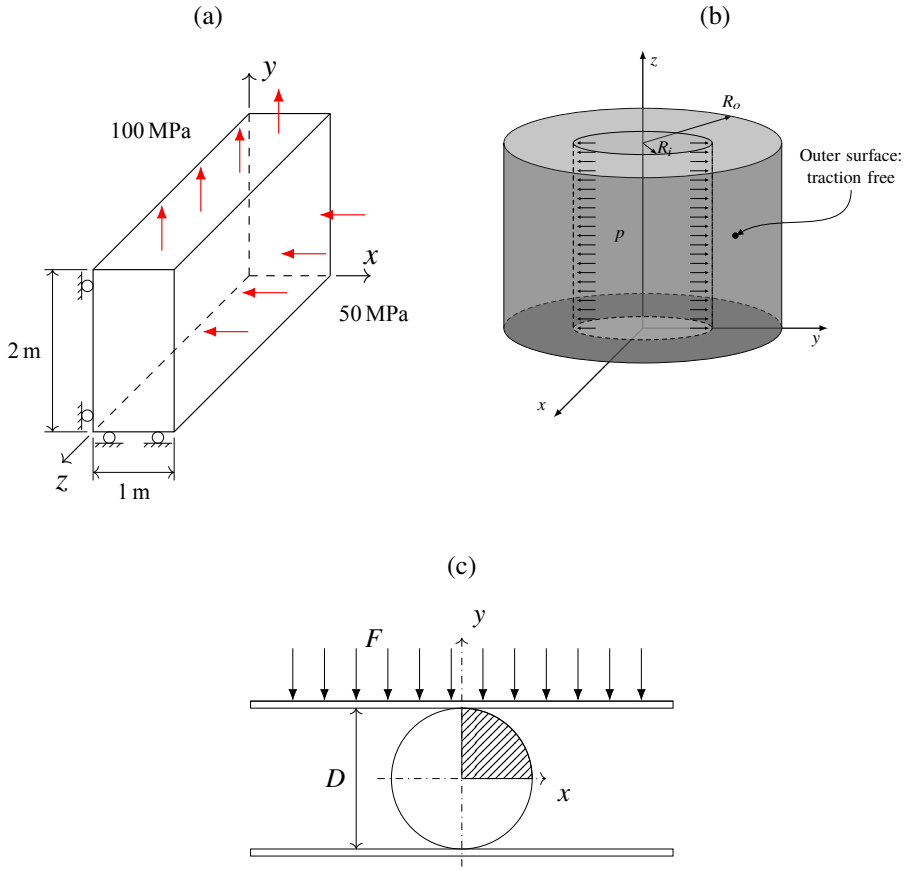

Source: Prepared by the author.

Table G.1 – Comparison between the results of the long wall benchmark for solids4foam, the solution provided by the algorithm presented in Bijelonja et al. (230), and the analytical solution as also presented by Bijelonja et al. (230). All numerical solutions were found after solving for 100 incremental steps along time.

Solution	E_{xx}	E_{yy}	σ_{xx} (MPa)	σ_{yy} (MPa)	u_x (m)	u_y (m)
solids4foam	−0.1537	0.2205	−49.99	100.0	−0.1636	0.4010
Ref. (230)	−0.1533	0.2213	−49.00	100.0	−0.1676	0.4022
Analytical	−0.1535	0.2215	−50.00	100.0	−0.1675	0.4025

Source: Prepared by the author.

A close agreement between the solids4foam solution and both numerical solutions with the method proposed by Bijelonja et al. (230) and the analytical solution is verified. To achieve the results given in Table G.1 in terms of compressibility, the Poisson ratio was assumed equal to 0.499, which yielded $J = 0.9989$.

Benchmark 2: Cylindrical Pressure Vessel

This benchmark consists in a thick cylindrical shell with inner radius $R_i = 7\,\text{m}$ and outer radius $R_o = 18.625\,\text{m}$ with material parameters $c_{10} = 80\,\text{MPa}$ and $c_{01} = 20\,\text{MPa}$. The strain state is assumed to be plane due to the geometric symmetry along the z axis direction (see Fig. G.1b). The inner pressure was applied in equal increments until $p = 100\,\text{MPa}$.

Due to symmetry, only a quarter of the cylinder section was simulated with a mesh density of 20×20 cells in the radial and circumferential directions, respectively. A residual tolerance for the momentum equation of 1×10^{-9} was selected.

Figures G.2a and G.2b show the radial and circumferential (or hoop stress) components of the Cauchy stress tensor along the undeformed radius of the cylinder when $p = 100\,\text{MPa}$. For both plots, a close agreement between the simulated and analytical distribution can be seen, the error being smaller than 5 % for all points.

Figure G.2 – Cauchy stress components along the undeformed cylinder radius: (a) radial component; (b) circumferential component, or hoop stress.

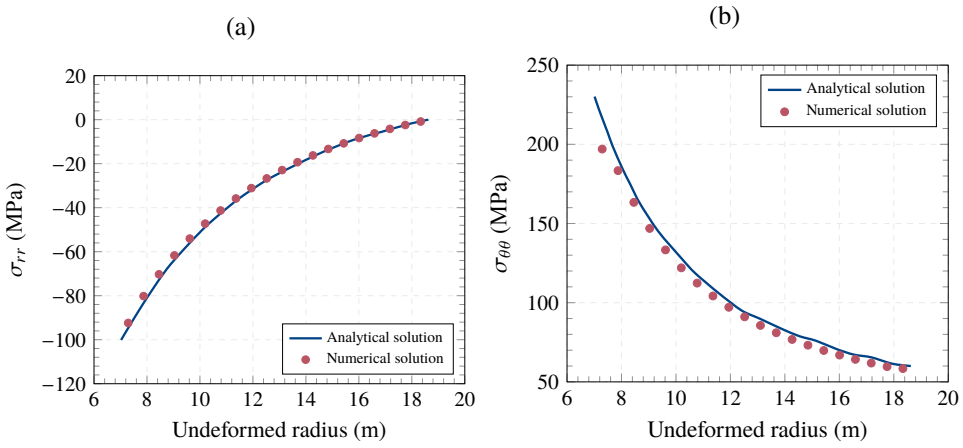

Source: Prepared by the author.

The results shown in the plots were obtained with $\nu^s = 0.49$, which yielded a Jacobian in the interval $0.98 < J < 0.99$ for the last time-step. This departure from the incompressible behavior may explain the small discrepancies between the solution close to the boundaries.

Benchmark 3: Cylinder Being Smashed

The third benchmark is a solid cylinder crushed between rigid plates, as schematically shown in Fig. G.1c. The cylinder has a diameter of 0.4 m and is compressed between rigid plates with a total compressed displacement of half its diameter. The contact between the cylinder and plate surfaces was modeled as frictionless.

This problem was investigated by Sussman et al. (229) and also by Bijelonja et al. (230). The latter modeled the material of the cylinder as purely incompressible and the former assumed a nearly-incompressible behavior, which is characterized by the authors as when "the ratio of the bulk modulus to the shear modulus is typically several thousand". The same material law as Sussman et al. (229) was used, i.e. the MR law with $c_{10} = 0.293\,\text{MPa}$ and $c_{01} = 0.177\,\text{MPa}$, with $\nu^{\text{s}} = 0.499$.

Three increasingly refined meshes with, approximately, 200, 500, and 1000 quadrilateral control volumes arranged in a block-structured mesh were simulated. Both the updated and total Lagrangian approaches were tested by simulating a quarter of the cylinder due to symmetry (hatched area in Fig. G.1c). The plate is linearly displaced in 30 increments. Figure G.3 shows the displacement force applied to the cylinder obtained with both the total Lagrangian and updated Lagrangian approaches, compared with the numerical solution by using the Finite Element Method (FEM) provided by Bijelonja et al. (230), and also with an approximate curve used by Sussman et al. (229) based on experimental data:

$$F = ED\left[1.25\left(\frac{\delta}{D}\right)^{3/2} + 50\left(\frac{\delta}{D}\right)^{6}\right], \tag{G.1}$$

where F is the displacement force per cylinder length, E is the small-strain Young's modulus of the material, given by Eq. (5.74), which yields $E = 6(c_{10} + c_{01})$ for the two-parameter MR model—, D is the cylinder diameter and δ is the plate deflection.

Figure G.3 – Displacement force applied by the plates to deform the cylinder: approximated experimental results and FEM solution given by Bijelonja et al. (230); both solution with the total Lagrangian and updated Lagrangian formulations are plotted.

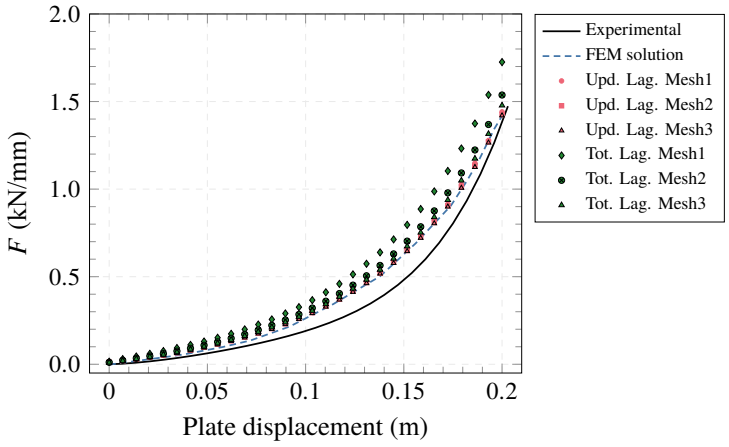

Source: Prepared by the author.

We can see that the solution with solids4foam is perfectly in agreement with the numerical

solution provided by Bijelonja et al. (230) for the updated Lagrangian approach with any mesh, whereas for the total Lagrangian approach the coarse mesh gives a slight inaccurate solution, that is improved as the mesh was refined, and this seems more pronounced for larger displacements of the plates. This behavior probably occurred due to the amount of Rhie-Chow correction also applied to the momentum equation discretization: for the total Lagrangian approach, this correction term is proportional to the total displacement of the solid and, therefore, is larger than the correction term for the updated Lagrangian approach.

Finally, the error with respect to the experimental solution is probably due to the assumption of constant Young's modulus, as explained by Sussman et al. (229), as also present by comparing the FEM solution also used in Bijelonja et al. (230).

Uniaxial Extension

Finally, the uniaxial extension problem was also used to verify the biomechanical laws. This was motivated by the fact that specific benchmarks, with analytical or experimental solutions for the Yeoh, and the isotropic Fung laws, were not found. Hence, the classical problem of the uniaxial extension deformation of a homogeneous incompressible material, assumed to be a cubic sample with dimensions $1\,\mathrm{m} \times 1\,\mathrm{m} \times 1\,\mathrm{m}$ that is stretched along its height (y axis), was used as a verification benchmark for all models because it can be solved analytically for an arbitrary strain energy function, Ψ.

The analytical solution of this problem is given by the following stress-stretch curve:

$$\sigma = 2\left(\lambda^2 - \frac{1}{\lambda}\right)\left(\frac{\partial \Psi}{\partial I_1} + \frac{1}{\lambda}\frac{\partial \Psi}{\partial I_2}\right), \tag{G.2}$$

where σ is the Cauchy stress in the stretched direction and λ is the stretch. Since incompressibility is assumed, the hydrostatic pressure is given by:

$$p = 2\left[\frac{1}{\lambda}\frac{\partial \Psi}{\partial I_1} + \left(\lambda + \frac{1}{\lambda^2}\right)\frac{\partial \Psi}{\partial I_2}\right]. \tag{G.3}$$

The application of Eq. (G.2) for each of the laws presented in Section 5.3.6 was given in Appendix E.

The material constants used in the verification tests were typical values found for unruptured IAs tissue from different works (see Section 2.4) and are collected in Table G.2 (note that for the Yeoh model, the c_{10} and c_{01} correspond to the c_{10} and c_{20}, respectively). The table also shows the Poisson's ratio, used to calculate the bulk modulus κ^s, that yielded a nearly-incompressible

Table G.2 – Material constants used to verify the implemented laws in solids4foam with the uniaxial extension problem.

Law		Material Constants			
		k_1 (MPa)	k_2		ν^s
Exponential	Fung	1.0	16.7		0.49
		c_{10} (MPa)	c_{01} (MPa)	c_{11} (MPa)	ν^s
Polynomial	Neo-Hookean	0.17	-	-	0.49
	MR	0.19	0.023	11.78	0.499
	Yeoh	0.12	6.8	0.0	0.499

Source: Prepared by the author.

behavior. The neo-Hookean law, which was already implemented in solids4foam, was also included in this particular analysis to assess its behavior in comparison to the other hyperelastic laws; its material constants in the table are equivalent to a Young's modulus of 1 MPa and Poisson's ratio of 0.49.

The numerical solution was found in a mesh with 3×3 cells and displacement was imposed at the top face of the cubic sample with zero shear to allow the face to slide along the tangential direction. The imposed displacement was such to yield a stretch from 1 to 1.2 along the y-axis and applied along 10 time-steps.

Figure G.4 shows the stress-stretch behavior of each law obtained with the analytical solution, Eq. (G.2), and the numerical solutions from the implementation in solids4foam. The agreement is quite good for all models, with poorer accuracy for larger stretches probably due to the volumetric motion, since it was observed that to get a closer agreement between the analytical solution and the numerical ones for stretches above 1.15, one would need to use a larger Poisson ratio than the ones shown in Table G.2.

In the last plot of Fig. G.4, a comparison between the response of all laws was plotted. It is interesting to compare the stress-strain behavior of each model and verify that the response of the neo-Hookean law is nearly linear in the range of stretches plotted compared to the other models.

G.2 THE WEAKLY COMPRESSIBLE LAW

The weakly compressible law implemented in solids4foam was verified with an FSI benchmark that has been proposed originally by Formaggia et al. (231) and used extensively to validate

Figure G.4 – Comparison between the analytical Cauchy stress (Eq. (G.2), dashed lines) and the numerical results from solids4foam. The last plot shows a comparison between the five models (we included the neo-Hookean model for completeness) for an assessment of their behavior.

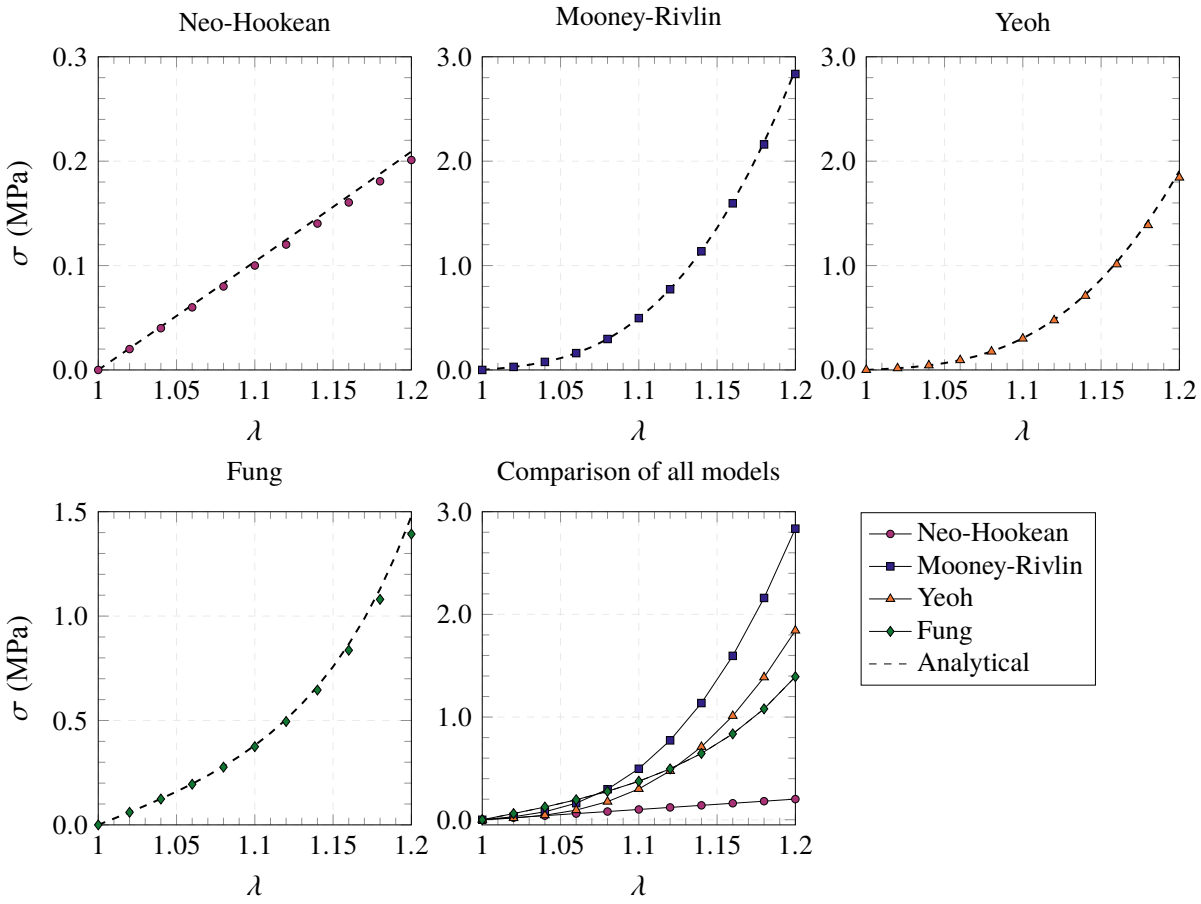

Source: Prepared by the author.

numerical FSI solvers (232, 162). It consists of a three-dimensional elastic tube (see Fig. G.5), with the following properties: Newtonian incompressible fluid with density $\rho_f = 1000\,kg/m^3$ and kinematic viscosity $\nu^f = 3\,mm^2/s$ flowing in a laminar regime after an inlet pressure pulse of $p = 1.3332\,kPa$, kept during 3 ms and then suddenly dropped to zero; the elastic tube was modeled as a St. Venant-Kirchhoff (SVK) material with density $\rho_s = 1200\,kg/m^3$, Young's modulus $E = 0.3\,MPa$, and Poisson's ratio $\nu^s = 0.3$.

Figure G.5 – Schematic representation of the 3D tube FSI benchmark and its BCs.

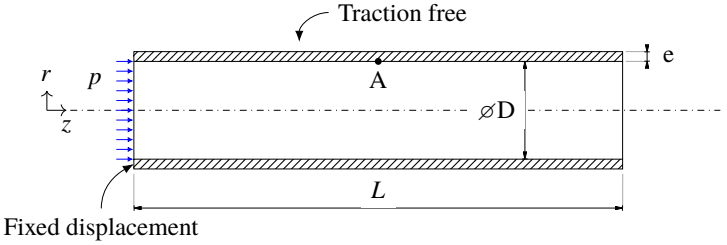

Source: Prepared by the author.

The solid problem was solved using the updated Lagrangian formulation of the momentum equation and, for the FSI coupling, the IQN-ILS technique (217) implemented in solids4foam, with a residual tolerance of 1×10^{-6} and a time-step for both the fluid and solid subdomains of 1×10^{-4} s. Measurements of the radial and axial displacements were recorded at the tube mid-point (point A in Fig. G.5).

Figure G.6 shows the radial and axial displacements of the point A over time. The flow in the tube was simulated for different values of bulk modulus from 1 MPa to 10 MPa. As the plots show, these values of κ^{f} were sufficient in this case to reach the incompressible fluid behavior.

Figure G.6 – (a) Radial and (b) axial displacement of the mid-point of the tube inner surface for different values of fluid bulk modulus, κ^{f} and for the solution reference given by Lozovskiy et al. (232).

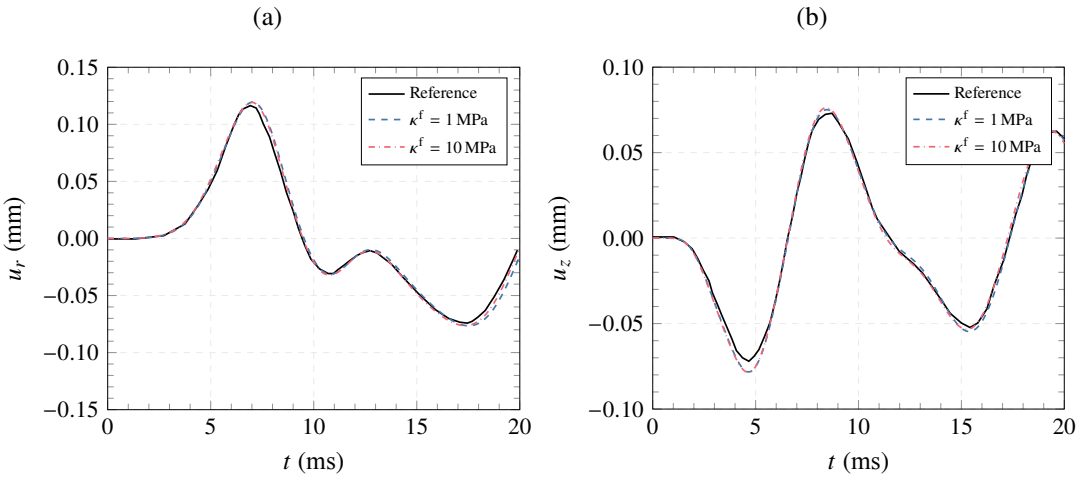

Source: Prepared by the author.

Finally, although this benchmark assumes the incompressible fluid model, it is possible to use it to verify the implementation of the weakly compressible liquid law because, as explained in Section 5.2.2, the latter must approach the incompressibility limit as the bulk modulus increases, whose limiting value that mimics the incompressibility behavior will depend on the pressure levels of the specific problem.

Appendix H

NUMERICAL SENSITIVITY STUDIES

H.1 TYPE OF SOLID MESHES EMPLOYED

As explained in the main text, the triangulated surfaces extracted with VMTK®, that corresponds to the lumen surface of the vessels were initially converted to quadrilateral discretized surfaces by using the `cartesianMesh` utility of `cfMesh`. One example of a such a surface is shown in Fig. H.1a. This surface mesh was, then, extruded on the outward direction with the thickness field defined in Section 5.3.8, e_w, by using VMTK's script `vmtkboundarylayer`, which has support for a spatially-varying thickness field, to generate the solid wall meshes. In this case, the computational meshes had hexahedral cells. This procedure was initially preferred due to the well-known superiority of hexahedral cells when using the FVM, at least for fluid problems.

However, severe oscillations in the hydrostatic pressure fields were detected when using these meshes, as Fig. H.1b shows, evidence of the numerical phenomenon called "volumetric locking" (233), where unrealistic small displacements are found when solving for the motion of nearly-incompressible or incompressible materials with displacement-based solvers, as was the case in this work. These oscillations were not elliminated even when solving a Laplacian equation for the pressure, as explained in Section 6.2, and changing others simulation's parameters were also not able to quell them. The example shown in Fig. H.1b was taken from case urICA1 using the Yeoh hyperelastic law with $\nu^s = 0.49$.

The solution was to use a surface with triangular elements, as shown in Fig. H.1c, computed using the script `vmtksurfaceremeshing` of VMTK, as explained in the main text. The remeshed surface was then similarly extruded, generating a solid wall mesh with triangular primatic cells. As shown by Wheel (234), quadrilateral cells are proner to show vol-

Figure H.1 – (a) Quadrilateral surface mesh from the fluid-meshing with `cfMesh`; (b) severe oscillations in the hydrostatic pressure field in case urICA1's hexahedral mesh for $\nu^s = 0.49$, evidence of volumetric locking; and (c) triangular surface remeshed using VMTK® used subsequentely to avoid volumetric locking.

(a) (b) (c)

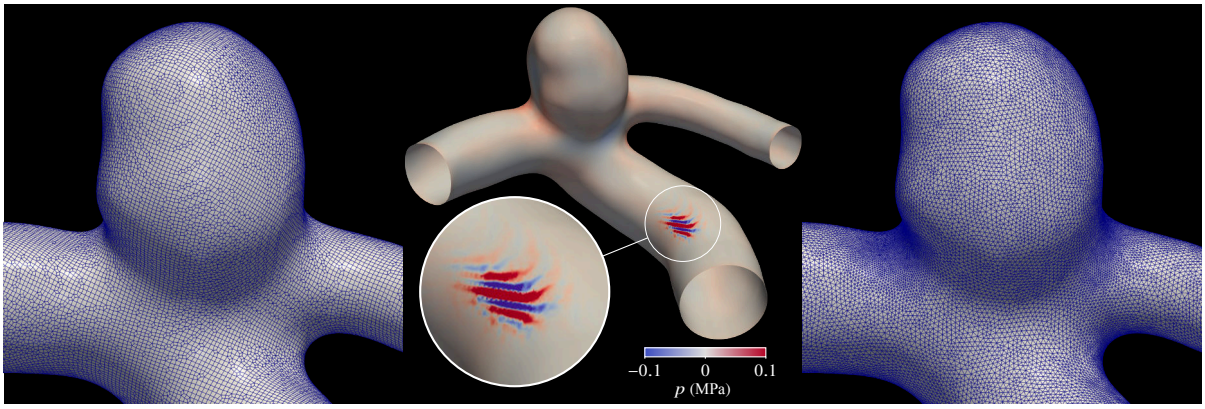

Source: Prepared by the author.

umetric locking when using the FVM, and the checkerboard pressure pattern was not found anymore for the geometries used. The triangular surfaces were generated with VMTK's script `vmtksurfaceremeshing`.

H.2 MESH AND TIME-STEP DISCRETIZATION ERRORS

Solid Sub-problem

Both mesh and time-step convergence studies were carried out using the triangular meshes for the geometry of case urICA1. Three meshes were created to allow the assessment of the discretization error with Richardson's extrapolation. The total number of cells and the surface cell density are shown in Table H.1, with also the maximum edge size of the mesh as given by foam-extend's utility `checkMesh`, which was used to guide the resulting mesh's size by roughly trying to half the edge size. Every mesh was consistently created with 6 layers of cells along its thickness. In the presentation below, each mesh was labeled as M_1, M_2, and M_3, corresponding to the coarser, intermediate, and finest meshes, respectively. Once the acceptable mesh size was found, the time-step convergence study was carried-out by simulating the selected mesh again with time-steps of $\Delta t_1 = 1 \times 10^{-3}$ s, $\Delta t_2 = 1 \times 10^{-4}$ s, and $\Delta t_3 = 1 \times 10^{-5}$ s.

The simulations were carried out using the 1WFSI strategy, the solid wall thickness field corresponding to the abnormal-wall model model, and the Yeoh hyperelastic law (chosen due to the smaller computational times of the simulation using this material law compared with the MR and Fung laws).

Table H.1 – Solid wall mesh sizes, cells surface density for meshes of case urICA1 (the surface area of this geometry was approximately 350 mm^2), and the maximum edge size as reported by the `checkMesh` utility.

Mesh Size	N_M	ρ_S (cells/mm^2)	l_e (mm)
M_1 (coarsest)	188,664	89.9	0.36
M_2 (intermediate)	506,598	241.3	0.21
M_3 (finer)	1,160,976	552.9	0.13

Source: Prepared by the author.

Figure H.2 shows the comparison of the largest principal Cauchy stress, σ_1, at peak systole, on the lumen surface of case urICA1, obtained by solving the wall motion with the 1WFSI strategy using the Yeoh hyperelastic law. It is straightforward to see that even the coarsest mesh produces reasonable results compared to the finest mesh, although visible differences can be perceived by a closer inspection (upper panel of the figure). Nevertheless, the intermediate mesh size (M_2) results in a stress distribution that is visibly identical to the one of the finest mesh. Similar conclusions can be drawn by comparing σ_1 among different time-steps (lower panel of Fig. H.2), where no visible differences can be perceived irrespective of the time-step.

To verify whether the agreement between all the meshes is consistent along the cardiac cycle, the surface-averaged σ_1 was computed over the aneurysm sac luminal surface, S^{l}_{ia}, defined as:

$$\langle \sigma_1 \rangle (t) = \frac{1}{A(S^{\mathrm{l}}_{ia})} \int\limits_{S^{\mathrm{l}}_{ia}} \sigma_1(\boldsymbol{x}, t) \mathrm{d}S^{\mathrm{l}}_{ia} \,. \tag{H.1}$$

Figures H.3a and H.3b show $\langle \sigma_1 \rangle$ for each mesh and time-step tested. The plots confirm that the differences between each mesh are negligible, especially between meshes M_2 and M_3, which further supports the use of mesh M_2. Regarding time-step, the plot shows a small gap between the curves of the time-step levels Δt_1 and Δt_2 and that of level Δt_3, mainly around the peak systole ($0.1 < \frac{t}{T_c} < 0.3$), nevertheless the percentual difference at the peak-systole between the levels Δt_2 and Δt_3 was, approximately, 0.77 %, with a mean percentual difference along the cardiac cycle of, approximately, 0.48 %.

The data shown in Figs. H.2 and H.3 and the considerations made above suggest that either time-step Δt_1 or Δt_2 are acceptable to be employed with mesh M_2 to yield mesh- and time-step independent results. To assess the discretization error of this selection, Richardson's extrapolation was used, based on meshes M_2 and M_3 for the spatial discretization error, and time-steps levels Δt_2 and Δt_3, for temporal discretization error (235). For a generic variable ϕ,

Richardson's extrapolation predicts that the exact solution, to a certain accuracy, is:

$$\phi_{exact} \approx \frac{r^p \phi_2 - \phi_3}{r^p - 1}, \tag{H.2}$$

where p is the formal order of accuracy of the discretization method and r is the ratio of cell sizes between the two discretization levels — $r = \dfrac{l_{e3}}{l_{e2}}$ and $p = 2$ for the spatial discretization using the FVM and $r = \dfrac{\Delta t_3}{\Delta t_2}$ with $p = 1$ for the temporal discretization where the first-order accurate Euler scheme was used.

In their review on the subject of verification and validation, Oberkampf et al. (236) explains that the extrapolated prediction can be also employed for integrated quantities of the primitive variables of the particular PDEs being solved. Hence, Eq. (H.2) was used to predict the discretization error of the surface-average and the maximum statistics of the wall displacement,

Figure H.2 – Largest principal Cauchy stress on the luminal surface of case urICA1 at peak systole for the three systematically-refined meshes (upper panel) and different time-steps (lower panel, using mesh M_2) (results obtained with the Yeoh hyperlastic law).

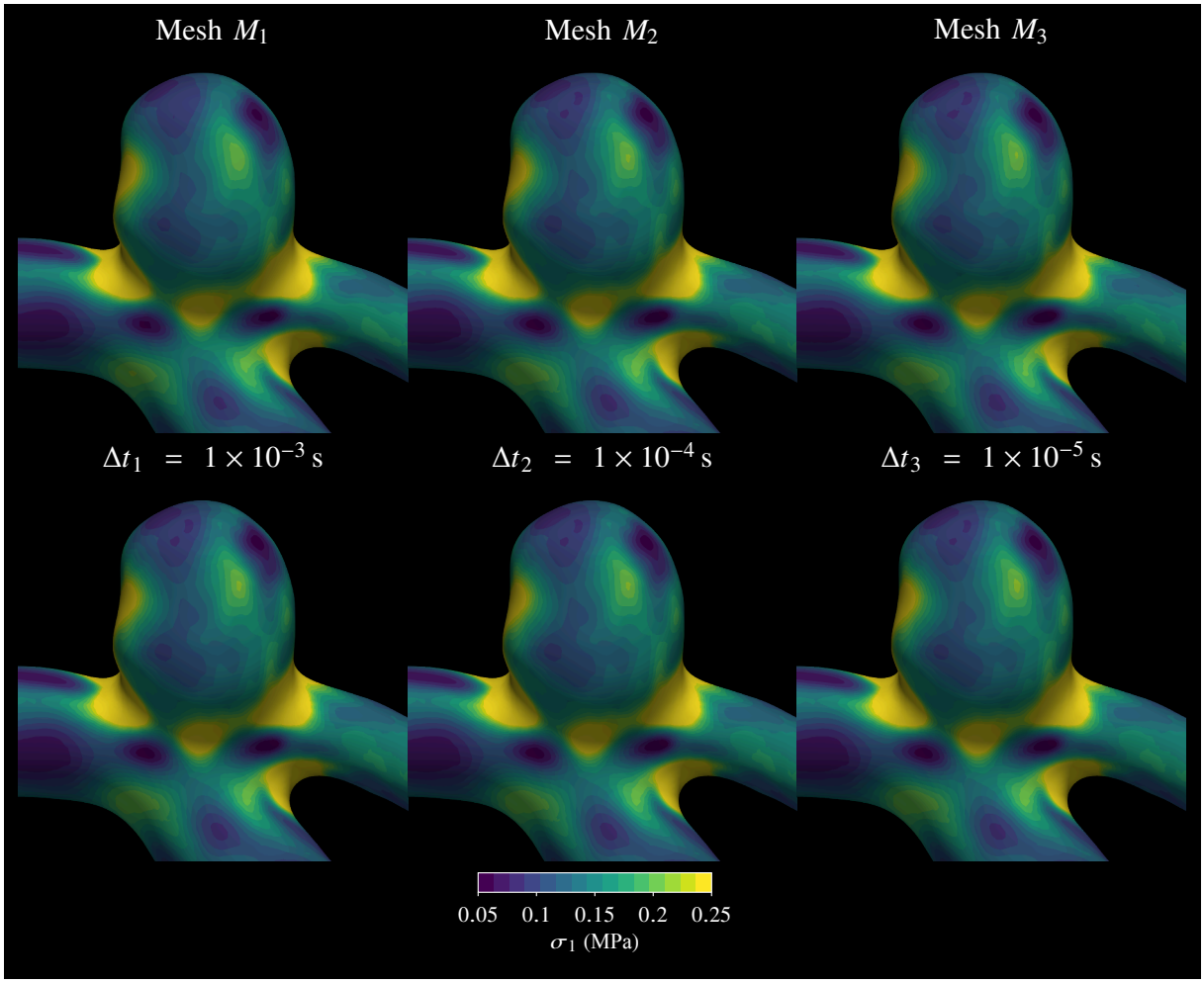

Source: Prepared by the author.

Figure H.3 – Surface-averaged σ_1 over time (show as a percentage of the cardiac period, T_c) on S^{l}_{ia} of the case urICA1 for (a) different spatial meshes and (b) different time-steps tested.

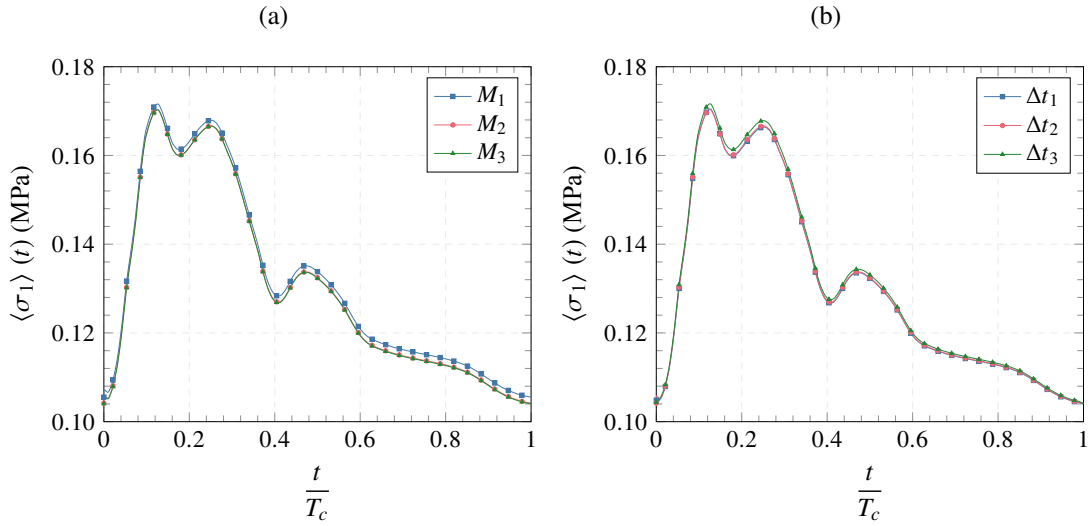

Source: Prepared by the author.

$\boldsymbol{u}$, the von Mises stress, σ_0, σ_1, and the largest eigenvalue of the stretch tensor, λ_1, on S_{ia}, shown in Tables H.2 and H.3, where the percentual error was defined as:

$$e^{\mathrm{R}}{}_i = 100.0 \times \frac{\phi_i - \phi_{exact}}{\phi_{exact}}, \tag{H.3}$$

where $i = 1, 2, 3$ indicates a discretization level.

Table H.2 – Surface-averaged and maximum values of selected variables on the aneurysm luminal surface, S^{l}_{ia}, of case urICA1, at peak systole for the three mesh levels, the Richardson's extrapolation computed from the meshes M_2 and M_3, and the discretization error for each mesh.

Statistic	Variable, ϕ	Absolute Value				Percentual Error, $e^{\mathrm{R}}{}_i$ (%)		
		M_1	M_2	M_3	ϕ_{exact}	M_1	M_2	M_3
$\langle\phi\rangle_{S_{ia}}$	u (mm)	0.2583	0.2557	0.2623	0.2664	3.0	4.0	1.5
	λ_1	1.038	1.037	1.037	1.038	0.020	0.028	0.045
	σ_0 (kPa)	169.0	167.9	167.9	168.1	0.57	0.075	0.12
	σ_1 (kPa)	171.5	170.3	170.2	170.3	0.72	0.029	0.047
$\max_{S_{ia}}(\phi)$	u (mm)	0.4199	0.4094	0.4197	0.4261	1.5	3.9	1.5
	λ_1	1.104	1.101	1.098	1.105	0.086	0.40	0.64
	σ_0 (kPa)	659.9	650.2	646.1	656.7	0.48	1.00	1.6
	σ_1 (kPa)	690.8	683.4	678.5	691.5	0.099	1.2	1.9

Source: Prepared by the author.

Both the stresses and the stretch show a smaller percentual discretization error than the displacement error. Mesh M_2 was accepted as sufficiently good also in light of Table H.2 because this work was maily concerned with analyzing the stresses and stretches on the IAs walls, hence an error of approximately 4 % for mesh M_2 was tolerated. It must be noted that

Table H.3 – Surface-averaged and maximum values of selected variables on S^{l}_{ia} of case urICA1, at peak systole for the three time-steps tested, the Richardson's extrapolation computed from the solutions with time-steps Δt_2 and Δt_3, and the discretization error of the solutions of each time-step.

Statistic	ϕ	Absolute Value				Percentual Error, $e^{\mathrm{R}}{}_i$ (%)		
		Δt_1	Δt_2	Δt_3	ϕ_{exact}	Δt_1	Δt_2	Δt_3
$\langle\phi\rangle_{S_{ia}}$	u (mm)	0.2549	0.2557	0.2544	0.2572	0.90	0.57	1.1
	λ_1	1.037	1.037	1.038	1.038	0.044	0.056	0.0056
	σ_0 (kPa)	168.1	167.9	169.2	169.3	0.73	0.81	0.081
	σ_1 (kPa)	170.4	170.3	171.6	171.7	0.76	0.86	0.086
$(\phi)_{max}$	u (mm)	0.4086	0.4094	0.4058	0.4134	1.2	0.97	1.8
	λ_1	1.101	1.101	1.102	1.102	0.063	0.067	0.0067
	σ_0 (kPa)	650.4	650.2	654.8	655.3	0.74	0.78	0.078
	σ_1 (kPa)	683.7	683.4	688.2	688.8	0.73	0.77	0.077

Source: Prepared by the author.

asymptotic convergence was not verified for the stresses and stretches, although this is expected, as explained by Oberkampf et al. (236), because *a-posteriori* variables, i.e. that are dependent of the primitive variables and computed after the PDE's solution, will probably need an extremely refined mesh to achieve the asymptotic convergence region. Furthermore, the errors shown in the table must also be viewed in light of strong nonlinearities and coupling present in the governing equations of the solid motion, which may hinder the application of Richardson's extrapolation.

Fluid Sub-problem

As mentioned in the main text, the computational meshes of the fluid sub-problem were tested extensively in previously published works and yielded a mesh with volumetric density of cells between 3000 and 4000 cells/mm^3 to be used. An example of the mesh-independence performed is reproduced here and based on a qualitative comparison of the TAWSS and OSI because the first is part of the forces interpolated to the solid wall during the pulsatile simulations and both fields are essential to the construction of the abnormal-wall model.

The fluid mesh convergence study was then performed by simulating three systematically finer meshes for each geometry (all cells were refined in this analysis). The total number of cells and the cell volumetric density are given in Table H.4 for case urMCA5.

The resulting TAWSS and OSI fields can be seen for case urMCA5 in Fig. H.4. Qualitatively, all meshes provide similar fields of the two variables, although small differences can be seen in the mesh M_1. Therefore, all meshes were build with at least the intermediate level size.

Additionally, because the TAWSS and OSI are defined on the luminal surface, a study of the

Table H.4 – Fluid mesh sizes and cells volumetric density for the meshes of case urMCA5 (the total volume of this geometry was approximately 386.72 mm^3).

Mesh Size	N_M	ρ_V (cells/mm^3)
M_1 (coarsest)	624,601	1615.1
M_2 (intermediate)	1,509,574	3903.5
M_3 (finer)	3,307,698	8553.2

Source: Prepared by the author.

Figure H.4 – TAWSS (top panel) and OSI (bottom panel) fields on the luminal surface of aneurysm case urMCA5 with computational meshes with the three computational meshes tested.

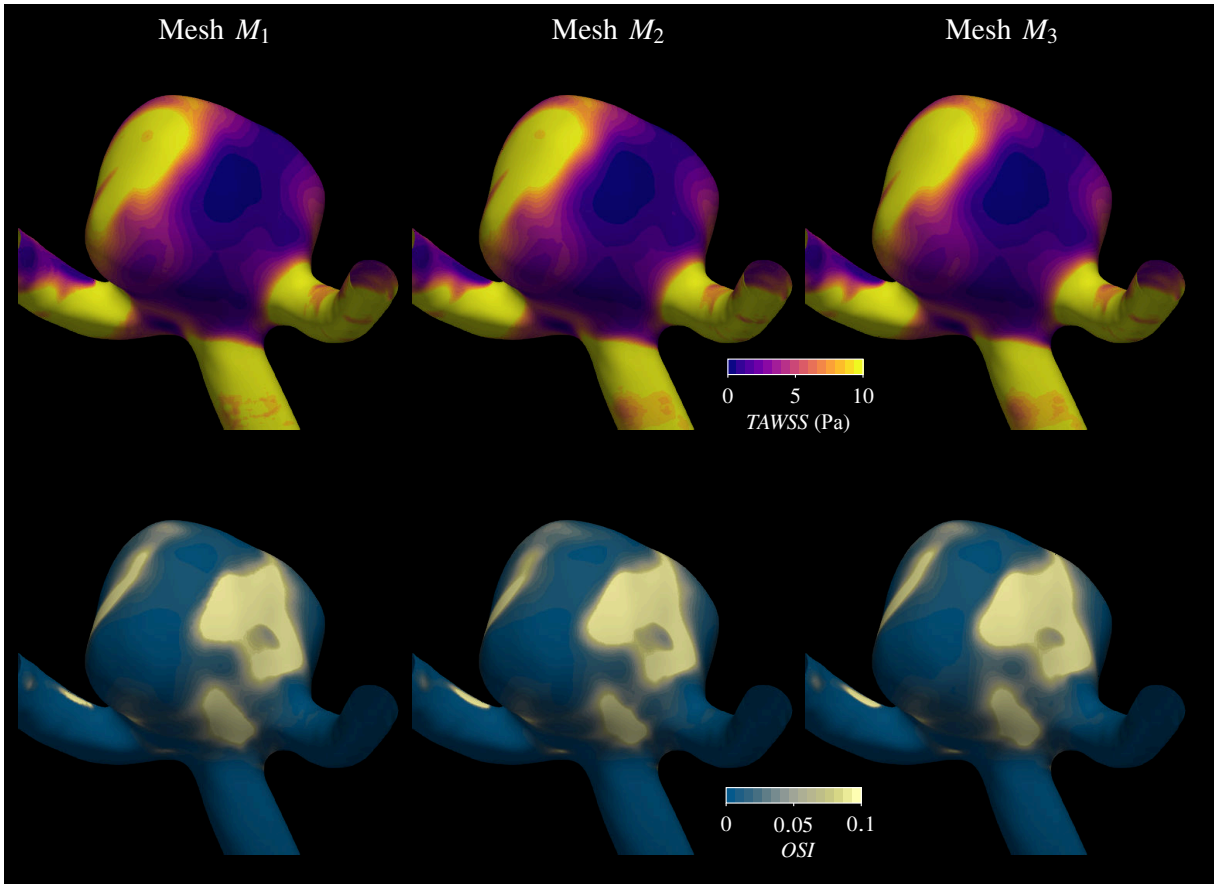

Source: Prepared by the author.

boundary-layer refinement influence was carried out with a number of layers of 4, 8, and 12, also for case urMCA5. Although not presented here, these results did not show any differences in the TAWSS and OSI for different numbers of layers.

Finally, a time-step convergence analysis was also performed with systematically smaller time-steps: 1×10^{-4} s, 1×10^{-5} s, and 1×10^{-6} s. The differences between the time-steps were even less perceptible then when comparing different meshes and thus were not shown here. A time-step of 1×10^{-4} s was then used for consistency with the value used for the solid sub-problem.

Appendix I

PARAMETRIC STUDIES OF WALL-RELATED VARIABLES

The decisions when modeling arterial and IAs wall tissue were particularly challenging, not only due to the lack of experimental measures of certain physical parameters — such as the tissue mechanical properties —, but also to the lack of agreement on the BCs that should be employed on the vascular wall's motion, in view of the literature on the subject.

To fill such gaps and bring more robustness to this work, a better understanding of the impact of the BCs at the artificial sections made at the arterial branches and the compressibility of the arterial model on the mechanical response was sought through a series of numerical parametric tests whose results are presented in this chapter.

I.1 BCs AT THE BRANCHES SECTIONS

Due to the "cuts" that needed to be performed at sections of the arteries to delimit the region where a specific IA grew (see Chapter 4), the BCs specified at these locations are of special importance, since the most correct one is not known. The majority of the literature on the subject of the numerical modeling of FSI in blood flowing through arteries with IAs model these sections with fixed sections, Eq. (5.80) (24, 127, 117, 139, 133), i.e.:

$$\boldsymbol{u} = \mathbf{0}, \tag{I.1}$$

where $\boldsymbol{u}$ is the solid displacement field — referenced herein as "zero-displacement BC". A few used a BC that allows the arterial branch to slide along its tangential, but constrains the displacement along its normal, i.e. a zero-fixed normal displacement with zero shear traction,

as given by Eq. (5.81):

$$\begin{aligned} \boldsymbol{n}^{\mathrm{s}} \cdot \boldsymbol{u} &= 0 \\ \boldsymbol{t}^{\mathrm{s}} - (\boldsymbol{n}^{\mathrm{s}} \cdot \boldsymbol{t}^{\mathrm{s}})\, \boldsymbol{n}^{\mathrm{s}} &= \boldsymbol{0}, \end{aligned} \tag{I.2}$$

where $\boldsymbol{n}^{\mathrm{s}}$ is the outward normal to the boundary and $\boldsymbol{t}^{\mathrm{s}} = \boldsymbol{n}^{\mathrm{s}} \cdot \boldsymbol{\sigma}^{\mathrm{s}}$ is the traction on the boundary, $\boldsymbol{\sigma}^{\mathrm{s}}$ being the Cauchy stress in the solid domain. Equation (I.2), mentioned herein as "zero-shear BC", can be thought of as a more realistic BC because it allows the branch to move normally to its longitudinal direction (131). No study was found that assessed the influence of these different BCs on the motion and on the stresses in an IA or arteries walls, only a suggestion made by Bazilevs et al. (121) noting that "the effect of this boundary condition [i.e. Eq. (I.2)] on the wall shear stress and wall tension appears to be minor" (the reference the authors cite at this point in their paper mention "private communication").

To assess this influence on an IA wall complete mechanical response, numerical simulations were carried out in solids4foam using a simplified modeling of the wall motion and the two BCs shown in the preceding paragraph. The motion of the vascular wall was assumed to be under conditions similar to "inflation experiments", where the vessel is subjected to uniform outer and inner pressures — these were already used to study the mechanical properties of IAs (68) and also as a modeling approach in numerical simulations (139). Figure I.1 shows a schematic representation of this model. The inner surface was subjected to a time-varying pressure corresponding to the physiologically normal cardiac cycle, i.e. from 80 to 120 mmHg (approximately 10 to 16 kPa), shown in Fig. 5.3b. On the outer surface, a pressure of p_o = 5 mmHg, corresponding to the intracranial pressure, was imposed.

The uniform IA wall morphology model was employed to predict the wall thickness, hence a

Figure I.1 – Schematic 2D drawing of the vascular wall domain, Ω^{s}, and the BCs applied in the pressure-inflation modeling of the vascular wall.

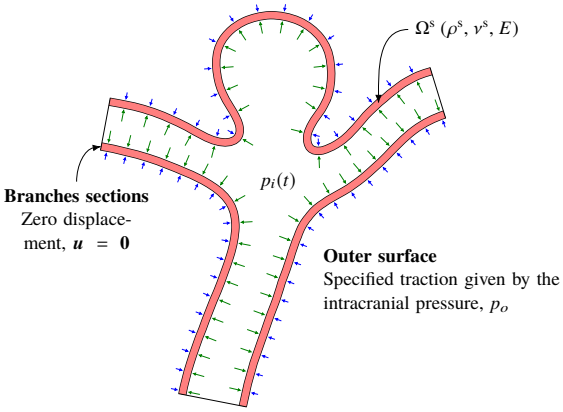

Source: Prepared by the author.

uniform thickness on the IA sac and a lumen-diameter-dependent thickness field on the branches (see Section 5.3.8), whereas the material properties were assumed uniform throughout the vascular domain for simplicity. To avoid large simulation duration, a simpler hyperelastic law, the classical neo-Hookean material law, was used, in which the Cauchy stress is given by:

$$J\boldsymbol{\sigma} = \frac{\kappa^{\mathrm{s}}}{2}\left(J^2 - 1\right)\boldsymbol{I} + \mu^{\mathrm{s}}\,\mathrm{dev}\,\boldsymbol{B}^{*}\,. \tag{I.3}$$

The first Lamé's constant, μ^{s}, depends on the Young's modulus, assumed $E = 1\,\mathrm{MPa}$, and Poisson's ratio, assumed $\nu^{\mathrm{s}} = 0.45$, (see Eq. (C.28)) values typically employed to characterize rubbery materials and that already have been used to model arteries and IAs tissue (131). The model's density was the same used in the simulations presented in the main text $\rho^{\mathrm{s}} = 1200\,\mathrm{kg/m^3}$.

Figure I.2 shows the displacement magnitude field, $u(\boldsymbol{\xi})$, and the largest principal value of the Cauchy stress field, $\sigma_1(\boldsymbol{\xi})$ — Lagrange coordinates, $\boldsymbol{\xi}$, were made explicit to highlight that the results are displayed in the reference geometry — for cases urICA1, rICA2, and urMCA2, respectively, at the peak systole. Both the surface-averaged and the 99-percentile of the σ_1 distribution and the 99-percentile of the u distributions over the IA sac are also shown next to each aneurysm in the figure.

As expected, the displacement fields are different between each BC (upper panel of Fig. I.2) because the motion is less constrained by the zero-shear BC than by the zero-displacement one. Hence, the former has more degrees of freedom as, in this case, it is allowed to translate and rotate when the zero-shear BC is employed. However, this does not seem to impact the strain measures, as can be confirmed by inspecting the left and right Cauchy-Green deformation and the stretch tensors (not shown here for the sake of space), or the stress (lower panel of Fig. I.2). Note that both 99-percentile and the surface-average are similar, with a mean percentual difference between the zero-shear and zero-displacement of $1.76 \pm 0.18\,\%$, for $\langle\sigma_1\rangle$, and $2.67 \pm 1.13\,\%$, for $(\sigma_1)_{99}$. The stretch fields were also analyzed and have shown similar results.

Therefore, the impact on σ_1 on the IA surface is small and not visually perceptible in the σ_1 fields shown in Fig. I.2. The only exception occurs in an annular region adjacent to the section boundaries, where, with the zero-shear BC, they are allowed to expand and/or contract radially over the cardiac cycle, increasing the stresses there. However, this effect quickly fades towards the aneurysmal region.

Therefore, although the BC produce different results in a small portion of the geometries, if the sections locations are *far enough* of the aneurysmal region, the results suggest that it seems

Figure I.2 – Displacement magnitude, u, (upper panel) and σ_1 (lower panel) fields at peak systole for the zero-displacement and the zero-shear BCs applied at the branch sections (data on the lumen surface at the reference configuration for the neo-Hookean model for cases urICA1, rICA2, and urMCA2).

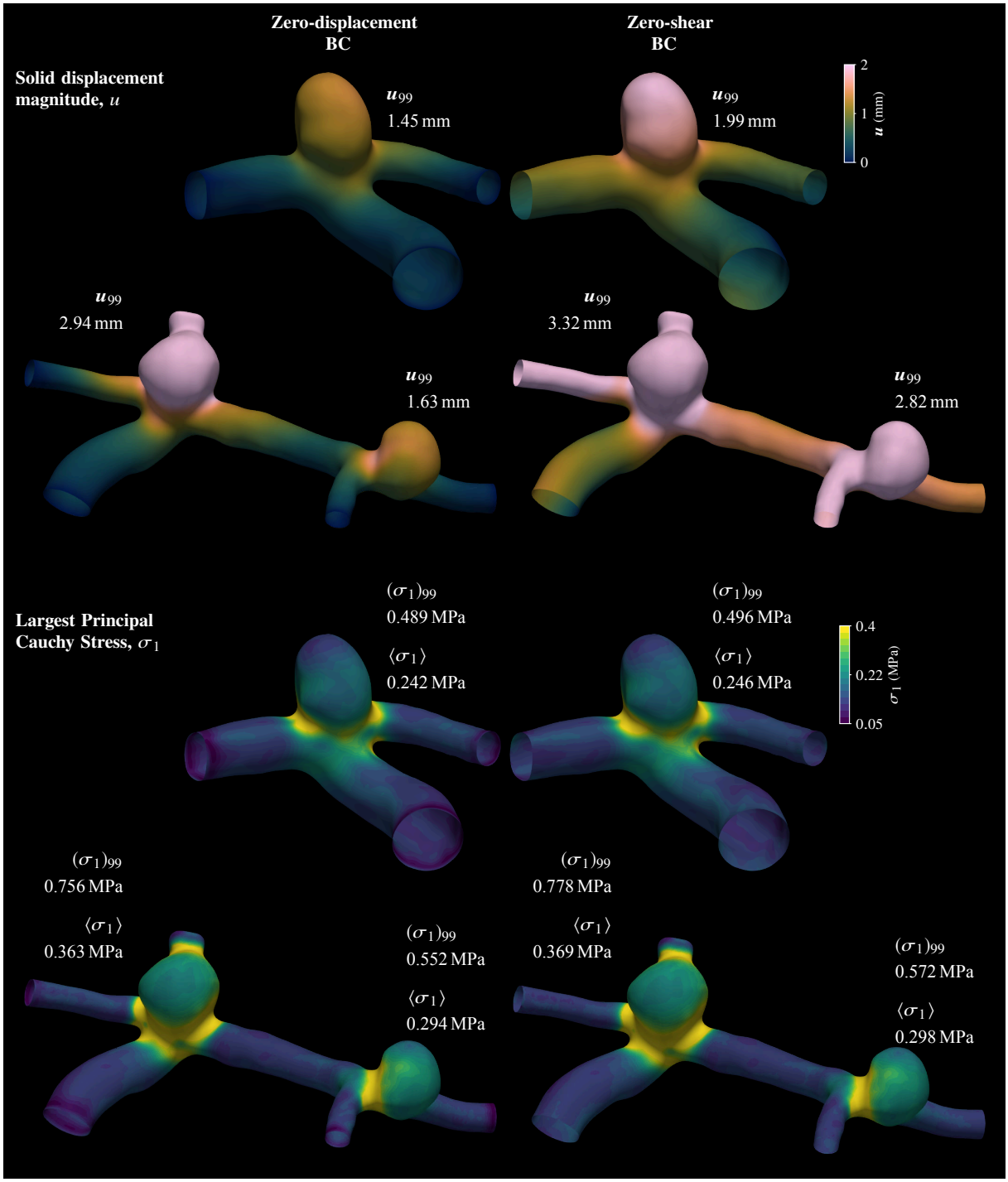

Source: Prepared by the author.

to be reasonable to use the zero-displacement BC to simulate the motion of IAs geometries, at least if the variable under study is the stress and/or the stretch.

How *far* from the IA is actually enough is harder to assess for a large number of cases, but the three cases studied here may give some guidance, once they indicate that the position of the

sections made for them is far enough to yield similar once on the statistics of the stresses on the IAs sac. The distance of the sections to each IA was measured by computing the geodesic distance to the IA neck line along the branches surface, g_n (used in the computation of the aneurysm sac surface, Section 5.3.8), and dividing it by the local vascular lumen diameter, d_l. This ratio is clearly defined only on the branches surface, S_b, and it is shown for cases urICA1, rICA2, and urMCA2 in Fig. I.3.

Figure I.3 – Ratio between the distance to neck line, g_n, and the lumen diameter, d_l, defined on S_b, for cases urICA1, rICA2, and urMCA2.

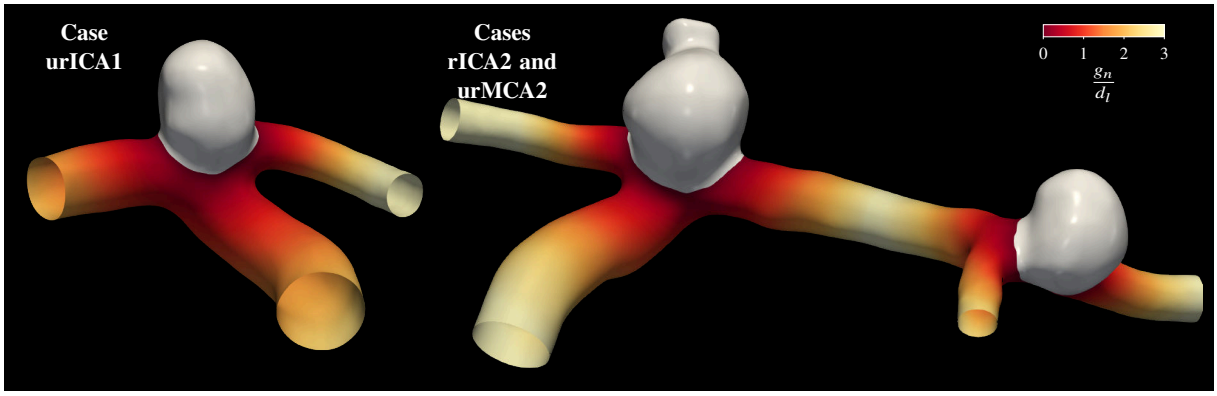

Source: Prepared by the author.

Clearly, the sections are at least two local diameters away from the IAs neck lines, which suggests that this limiting value could be used to safely assume that the zero-displacement BC will not influence the stress and stretch distribution on the IA. For all the models used in the simulations, this value was assured for all the branches, including the parent artery.

This conclusion had a strong impact on computational times reported in the main text. The zero-shear BC takes relatively longer to converge per time-step than a similar simulation with the zero-displacement BC. For instance, the average number of outer iterations per time-step for convergence is 180 with the zero-displacement BC whereas the zero-shear one required, on average, 1000, when convergence is reached in all time-steps. Hence, a gain in performance of at least 5 times, on average.

I.2 TISSUE COMPRESSIBILITY

As mentioned in the main text, soft tissues such as arteries are incompressible solids, an assumption normally assumed for IA tissues as well. Mechanically, this modeling translates to a restriction to the motion known as the incompressibility constraint (see Section D.1), which poses severe difficulties to numerically solve for the tissue displacement with segregated

algorithms, such as the one employed in this work. To overcome this issue, the multiplicative decomposition approach was used to model the volumetric part of the tissue motion, where the compressibility was ultimately measured by the Poisson's ratio of the tissue, ν^{s}, through the bulk modulus, κ_{s} (see Eq. (5.72), the incompressible limit, mathematically represented by $\kappa_{\mathrm{s}} \rightarrow \infty$, can be reached through $\nu^{\mathrm{s}} \rightarrow 0.5$).

Thus, to assess the influence of the compressibility on the tissue's mechanical response, a parametric study was performed by varying ν^{s} in the volumetric part of the model from 0.45 to 0.49, incrementally by 0.01. The three hyperelastic laws were tested using the 1WFSI strategy and, for the sake of computational time, a steady-state regime was used to model the blood flow where the inflow rate was chosen at peak-systolic conditions of the cardiac cycle. This simplifying hypothesis is suitable because the effect of compressibility would not change due to the temporality of the pulsatile flow. Five simulations were then carried out for each hyperelastic law for a single IA case, urICA1.

First, it is important to assess the impact of ν^{s} on the convergence rate of the solid's numerical model. As already mentioned in the main text, segregated algorithms employed to solve the momentum equation exhibit an increasingly tougher convergence as $\nu^{\mathrm{s}} \rightarrow 0.5$. This was confirmed for the nonlinear models used in this work, as can be seen in Fig. I.4. Irrespective of the hyperelastic law, the number of iterations to converge, at a momentum equation's normalized residual level of 1×10^{-9}, was at least 1000 (Yeoh's law, $\nu^{\mathrm{s}} = 0.46$) and up to 9920 (Fung's law, $\nu^{\mathrm{s}} = 0.49$). Although it was already verified that in the pulsatile simulations the number of iterations per time-step is much smaller due to the time-step size, the relative behavior of convergence is most certainly the same. Therefore, it would be prohibitively expensive to simulate a case with $\nu^{\mathrm{s}} > 0.49$ with the current employed methodology, and consequently a nearly-incompressible modeling was used instead.

Due to this simplifying limitation, it was important to assess how the mechanical response would be affected by the selection of a ν^{s} smaller than 0.5. The largest principal stress, σ_1, and largest principal stretch, λ_1 were investigated to that end, because they were the main variables studied. Additionally, the solid displacement magnitude, u, was also analyzed here because it is the single primitive variable of the solid's motion problem.

Fig. I.5 shows the σ_1 and λ_1 fields over the aneurysm sac luminal surface of case urICA1 for ν^{s} equals to 0.45, 0.48, and 0.49. There are clear differences in the patterns of both variables for different ν^{s}, nonetheless the overall patterns of stress and stretch are very similar.

Figure I.4 – Residuals drop in the simulation of each hyperelastic law varying with ν^s (the annotations in the plots indicates the convergence values of the cases that go beyond the plot's area).

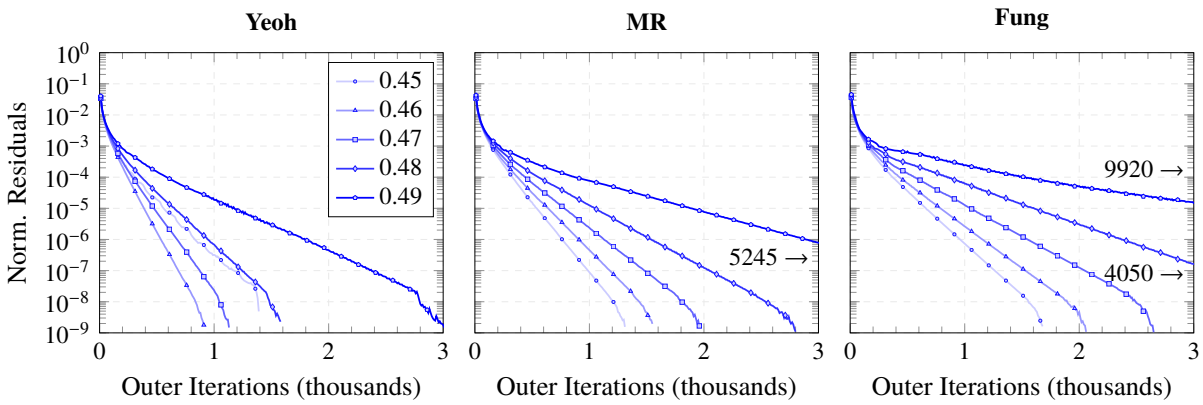

Source: Prepared by the author.

Figure I.5 – Largest principal stress, σ_1, (upper panel), and largest principal stretch λ_1, (lower panel), for IA case urICA1 for Poisson's ratio of 0.45, 0.48, and 0.49, using the Yeoh hyperelastic law and steady-state flow at peak-systole flow conditions.

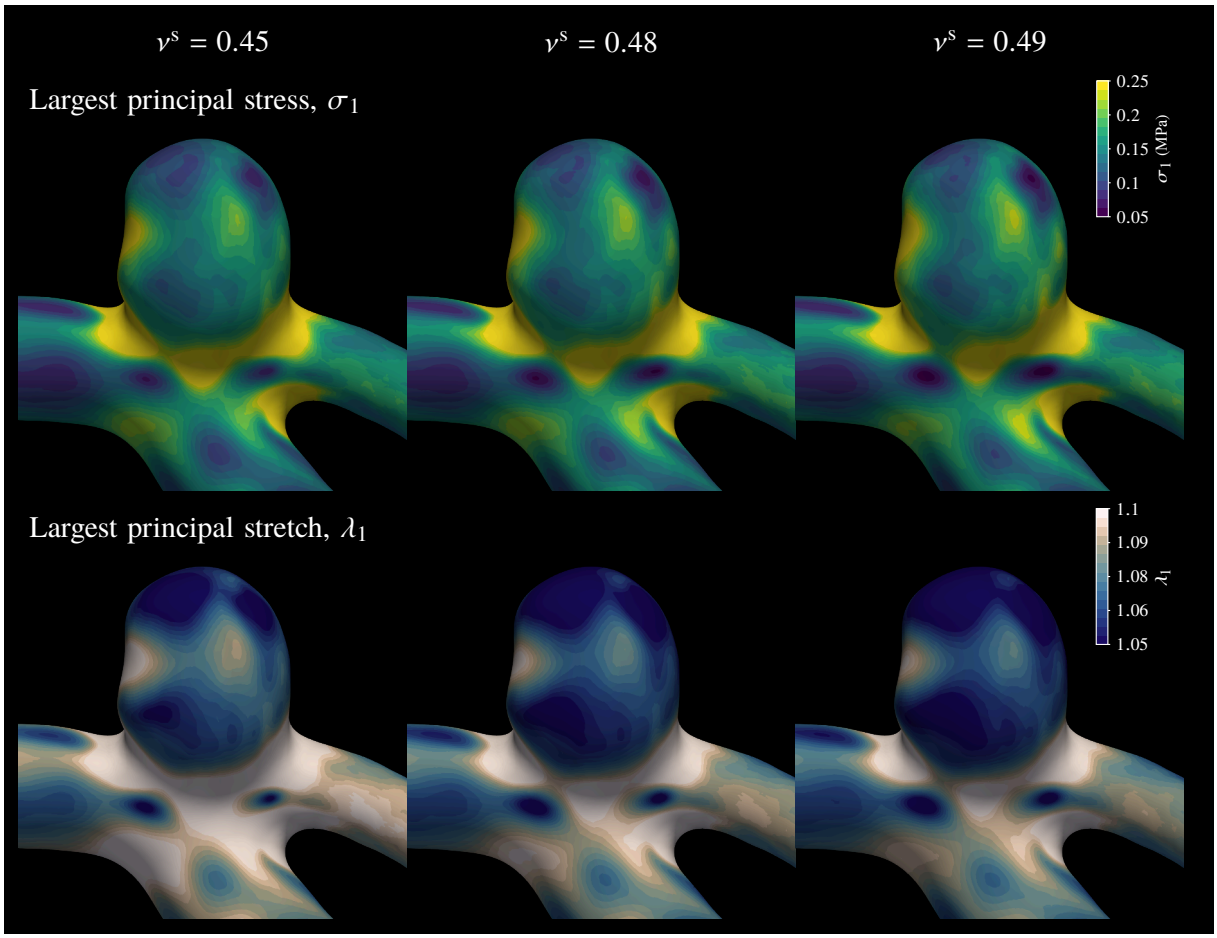

Source: Prepared by the author.

Figure I.6 shows how the surface-average and the 99-percentile statistics of σ_1, λ_1, and u over S^{l}_{ia} change with ν^s. The behavior of each variable are considerably different, but consistent among the different hyperelastic laws. For example, $\langle\sigma_1\rangle$ remains almost unchanged up to

$\nu^s = 0.48$ where it shows a slight inflection. The same is observed for $(\sigma_1)_{99}$, although an increase of σ_1 with ν^s is more evident.

Figure I.6 – Surface-averaged (upper panel) and 99-percentile (lower panel) of σ_1, λ_1, and u over the IA sac surface, S_{ia} versus ν^s for different hyperelastic laws.

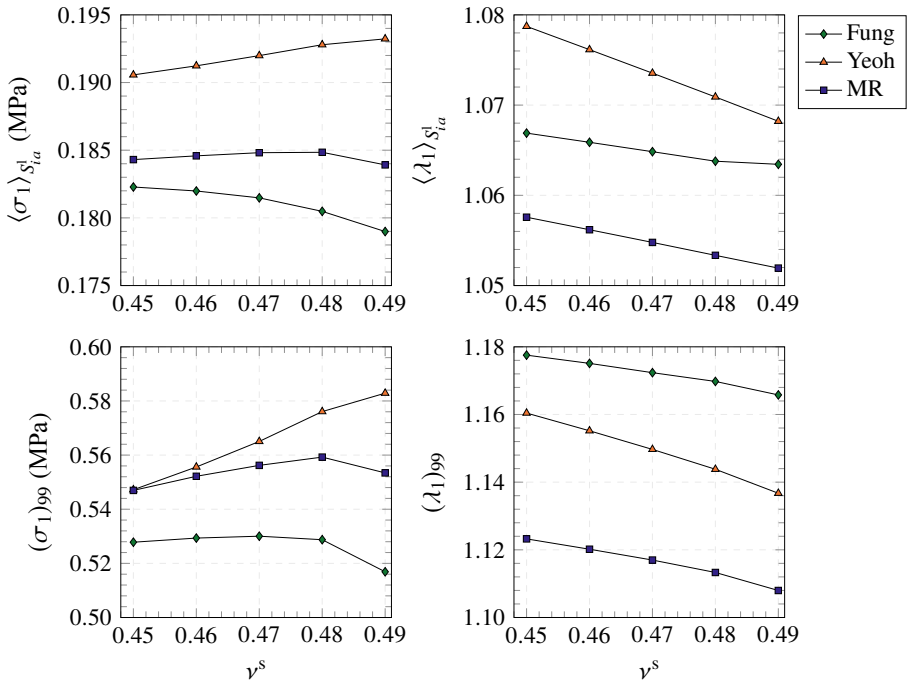

Source: Prepared by the author.

On the other hand, both $\langle\lambda_1\rangle$ and $(\lambda_1)_{99}$ decrease with ν^s, but at a very small pace, with the maximum relative difference between $\nu^s = 0.45$ and 0.49 of, approximately, 2.1 % for the Yeoh's law, as can be seen in Table I.1, which shows the percentual difference between each metric between the results with $\nu^s = 0.45$ and 0.48 and the reference value 0.49 — i.e. the value closest to 0.5. However, the displacement shows the largest variations as $\nu^s \to 0.49$, of up to 35 % for the Fung's law ($\langle u\rangle$ when comparing $\nu^s = 0.45$ and 0.49). Interestingly, the Fung's law shows a sharp increase of both u metrics when $\nu^s > 0.48$. Furthermore, although big variations in u were found, the plots of Fig. I.6 confirms that volumetric locking did not occur for this type of simulation.

Rigorously, the ideal approach would be to solve $\nu^s > 0.49$ to find a solution as close as possible to the incompressible limit. However, in view of the convergence behavior shown in Fig. I.4, a value of 0.48 was employed for ν^s for all the simulations to strike a balance between *realizability* — i.e. to get results at a reasonable amount of time — and an accurate solution, because for this value of ν^s both σ_1 and λ_1 differ less than 3 % in terms of the statistics chosen. Furthermore, as evidenced by Fig. I.5, both fields of σ_1 and λ_1 remain very similar.

Table I.1 – Relative difference of two statistics — surface-average and 99-percentile, over S_{ia} — between distributions for results of $\nu^s = 0.45$ and 0.48 relative to 0.49 of the three variables: u, σ_1, and λ_1.

Percentual Difference	Metric, $\mathcal{M}$	σ_1			λ_1		
		MR	Yeoh	Fung	MR	Yeoh	Fung
$\frac{\mathcal{M}_{0.45} - \mathcal{M}_{0.49}}{\mathcal{M}_{0.49}}$, %	$\langle\phi\rangle_{S_{ia}}$	0.213	1.38	1.84	0.536	0.985	0.325
	ϕ_{99}	1.17	6.12	2.11	1.38	2.09	1.01
$\frac{\mathcal{M}_{0.48} - \mathcal{M}_{0.49}}{\mathcal{M}_{0.49}}$, %	$\langle\phi\rangle_{S_{ia}}$	0.507	0.224	0.834	0.135	0.252	0.0324
	ϕ_{99}	1.05	1.17	2.29	0.481	0.624	0.342

Source: Prepared by the author.

I.3 LOCAL THICKNESS AND MATERIAL CONSTANTS

The "abnormal wall morphology model", i.e. based on the abnormal hemodynamic conditions in the aneurysm lumen, depended on the adjustment of both aneurysm thickness, e_{ia}, and material constants, c_{ij}, for each hyperelastic law, on the type-I and type-II patches of S^{l}_{ia}. As depicted in Fig. 5.4, type-I patches were assumed 5 % thinner and 20 % stiffer, whereas type-II patches were 20 % thicker and 20 % stiffer, although no supporting evidence, indicating these particular values, was found in the literature — except for ranges of how thick atherosclerotic plaques can be in IAs walls, up to 50 % thicker. Consequently, it was natural to ask what would be the influence of these local increments of e_{ia} and c_{ij} on the mechanical response of an IA wall motion.

In this regard, two parametric studies were carried out by changing those percentage values and simulating the mechanical response of the IA wall. Similarly to the compressibility study, presented above, a steady-state blood flow model at peak-systole conditions was assumed as the driven force of the arterial and IA wall motion, and also numerically solved with the 1WFSI strategy with the same BCs presented in Chapter 5. Although only the Yeoh hyperelastic law was used — it is reasonable to assume that the same behavior would be found for the MR and Fung laws, as it was the case, e.g., with the different Poisson ratios in Fig. I.6 —, with $\nu^s = 0.48$. The study was carried out in two stages: first, by varying e_{ia}, locally, and, in the sequence, changing the fields of the material constants, c_1 and c_2. Due to the relevance of this particular study for the main results of this work, all geometries of the IA sample presented in Section 4.2 were simulated — this was facilitated by the relatively small computational time required by the steady-state modeling of the flow.

In the first stage, uniform material constants over the aneurysm, c_1 and c_2, were assumed to

isolate the effect of the varying e_{ia} on each patch type, calculated as follows:

1. on type-I patches, e_{ia} was first kept unchanged and then decreased by 5, 10, 20, and 30 %, while keeping the type-II patches 20 % thicker;

2. on type-II patches, e_{ia} was first kept unchanged and then increased by 5, 10, 20, and 30 %, while keeping the type-I patches 5 % thinner.

The computational meshes were created similarly as in the main study (see Section 6.4), but, in this case, for each new thickness field, a new mesh was generated, whereas a single fluid computational mesh was used.

In the second stage, uniform e_{ia} was assumed over S^{l}_{ia} — thus, a single mesh was used — to isolate the effect of varying the material constants, c_1 and c_2, which were both, first, kept uniform and, then, decreased by 10, 20, and 30 %, on type-I and type-II patches at the same time.

Note that the parametric intervals employed ($[5\,\%, 30\,\%]$) included the actual values selected for the abnormal wall morphology model. The surface-averages of σ_1 and λ_1 were computed over S^{l}_{ia} at the deformed configuration. The results are shown in Fig. I.7.

The plots show how $\langle \sigma_1 \rangle_{S^{\mathrm{l}}_{ia}}$ and $\langle \lambda_1 \rangle_{S^{\mathrm{l}}_{ia}}$ changed with both local changes in e_{ia} and c_{ij}. The absolute difference between the extremes of the parametric intervals was computed for each IA case, and its average annotated above each plot. As can be seen, a maximum absolute difference of 22.5 kPa and 4.13×10^{-3}, respectively, were found when the thickness of type-II patches was varied — all the other yield smaller differences. Most importantly, the variation induced by focal changes in thickness and material constants were consistent among all IAs.

Figure I.7 – Surface-averaged σ_1 (left column) and λ_1 (right column) over S^{l}_{ia}, grouped by rupture status, versus the percentual variation of e_{ia} (first row) and material constants, c_{10} and c_{20}, (second row) applied separately on type-I and type-II patches. Above each plots is annotated the mean maximum absolute difference among all IAs.

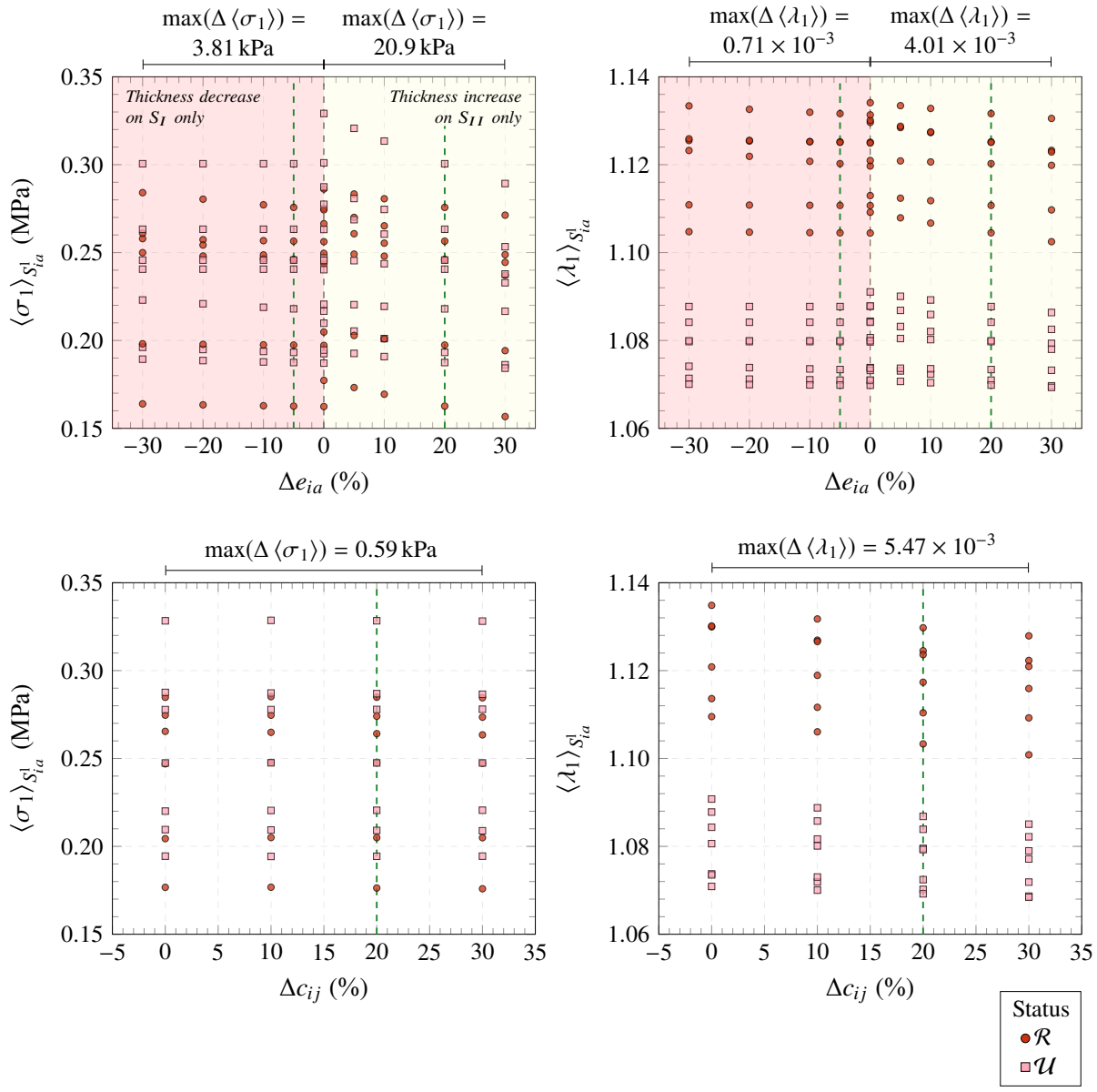

Source: Prepared by the author.